HYDROLOGY AND SOLUTE TRANSPORT OF OXIDISED WASTE ROCK FROM STRATMAT SITE, N.B.

MEND Report 2.36.2b

This work was done on behalf of MEND and sponsored by
Noranda Inc. as well as
The Probince of New Brunswich, and
The Canada Centre for Mineral and Energy Technology (CANMET)
Through the Canada/New Brunswich Mineral Development Agreement (MDA)

March 1999

FINAL REPORT

HYDROLOGY AND SOLUTE TRANSPORT IN OXIDISED WASTE ROCK FROM STRATMAT SITE, N.B.

Prepared for

CANMET - MMSL Division
Natural Resources Canada
555 Booth Street, Ottawa, Ontario K1A 0G1
PWGSC Contract No. 23440-4-1316/01-SQ

by

M. Li
Noranda Inc., Technology Centre
240 Hymus Blvd., Pointe-Claire, Québec H9R 1G5

March 1999

noranda

EXECUTIVE SUMMARY

This report documents the results of the second part of a research project jointly funded by Noranda Inc. and the Mine Environment Neutral Drainage program. The first part is covered in a separate report entitled *Hydrogeochemistry of Oxidised Waste Rock from Stratmat Site, N.B.*, published concurrently with this report. The overall objective of the project was to understand the geochemical and hydrological interactions between partially oxidised waste rock and water, and to improve our capabilities and techniques in the prediction of acidic drainage from waste rock piles.

The main objective of this part of the research was to understand the hydrology and solute transport within waste rock piles during infiltration and drainage events in response to precipitation. Large column tests were conducted to achieve this objective. Three columns measuring 1.2 m in diameter and 2 m in height and containing up to 3.7 t of partially oxidised Stratmat waste rock were subjected to ten rain simulations. The bottom area of each column was divided into drainage partitions. During and after each rain simulation, the volume and the chemistry of the drainage in each partition was monitored independently over time.

Geochemically, the experimental results suggest that the concentrations of Ca, Pb, and Al in the drainage are solubility-controlled by gypsum, anglesite, and jurbanite, respectively. In contrast the concentrations of Zn, Fe, and SO_4^{2-} in the drainage are not subject to solubility controls. A dilution hypothesis is proposed to explain the concentration variations of Zn and SO_4^{2-}. The hypothesis states that the variations of these concentrations and the pH are a result of successive dilutions and/or intermixing of various-stage dilutions of the original pore water, subject to the regulation by redox reactions and mineral precipitation. All soluble zinc seems to originate from the pore water and not from dissolution of secondary minerals. The zinc loading in the drainage is a function of the mass transfer that occurred during dilution and mixing processes.

Hydrologically, the experiments have demonstrated that channelling is a ubiquitous phenomenon in the waste rock studied. Large channels representing < 5% of the total drainage area conduct 20-30% of the total drainage flow. Intermediate-size channels accounting for ~20% of the drainage area carry ~ 40% of the total flow. About 50% of the drainage area has background or matrix flows that carry ~30-40% of the total flow. Finally, ~30% of the column base area does not intercept any flow. Channelling is more pronounced in earlier stages of drainage events and tends to attenuate as the draining process continues. Channel stability is influenced by variables related to the rock bed properties and simulated rain characteristics.

On solute transport, the Zn mass balance shows an efficiency of Zn removal from the pore water that is comparable to the efficiency of a well-mixed system. Whereas the mechanism giving rise to this observation is unclear, it is unlikely that the transport of solutes takes place by pore water displacement. There is no simple relation between solute concentrations and drainage flow rates. A conceptual dendritic-reticulate channelling model is proposed on the basis of the experimental observations.

Statistical analysis suggests that the flow density and the zinc loading can be appropriately described by the lognormal distribution, whereas the Zn concentrations are distributed normally.

The main challenges in flow and solute transport modelling are channelling and interactions between flows and geochemical processes. In this study, porous media flow rock is differentiated from channelling flow rock based on hydraulic properties. Furthermore, five basic component structures that make up a waste rock pile are identified. Each structure has distinct characteristics and should be modelled with different approaches. Factors influencing water flows and flow effects contributing to flow heterogeneity are discussed. A mathematical representation of channelling phenomena is developed, which can be coupled with statistical relationships between solute concentrations and flow rates to model solute transport in waste rock piles.

The kinematic wave model, recommended by an earlier MEND study, was applied to the experimental data. The model did not appear to adequately predict the channelling flow characteristics of the waste rock. It over-predicted the extent of larger channel flows at the price of smaller channel flows. The lack of applicability probably stems from the fact that the kinematic wave model precludes merges and splits of flows within waste rock. The model may be more appropriate to coarser waste rocks.

Further fundamental research and case studies are needed to advance our understanding of flow and solute transport in waste rock piles to a point where concentrations and loadings in the drainage can be reliably modelled.

TABLE OF CONTENTS

LIST OF TABLES

LIST OF FIGURES

LIST OF APPENDICES

1.0 INTRODUCTION

1.1 RESEARCH OBJECTIVES

In this study, large column tests were conducted to understand the hydrology and solute transport in partially oxidised Stratmat waste rock that is subjected to infiltrating water and to improve our capabilities and techniques in the prediction of acid rock drainage (ARD) from waste rock piles. The specific objectives were as follows:

- to observe and to attempt to quantify hydrological and solute transport phenomena in the partially oxidised Stratmat waste rock,
- to study the main factors and processes controlling the concentrations and loadings of dissolved species in the drainage in response to simulated rain, and
- to attempt to model the drainage chemistry and loadings and, in particular, to test the applicability of a specific model (the kinematic wave model) to the experimental data.

Variables for the large column tests included the waste rock bed thickness, the precipitation intensity and duration, and the mode of simulated rain application.

1.2 ROLE OF CHANNELLING AND SOLUTE TRANSPORT IN ARD PREDICTION

The requirements for acid rock drainage (ARD) prediction for waste rock piles vary with the intended end use of the information to be generated. According to the time frame for which the prediction is to be made, it can be short-term, mid-term, and long-term. According to the level of details required, ARD prediction can entail a range of tasks, listed below in increasing degree of complexity:

1. Predicting whether a waste rock will ever become acid-generating (yes/no),
2. Predicting how soon a potentially-acid generating rock will become acidic (lag time),
3. Predicting the long-term trend in acidity loadings from a waste rock pile,
4. Predicting the temporal variations in contaminant loadings and water quality (i.e. contaminant concentrations) over time.

The first two tasks can usually be accomplished by means of laboratory tests (such as acid base accounting and humidity cells) of representative waste rock samples, supplemented by field weathering tests when necessary.

Task 3 normally involves two steps. The first step is the collection of data for deriving the values of input parameters necessary for running a model of choice. The data collection may involve a full characterisation of the waste rock pile with respect to its chemical and physical properties, meteorological information, and so forth. When the waste rock pile is sufficiently heterogeneous, the spatial distribution of relevant chemical and physical properties must be considered. If the purpose of ARD prediction is to compare different control or abatement alternatives, the input parameter values must be accordingly modified to reflect the specificity of each alternative when the alternative is modelled. The second part is application of the model. The model must have a minimum of two parts: one kinetic oxidation module to predict the rate of sulphide oxidation and acidity generation, and another to predict the transport of the contaminants generated from sulphide oxidation and subsequent reactions. In some cases, one may reasonably assume that all soluble products of oxidation and neutralisation are completely flushed out annually by rain and there is no net accumulation in the waste rock pile. In this instance information regarding flow heterogeneity (i.e. channelling) is not required. In other cases, the net accumulation (which forms the “geochemical reservoir”) within the waste rock pile cannot be neglected, and information on flow heterogeneity is required to predict loadings from the waste rock pile. At the present status of science and with currently available models, prediction of long-term loadings is possible but the uncertainty associated with the prediction results is generally high.

Task 4 is generally impossible to accomplish at the present time. A first step towards achieving this task is the understanding and quantification of flow heterogeneity and its interaction with pore water and soluble minerals. If the channelling phenomenon and its effects on solute transport could be modelled and the geochemical reservoir in the waste rock pile can be sufficiently characterised, then task 4 may be accomplished for the very short term.

Increasing our understanding and capability of modelling the channelling and solute transport phenomena will likely advance our capability of accomplishing ARD prediction tasks 3 and 4 above. This is but one of the important reasons for studying channelling and solute transport in waste rock piles.

1.3 LITERATURE REVIEW ON FLOW AND SOLUTE TRANSPORT IN WASTE ROCK

Prediction of acid rock drainage (ARD) from waste rock piles has been a research priority for the Canadian Mine Environment Neutral Drainage (MEND) program. As a result of MEND's effort, many reports have been produced on this subject. Of these reports, those that deal with aspects of flow and solute transport in waste rock piles include Morin et al., 1991, Smith et al., 1995, SRK, 1995 (draft), and Synergetic Technology, 1996 (draft). The report by Morin et al. (1991)

is a literature review of which one of the focuses is water movement through waste rock piles. Smith et al. (1995) focuses on the hydrogeology of waste rock piles and includes many case studies. The SRK (1995) report contains a survey of existing models for ARD prediction from waste rock piles. The report by Synergetic Technology examines the theoretical representation of some waste rock properties by geostatistics and fractal theory. Besides the report by Morin (1991) of which the main task is critical literature review, the other reports listed above also contain various degrees of literature review on their respective topics. The reader is referred to these authors. In the following paragraphs, several original researches found in the literature that deal with channelling and solute transport phenomena and their modelling are critically discussed.

Literature in three related fields of research may prove of great help to the study of flow and solute transport in waste rock piles. These three fields are heap (dump) leaching, spent heap decommissioning by rinsing, and trickle bed reactors. Studies of flow and solute transport in heap leaching are exemplified by Murr et al. (1981, large scale experiments, and references contained therein), Cathles (1981, modelling of leaching, and references contained therein), Sanchez-Chacon and Lapidus (1997, modelling of gold heap leach by cyanide), and Schlitt and Nicolai (1987, random walk model). The spent heap rinsing literature include, for example, Catalan and Li (1999), Catalan et al. (1998, pilot study of rinsing acid-leached spent ore), Li et al. (1995, laboratory study of rinsing of acid-leached spent ore), and Dixon (1993, model for rinsing cyanide-leached spent ore). Trickle bed reactor literature is illustrated by Funk et al. (1990), Ng and Chu (1987), and Satterfield (1975).

Elboushi (1975) is probably the first to report direct measurements of channelling effects in coarse rocks. His results showed that in rock beds consisting of narrow-sized particles, it is unnecessary to satisfy the field water retention capacity of the material to initiate flow. Using diluted paint and visible tracers, he showed that as water infiltrates deeper into the rock bed consisting of 5-mm particles, the percentage of rock particles wetted by water decreases rapidly and nearly linearly from 100% at the surface to 15-20% at a depth of 30 cm (hence water channels are formed); for individual particles contacted by water, the average percentage of wetted surface relative to the total particle surface also decreases with depth, from 100% at the surface to about 30% at 30 cm. The major limitation of Elboushi's experiments is that narrow size fractions are used, which do not represent the majority of waste rock materials, which usually have very wide size ranges.

In a quite elaborate study of copper leaching from waste rock, Murr et al. (1981) examined solution flows in large columns measuring 3.1 m in diameter and 10.8 m in height and loaded with -100 mm rock. At the end of two years' of acid leaching a soluble fluorescent dye tracer was infiltrated into the leached waste rock. Ultraviolet photographs were taken when the spent material was excavated by horizontal slices. The photographic composites show that the channel cross-sections are irregularly shaped. In one column (Kennecott) the percentage of solution channel area varied almost randomly from a maximum of 65% to a minimum of 25% between the depths of 0.6 m and 7.6 m. In another column (Duval-Sierrita) the channel shapes were also irregular and the percentage of channelled area varied randomly, but both the maximum and the minimum were lower at 20% and 7%, respectively. It needs to be noted however that the conditions of infiltration are very different from those of a typical rain storm: the dye tracer was applied at the end of a very long (two

years) period of continuous solution application, and because of the acid attack the size distribution, texture, and compactness of the rock have been altered from the original material.

A commonality of Elboushi's and Murr's study of channelling is that, although the percentages of cross-sectional areas contacted by the dye (or paint) were measured, no information was given concerning the flux (i.e., flow rate per unit area) at different parts of the channelled areas.

Smith et al. (1995) applied the kinematic wave theory, first pioneered by Lighthill and Whitham (1955), to model a waste rock dump drainage discharge hydrograph after a rain event at the now-closed Island Copper Mine on Vancouver Island. They followed the approach developed by Germann and Beven who adapted the original kinematic wave theory to describe macropore flows in structured soils (Germann and Beven, 1981a; Beven and Germann, 1981; Germann and Beven, 1981b;Germann and Beven, 1985; Germann and Beven, 1986). They adjusted the statistical parameters describing the waste rock dump to obtain the best fit between the model-predicted hydrograph and the observed hydrograph. The optimised parameters revealed information about the channelling structure within the waste rock dump. A logical step following this work would be the independent verification of the derived channelling structure.

The University of Saskatchewan group of researchers examined evidences to study internal flow and solute transport phenomena within a waste rock pile when 15 million tons of waste rock was excavated from a 100 million ton dump at the Golden Sunlight Mine in Montana (Herasymuik et al., 1995). They documented the heterogeneity within the rock pile and mapped moisture and matric potential profiles at selected locations. Their research focuses on the inter-relationships between hydraulic conductivity, moisture, and suction within the waste rock pile. This approach provides snapshots of the waste rock pile at various times, which are used to infer information about flows in the rock pile.

Laboratory or field studies that couple channelling phenomena and solute transport are noticeably lacking in the literature. However, there is theoretical work in this respect. An example is Erriksson and Destouni (1994) who used a stochastic-advective approach to examine the effects of channelling on the solute flux from a mine waste rock dump undergoing active oxidation. They found that, for a simplistic unimodal residence time distribution, flow heterogeneity (i.e., channelling) does not have a significant influence on the solute flux when realistic model parameter values are used.

Generally speaking, literature on the subject of flow and solute transport within waste rock is scarce, but is constantly emerging. The key feature of flows in waste rock piles is channelling. In contrast, large amounts of literature exist on flow and solute transport modelling of soils. In referring to the soil literature, one should take note that the hydraulic properties of soils are fundamentally different from those of coarse waste rocks, the main difference being the particle size range and presence of pebble- and boulder-sized rock.

1.4 PROJECT HISTORY

In December 1994, Supply and Services Canada and Noranda Technology Centre (NTC) signed a contract (DSS Contract No. 23440-4-1316/01-SQ) to share the cost of a research project entitled *Hydrogeochemistry of Oxidised Waste Rock and ARD Prediction Techniques for Stratmat/N5 Waste Rock at Heath Steele Mines, New Brunswick*. The study was to be carried out under the auspices of the Mine Environment Neutral Drainage (MEND) program. The government funding was made available under the Canada-New Brunswick Mineral Development Agreement (MDA).

The field work was completed in 1994-95 and the column rinsing dissolution tests were finished in 1995-96. The large column tests reported here were conducted in 1997-1998.

This report is one of two concurrent reports resulting from the research project. The focus of this report is the large column tests. The other report, entitled *Hydrogeochemistry of Oxidise Waste Rock from Stratmat Site, N.B.* (Li, 1999), describes the field work and the column dissolution experiments. That report should be consulted for information on the sampling and characterisation of the Stratmat waste rock material used in the large column tests discussed in this report.

1.5 THE DATA DISKETTE

Thousands of data points have been generated in the large column tests. These data have been used in the analysis and interpretation reported here. It is hoped that other researchers would take advantage of the data to explore beyond what is presented in this report, to add to our understanding of the hydrology and solute transport phenomenon in waste rock piles. For this purpose, the raw experimental data have been provided in an electronic format on a diskette attached to this report.

2.0 EXPERIMENTAL METHODOLOGY

2.1 SCALE OF HETEROGENEITY AND REV

It is generally accepted that waste rock piles and dumps are heterogeneous structures. The initial heterogeneity structure of a waste rock pile can change with time after the pile is constructed as a result of many physical and chemical processes. Waste rock heterogeneity can be physical or chemical. Physical heterogeneity is the spatial variation of particle size, porosity, specific surface area, density, hydraulic conductivity, gas diffusivity, heat capacity, etc. Chemical heterogeneity is the spatial variation of rock composition which includes contents of acid-producing minerals, acid-consuming minerals, and secondary minerals. Physical heterogeneity has a large influence on the hydrological processes within a waste rock pile, whereas both physical and chemical heterogeneity can affect solute transport processes.

The concept of heterogeneity depends on the scale. A uniform porous media, such as well-mixed silt- and sand-sized tailings, is heterogeneous on a scale of micrometers to centimetres, consisting of individual particles and individual pores filled with liquid or gas. The same media can be, however, homogeneous on a scale greater than decimetres. This porous media therefore has microheterogeneity and mesohomogeneity. A well-blended, unsegregated waste rock pile ranging in size from clay and silt to boulders is heterogeneous on a scale of less than a few meters, but can be treated as homogeneous on a greater scale. This waste rock has mesoheterogeneity and macrohomogeneity. Finally, a typical waste rock dump may show heterogeneity on a scale of tens of meters or greater, and therefore may have macroheterogeneity.

To obtain valid results, experimental studies of hydrological and solute transport behaviours of waste rock piles, typically macroheterogeneous, should be carried out in a representative elementary volume (REV) at least tens of meters long in the dimension of interest (such as flow). This means that such studies should be done on a field scale. Because of the difficulties in controlling variables and instrumentation, such field studies are scarce and the limited number of reported studies generally do not have sufficient data for substantiating quantitative models.

To a first approximation, a macroheterogeneous waste rock pile can be viewed as being composed of many macrohomogeneous but mesoheterogeneous regions. An understanding of processes in waste rock piles can be gained by first studying such building blocks.

The intention of the large column tests reported here was to approach an REV of a waste rock media having macrohomogeneity and mesoheterogeneity. The dimensions of the cylinder-shaped large columns employed are 1.2 m in diameter and 2 m in height. Each column was loaded from

1.2 to 3.7 t of waste rock. Since rocks greater than 12 inches (30 cm) were removed from the waste rock sample, the dimensions of the large columns were thought to be appropriate to accommodate an REV possessing the properties of macrohomogeneity and mesoheterogeneity. Clearly, the more conventional columns, normally 6 to 10 inches (15 to 25 cm) in diameter, are too small to contain an REV for waste rock.

2.2 EXPERIMENTAL DESIGN

The basic premise for experimental design is to construct an REV of a mesoheterogeneous and macrohomogeneous waste rock bed (refer to Section 2.1) and observe its response to simulated rain applied on the top surface. To avoid the masking effects when only one drainage is collected, the bottom of the column was partitioned into many separate drainage basins each of which collected only the drainage from the part of the sample bed directly above it. The variations of drainage volume, pH, conductivity, and selected elemental concentrations were monitored for each drainage port over time after the simulated precipitation was applied.

Tracer tests were performed by imposing a continuous step pulse of the tracer in the simulated rain water at the beginning of each simulation and monitoring the variation of the tracer concentration with time in each drainage port. Three tracers, NaCl, KNO_3, and LiCl, were used in consecutive simulations.

Variables for the tests include sample bed height (0.5, 1.0, 1.5 m), duration, pattern, and intensity of simulated precipitation, bottom drainage area partition patterns (square grid and concentric), and type and concentration of tracers.

By examining the spatial (two-dimensional) and temporal variations of the drainage volume and physicochemical parameters, information about the internal hydrologic and solute transport processes such as channelling, mode of flow, secondary mineral dissolution, etc. can be inferred. The tracer tests were designed to generate data leading to the quantification of channelling, adsorption, and residence time distribution (RDT).

2.3 EXPERIMENTAL SET-UP

A photograph of the three loaded columns with the rain simulator installed on Column 1 is shown in Figure 2-1. The design drawings (excluding the rain simulator) are given in Figure 2-1.

Figure 2-1 Photograph of Installed Columns

2.3.1 Columns

As seen in Figure 2-1 and Figure 2-1, the columns and accessories were constructed of thick, black, heavy-duty plastics to provide the strength to support heavy weight of rocks. The combined weight of loaded rock and the column equipment was greater than 5 t. The main column body measures 1.2 m in inside diameter and 2 m in height and holds 3.7 t of waste rock when the rock bed is 1.5 m thick.

Both the top and the bottom of the main column body are flanged for connection with a rain simulator and a bottom drain structure. The weight of the entire structure is supported by the bottom drain structure, which is in turn supported by a steel frame to a height of 1 m above the concrete floor. The space underneath the bottom drain structure was needed to collect drainage.

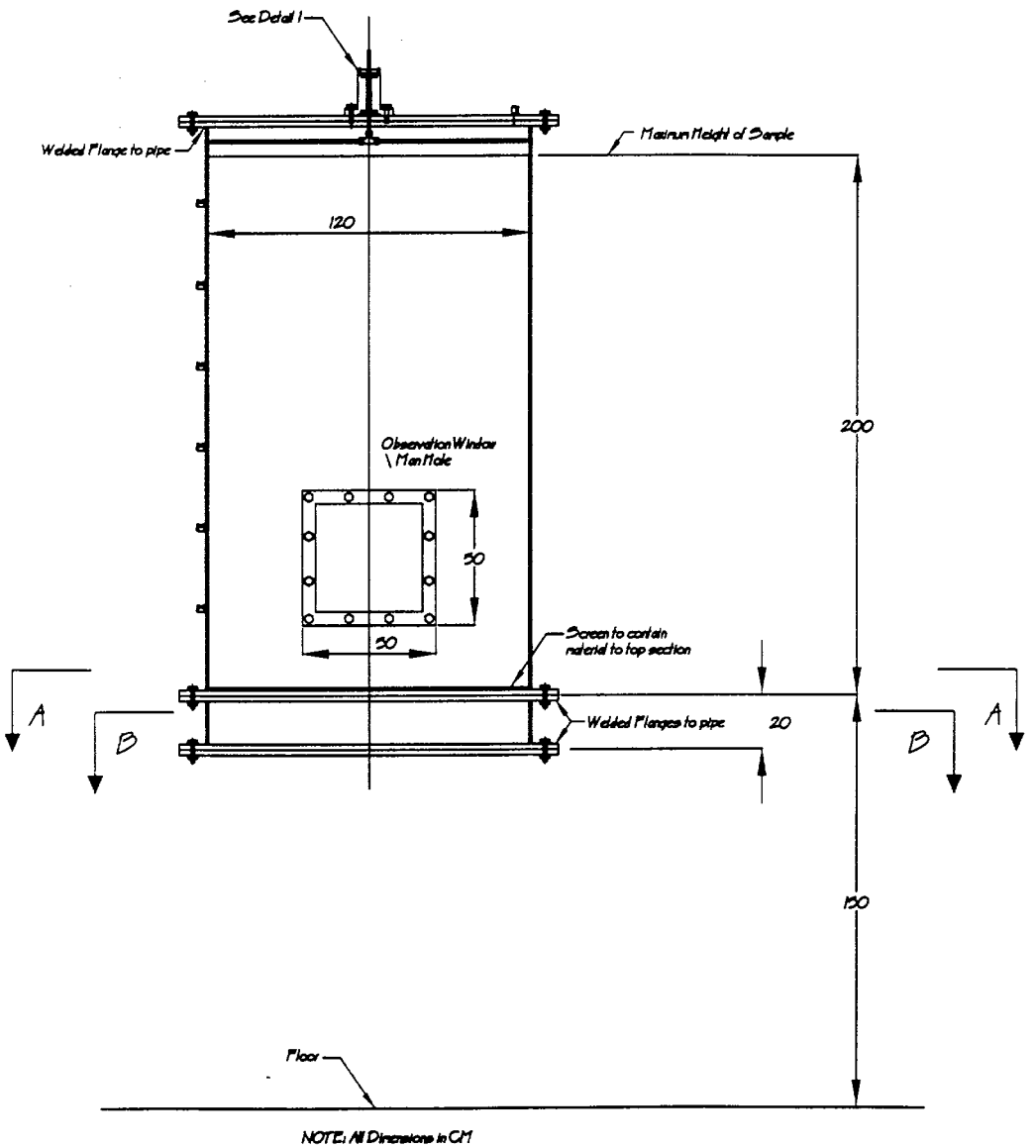

Figure 2-2 Design Drawings of the Large Columns

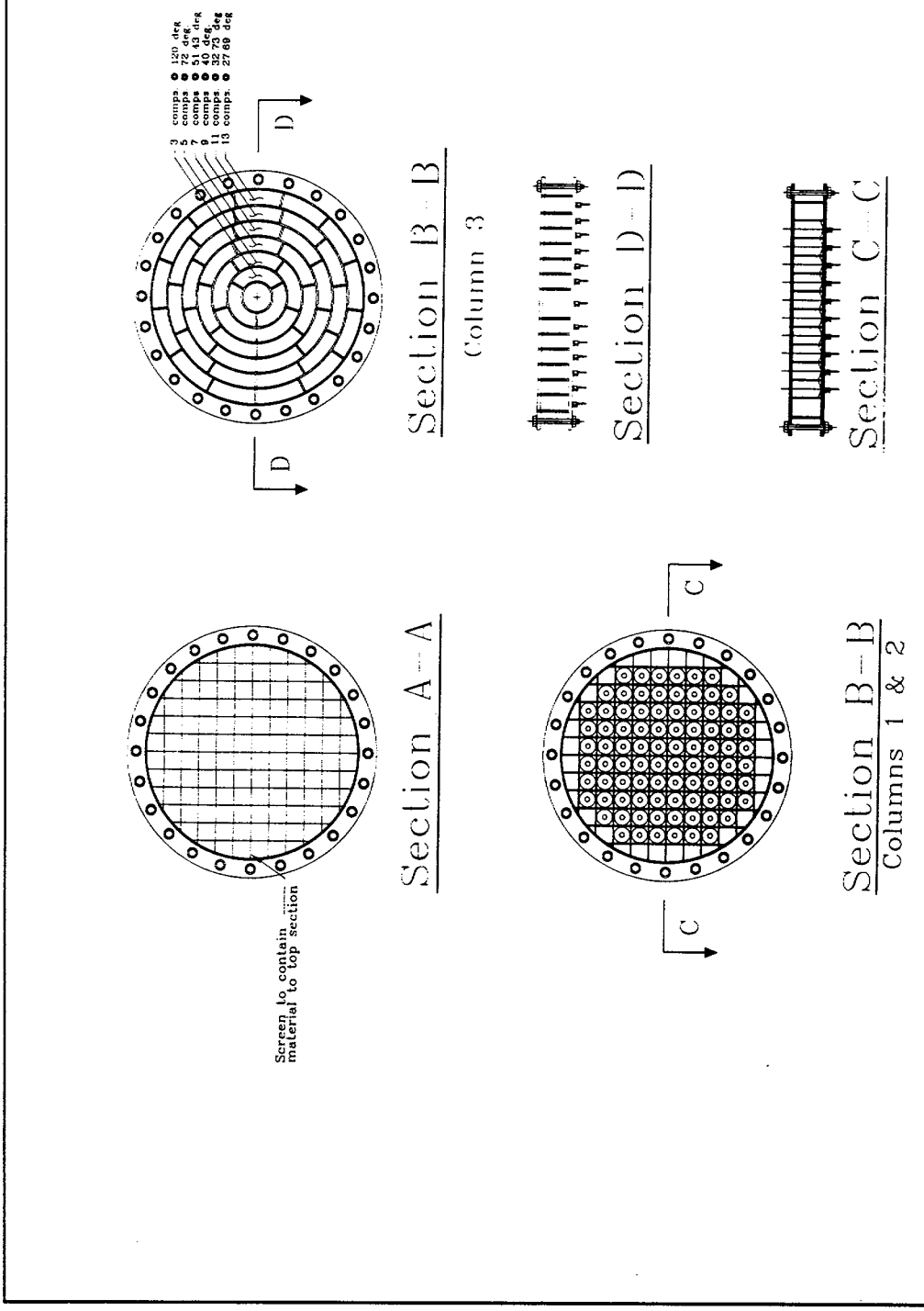

Figure 2-2 Design Drawings of the Large Columns (Continued)

2.3.2 Rain Simulator

The main consideration for the rain simulator is its ability to dispense a stable, uniform “rain” at required rates over the surface of the waste rock bed.

Photographs of the rain simulator are shown in Figure 2-1. It consists of two plastic plates connected by nuts and bolts with a gap of about six inches in between (lower photo). On the lower plate are mounted hollow stainless steel needles arranged in a square grid which deliver water to the sample bed surface. On top of the upper plate are mounted a water reservoir, five peristaltic pumps each having 8-channels, one water circulation peristaltic pump, pump speed controllers, and the connecting tubing. Water is drawn from the central reservoir in a large tubing and split into eight small tubings before entering the pumps. The other end of each tubing (after the pump) is connected to a steel needle. The water level in the central reservoir is fed from a large (200 L) reservoir via a peristaltic pump and maintained at a constant head by means of overflow. The overflow is returned to the large reservoir via a separate peristaltic pump.

The speed of each of the delivery pumps can be adjusted independently. The flow rate in the eight channels on the same pump cannot be changed independently, but the variation was found to be small. The flow rate in each channel was normally calibrated at 3.2 mL/min and with a total of 37 channels the rain simulator delivers 7.1 L of water per hour. Independent measurement of each of the 37 channels showed that the flow rate variation was small and that the flow rate was stable over time.

The total water input in each simulation session was measured by the water level change in the 200-L reservoir. Experimental data for all runs indicate that the water inputs recorded in the large reservoir consistently agreed very well with the flow rate of 3.2 mL/min/channel.

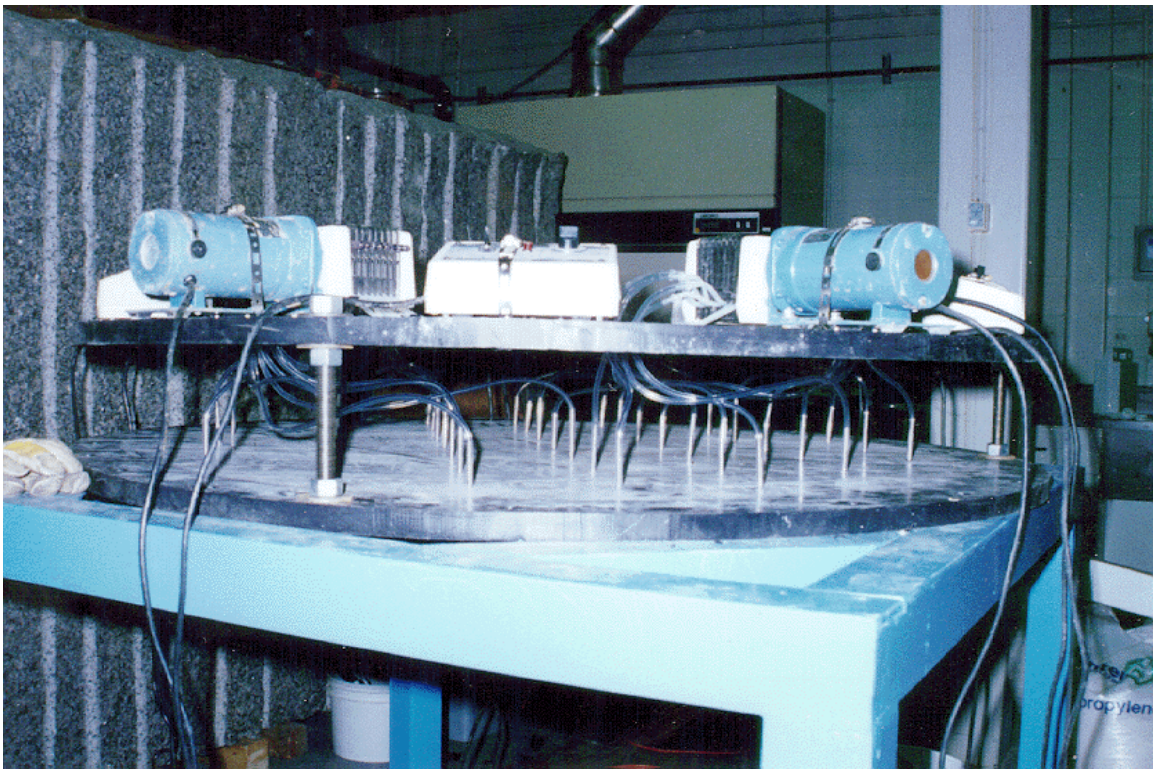

Figure 2-3 Photograph3s of the Rain Simulator

2.3.3 Bottom Drains

The main considerations for the bottom drain structure were two fold: (1) its ability to avoid lateral "cross flow" at the bottom boundary of the waste rock bed so that each partitioned square drainage area receives drainage only from the part of the rock bed that is directly above it, and (2) to structurally support the weight (up to 3.7 t) of the rock bed.

Schematic drawings of the bottom drain structure are provided in Figure 2-1, and photographs are shown in Figure 2-1. Figure 2-2 shows a view of the installed bottom drain structure looking down the inside of a empty column. Figure 2-3 and Figure 2-4 illustrate how the bottom of each column is partitioned into drainage areas. Figure 2-5 shows the valves and drainage collection system on the underside of the bottom drain structure.

The bottoms of Columns 1 and 2 are partitioned into square drainage areas, as shown in Figure 2-1 and Figure 2-1. The upper photo in Figure 2-1 shows that water collected by each partitioned drainage area flows into a cylindrical chamber, each of which has a valve to turn on or off the drainage flow into its collection bottle, as shown in Figure 2-5. Each cylindrical drainage chamber is filled with -1/4 inch polyethylene beads to establish hydraulic contact with the rock bed. A steel screen with - 1 inch mesh sizes is placed on top of all the cylindrical drainage chambers to support the rock sample bed, as seen in Figure 2-2.

The bottoms of Columns 1 and 2 are partitioned into 37 drainage areas, sequentially labelled from 1 to 37, as illustrated in Figure 2-3. There are no drainage chambers for the areas labelled from A to H and the tiny unlabeled triangular areas. As a result, drainage reaching these areas must flow into neighbouring drainage chambers, as indicated by arrows in Figure 2-3. The geometric areas of drainage sections 1 through 37 and A through H are given in Table 2-1.

The physical set-up for Column 3 is similar to that of Columns 1 and 2, except that the bottom of Column 3 is partitioned differently, into annular drainage sections, as shown in Figure 2-1 and Figure 2-1. Sixteen annular drainage sections are formed, as shown in Figure 2-4, by joining 2, 3, or 4 neighbouring drainage chambers (except the central section). The annular sections are labelled sequentially in a spiral from the perimeter to the centre. Each of the 16 drainage sections flows to an individual bottle through an on/off valve. The areas of the sections are given in Table 2-1.

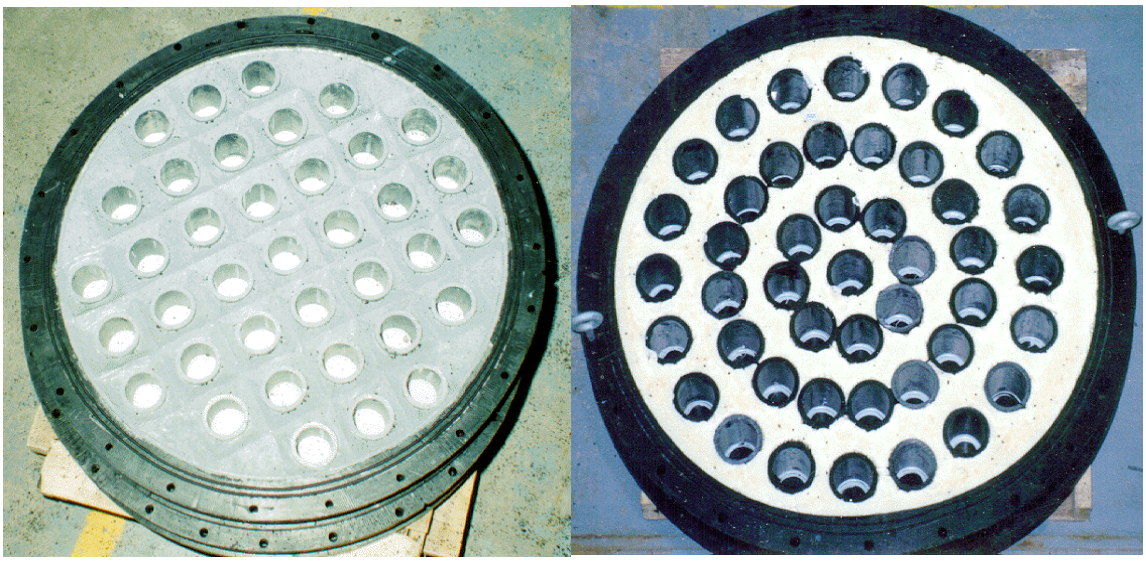

Figure 2-4 Photographs of Column Bottom Drain Structures

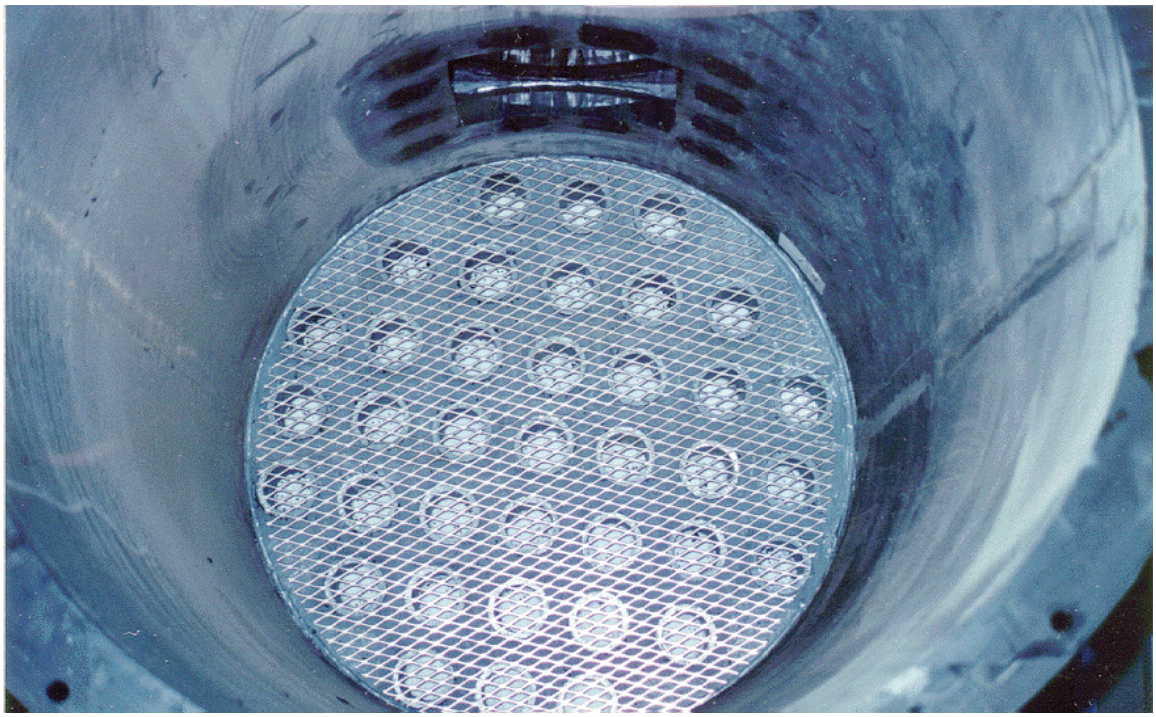

Figure 2-5 View of Installed Bottom Structure Looking Down Inside a Empty Column

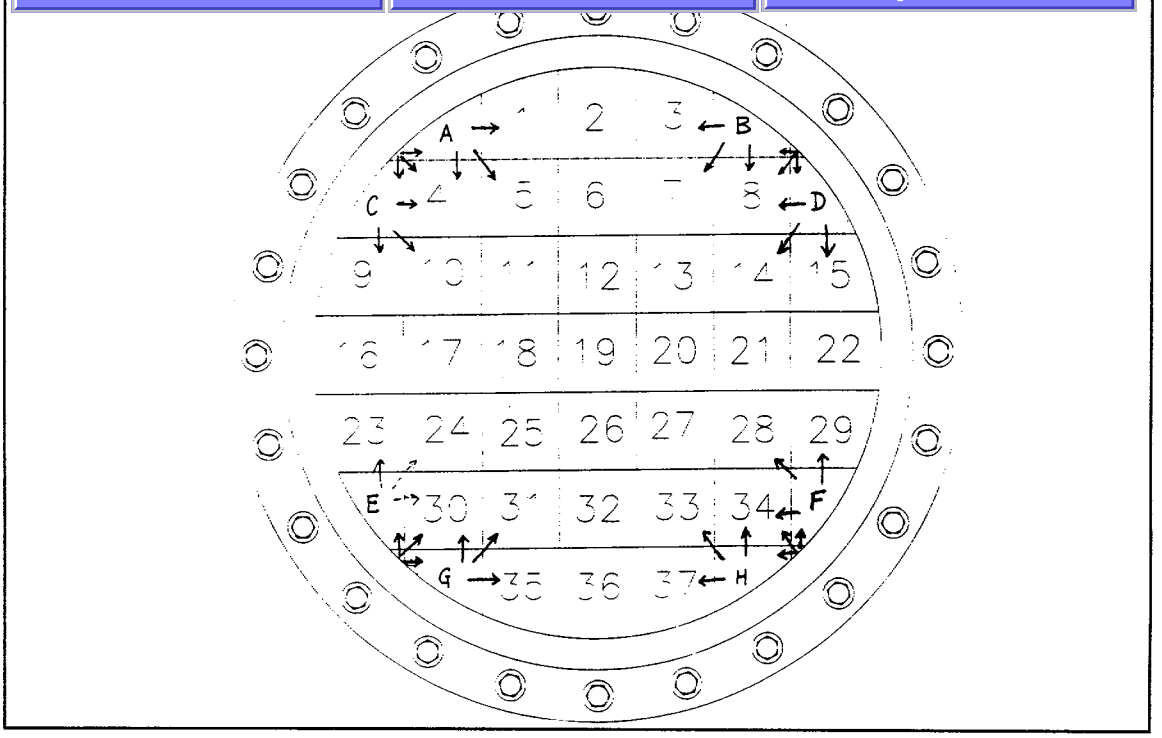

Figure 2-6 Partitioning of the Bottom into Square Drainage Areas for Columns 1 and 2

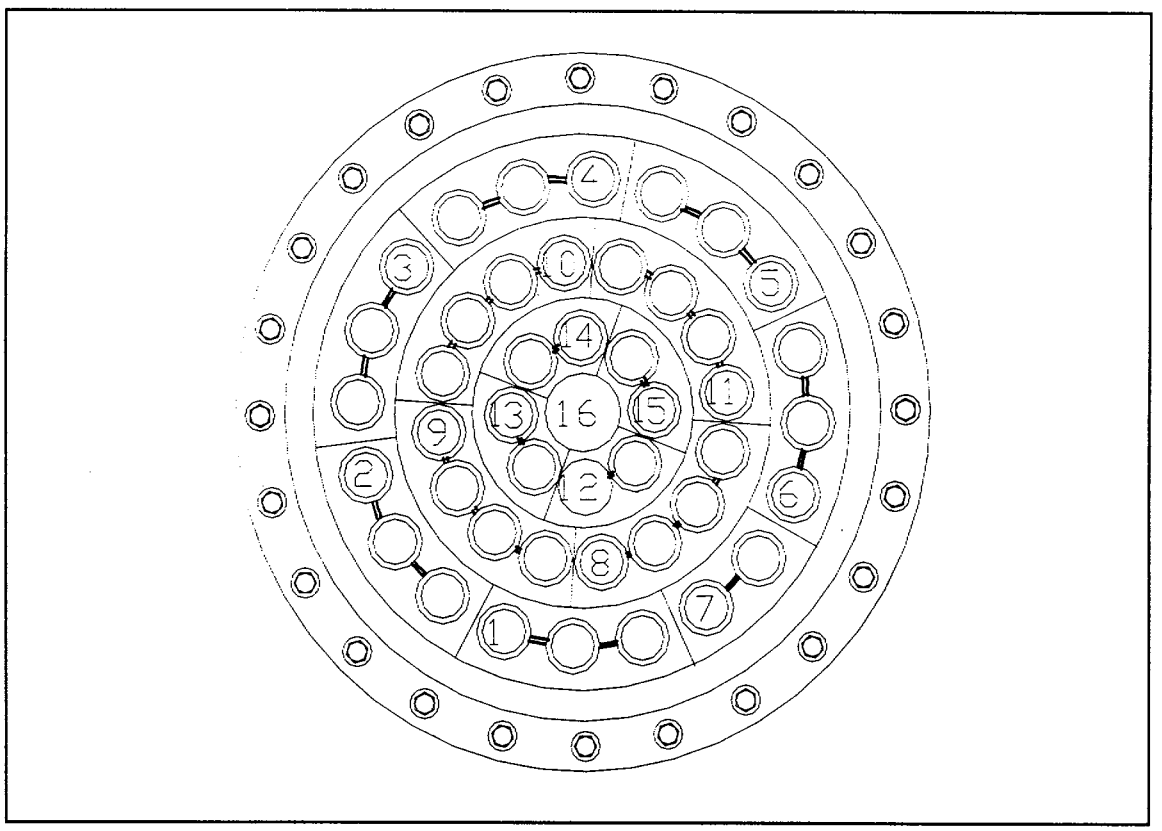

Figure 2-7 Partitioning of the Bottom into Annular Drainage Areas for Column 3

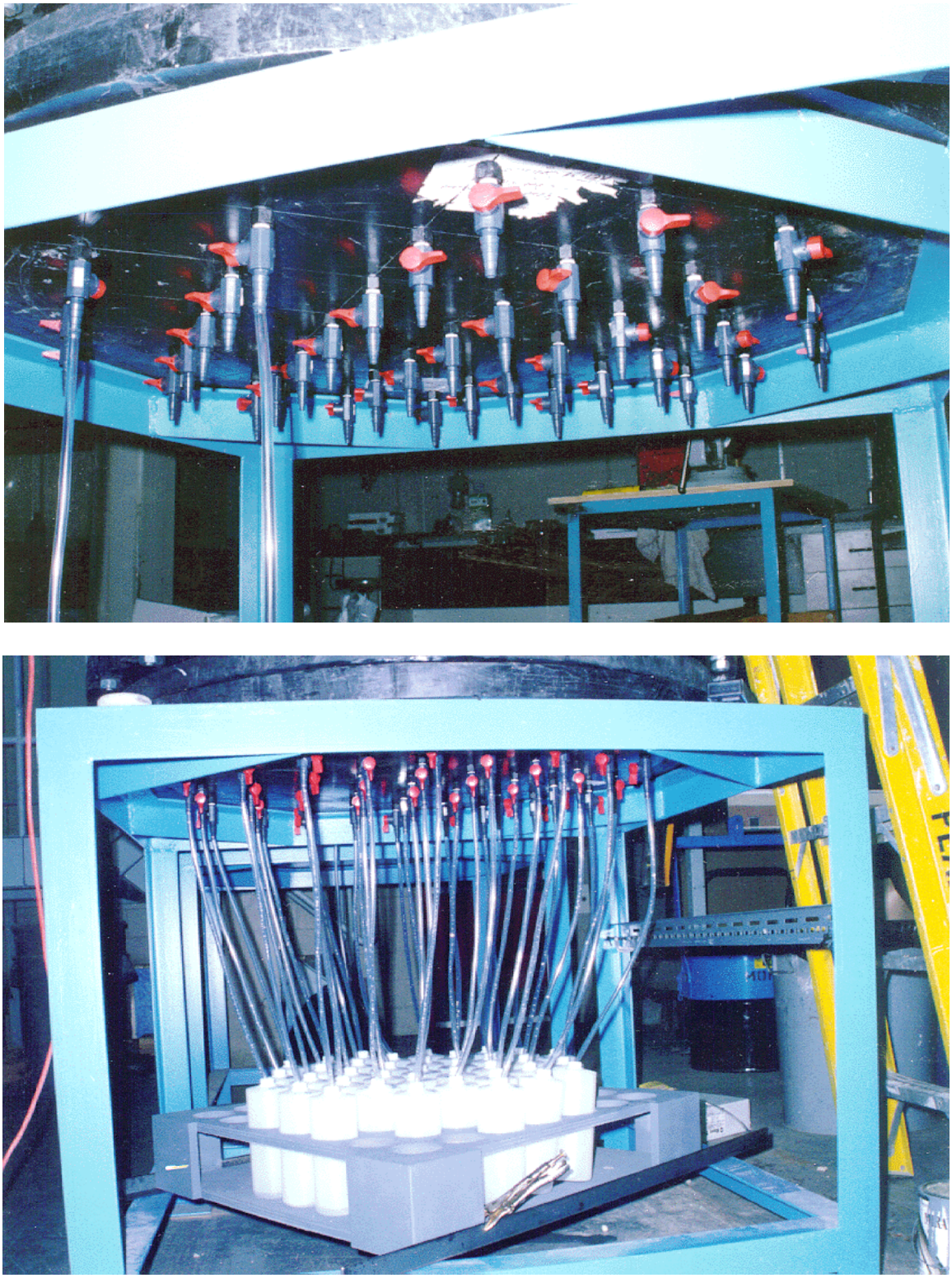

Figure 2-8 Collection System on Underside of Bottom Drain Structure for C1 and C2

Table 2-1 Areas of Drainage Sections

Columns 1 & 2					Column 3	
Section	Area Cm^2	Section	Area cm^2		Section	Area cm^2
1	221.6	A	110.8		1	821.7
2	253.7	B	111.0		2	912.4
3	217.0	C	115.5		3	878.8
4	225.0	D	114.2		4	720.8
5	225.0	E	117.1		5	754.8
6	225.0	F	115.8		6	734.6
7	225.0	G	121.3		7	488.1
8	225.0	H	120.2		8	680.2
9	222.9				9	683.5
10	225.0				10	708.7
11	225.0				11	681.5
12	225.0				12	336.9
13	225.0				13	336.3
14	225.0				14	345.1
15	221.6				15	355.8
16	255.4				16	167.6
17	225.0				**Total**	**9606.6**
18	225.0					
19	225.0					
20	225.0					
21	225.0					
22	254.2					
23	223.5					
24	225.0					
25	225.0					
26	225.0					
27	225.0					
28	225.0					
29	222.2					
30	225.0					
31	225.0					
32	225.0					
33	225.0					
34	225.0					
35	223.9					
36	255.9					
37	223.5					
Total	**8420.3**		**925.8**	**9346.2**		

2.4 EXPERIMENT PREPARATION

2.4.1 Calibration of Rain Simulator

After the flow rates in the 37 channels of the rain simulator were fine-tuned, the accuracy and the repeatability of the flow rates were tested. The rain simulator was run three times, for 1, 1.5 and 2.0 hours, respectively, and the water pumped in each channel was collected in an individual bottle and measured. The results are shown in Table 2-1. It can be seen that, among the three runs, the repeatability is acceptable, with standard errors (defined as one standard deviation divided by the mean) generally less than 6% for all channels except 6, 10 and 35. The 37 means of the three runs have an overall mean of 3.34 mL/min (the target flow rate is 3.2 mL/min) and an overall standard error of 9.8%.

To test the homogeneity of water distribution, Column 2 was packed with about 0.5 m of "bird balls" - uniform-sized hollow plastic balls about 2 inches in diameter. The rain simulator was run twice for two hours and the volume collected in each drain port was measured. The results are given in Table 2-2 and shown graphically in Figure 2-1. It can be seen that the repeatability is acceptable, with standard errors based on the duplicate tests generally within 10% except four ports: 9, 28, 33 and 34. The 37 two-test means had an overall mean of 3.15 mL/min, which is slightly less than the target of 3.2 mL/min. The difference can be accounted for by the small amounts of water retained by the media (the plastic "bird balls"). The water distribution among the 37 ports is reasonably homogeneous, although a few drain ports reported low flow rates less than 2 mL/min (Ports 9, 13, 28, 34) and high flow rates greater than 4 mL/min (Ports 4, 8, 36). The standard error of the 37 means is 23.8%.

The rain simulator, with the performance described above, was used for all tests in Columns 1 and 2. For Column 3, because water was applied at just one point (centre of the sample bed surface), there was no need for calibration of the simulator.

Table 2-1 Result of Rain Simulator Channel Flow Rate Calibration

Channel No.	Volume of Water Pumped, mL			Statistics		
	Run 1 1 hr	Run 2 1.5 hr	Run 3 2 hr	Mean of 3 Runs mL/min	Std. Dev. 3 Runs	Std. Error 3 Runs
1	196.7	288.8	379.3	3.22	0.06	1.84%
2	200.5	284.7	386.1	3.24	0.09	2.82%
3	200.1	281.7	385.7	3.23	0.10	3.19%
4	192.6	287.1	374.0	3.17	0.05	1.55%
5	192.7	282.9	373.7	3.16	0.05	1.59%
6	259.6	348.6	454.0	3.99	0.29	7.29%
7	204.7	291.1	397.3	3.32	0.09	2.68%
8	207.0	283.9	401.7	3.32	0.15	4.52%
9	227.6	317.5	410.2	3.58	0.19	5.38%
10	199.8	193.5	389.9	2.91	0.66	22.7%
11	200.3	296.9	388.7	3.29	0.05	1.51%
12	206.5	296.1	400.8	3.36	0.08	2.30%
13	209.6	304.7	410.8	3.43	0.05	1.59%
14	227.6	332.8	439.0	3.72	0.07	1.86%
15	197.5	289.6	381.3	3.23	0.06	1.79%
16	225.8	326.6	441.2	3.69	0.07	1.85%
17	194.7	284.1	373.1	3.17	0.07	2.17%
18	194.6	282.7	373.5	3.17	0.07	2.18%
19	200.8	282.1	386.7	3.23	0.11	3.29%
20	229.3	329.3	439.6	3.71	0.09	2.50%
21	191.4	280.4	373.6	3.14	0.04	1.38%
22	201.5	293.9	389.2	3.29	0.06	1.85%
23	189.5	275.6	365.2	3.09	0.06	2.00%
24	203.0	302.3	389.7	3.33	0.07	2.18%
25	255.7	347.2	464.5	4.00	0.23	5.74%
26	180.3	267.8	350.7	2.97	0.04	1.41%
27	197.9	293.7	383.4	3.25	0.05	1.62%
28	215.5	313.4	414.7	3.51	0.07	2.05%
29	212.4	311.0	407.1	3.46	0.07	2.14%
30	178.6	263.2	343.4	2.92	0.06	1.97%
31	182.6	266.2	349.6	2.97	0.07	2.22%
32	193.1	288.0	372.3	3.17	0.06	1.97%
33	197.3	288.8	381.4	3.23	0.06	1.77%
34	192.0	280.7	368.4	3.13	0.07	2.10%
35	335.8	450.8	362.6	4.54	1.35	29.7%
36	202.9	298.2	391.9	3.32	0.06	1.75%
37	195.3	289.3	380.3	3.21	0.04	1.34%
			Mean	3.34		
			Std. Dev.	0.3273		

Std. Error	9.79%

Table 2-2 Results of Water Distribution Calibration Tests

Channel No.	Water Volume Collected (mL)		Mean, Runs 1 & 2	Std. Dev.	Std. Error
	Run 1	Run 2	mL/min	Runs 1 &2	Runs 1 &2
1	411.8	415.3	3.4	0.02	0.60%
2	349.9	339.6	2.9	0.06	2.11%
3	336.2	355.6	2.9	0.11	3.97%
4	549.8	547.4	4.6	0.01	0.31%
5	419.6	408.0	3.4	0.07	1.98%
6	421.2	479.6	3.8	0.34	9.17%
7	308.2	294.2	2.5	0.08	3.29%
8	520.9	495.2	4.2	0.15	3.58%
9	76.3	296.6	1.6	1.30	83.5%
10	322.3	366.1	2.9	0.26	9.00%
11	447.7	394.2	3.5	0.32	8.99%
12	393.4	383.9	3.2	0.06	1.73%
13	199.3	191.8	1.6	0.04	2.71%
14	421.2	391.2	3.4	0.18	5.22%
15	377.7	390.6	3.2	0.08	2.37%
16	389.5	379.5	3.2	0.06	1.84%
17	380.7	403.1	3.3	0.13	4.04%
18	367.6	354.6	3.0	0.08	2.55%
19	389.0	381.2	3.2	0.05	1.43%
20	449.2	456.8	3.8	0.04	1.19%
21	432.3	458.2	3.7	0.15	4.11%
22	416.2	412.2	3.5	0.02	0.68%
23	367.9	366.4	3.1	0.01	0.29%
24	385.8	390.2	3.2	0.03	0.80%
25	434.7	467.0	3.8	0.19	5.07%
26	361.2	352.8	3.0	0.05	1.66%
27	429.6	402.0	3.5	0.16	4.69%
28	161.4	239.4	1.7	0.46	27.5%
29	400.6	389.9	3.3	0.06	1.91%
30	450.1	455.6	3.8	0.03	0.86%
31	316.9	325.7	2.7	0.05	1.94%
32	374.4	377.2	3.1	0.02	0.53%
33	486.3	404.3	3.7	0.48	13.0%
34	155.5	108.3	1.1	0.28	25.3%
35	329.4	304.2	2.6	0.15	5.63%
36	558.5	530.2	4.5	0.17	3.68%
37	348.2	354.3	2.9	0.04	1.23%

	Average	3.15
	Std. Dev.	0.75
	Std. Error	23.8%

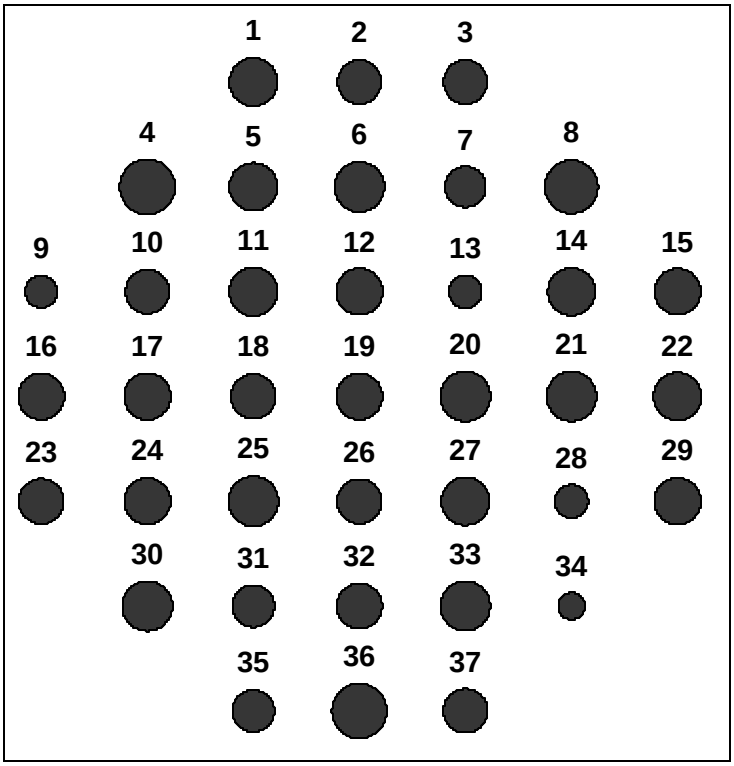

Figure 2-9 Distribution of Water among Drain Ports in Duplicate Calibration Tests

(Area of a bubble is a measure of the flow rate in the drain port identified by the number)

2.4.2 Mixing and Loading of Waste Rock

The rock samples taken from the Stratmat pile (for detailed description refer to Li, 1999, Section 2.4) were stored in large nylon bags in open air before the large column tests. In preparation of the tests, the rocks were dumped on to a paved area. The rock pile was thoroughly mixed by coning and quartering three times with a combined hydraulic back hoe/front loader, as shown in Figure 2-1.

Figure 2-10 Mixing of Waste Rock before Loading of Columns

The mixed rock was loaded into the columns to specified bed heights using a drum loader as shown in Figure 2-2. The mechanism on the side of the loader is used to overturn the drum to empty the sample inside. The primary concern in loading the rocks was to prevent size segregation. Loading was achieved by filling the loader with rock, lifting the loader with an overhead crane, lowering the loader inside the column, then dumping out the content by pulling the chain attached to the wheel (Figure 2-2). The rock falling distance was less than 30 cm at all times. After dumping each load, the rock bed surface was levelled with a shovel. Figure 2-3 shows a top view (left photo) and a side view (through the observation window, right photo) of the loaded rock in Column 2. Size segregation was prevented by the use of this loading method.

Figure 2-11 Drum Loader Used for Loading Rock into Columns

Figure 2-12 Photographs of Loaded Rock Sample Bed

2.5 EXPERIMENTAL CONDITIONS AND PROCEDURES

Ten experimental runs were conducted on the three columns. Table 2-1 summarises the experimental conditions, and the following text is a brief description. The experimental conditions and procedures are described in detail in APPENDIX I.

Column 1

The column was filled with a 1.5-m thick sample bed and three runs were performed consecutively (the sample bed was not changed between runs). The objectives of these three runs were threefold: (1) to compare with Column 2 runs, (2) to investigate the effects of simulated rain intensity, and (3) to gather tracer data for determination of residence time distribution (RTD).

Column 2 tests were carried out before Column 1 tests. To generate data for RTD determination, three tracers were used consecutively: NaCl, KNO_3, and LiCl.

Column 2

Four runs were conducted on Column 2. The sample bed was first filled to 0.5 m and Run 1 was conducted. Then more rock was added on top of the existing sample to bring the sample bed to 1.0 m and Run 2 was carried out. Finally another 0.5 m of rock sample was added to bring the sample bed height to 1.5 m, and two runs, Run 3 and Run 4, were carried out consecutively. The objectives of these runs were (1) to explore experimental conditions and gain experience with the experiment procedure (this was the first column experimented), and (2) to investigate the effects of sample bed thickness.

Column 3

Three runs were carried out, respectively, at three different sample bed heights - 0.5, 1.0, and 1.5 m. Column 3 tests differed from those of Columns 1 and 2 in two aspects: (1) in Column 3 the bottom drain structure was concentric instead of square grid, and (2) the water was applied on the top at one point instead of a uniform grid of many points. These experiments were carried out to (1) study channelling, (2) investigate the effects of sample bed thickness, and (3) study horizontal dispersion of flow.

Table 2-3 Summary of Experimental Conditions for Large Column Tests

Col. No.	Run No.	Sample Bed Height (m)	Rain Simulator			Sampling				Tracer		ICP
			Feed Pattern	Feed Rate (mL/min/ channel)	Feed Duration (hour)	No. of Rounds	Max. No. of Samples per Round	Duration (hour)	No. of Rounds for ICP	Type	Conc. (mg/L cation)	List of Dissolved Elements Analysed
1	1	1.5	Grid	3.2	13	8	37	6	6	NaCl	1000	S, Fe, Zn, Na, K, Li
	2				7	8	37	6	5	KNO_3	500	S, Fe, Zn, Na, K, Li
	3			1.6	10	8	37	6	6	LiCl	500	S, Fe, Zn, Na, K, Li
2	1	0.5	Grid	3.2	5	7	37	4	7	None	-	S, Fe, Zn
	2	1.0			6	7	37	4	7	None	-	S, Fe, Zn
	3	1.5			10.77	7	37	6	6	None	-	S, Fe, Zn
	4	1.5			5.1	8	37	6	5	None	-	S, Fe, Zn
3	1	0.5	Centre Point	35	10	8	16	6	6	NaCl	1000	S, Fe, Zn, Na, K, Li
	2	1.0			13	8	16	6	7	KNO_3	1000	S, Fe, Zn, Na, K, Li
	3	1.5			12	8	16	6	6	LiCl	500	S, Fe, Zn, Na, K, Li

Notes:

1. Rain simulator position is -22.5° for all runs.
2. Selected samples were ICP-analysed for 14 elements.
3. Conductivity, pH, and solution mass were measured on all samples.
4. Redox potential was measured initially but its measurement was stopped later.
5. ICP analysis was done on unfiltered samples, as filtration was shown not to produce any difference in ICP results.

2.6 EXPERIMENT EXECUTION

The experiments required two full-time persons on a 12-hour shift. Automatic timers were used to control the rain simulator. Four sets of 37 1-L bottles were made to rotate for drainage collection. Switching of bottles was done by closing and opening the on/off valves on each drainage port.

Enough lap time (at least two days) was allowed between successive runs for the sample bed to drain off the water applied in the previous run until a field retention capacity is reached, after which time no more water would drain. Despite this, the moisture content of the sample bed varied at the beginning of each simulation. The beginning moisture of each run was not measured, but can be estimated using available information.

The determination of drainage breakthrough time was somewhat subjective. Initially, "drainage breakthrough" was defined as the moment when the drainage flow broke in any of the drainage ports. This criteria was later found impractical to discern, thus the definition was modified to "the time when about half of the drainage ports had flows". Since this definition is somewhat arbitrary, the breakthrough times identified had an inherent error of approximately ±0.5 hour.

The experiments were carried out in a "batch mode", i.e., each set of drainage bottles was removed at pre-determined time intervals for physicochemical characterisation. The parameters obtained such as solution mass, pH, conductivity, and dissolved elements, therefore, are those of a "batch" of solutions, not instantaneous values measured on the drainage flows. Instantaneous (more accurately, short-interval) flow rates, pH, conductivity, and elemental concentrations would be preferred for interpretation of data, but cannot be obtained within the resource limit.

Once the experiments were completed, the waste rock was returned to the Stratmat pile for disposal.

2.7 ANALYSIS OF DRAINAGE

Three parameters - pH, conductivity, and solution mass - were measured on all samples that had sufficient volume for these measurements. Measurement of redox potential was made on a small percentage of samples.

Based on available information on the rock material, only three dissolved elements were measured on all samples to optimise the cost effectiveness of acquired data. They were sulphur (S), iron (Fe), and zinc (Zn). For runs involving tracer additions, the concentrations of the tracer elements were also measured (see Table 2-1). All elemental concentration measurements were made using either ICP-AES or ICP-MS on unfiltered samples preserved with either HNO_3 or HCl. Unfiltered samples were used for ICP analyses because comparisons made at the beginning of the experiments between filtered and unfiltered samples showed no significant difference in elemental concentrations.

A number of samples were selected for ICP scans of over 30 elements to generate data for geochemical modelling.

Quality assurance and quality control (QA/QC) on chemical analyses were realised by established routines such as blind blanks, blind replicates, and timely verification of data. These QA/QC measures were conducted independently of and in addition to the routine QA/QC measures exercised by the analytical laboratory, which included blanks, standards, spikes, and repeats.

In this report, the terms "dissolved S" and "S" are used alternatively with the terms "dissolved SO_4^{2-}" and "SO_4^{2-}". It is assumed that in all drainage samples the only S species is SO_4^{2-}. The SO_4^{2-} concentration is simply related to the S concentration by $[SO_4^{2-}] = 3 \times [S]$. In addition, the terms "dissolved Fe" and "Fe" are meant to include both Fe^{2+} and Fe^{3+}.

3.0 RESULTS AND INTERPRETATION

3.1 RESULTS

To facilitate examination and analysis of the experimental data by other interested researchers, the raw data have been provided on a diskette in Microsoft Office 97 Excel® format (file name "Results.xls").

The stability of flow delivered by the rain simulator is satisfactory, as indicated by the agreement between the total pumped amounts measured by the water level changes in the water reservoir and those calculated from the target flow rates and pumping duration (Table 3-1). The draining time between separate experimental runs and the approximate time of solution breakthrough are given in Table 3-2. The "solution breakthrough time" is defined as the time elapsed from the beginning of simulated rain application to the time when about half of the drainage ports have reported flow.

Table 3-1 Comparison of Measured and Calculated Volumes of Water Delivered

Col. No.	Run No.	Delivered Volume (measured by water level changes in reservoir), L	Pumping Duration (hour)	Target Flow Rate (mL/min/ Channel)	No. of Flow Channels	Delivered Volume (calculated from target flow rate and pumping duration), L
1	1	92.5	13	3.2	37	92.4
	2	50.0	7	3.2	37	49.7
	3	36	10	1.6	37	35.5
2	1	36	5	3.2	37	35.5
	2	44	6	3.2	37	42.6
	3	75	10.77	3.2	37	76.5
	4	35	5.1	3.2	37	36.2
3	1	21	10	35	1	21.0
	2	N/A	13	35	1	27.3
	3	N/A	12	35	1	25.2

Table 3-2 Draining Time between Runs and Elapsed Time at Solution Breakthrough

Col. No.	Run No.	Number of Days Elapsed since Last Test but before this Test on this Column	Time Elapsed from Beginning of Simulated Rain to Solution Breakthrough, minutes
1	1	Not applicable	735
	2	2	170
	3	4	357
2	1	Not applicable	150
	2	2	240
	3	76	378
	4	5	165
3	1	Not applicable	349
	2	14	538
	3	2	870

3.1.1 Rain Simulation Tests

The individual port drainage hydrographs and whole-column drainage hydrographs composited from the individual port drainage hydrographs are plotted in APPENDIX II. The reader should consult the abbreviations and explanations at the beginning of this appendix to fully understand the graphs. Some points on the hydrographs are interpolated.

APPENDIX III presents the dissolved Zn drainage chemographs for individual ports and for the entire columns. Like the column drainage hydrographs, the column drainage chemographs are also composited from individual port drainage chemographs. Only dissolved Zn chemographs are plotted in this appendix. Chemographs for other parameters such as S, Fe, conductivity, etc., can be constructed from the raw data provided in the data diskette.

APPENDIX IV gives the pH chemographs for individual ports. Because pH is not a conservative parameter, it can not be composited from individual ports to derive the pH for the entire columns.

3.1.2 Tracer Tests

Tracer tests were carried out in Columns 1 and 3. NaCl was added in Run 1; KNO_3 in Run 2; LiCl in Run 3. The tracer elements were Na, K, and Li, respectively. The tracer concentrations and duration of rain simulations used are shown in Table 2-1. The tracer concentrations were selected to be at least two orders of magnitude higher than those of either the background water or the pore water associated with the waste rock samples.

Individual port tracer chemographs and whole-column chemographs composited from individual

port chemographs are both shown in APPENDIX V. Consult APPENDIX II for explanations of abbreviations and graphing details.

3.1.3 Radial Infiltration Dispersion Tests

One objective of Column 3 was to study the radial dispersion of flow in the horizontal direction. For this, water was applied at one point on the surface of the rock sample bed - the centre point - which is vertically above drainage area 16 (Figure 2-4). The bottom drain structure was divided into 16 annular drainage areas, with the central circle consisting of drainage area 16, the inner annular ring consisting of drainage areas 15, 14, 13 and 12, the middle annular ring consisting of drainage areas 11, 10, 9 and 8, and the outer annular ring consisting of drainage areas 7, 6, 5, 4, 3, 2, 1.

The flow rates in g/min and the flow flux in mg/cm^2/min for the central circle, the inner, the middle and the outer annular rings are plotted in APPENDIX VI.

3.2 DRAINAGE GEOCHEMISTRY

3.2.1 Minerals in Equilibrium with Drainage Solutions

One drainage sample was selected for each time interval in Column 2, Runs 1 and 2 for ICP analysis of twelve dissolved elements: Al, As, Ca, Cu, Fe, K, Mg, Mn, Na, Pb, S, and Zn. For each time interval, the selection of drainage sample was made on an arbitrary basis among the drainage ports that had collected sufficient solution during that time interval. The identification of drainage samples for plotting, tabulation, and discussion is exemplified as follows: C2R1T30P36 = Column 2, Run 1, Time 30 minutes, (drainage) Port 36.

The analytical results obtained for the samples described above were used to compute saturation indices (SIs) with the help of the computer program PHREEQC (Parkhurst, 1995) developed and maintained by the U.S. Geological Survey. In addition to elemental concentrations, pH and redox potential were necessary for the modelling exercise. Experimentally measured pH was used. Since redox potential was not measured on all the drainage samples, missing values were assumed to be E_h = 0.5015 V (the subscript h in E_h means that the potential is relative to the standard hydrogen electrode, or SHE), which is equivalent to pe = 8.5 at 25°C. The conversion from E_h to pe is

$$pe = E_h \cdot \frac{F}{2.303RT} \xrightarrow{25^\circ C} \frac{E_h}{0.0592}$$

The results of the PHREEQC modelling are shown in Table 3-1. All the minerals that showed an SI value greater than -2.0 in any of the simulations are listed. The SI's (excluding those of anhydrite and hematite) are also plotted in Figure 3-1.

Table 3-3 Saturation Indices Calculated by PHREEQC for Selected Drainage Samples

Drainage I.D.	pH	pe	ionic strength	Saturation Index									
				alunite KAl3(SO4)2(OH)6	anhydrite CaSO4	cuprousferrite CuFeO2	diaspore AlOOH	epsomite MgSO4.7H2O	goethite FeOOH	goslarite ZnSO4.7H2O	gypsum CaSO4.2H2O	hematite Fe2O3	jurbanite AlOHSO4
C2R1T30P36	2.94	8.92	0.285	0.485	-0.3	2.039	-1.734	-1.707	1.407	-2.073	-0.083	4.824	0.676
C2R1T60P14	2.74	8.50	0.385	-0.263	-0.182	1.306	-2.231	-1.542	0.425	-1.903	0.034	2.861	0.635
C2R1T120P1	2.70	8.50	0.289	-0.878	-0.203	1.177	-2.441	-1.727	0.388	-2.063	0.014	2.785	0.449
C2R1T180P21	2.79	8.50	0.371	-0.044	-0.183	1.483	-2.133	-1.55	0.545	-1.925	0.033	3.100	0.628
C2R1T240P6	2.80	8.50	0.362	-0.103	-0.177	1.355	-2.125	-1.579	0.496	-1.919	0.039	3.002	0.608
C2R1T600P21	2.84	8.50	0.355	0.132	-0.182	1.577	-2.004	-1.573	0.617	-1.95	0.034	3.245	0.65
C2R2T30P1	2.83	8.50	0.243	-0.307	-0.189	1.359	-2.126	-1.827	0.501	-2.161	0.028	3.011	0.472
C2R2T60P37	2.91	8.50	0.300	0.316	-0.156	1.630	-1.859	-1.685	0.709	-2.038	0.061	3.428	0.622
C2R2T90P37	2.78	8.50	0.271	-0.614	-0.166	1.061	-2.295	-1.747	0.337	-2.096	0.051	2.684	0.425
C2R2T120P34	2.74	8.50	0.293	-0.957	-0.176	1.047	-2.430	-1.702	0.337	-2.032	0.041	2.683	0.383
C2R2T180P34	2.75	8.50	0.271	-0.894	-0.178	0.939	-2.411	-1.747	0.256	-2.089	0.039	2.521	0.367
C2R2T240P6	2.82	8.50	0.274	-0.533	-0.192	1.183	-2.213	-1.733	0.471	-2.074	0.025	2.951	0.428
C2R2T600P30	2.83	8.50	0.307	-0.160	-0.165	1.669	-2.083	-1.675	0.674	-2.026	0.051	3.358	0.562

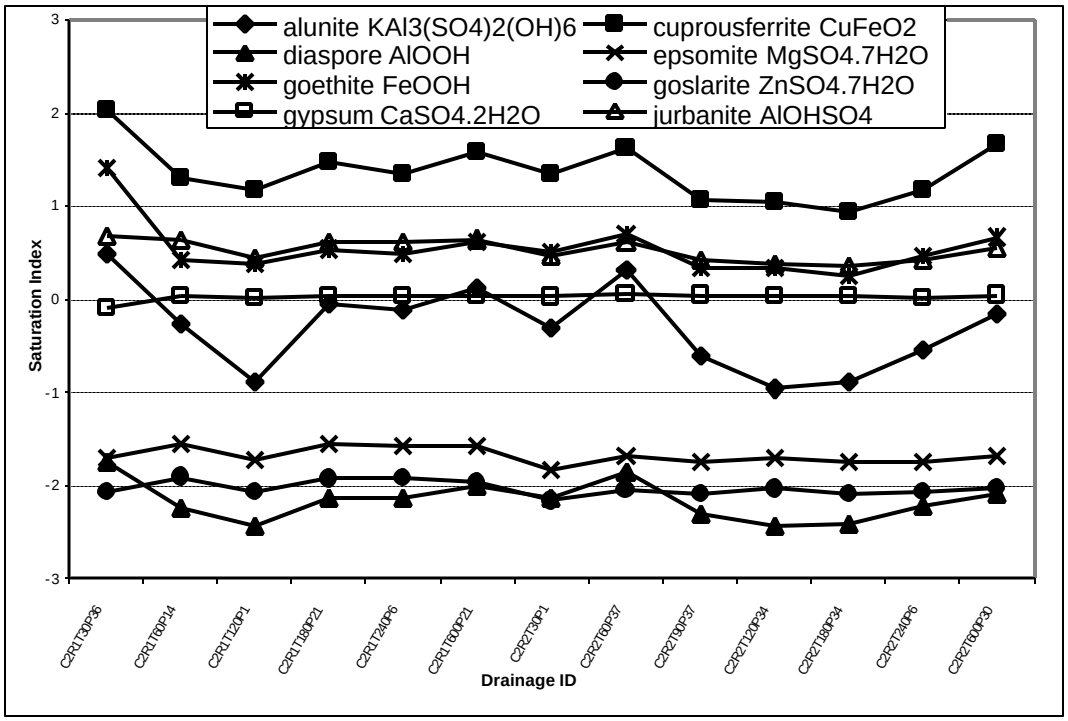

Figure 3-1 Mineral Saturation Indices in Selected Drainage Samples

The SI's are interpreted to infer what mineral phases are in equilibrium with the drainage solutions, as follows:

- Minerals known not to form in the environment of concern, i.e., moist waste rock under natural ambient temperatures, are disregarded. This applies to anhydrite and hematite. Anhydrite does not form because in the presence of moisture and within the naturally varying temperature range, gypsum is thermodynamically and kinetically favoured mineral phase to form. As to hematite, although it is thermodynamically favoured, within the normal natural temperature range it is much less kinetically favoured than goethite.

- If the solution SI for a certain mineral fluctuates widely (e.g., when SI_{max}-SI_{min}>1.0), this mineral is usually not in equilibrium with the solution. This criteria leads us to discard cuprousferrite, alunite, and diaspore.

- If the solution SI for a certain mineral is significantly below zero, the solution is under-saturated with respect to that mineral. This criteria applies to epsomite, goslarite, and diaspore. These minerals are then disregarded as they are unlikely to coexist with the solution.

The above interpretation leaves only three minerals as possible phases in equilibrium with the drainage solutions: gypsum, goethite, and jurbanite. It is clear that gypsum is in equilibrium with all the drainage solutions as the solution SI for gypsum neither fluctuates much nor deviates significantly from zero. In fact, it almost coincides with the ideal, horizontal straight line at an SI of zero.

For goethite and jurbanite, the SI's for different drainage solutions have a small fluctuation around the value of 0.5. This suggests that these two minerals are likely to be in equilibrium with the drainage solutions. The positive displacement of 0.5 in SI values can be explained by one or more of the reasons below:

- The true thermodynamic K_{sp} could differ from the K_{sp} listed in the thermodynamic database of the computer model by a factor of about 3.15 (note log3.15 = 0.5), i.e.,

$$[K_{sp}]_{actual} = 3.15 \times [K_{sp}]_{model}$$

- The thermodynamic K_{sp}'s listed in the thermodynamic database of the computer model are correct, but these minerals may tend to precipitate at a degree of saturation[1] of about 3.15.

- The relevant activity coefficients calculated by the computer model could be positively biased (i.e., larger than the true values).

- The relevant analytical concentrations could be positively biased (i.e., larger than the true values).

One more potential reason for the fluctuation and positive biases of the geothite SI's, especially the large positive bias of the first data point, is the use of assumed instead of measured E_h values. Since E_h is used by the computer model to speciate the Fe, which was measured, into dissolved Fe^{2+} and Fe^{3+}, which were not measured, inaccuracy in E_h would cause inaccuracy in Fe^{3+}, which in turn leads to biased values of SI for goethite.

In addition to these three minerals, another mineral, anglesite $PbSO_4$, is very likely to be in equilibrium with all the drainage solutions. This is the case found in the column dissolution test (Li, 1999, Chapter 4.0) where the SI's for the rinse solutions are all near zero. In the large column tests, however, SI's cannot be calculated because the concentrations of Pb are below the analytical detection limit of 0.25 mg/L. The Pb concentration is likely depressed to such low levels by the very high SO_4^{2-} concentrations, an indirect evidence that anglesite is in equilibrium with the drainage solutions.

In summary, the minerals inferred to be in equilibrium with the drainage solutions are gypsum, anglesite, goethite, and jurbanite.

3.2.2 Mineral Solubility Control of Concentrations in Drainage

The concentration of aqueous element A is said to be controlled by the solubility of mineral A_xB_y

[1] Degree of saturation, S = IAP/K_{sp}, where IAP = ion activity product, K_{sp} = thermodynamic solubility constant (or product). Saturation index SI = log10(S). S=1 or SI=0 means that the solution is in equilibrium with the mineral phase.

if (1) any small addition of A to a solution equilibrated with A_xB_y at an aqueous concentration of C_A causes precipitation of A_xB_y so that there is little change in C_A, and (2) any small removal of A from a solution equilibrated with A_xB_y at an aqueous concentration of C_A causes dissolution of A_xB_y so that there is little change in C_A.

The equilibrium between a mineral phase and a solution does not directly imply that the concentrations of the mineral's dissolved constituents in the solution are controlled by the mineral's solubility. For example, the equilibrium between a drainage solution and gypsum does not mean that the concentrations of both Ca and SO_4^{2-} are effectively controlled by the solubility of gypsum. The rule regarding which dissolved constituent's concentration is controlled by a mineral in equilibrium with the solution is stated as follows:

> Suppose a solution containing dissolved constituents A and B is in equilibrium with the mineral phase AB. The molar concentrations of A and B are C_A and C_B, respectively. If $C_A >> C_B$ then C_B is controlled by the solubility of AB whereas C_A is not; if $C_A \approx C_B$, then both C_A and C_B are controlled by the solubility of AB; if $C_A << C_B$, then C_A is controlled by the solubility of AB but C_B is not. (See APPENDIX VII for further discussion of this rule.)

Using the above rule, since $[Ca] << [SO_4^{2-}]$, $[Pb] << [SO_4^{2-}]$, we conclude that in the drainage solutions studied, the solubility of gypsum controls the concentration of Ca and the solubility of anglesite controls the concentration of Pb. Neither mineral controls the concentration of SO_4^{2-} in the drainage solutions.

In the case of the mineral goethite FeOOH, the precipitation reaction can be written as

$$Fe^{3+} + 3OH^- = FeOOH + H_2O$$

In the drainage solutions, the Fe^{3+} concentration is 1.0×10^{-6} to 2.0×10^{-4} mol/L whereas the pH is usually 2.5 to 3.5, equivalent of 3.0×10^{-12} to 3.0×10^{-11} mol/L OH^-, thus $[Fe^{3+}] >> [OH^-]$. According to the above rule, the presence of goethite will control the concentration of OH^- but not that of Fe^{3+}. In other words, any small amounts of OH^- added to the solutions (e.g., as NaOH) will be nearly 100% precipitated as goethite, whereas any small amounts of Fe^{3+} added (e.g., as $Fe_2(SO_4)_3$) will be nearly 100% retained in solution. One can consider that Fe^{3+} in the solution behaves as a buffer against pH rise.

For the case of jurbanite, $AlOHSO_4$, since the least abundant constituents are OH^- and then Al^{3+}, the mineral would exert a strong concentration control on OH^-, a moderate concentration control on Al^{3+}, and virtually no concentration control on SO_4^{2-}.

In summary, the concentrations of Ca, Pb, Al, and OH^- are controlled by the solubility of gypsum, anglesite, jurbanite, and goethite. This means that any small addition of these ions to the drainage solution will force the entire added amount to be precipitated as their respective controlling minerals. This also means that the concentrations of these ions in the drainage solutions are stabilised.

Somewhat counter-intuitive is that the Fe^{3+} concentration is not controlled by the solubility of goethite, as explained above. This means that small amounts of Fe^{3+} added to the drainage (e.g. as $Fe_2(SO_4)_3$ dissolves) will cause little precipitation of goethite, thus allowing the Fe^{3+} concentration to fluctuate in a wider range than if Fe^{3+} were controlled by the solubility of some mineral.

No mineral solubility controls appear to exist for SO_4^{2-}, Zn, and Mg, the three most concentrated dissolved constituents in the drainage solutions. Neither appear there to be any mineral solubility controls for Fe^{2+} and Fe^{3+} (generally Fe^{2+} is two orders of magnitude more concentrated than Fe^{3+} and thus dominate the Fe). The concentrations of these constituents can therefore vary in wide ranges, as is indeed observed for SO_4^{2-}, Zn, and Fe.

The above findings are made on the test results of Column 2, Runs 1 and 2. Generally, they should apply to other column tests as long as the test conditions do not deviate from those of C2R1 and C2R2 drastically.

In the absence of mineral solubility control, what other factors and processes determine the concentrations of SO_4^{2-}, Zn, and Fe in the drainage? This question is dealt with below.

3.2.3 Correlation among S, Zn, Fe, and Conductivity

Studying the relationships among different solution parameters may help reveal the factors or processes which regulate the concentrations of these parameters. An examination of the solution analysis data reveals that the drainage in all the ports from all the columns and runs is basically a mixed solution containing a few cations and one major anion. In an approximately decreasing order of concentration, the cations are Zn^{2+}, Mg^{2+}, Fe^{2+}, Al^{3+}, and Ca^{2+}. The major anion is SO_4^{2-}. Since for the majority of drainage samples solution analysis is available only for Zn, Fe, and S, attention is given mainly to these three elements below.

In Figure 3-1, dissolved Zn and Fe are plotted against S and conductivity for the 10 individual runs of the three columns. The S exists in the solution all in the form of SO_4^{2-}. The following can be observed:

- For all the runs, there is a good, positive, linear correlation between Zn and S with little scatter. A similar correlation exists between Zn and conductivity, but with more scattered points.

- The degree of correlation between Fe and S is dependent of the Fe concentration. When the Fe concentration is greater than about 500 mg/L, a fair, positive, linear correlation exists. When the dissolved Fe is below about 200 mg/L, the correlation disappears. The correlation between Fe and conductivity has a similar pattern, albeit with more scattered points.

- Generally, the linearity and the degree of correlation are higher between Zn and S (or conductivity) than between Fe and S (or conductivity).

Figure 3-2 shows how the correlation among S, Zn and conductivity varies from run to run for the three columns.

All Columns

The are some scattered points away from the main trends in the S-conductivity plots. As S (in the form of SO_4^{2-}) accounts for the majority of anions, a good correlation between S and conductivity is expected and indeed observed. The outlier points in the S-conductivity plots likely represent measurement errors in conductivity. The reason for some erratic conductivity measurements is most likely shortage of solution samples in some ports, in which case the electrode cannot be fully immersed.

Column 1

For C1, the Zn-S plot is a straight line with little scatter. This means that the concentration ratio of Zn/S is constant in all three runs. From R1 (Run 1) through R2 to R3, the data point cluster moves towards the origin. This can be explained by partial depletion of Zn and SO_4^{2-} in the pore water as simulated rain was passed through it. Note that the intervals between R1 and R2 and between R2 and R3 are short: two days and four days, respectively (Table 3-2). The short intervals did not allow the washed rock to oxidise sufficiently to replenish the Zn and SO_4^{2-} washed away during the previous test.

The solid line represents the locus of a pure $ZnSO_4$ solution on the Zn-S plot. Comparison of the solid line with the line defined by the data points shows that about 30% of the S in the solution exists as counter-ions to dissolved Zn^{2+}, and the remaining 70% mainly as counter-ions to Mg^{2+}, Fe^{2+}, Al^{3+}, and Ca^{2-}. The addition of different tracers in R1, R2 and R3 did not produce noticeable shifts in conductivity, this is understandable since the concentrations of the tracers added were only small fractions of the total electrolyte concentrations in the drainage solutions.

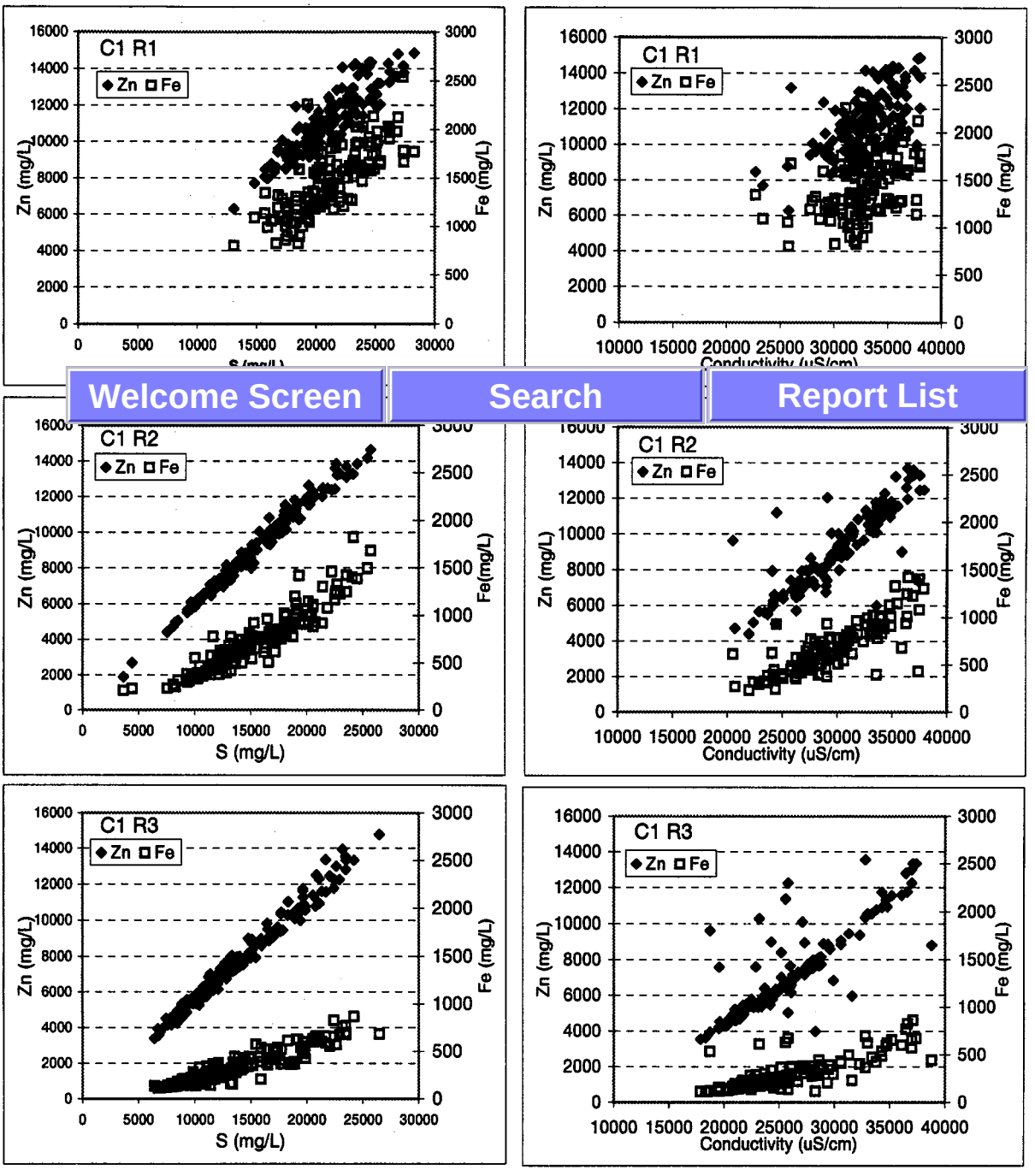

Welcome Screen | Search | Report List

Figure 3-2 Zn and Fe Plotted against S and Conductivity for Individual Runs

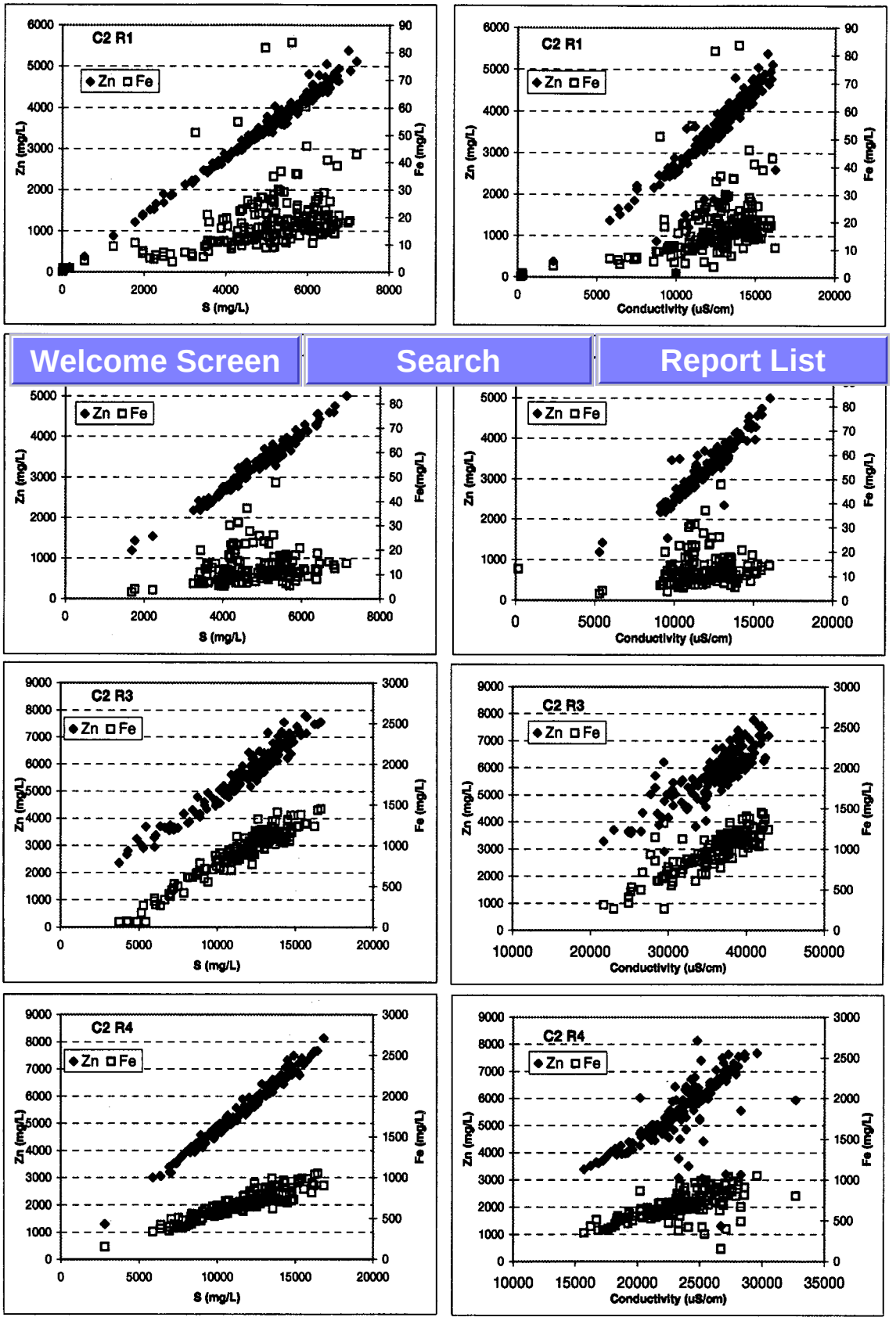

Figure 3-2 Zn and Fe Plotted against S and Conductivity for Individual Runs (Continued)

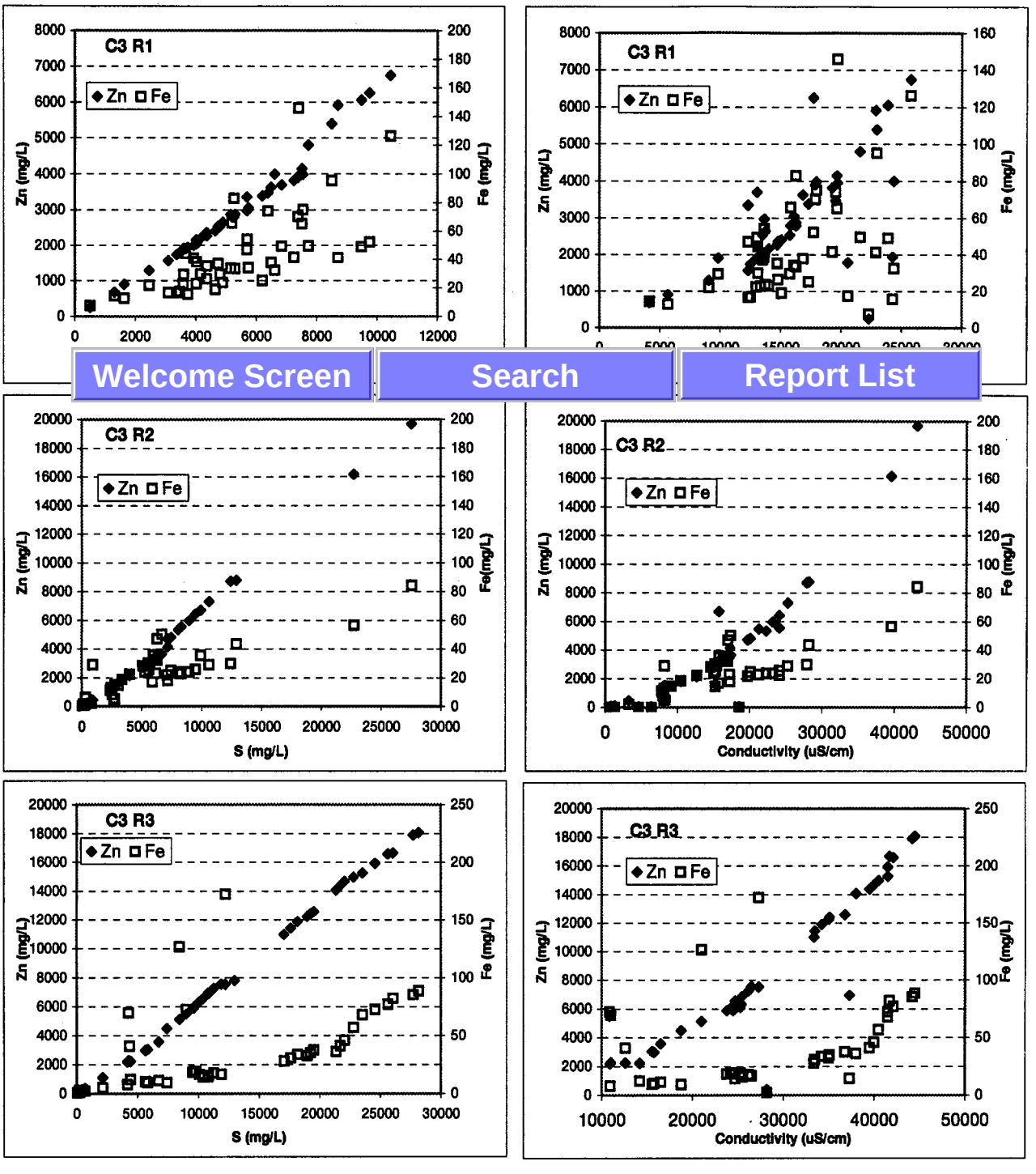

Figure 3-2 Zn and Fe Plotted against S and Conductivity for Individual Runs (Continued)

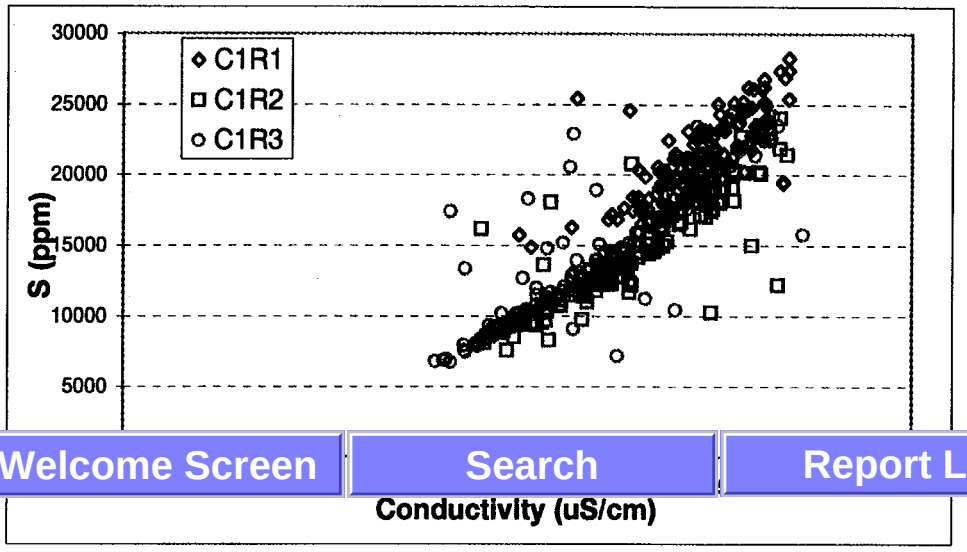

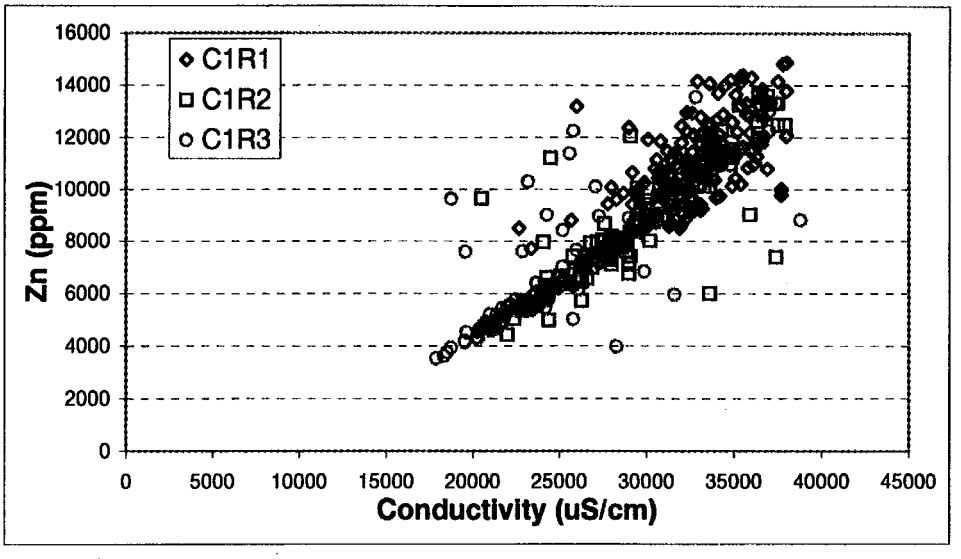

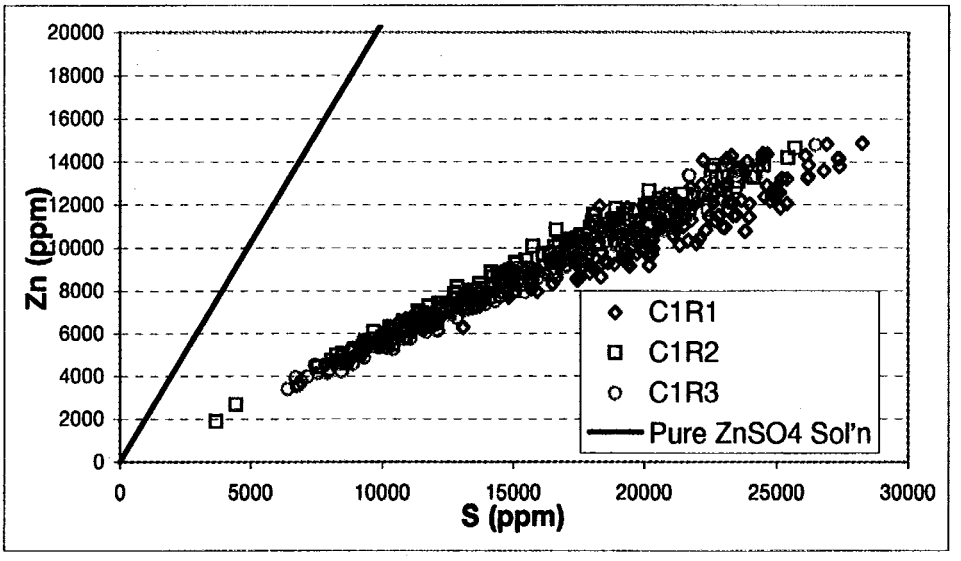

Figure 3-3 Correlation among S, Zn, and Conductivity for Individual Columns

Welcome Screen Search Report List

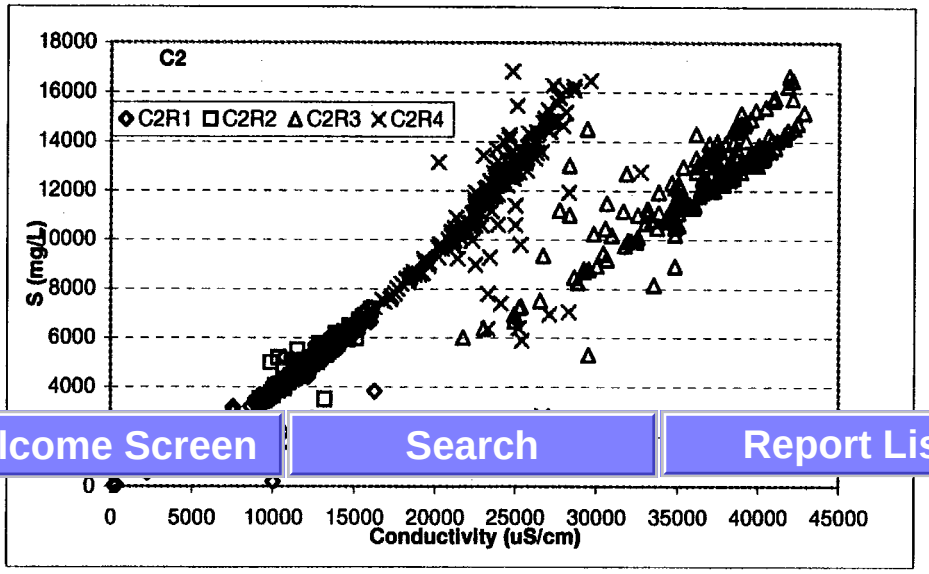

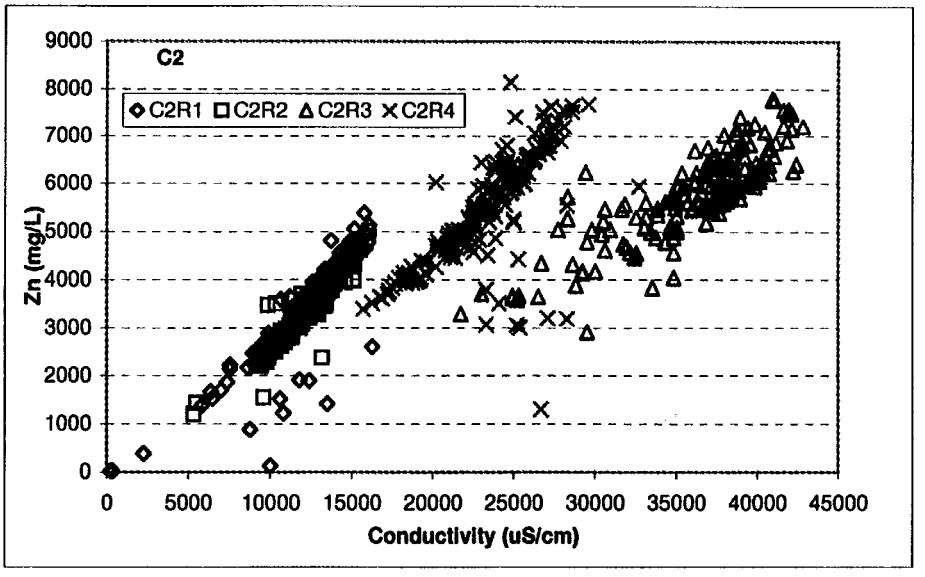

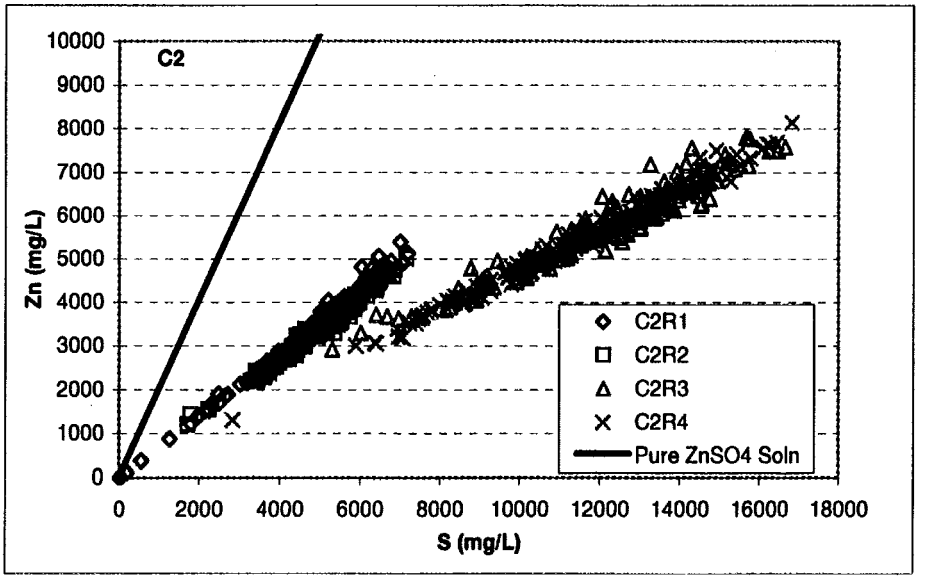

Figure 3-3 Correlation among S, Zn, and Conductivity for Individual Columns (Continued)

Welcome Screen Search Report List

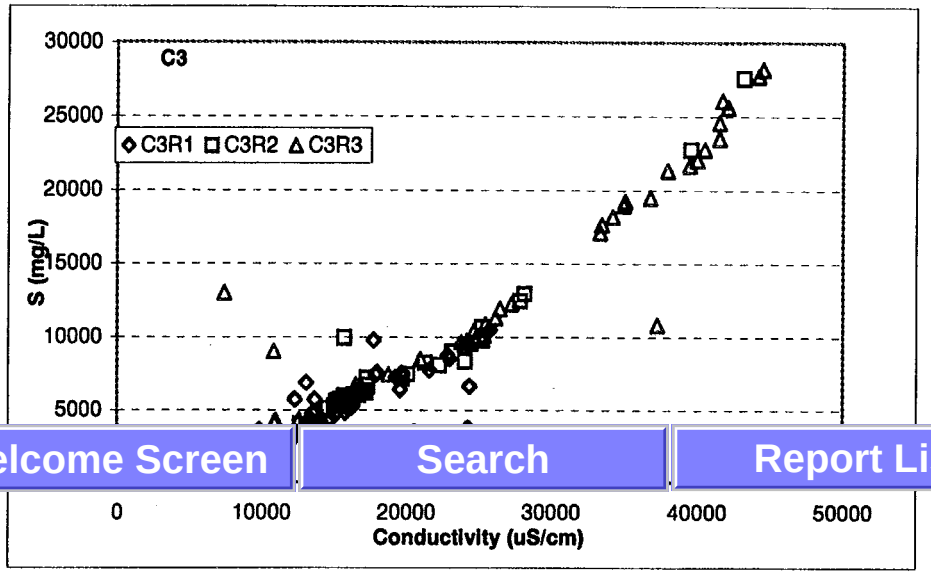

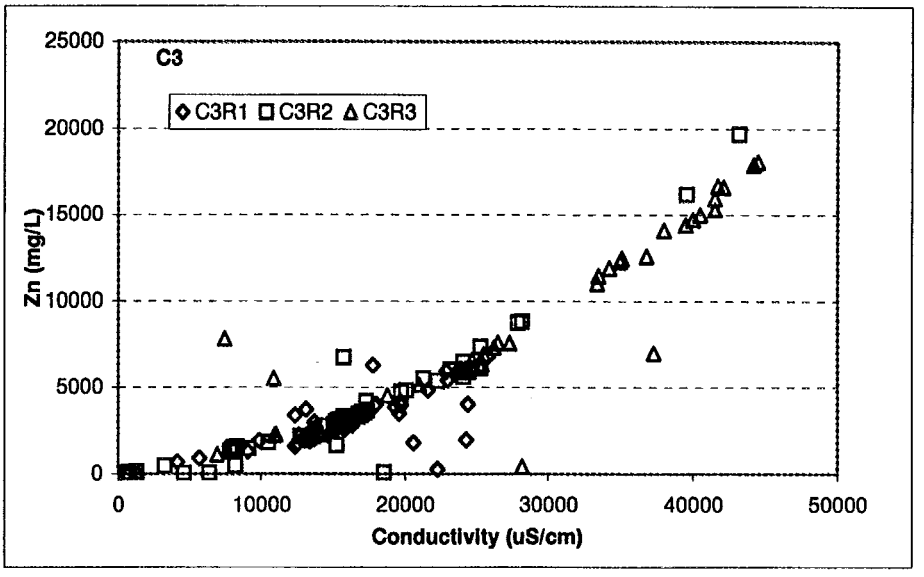

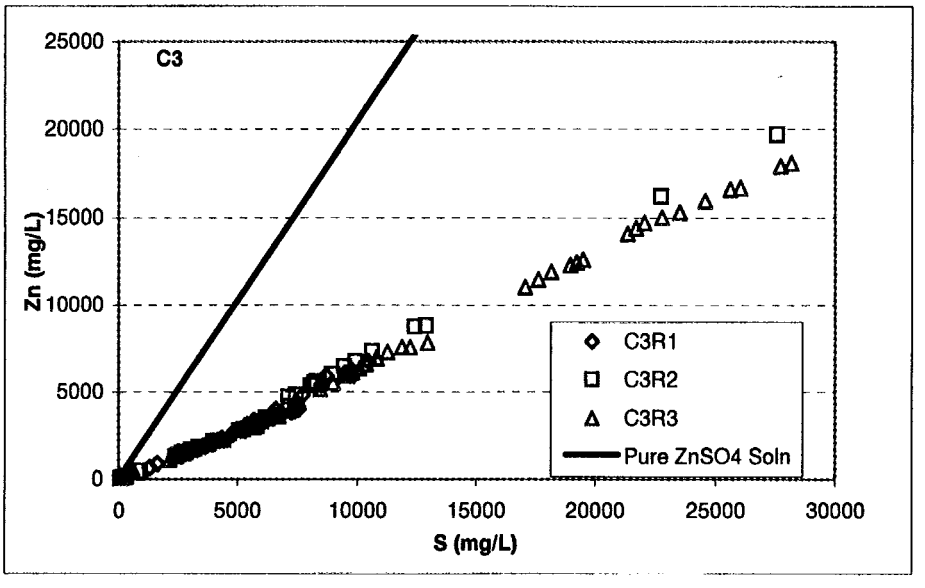

Figure 3-3 Correlation among S, Zn, and Conductivity for Individual Columns (Continued)

Column 2

For C2, two straight lines are defined by the experimental data points on the Zn-S plot: R1 and R2 follow one line; R3 and R4 follow another. The most likely reason for the difference between the slopes of the R1-R2 trend and the R3-R4 trend is the long delay between R2 and R3 (Table 3-2): the delays between R1, R2, R3, R4 are 2, 76, and 5 days, respectively. The 76 days of delay between R2 and R3 gave the rock mass, after the particle surfaces were washed clean, sufficient time to oxidise. When the re-oxidised rock was washed again in R3, much higher Zn concentrations resulted. The smaller slope for R3-R4 data means that dissolved $ZnSO_4$ accounts for a smaller percentage of the total dissolved SO_4^{2-} in the R3-R4 drainage solutions than in the R1-R2 drainage solutions. This can be explained if we assume the ratio of (sphalerite oxidised)/(pyrite oxidised) was smaller during the 76 days of oxidation between R2 and R3 than the total cumulative oxidation prior to R1. The ground for this assumption is that in the field preferential oxidation of sphalerite was likely to have occurred. This preferential depletion of sphalerite would have reduced the sphalerite/pyrite ratio in the rock mass, hence later oxidation such as that which took place between R2 and R3 would produce more $FeSO_4$ and less $ZnSO_4$, or a smaller ratio of (sphalerite oxidised)/(pyrite oxidised).

Now that the change in slope from R1-R2 to R3-R4 is explained, what is responsible for the large increases in Zn concentrations from R1-R2 to R3-R4? The increase in the rock bed thickness from 1.0 to 1.5 m from R2 to R3 may explain some of the increases. This, however, cannot be the main reason, since when the bed was increased from 0.5 to 1.0 m from R1 to R2, the drainage Zn concentrations did not show noticeable elevation. In addition, the deviation of the R3-R4 slope from the R1-R2 slope suggests that the dissolved SO_4^{2-} salts in the R3-R4 drainage originated more likely from the new oxidation products in the lower 1.0 m rock bed than the old, accumulated oxidation products that prevails in the upper 0.5 m rock bed. This leads to the hypothesis that the 76 days of new oxidation resulted in a higher Zn concentration in the drainage than all the previous accumulated oxidation combined. Considering that the new oxidation took place at a lower ratio of (sphalerite oxidised)/(pyrite oxidised), to produce this higher Zn concentration, much more pyrite would have to be oxidised, causing much higher Fe concentrations than previously observed in R1-R2 drainage. Also, since the oxidation of sphalerite does not produce acid whereas the oxidation of pyrite does (reactions below), the new oxidation would yield lower pH in the R3-R4 drainage than in the R1-R2 drainage. This is indeed observed. In Section 3.2.5 , it is shown that the dissolved Fe is roughly two orders of magnitude higher, and the pH is significantly lower in the R3-R4 drainage than in the R1-R2 drainage (Figure 3-2). Nevertheless, as will be shown in Figure 3-1, the change in the slope of the Zn-S trend line, on a broader scale, is not very large and falls within the normal variations exhibited by the three columns.

$$ZnS + 2O_2 = Zn^{2+} + SO_4^{2-}$$
$$FeS_2 + 3.5O_2 + H_2O = Zn^{2+} + 2SO_4^{2-} + 2H^{2+}$$

Column 3

For C3, water was applied at one central location on the sample bed surface, in contrast with the

simulated rain application for C1 and C2. The sample bed thickness increased from 0.5 to 1.0 to 1.5 m from R1 to R2 to R3, as opposed to one sample bed thickness of 1.5 m in all three runs for C1. Despite these differences, the Zn-S responses are similar to those of C1, that is, a good linear correlation exists between Zn and S. The number of data points for C3 is much less than that for C1 and C2 because of the reduced number of drainage ports.

Again, the S in the SO_4^{2-} anions counter-balancing the Zn^{2+} cations accounts for approximately 30% of the S. The time intervals between R1, R2 and R2, R3 are 14 and 2 days, respectively. As a result of the 14 days of delay between R1 and R2, some limited pH lowering and Zn rise are observed in R2-R3 when compared with R1, but the delay was not long enough to cause noticeable elevation of Fe (Figure 3-2, Figure 3-2). Refer to the discussion under Column 2 above for explanation of these phenomena.

3.2.4 Concentration-Controlling Mechanism Inferred from Zn-S Correlation

The correlation between dissolved Zn and S in the drainage solutions for all ten experimental runs is illustrated in Figure 3-1. The data points can be contained in a triangle 0AC with its apex situated at the origin. A straight line 0B can be fitted to the data which defines an average fixed Zn/S ratio. This fixed ratio means that dissolved $ZnSO_4$ accounts for a constant percentage of the dissolved SO_4^{2-}. Recall that the ten runs varied widely in experimental conditions, including sample bed height, simulated rain intensity and duration, pattern of water application, and so on. Also note that the Zn and S concentrations varied widely, from zero to about 16 000 mg/L Zn and 27 000 mg/L S. Now the question to ask is this: does this approximately constant Zn/S ratio delineate some underlying geochemical process?

The answer is probably yes, and one possibility of such an underlying process is successive dilutions and mixing of diluted solutions. To show that dilutions and mixing of dilutions can produce this linear relationship, two prerequisites are necessary: First, within the concentration range considered, dissolved Zn and S are not subjected to mineral solubility control, that is, no Zn or S is chemically precipitated from a solution when it is diluted. This is satisfied, as explained in Section 3.2.2 . Second, successive dilutions and mixing of various dilutions of an original solution must maintain a constant Zn/S ratio (for the proof of this point see APPENDIX VIII).

Graphically, the dilution of a solution with pure water corresponds to a movement of the point representing the undiluted solution towards the origin along the straight line defined by that point and the origin. For example, dilution of the solution represented by point B will produce a new solution that can be represented by a point on the straight line 0B, with the exact location of the point determined by the magnitude of the dilution factor. Mixing of two solutions with the same Zn/S ratio (whose representative points must necessarily fall on a straight line radiating form the origin) produces a new solution represented by a point on the line segment connecting the two points representing the two original solutions. Similarly, mixing of two solutions with different Zn/S ratios generates a new solution which can be represented by a point on the line segment connecting the two points representing the two mixing solutions, the only difference being that this time the extension

of the line segment do not pass the origin. It then follows that using two solutions represented by two arbitrary points P and Q on the Zn-S plot, the solution composition corresponding to any arbitrary point X within the triangle 0PQ can be recreated by dilutions and/or mixing.

It can be postulated that all the solutions represented by the points in the data triangle 0AC in Figure 3-1 are created by dilutions and/or intermixing of a set of solution compositions represented by points within the circle R. For simplicity, we can regard all observed solution compositions as a result of dilutions of one composition, situated at point D (not shown in Figure 3-1) on the line 0B and beyond point B, and treat the scatter above and below line 0B as random variations. Clearly, point D represents the original pore water Zn and S concentrations.

To show that the observed Zn and S concentrations resulted entirely from dilutions of one solution composition representing the original pore water, another possibility which may give rise to the observed linear trend shown in Figure 3-1 must be ruled out: the dissolution of solid zinc sulphate minerals (such as goslarite $ZnSO_4 \cdot 7H_2O$) at a constant Zn/S ratio.

The -2 inch fraction of the waste rock has a moisture of about 6%. The soluble sulphate storage in the waste rock determined in the column dissolution tests is 6.15 kg SO_4^{2-}/t of waste rock (Li, 1999), mainly in the form of Zn, Fe, Al, and Mn sulphates. Assuming 30% of the soluble sulphate stored is in the form of $ZnSO_4$ (this is an experimental average represented by line 0B), then there would be 3.10 kg $ZnSO_4$/t of rock. Calculations using these data give 51.6 g/L $ZnSO_4$ in the pore water. This is about one order of magnitude less than the solubility of $ZnSO_4$ (419 and 544 g/kg of water at 0 and 25 °C, respectively, Perry and Green, 1997). Therefore, all the stored $ZnSO_4$ is accommodated in the pore water and not in zinc sulphate minerals.

The pore water Zn concentration corresponding to 51.6 g/L $ZnSO_4$ is roughly 21 g/L. Extending line 0B passing point B to a Zn concentration of 21000 mg/L gives a corresponding S concentrations of 39 000 mg/L. The point representing Zn=21000 mg/L and S=39 000 mg/L is point D - the Zn and S composition of the original pore water. The highest S concentration observed in all runs is about 28 000 mg/L, 1.4 times smaller than the S concentration at point D.

“Original pore water” refers to the pore water associated with the waste rock before the simulated rain experiment began. Thus the solute concentrations in the original pore water are a reflection of the history of the waste rock. Once rinsed, the original pore water is diluted and the pore water in the waste rock can no longer be called original.

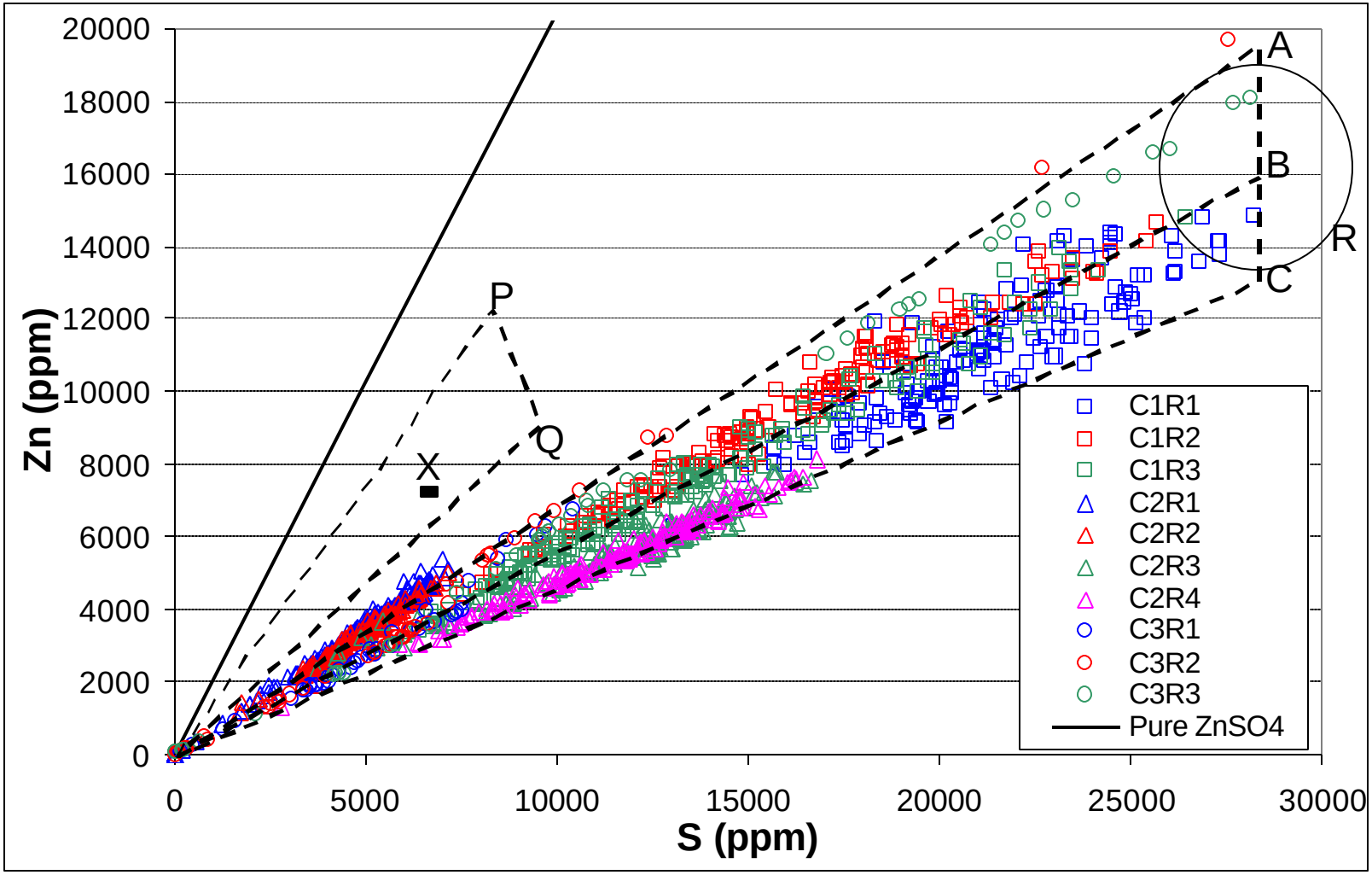

Figure 3-4 Overall Correlation between Zn and S for All Runs

The above calculations are approximate because (1) the rock samples used in the large column tests are not exactly the same as that used in the column dissolution tests, (2) the moisture content of 6% used may not be sufficiently accurate. In fact, intuitively one would expect that the highest observed Zn and S concentrations correspond to the original pore water concentrations. If this were the case, the original pore water concentrations would correspond to point B at 28 000 mg/L S and 16 000 mg/L Zn. It is believed that these concentrations better represent the original pore water S and Zn concentrations and thus will be used in later analysis. In any event, point D and point B differ only by a factor of 1.4, which is not very large.

3.2.5 Correlation among Zn, Fe, S, pH, and Flow Rate

Figure 3-1 plots dissolved Zn and Fe against flow rate and pH for the ten individual test runs. Figure 3-2 plots dissolved S, Zn and Fe against pH and dissolved S, Zn, Fe, pH against flow rate.

Lack of Relationship between Dissolved Zn, Fe, S, pH and Flow Rate

Both graphs show a lack of relationship between dissolved elements Zn, Fe, S and flow rate, as well as a lack of relationship between pH and flow rate. This lack of relationship has been documented in a number of field cases (e.g., Smith et al., 1995, Morin et al., 1994). There is, however, a downward shift in the S, Zn, and Fe data clusters and upward shift in the pH data clusters from C1R1 to C1R3, reflecting the dilution of pore water concentrations at the beginning of each run.

This lack of relationship simply means that the flow rate is not a main controlling variable for the concentrations and the pH of the drainage. However, one must be careful not to take this further to mean that the concentrations and the pH are not at all related with dilution.

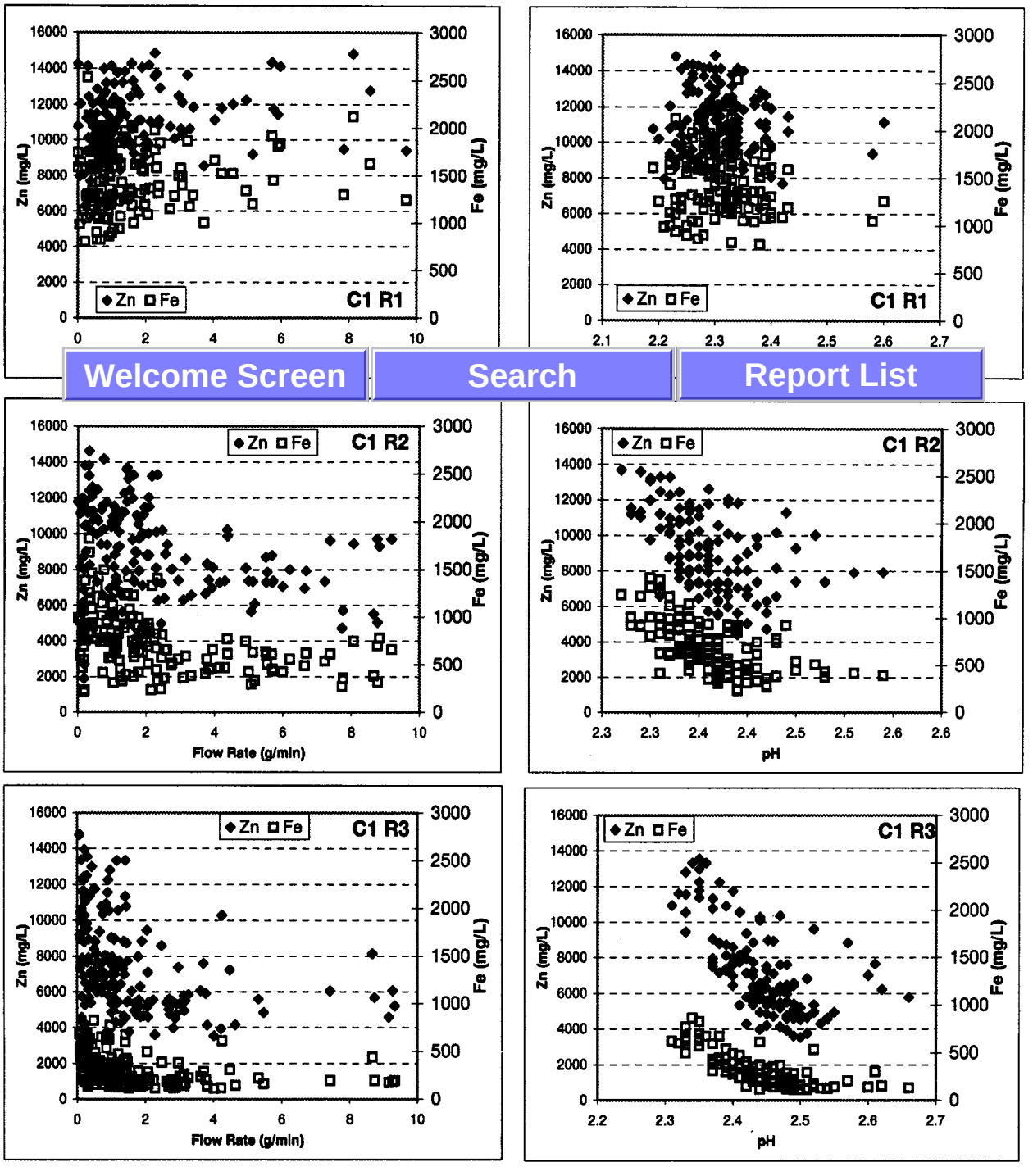

Welcome Screen | Search | Report List

Figure 3-5 Correlation between Zn, Fe and Flow Rate, pH for Individual Test Runs

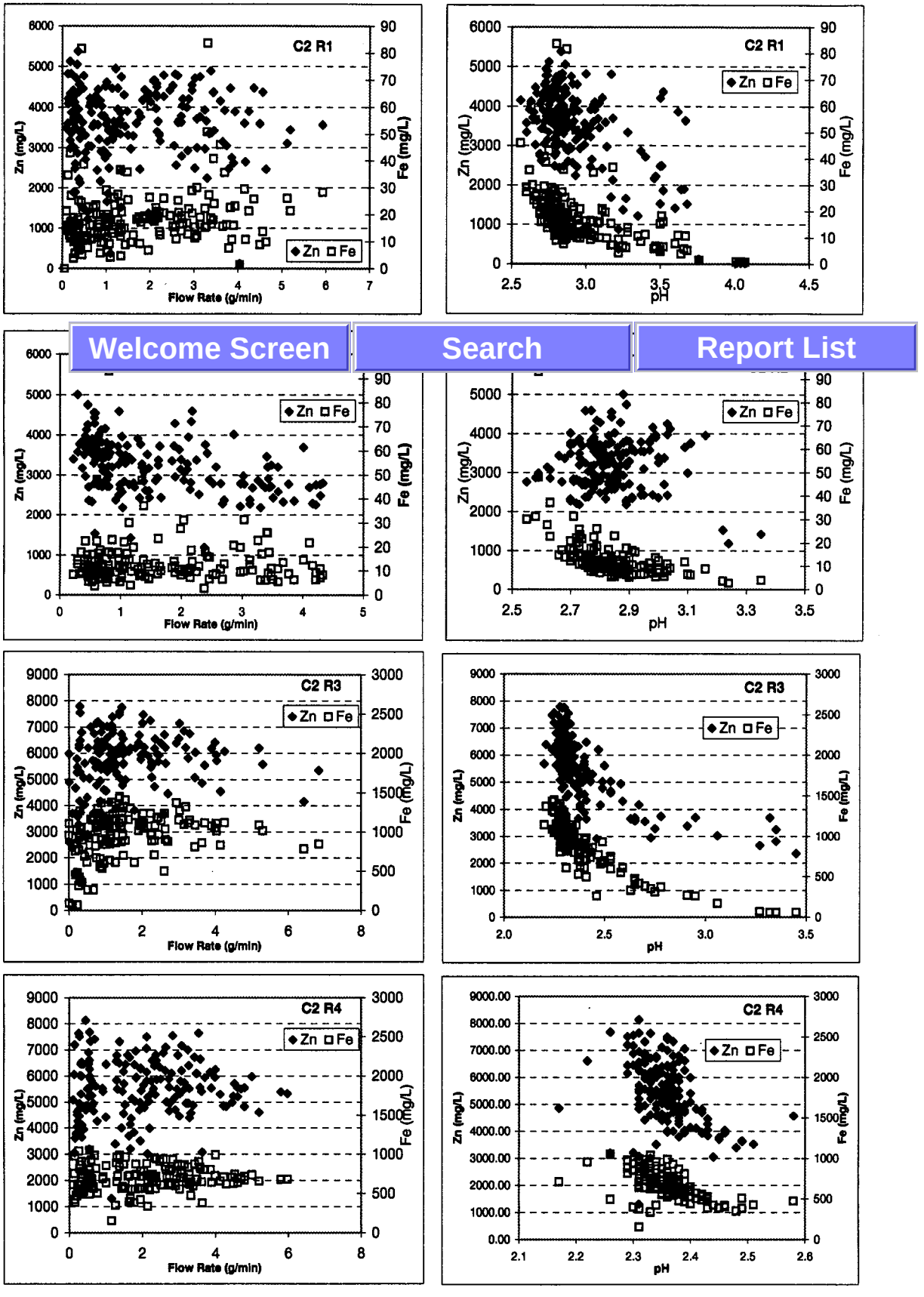

Figure 3-5 Correlation between Zn, Fe and Flow Rate, pH for Individual Test Runs (Cont'd)

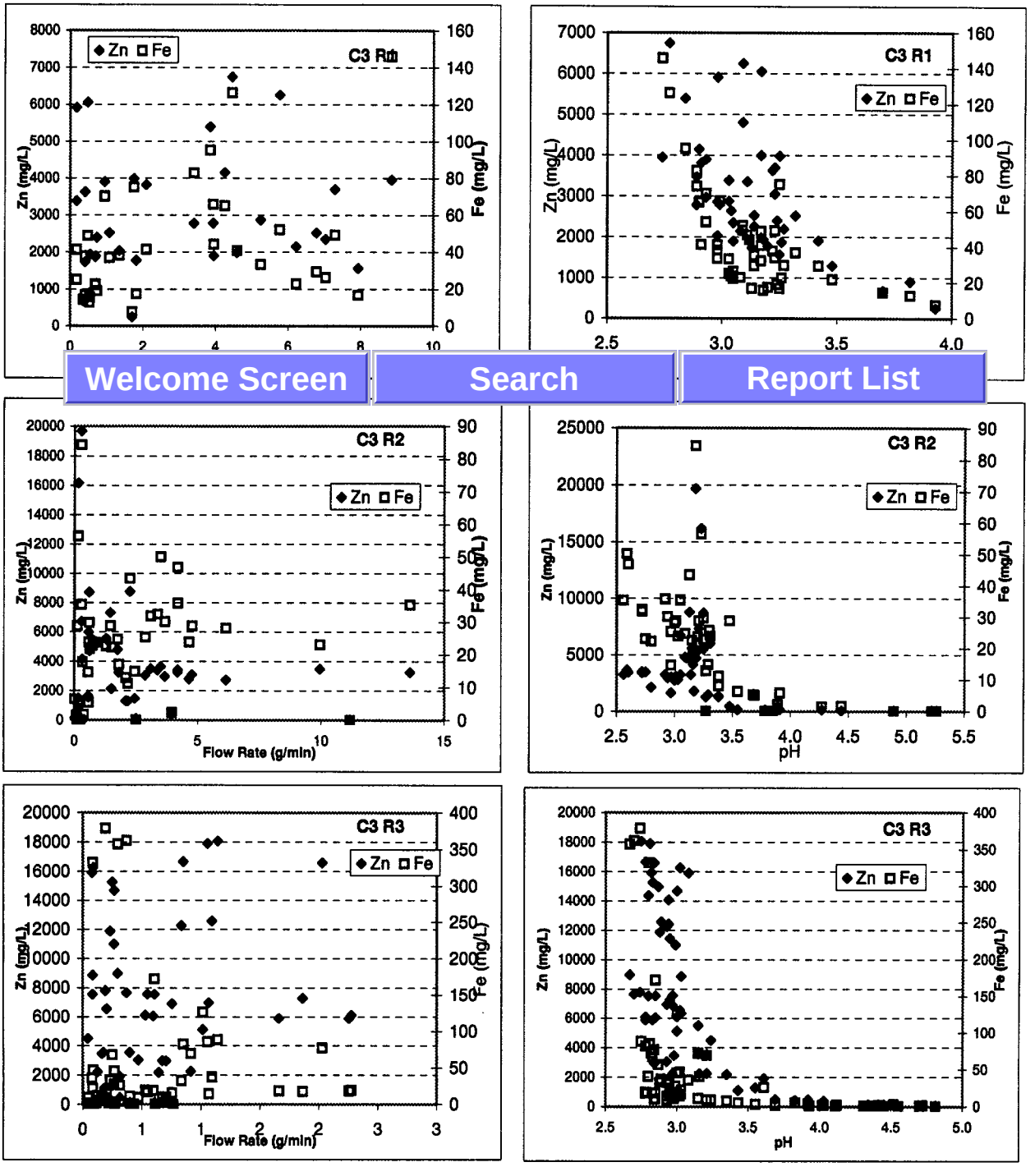

Figure 3-5 Correlation between Zn, Fe and Flow Rate, pH for Individual Test Runs (Cont'd)

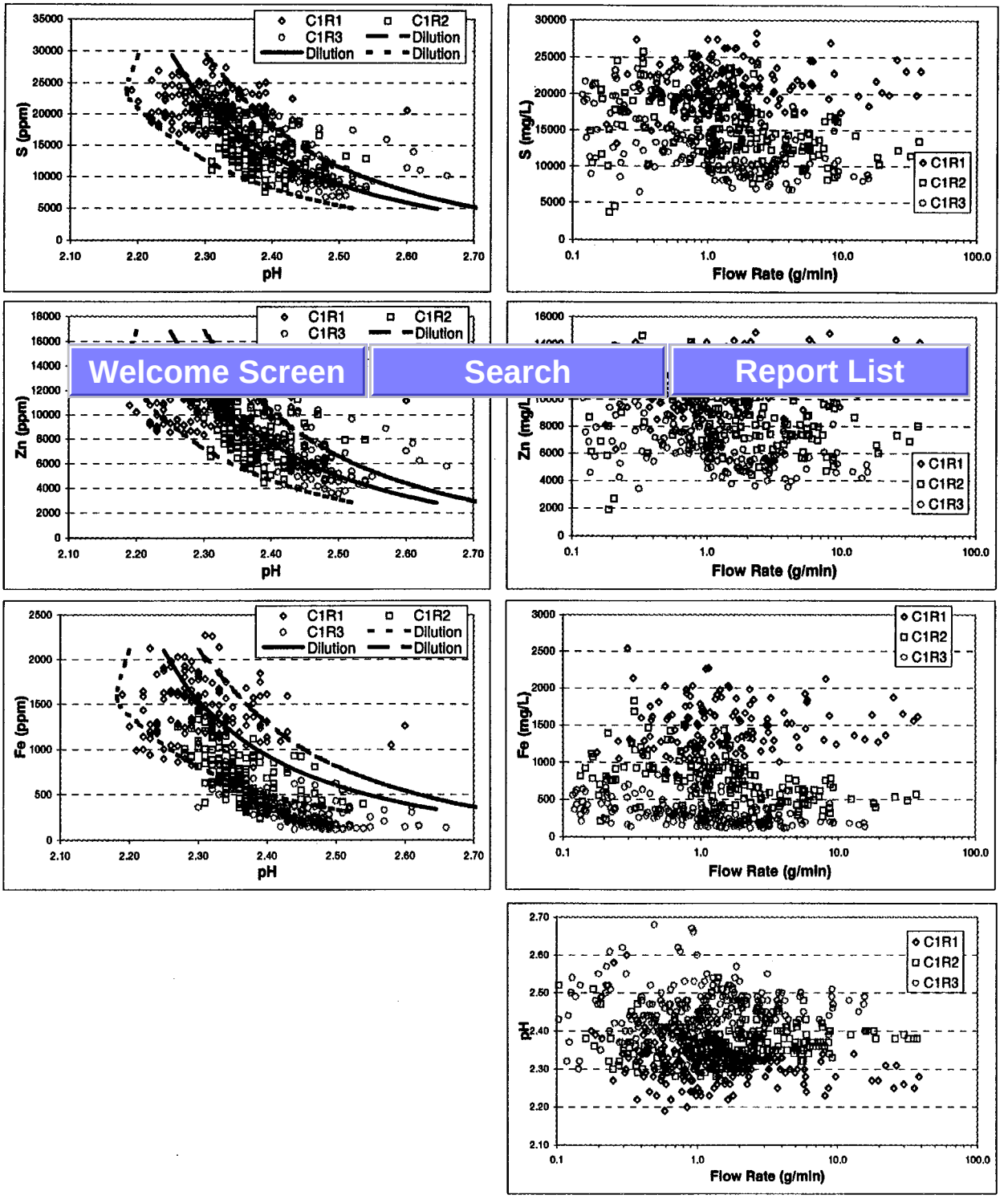

Figure 3-6 S, Zn, Fe vs. pH and S, Zn, Fe, pH vs. Flow Rate for Individual Columns

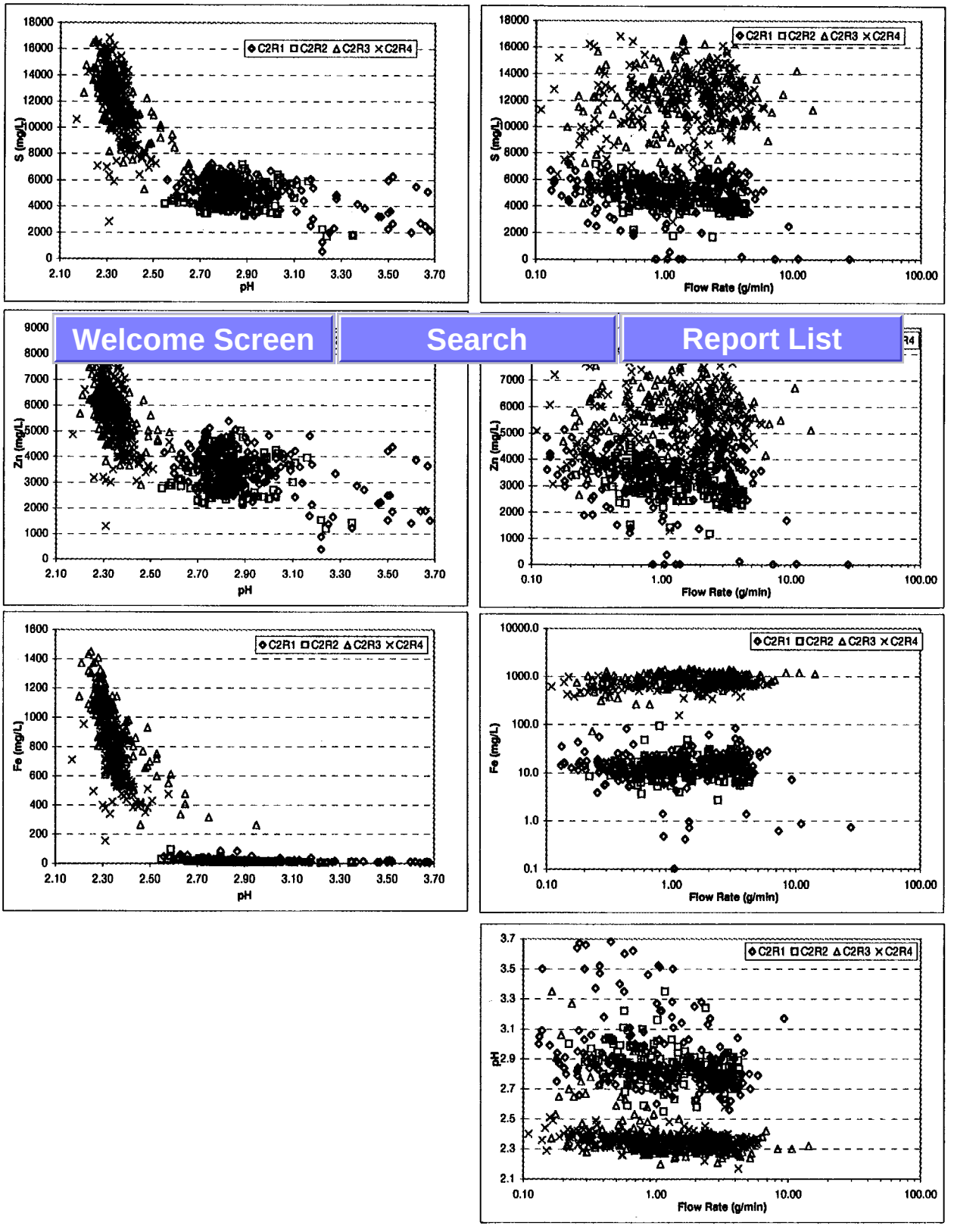

Figure 3-6 S, Zn, Fe vs. pH and S, Zn, Fe, pH vs. Flow Rate for Individual Columns (Cont'd)

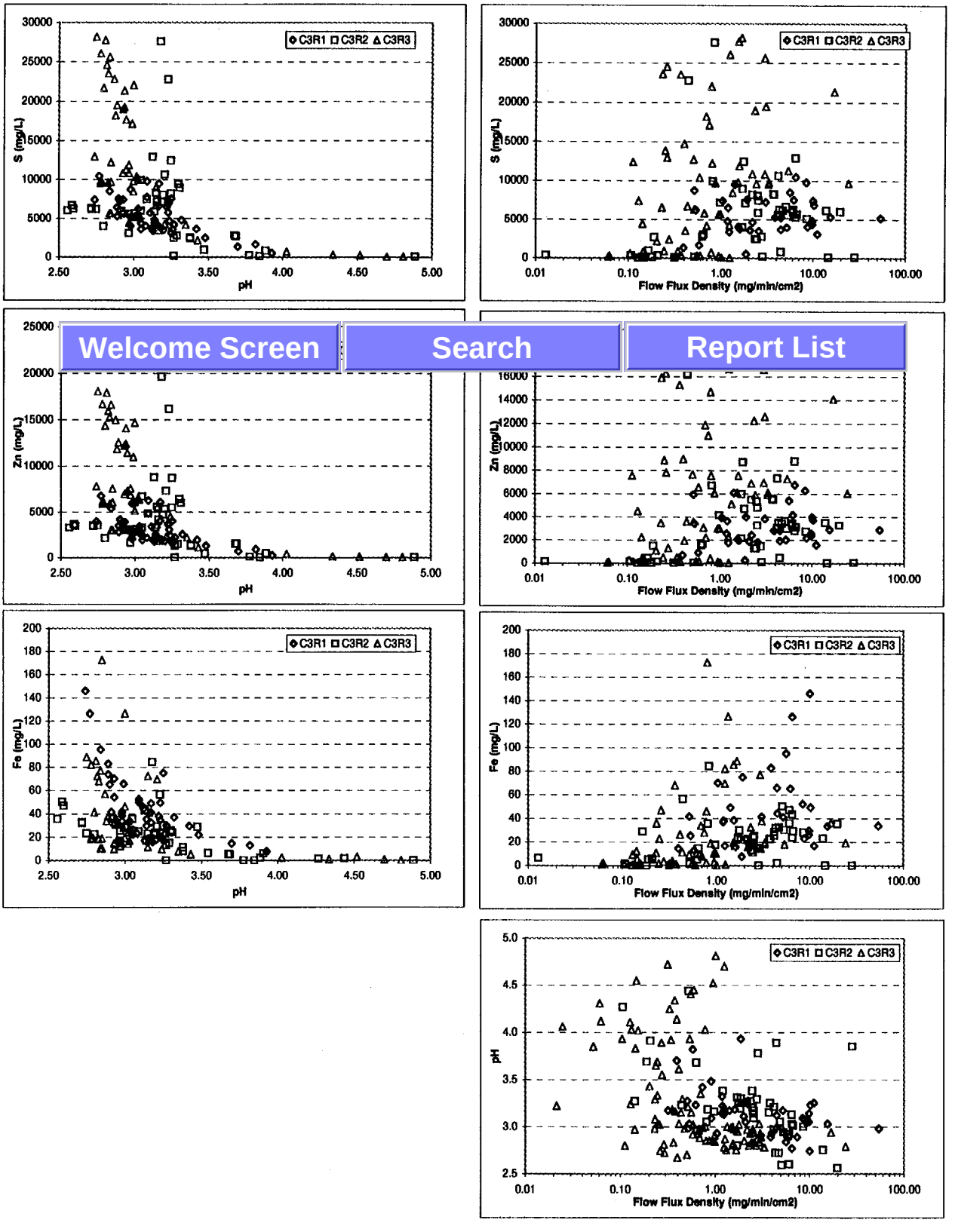

Figure 3-6 S, Zn, Fe vs. pH and S, Zn, Fe, pH vs. Flow Rate for Individual Columns (Cont'd)

Relationship between Zn, Fe, S and pH

It appears from Figure 3-1 and Figure 3-2 that the dissolved Zn, Fe and S are, to a certain extent, inversely related with the drainage pH, although there is a large degree of scatter in all runs and columns. However, correlation does not necessarily imply a cause-effect relationship and in the present case, it does not. One must avoid the mistake of concluding that the Zn, Fe, and S concentrations are controlled by the pH. The reasons why these concentrations are not pH-controlled are as follows:

- Geochemical equilibrium modelling of the drainage solutions reveals no Zn, Fe, or S-containing mineral phases that would limit the concentrations of these elements (Sections 3.2.1 and 3.2.2).

- At any given pH, there is a wide variation of dissolved Zn, Fe, or S. By definition, for a truly pH-controlled concentration, the variation at a given pH should be quite narrow, comparable in magnitude to the uncertainties in measurement and analysis.

- There is no ground to believe that dissolved S is subject to pH control, yet it varies in a fashion similar to that of Zn and Fe. This suggests an alternative control on these concentrations other than the pH.

Since the concentrations are not pH-controlled but are somewhat related to pH, there must be a third variable that underlies the apparent correlation. As it turns out, this third variable appears to be the dilution factor, as explained in Section 3.2.4 . More discussions based on the S-, Zn-, and Fe-pH relationships (Figure 3-2) for Column 1 follow.

3.2.6 Concentration-Controlling Mechanisms Inferred from S, Zn, Fe-pH Relationships

In Section 3.2.4 it was shown that the Zn-S correlation observed for all the test runs is consistent with the hypothesis that all the drainage solutions resulted from successive dilutions and/or intermixing of various-stage dilutions of the original pore water. Now let us examine whether this dilution hypothesis is consistent with the S-, Zn-, and Fe-pH relationships observed for C1.

On the graphs for C1 in Figure 3-2 (page 51), three curves are drawn: the upper (dashed), the middle (solid), and the lower (dotted) curve. These curves are drawn using data created by computer modelling (PHREEQC) of dilutions of typical pore water compositions, with details given below:

- The pore water S and Zn concentrations used are those determined in Section 3.2.4 : 28 000 mg/L S and 16 000 mg/L Zn. The pore water Fe concentration is estimated to be 2000 mg/L from the Fe-pH graph for C1 in Figure 3-2. The starting point on the upper left corner of each curve corresponds to a dilution factor of 1 (i.e., no dilution) and the end point on the lower right corner of each curve corresponds to a dilution factor of 0.2 (i.e. five times dilution).

- The three starting points differ only slightly in pH and Fe^{2+}/Fe^{3+} ratio: dashed curve - pH=2.30, Fe^{2+}/Fe^{3+}=39; solid curve: pH=2.25, Fe^{2+}/Fe^{3+}=19; dotted curve: pH=2.20, Fe^{2+}/Fe^{3+}=5.7. The range of the Fe^{2+}/Fe^{3+} ratios used, 39 to 5.7, corresponds to an equilibrated pe value range of 9.70 to 10.47, or an E_h range of 550 to 599 mV, which agree well with the limited number of E_h measurements.

- To create data for each curve, the starting solution composition (i.e., S, Zn, Fe, Fe^{2+}/Fe^{3+} ratio and pH; other elements were ignored) is diluted by mixing with water in 20 equal steps covering the dilution factor range from 1 to 0.2. At each step the solution is equilibrated under the constraints imposed by mass balances. The concentrations of S, Zn, Fe and pH, pe are determined by the equilibrium. The mineral goethite FeOOH is allowed to precipitate when saturation is achieved. The system is also brought to equilibrium with atmospheric carbon dioxide at $10^{-3.5}$ atm partial pressure.

- During the simulations, small percentages of Fe were precipitated as FeOOH, but no Zn-containing minerals (hydroxides, carbonates, sulphates, or mixed salts) nor sulphate-containing minerals reached saturation.

Figure 3-2 shows that the observed trends in the S-, Zn-, and Fe-pH relationships are in agreement with the three curves constructed based on the dilution of pore water. The observed data trends in the S-pH, Zn-pH, and Fe-pH plots can fully be explained by dilutions of varying degrees of the original pore water, with the pH regulated by hydrolysis of cations (Fe^{3+}, Fe^{2+}, and Zn^{2+}) and precipitation of goethite, FeOOH. The observed scatter can be explained by small variations of redox conditions. The agreement between the modelling results and the observed data lends further support to the dilution hypothesis first introduced in Section 3.2.4 from analysis of the Zn-S correlation. This dilution hypothesis is now stated as follows:

> In the large column tests, the observed S, Zn, Fe concentrations and the pH of the drainage solutions result from dilution of the original pore water, subject to equilibrium with redox reactions and goethite precipitation which are themselves caused by the dilution process.

The foregoing analysis has basically established geochemical links among four groups of variables:

1. Pore water chemistry including analytical concentrations, pH, and E_h
2. Average dilution factor or dilution factor distribution
3. Dilution-controlled concentrations (S, Zn, Fe) in drainage and pH of drainage
4. Solubility-controlled concentrations (Ca, Pb, Al) in drainage

These relationships are used in this study to probe the internal flow structure and solute transport phenomena within the waste rock sample bed. The pore water chemistry was inferred from measurements. The pH and analytical concentrations of S, Zn, and Fe were measured for each separate drainage issuing from one of the 37 drainage ports. A dilution factor is therefore obtained for each

drainage port as a function of time. The dilution factor information is then integrated with other measurements such as port flow rates to uncover some of the internal hydrological and geochemical processes within the waste rock, including the phenomenon of channelling.

The dilution hypothesis does not rule out the existence of other geochemical processes influencing the drainage zinc concentration such as adsorption/desorption, coprecipitation, ion exchange, etc., but it does point out that dilution and mixing of infiltrating water with pore water is by far the dominant process regulating zinc concentration.

The dilution model also leads one to ask whether the zinc contained in the waste rock can be "rinsed out " efficiently by application of water to the top of a pile. This question cannot be answered within the dilution hypothesis itself since it does not deal with the internal flow structure within the rock. The conceptual flow model proposed in Chapter 4.0 is relevant to this question. In addition, research conducted by NTC and others (Catalan and Li, 1999; Catalan et al., 1998, Li et al., 1995, Dixon, 1993) examined rinsing of acid-leached and cyanide-leached ores. A brief summary of the information contained in these sources is as follows. Essentially, the pore water associated with the waste rock can be considered to exist in two types: the first type is that located on flow routes which can exchange solute mass with infiltrating water by direct mixing, and the second type is that located outside but connected to flow routes which exchanges solute mass with the flowing water predominantly through diffusion. If a continuous fresh water rinsing is applied to the waste rock, the majority of the pore water zinc, perhaps 80-90%, will be washed out in a short period. This would be achieved mainly by convective transport of the zinc in the first-type of pore water and by the initial diffusive transport of zinc in the second-type of pore water, which is at a high rate due to the large concentration gradient between the infiltrating water and the pore water. Past this initial rinsing phase, the remaining 10-20% solute would be released slowly, relying mainly on the diffusive mass transfer of dissolved zinc from the second-type of pore water. The zinc concentration in the rinse effluent could experience a fast decrease in the initial stage resembling an exponential decay, but would soon stabilise at a quasi-steady-state value that is largely dependent on the rinse water application rate. This quasi-steady state would last a long time, generating a rinse effluent of low zinc concentration. In our experience with the Mine Gaspé (Noranda) pilot test (Catalan and Li, 1999), the stabilised concentration (dissolved copper in this case) was around 20 mg/L. On the basis of this analysis, the answer to the question raised at the beginning of this paragraph would be yes if the objective is to recover the majority of the dissolved zinc stored in the waste rock and no if the objective is to decommission the waste rock by a quick rinse so that the drainage is suitable for direct discharge to the environment (even if further sulphide oxidation is assumed not to take place).

The relationship among the four groups of variables may apply to other rocks that are similar to the one studied. The "similarity" of behaviour among different rocks is a topic of discussion in Chapter 4.0 . Unfortunately, it is generally impossible to use the relationships to predict water quality from waste rock piles, because the second group of variables are usually not known and, at our present level of understanding of flows within waste rock piles, cannot be reliably predicted or estimated. Finding out how the dilution factor is controlled by variables such as rock height, grain size make-up, precipitation characteristics, etc. can be a subject of further research.

3.2.7 Summary

The discussion of drainage geochemistry focused on mechanisms regulating dissolved concentrations of metals and sulphate. Experimental data analysis suggests that the concentrations of Ca, Pb, and Al are solubility-controlled by precipitation of gypsum, anglesite, and jurbanite, respectively. No solubility control is found for the concentrations of Zn, Fe, and S, although geothite is among the precipitated phases. Experimental data support a dilution hypothesis, which states that the concentrations of Zn, Fe, S and the pH observed in the drainage are a result of successive dilutions and/or intermixing of various-stage dilutions of the original pore water, subject to equilibrium with redox reactions and goethite precipitation caused by the dilution process.

3.3 DRAINAGE HYDROLOGY

Natural precipitation-derived infiltration flows in mine waste rock piles are unsaturated and heterogeneous. Because of the wide grain size range, waste rock usually cannot be treated as simple porous media as described by Darcy's law or Richards' equation. The flow structure within waste rock piles is complex and poorly understood.

The most profound feature of flows in waste rock is the potential for channelling (synonymously, preferential flows). Channelling can be defined as the existence of regions in a waste rock pile where the volumetric flux of water across the horizontal plane far exceeds the average volumetric flux for the entire pile. Volumetric flux is the flow rate per unit cross-sectional area measured in $m^3 \cdot s^{-1} \cdot m^{-2}$ in the SI system, thus it has the dimension of $[L][T^{-1}]$, and is analogous to the specific discharge for a porous media.

Channelling affects many physical and chemical processes taking place within a waste rock pile. It affects, for example, the rate at which water is conducted, the residence time distribution of the water issuing at the toe of the pile, the amount of rock surfaces flushed, and the rate at which contaminant is transported out of the pile.

3.3.1 Experimental Observations of Channelling

Studying channelling phenomena was one of the major objectives for this study and thus a basic design consideration for all 10 experimental runs. The methodology for the large column experiments is described in Chapter 2.0 and the experimental conditions are condensed in Table 2-1, Table 3-1, and Table 3-2. In Figure 3-1, the bottom drainage partition pattern is illustrated on the first page, which is followed by eight pages of three-dimensional column graphs depicting the flow rate evolution for each drainage partition for all 10 experimental runs. The flow rate (vertical) scale

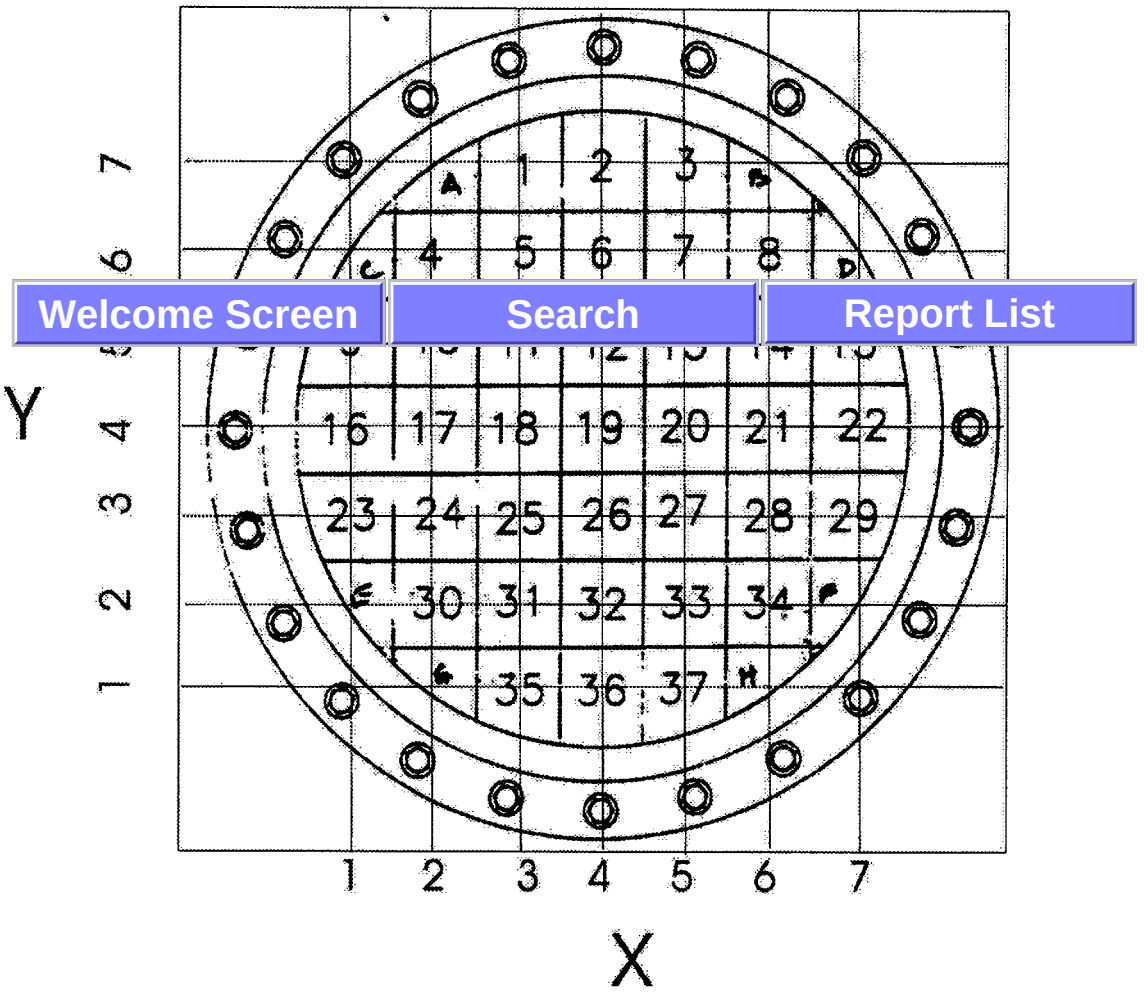

X and Y coordinates of drainage partitions for Columns 1 and 2 used in the graphs that follow. For Column 3 drainage partition pattern, see Figure 6-7. Numbered drainage partitions each have a separate drainage port connection and are approximately equal in area. Partitions labelled A through H do not have drainage port connections and water arriving at these partitions flow to nearby, numbered partitions.

Figure 3-7 Flow Rates at Sample Bed Base for Different Time Intervals

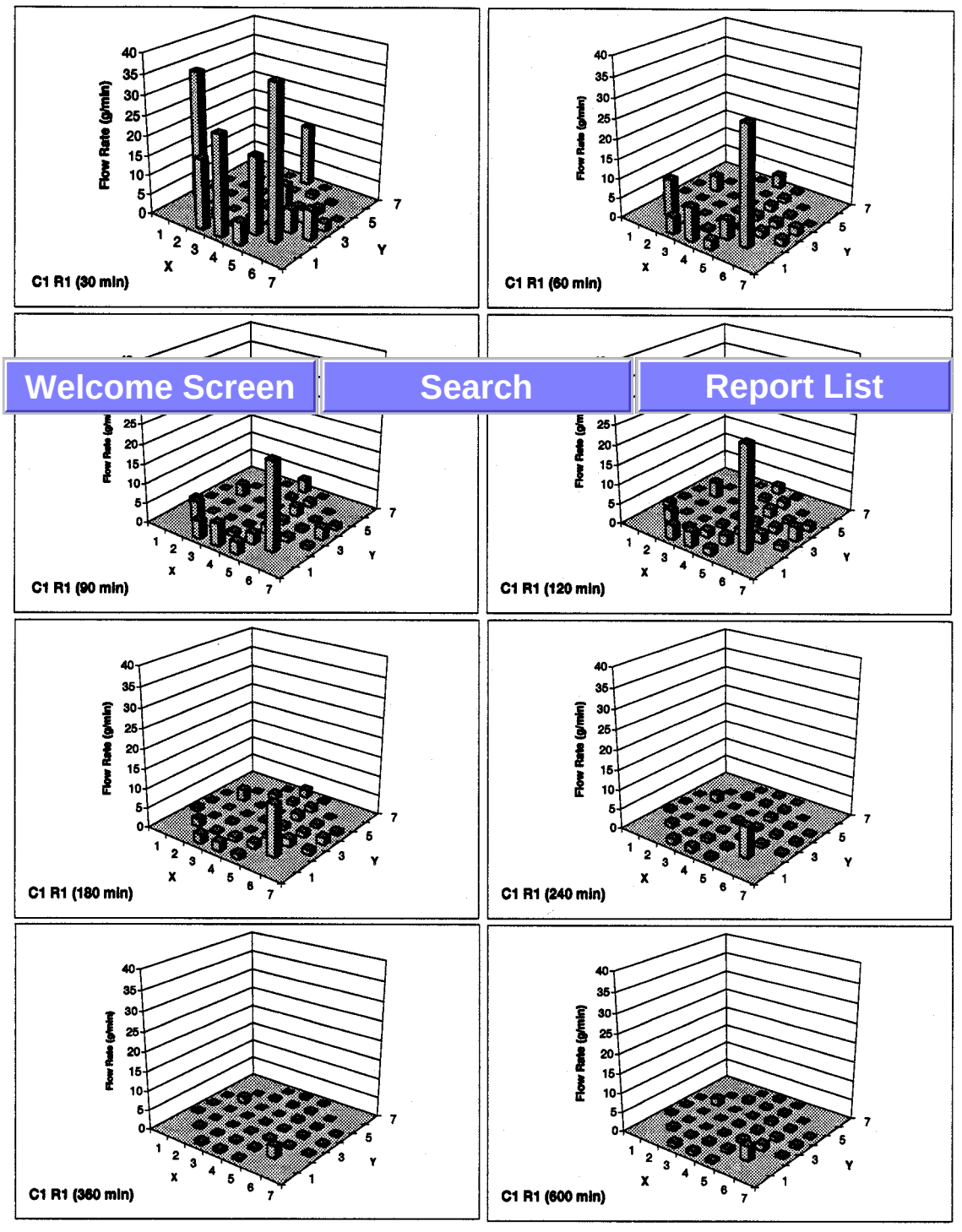

Figure 3-7 Flow Rates at Sample Bed Base for Different Time Intervals (Continued)

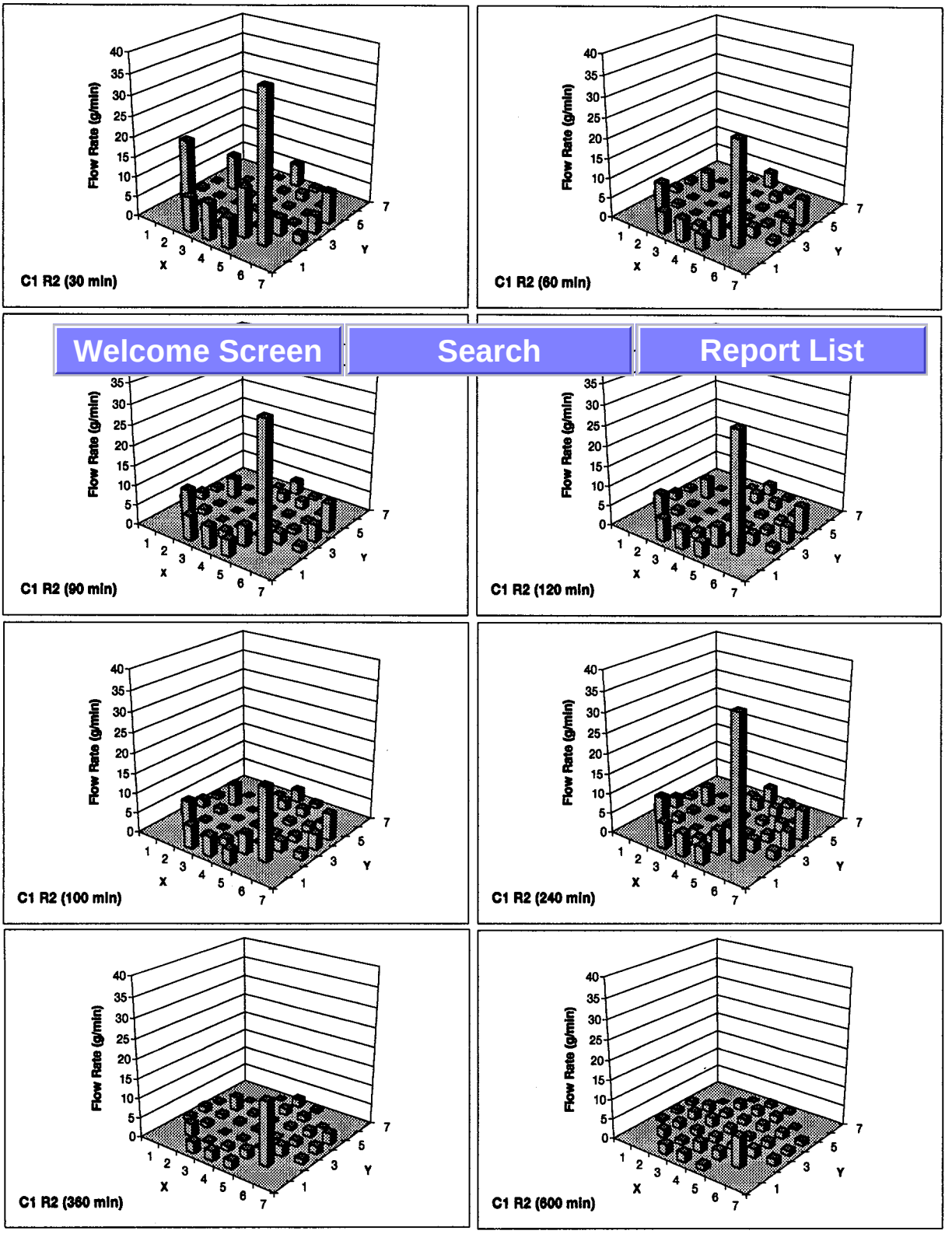

Figure 3-7 Flow Rates at Sample Bed Base for Different Time Intervals (Continued)

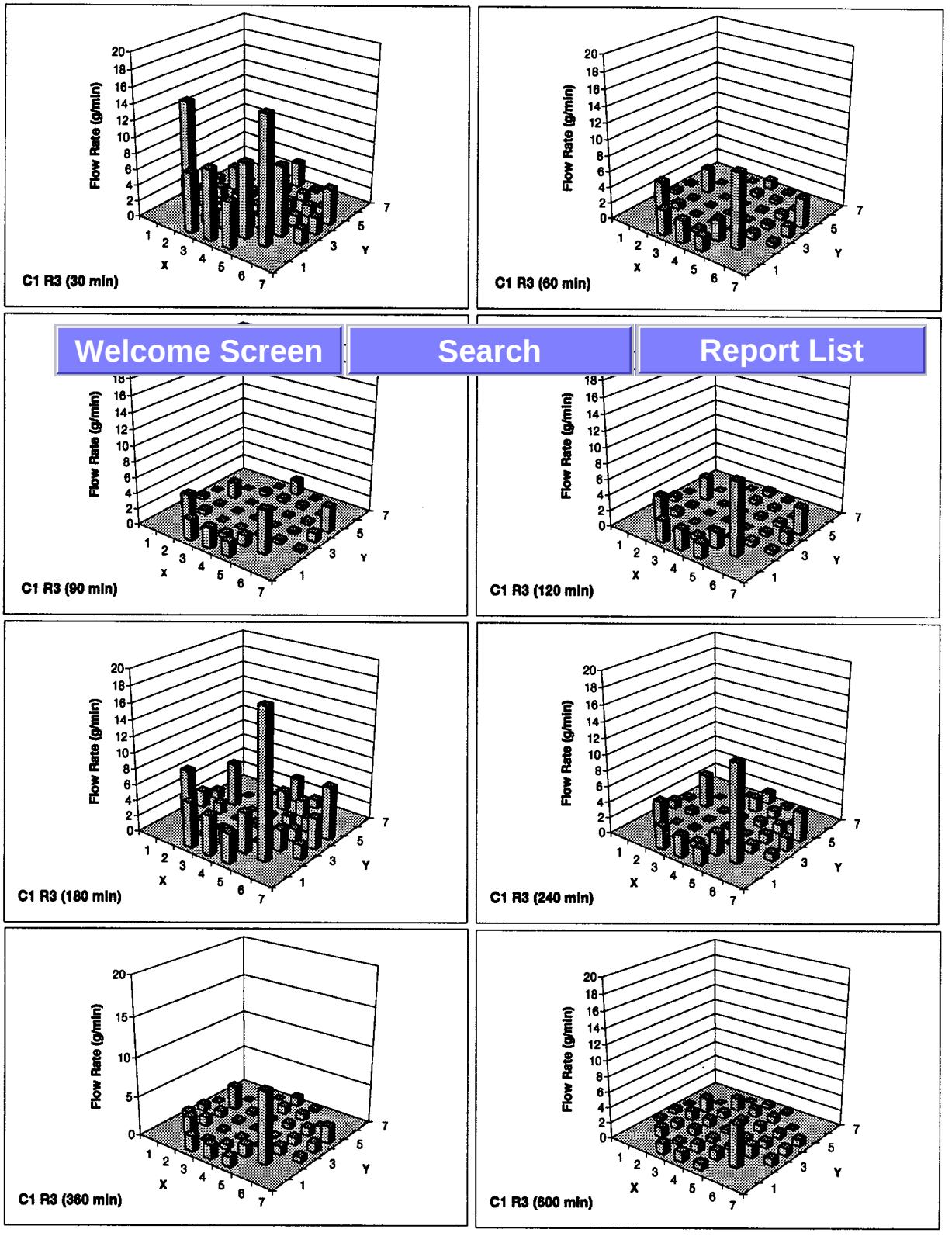

Figure 3-7 Flow Rates at Sample Bed Base for Different Time Intervals (Continued)

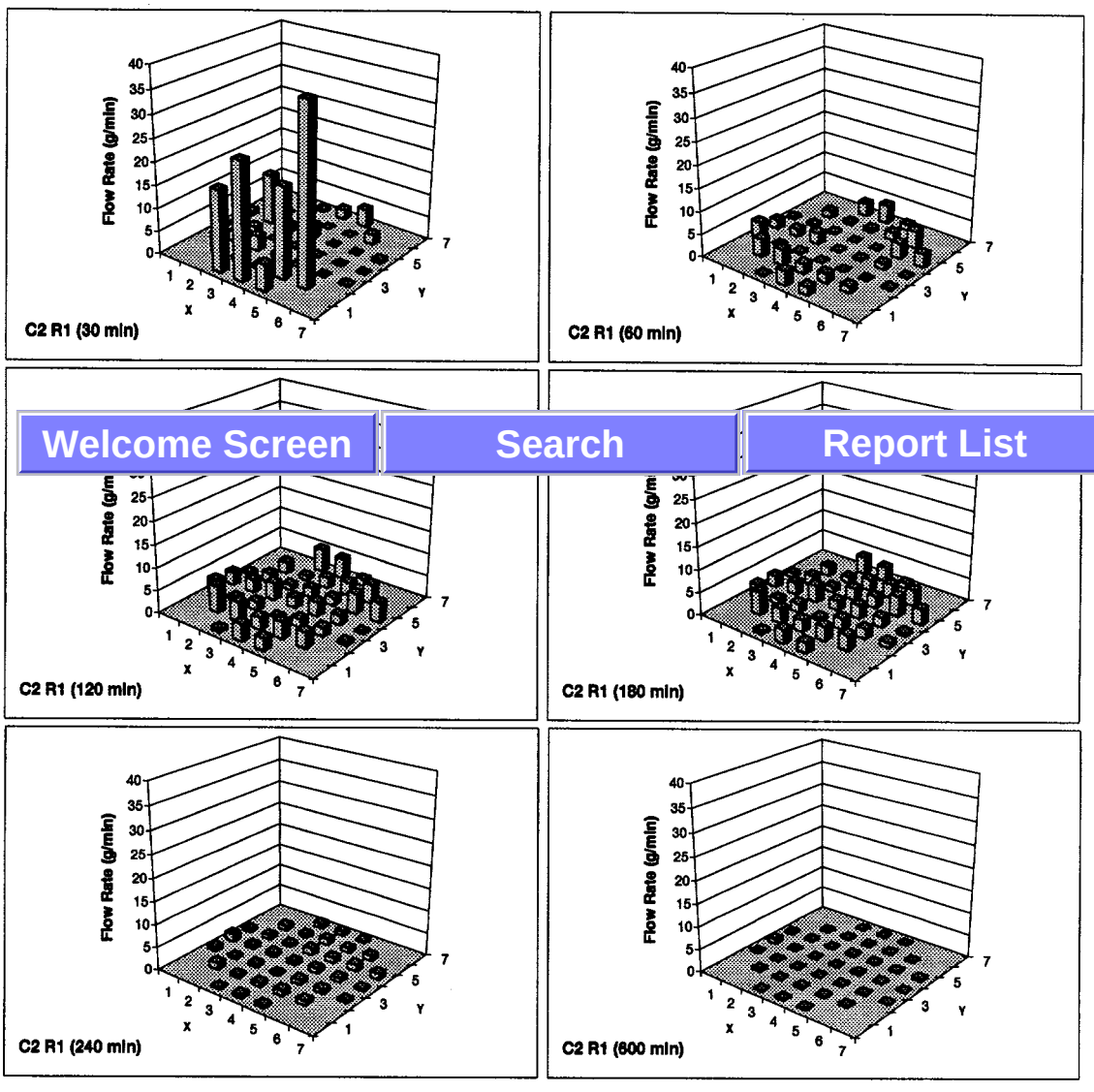

Figure 3-7 Flow Rates at Sample Bed Base for Different Time Intervals (Continued)

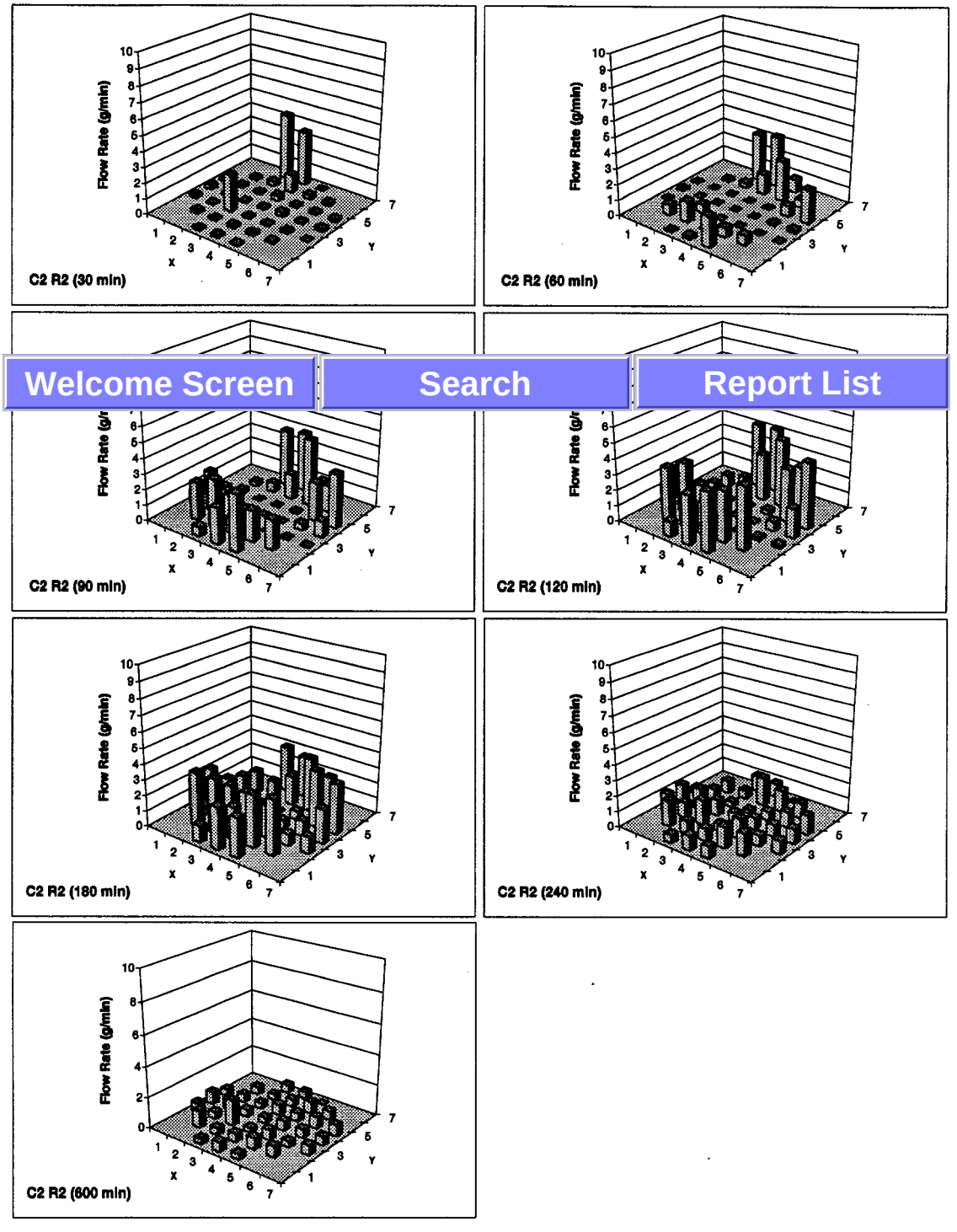

Figure 3-7 Flow Rates at Sample Bed Base for Different Time Intervals (Continued)

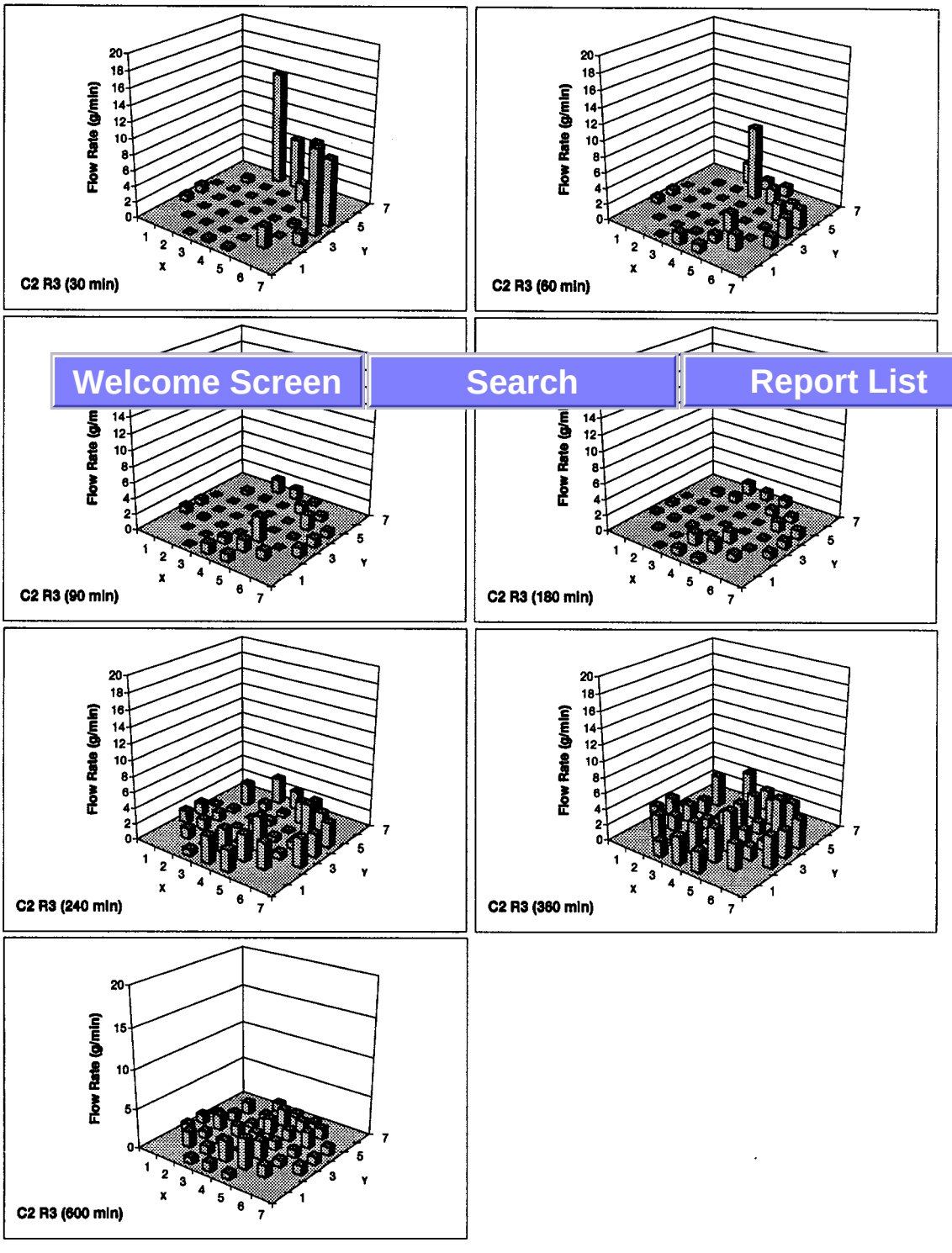

Figure 3-7 Flow Rates at Sample Bed Base for Different Time Intervals (Continued)

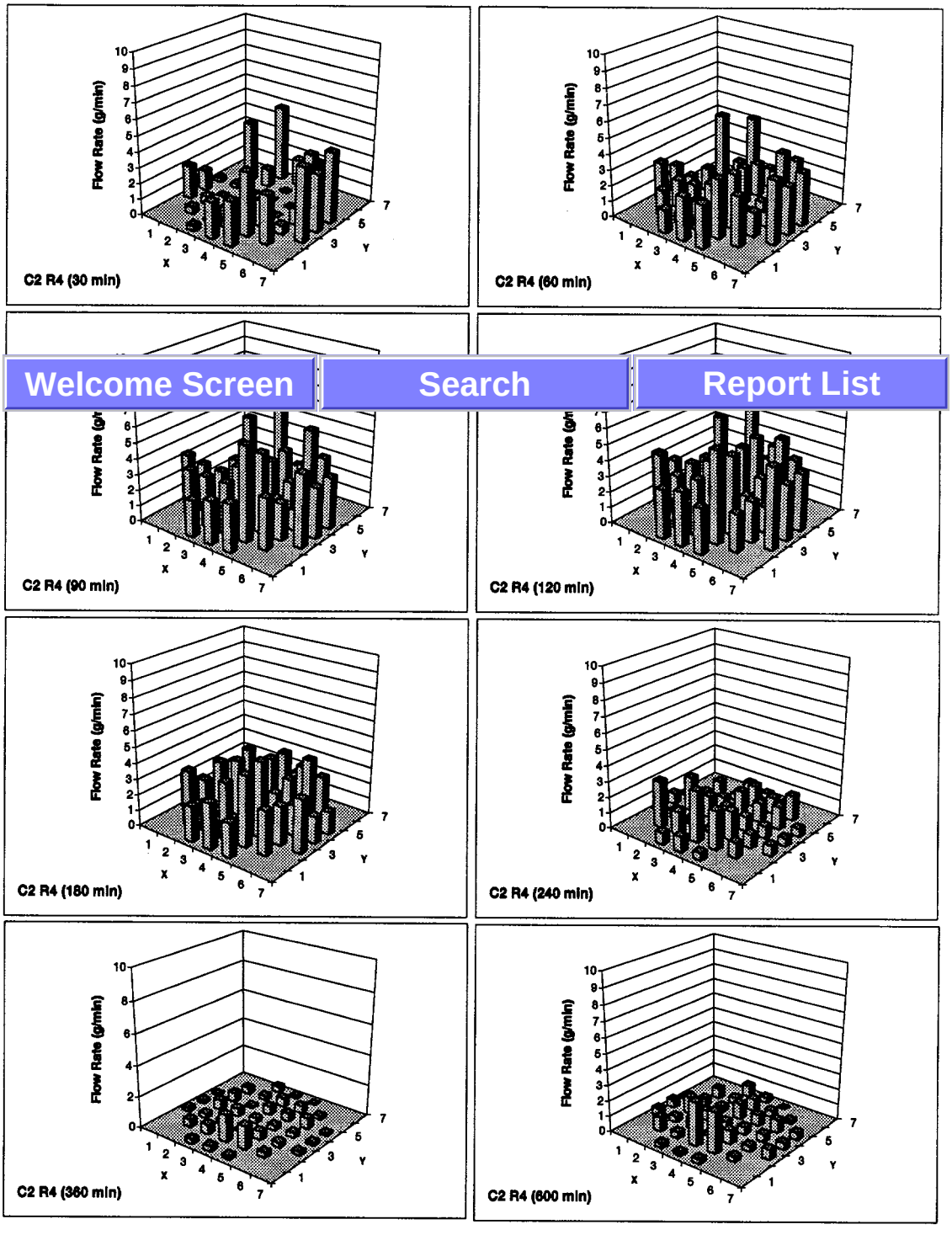

Figure 3-7 Flow Rates at Sample Bed Base for Different Time Intervals (Continued)

Welcome Screen Search Report List

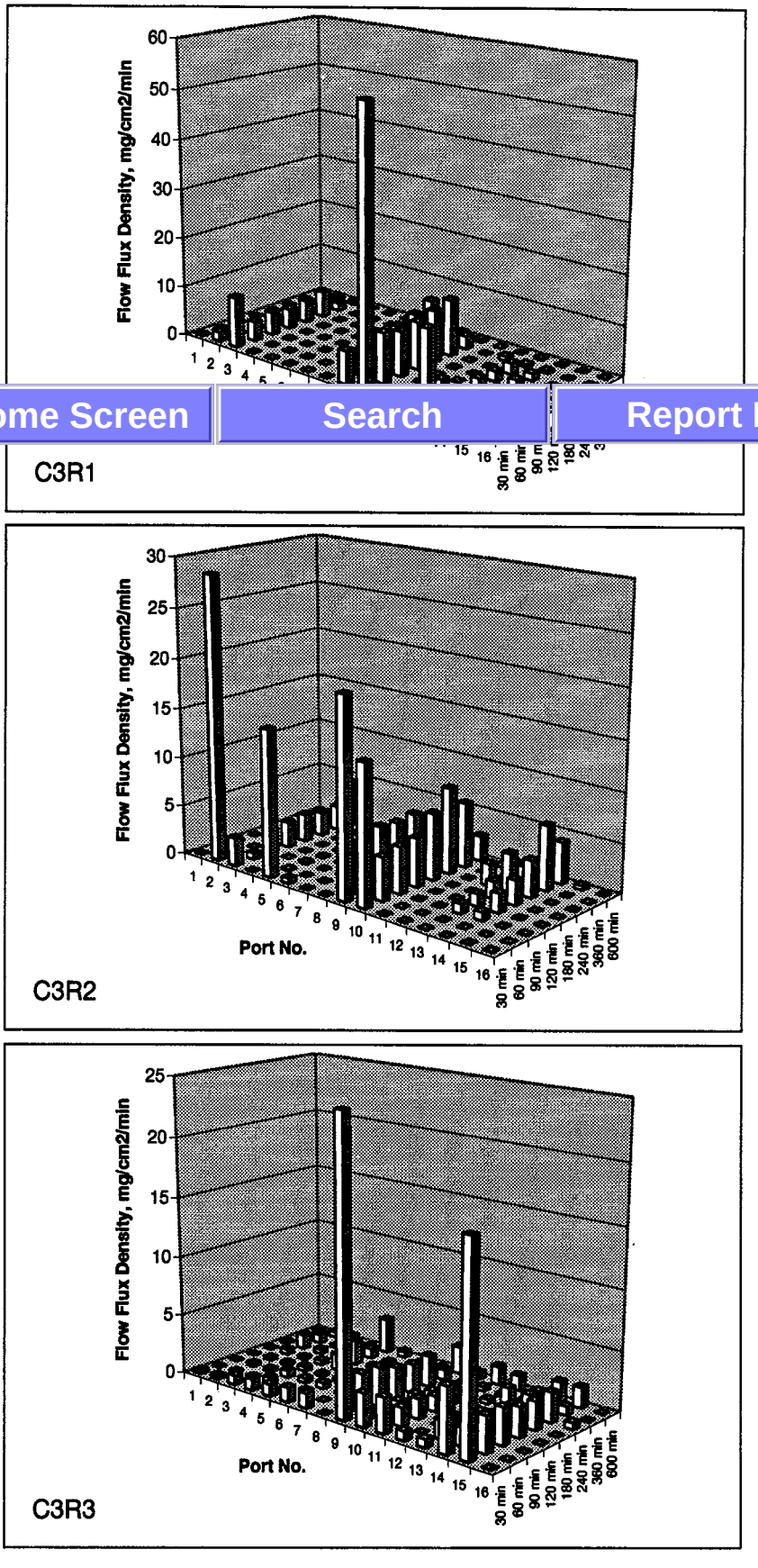

Figure 3-7 Flow Rates at Sample Bed Base for Different Time Intervals (Continued)

is made identical on each page (one page represents one run except the last page) so that the heights of the columns can be directly compared for each run.

In these column graphs, the flow rates are time-averaged (over the intervals), not *instantaneous*. Since the areas of the drainage partitions are approximately equal, the flow rate in each partition is directly proportional to the average (not *point*) volumetric flux on that partition. Abnormally tall columns represent flow channels. If we suppose that flow channels were sparingly spaced, each drainage partition would encounter no more than one channel. Furthermore, if we assume that channels were small in horizontal cross-sectional area, one channel would normally not encroach more than one drainage partition. Under these assumptions, the number of tall bars approximately represents the number of flow channels.

Examination of Figure 3-1 reveals the following qualitative observations:

- Channelling is ubiquitous and occurs in all experimental runs.
- There is no apparent pattern in the locations of channels; the locations of channel occurrences can be considered random.
- The total area of the partitions containing large channel flows represent a small percentage of the total area of the rock bed base.
- Channelling is much more pronounced in earlier stages than in later stages of flow for all runs. In later stages flows tend to become homogenised. This agrees with the intuition that channels conduct water rapidly and dry up quickly once the surface water application stops.
- For the same sample bed, channels persist (i.e., do not change location) from run to run (C1R1, C1R2, C1R3), even when simulated rain intensity was halved (from C1R2 to C1R3).
- When the intensity of the simulated rain was reduced by 50% from C1R2 to C1R3, the channel locations, relative flow rates, and duration of channel flows remains approximately constant. The main change is in the absolute flow rates, which are reduced roughly by 50%.
- The channel locations, relative flow rates, and duration of channel flows changed dramatically when the rock sample bed thickness was increased. This is evident for both C2, in which simulated rain was applied at the surface, and C3, in which water was applied at a central location at the surface.
- It appears that higher proportions of the total flow are conducted by fewer channels at a lower initial moisture content than at a higher initial moisture content. That is to say, channelling effects are more pronounced in a dry rock mass than in a wet rock mass. This is revealed by comparing C1R1 (lower initial moisture) with C1R2 (higher initial moisture), C2R1 (lower initial moisture) with C2R2 (higher initial moisture), and C2R3 (lower initial moisture) with C2R4 (higher initial moisture). This observation can be understood intuitively: for the same intensity and duration of precipitation, with a dry rock mass, in non-channelling regions, much of the water goes to replenish the moisture and does not yet have a chance to initiate flow before the rain is stopped. As a result the flow is mainly carried by channels. For a wet rock mass, flows in non-channelling regions are initiated sooner after the rain starts, because the pore water moisture content in these regions is already near the field retention capacity. As a result, more of the total flow is conducted by non-channelling regions of the rock mass, leading to a less pronounced channelling phenomenon.
- For the same sample bed thickness and the same rain intensity, drainage starts to flow sooner if the initial moisture is higher than if it is lower. This can be seen in the column hydrographs in APPENDIX II, by comparing C1R1 (lower initial moisture) with C1R2 (higher initial moisture), and by comparing C2R3 (lower initial moisture) with C2R4 (higher initial moisture). Again, this

agrees with intuition because for drier rock mass more water is needed to recharge the moisture to the field retention capacity.

Clearly, channelling is influenced by many variables in a complex way.

3.3.2 Channel Stability and Internal Channel Stability

Channel stability refers to the ability of the largest channels (as identified by their drainage ports) to persist from one run to another when environmental conditions change. *Internal channel stability* refers to the ability of the largest channels to maintain their ranks during a single drainage event. Figure 3-1 and Figure 3-2 are created to facilitate discussion of channel stability.

The eight largest channel flows (among 37 flows) are selected for plotting. The flow rate rank order of a channel is determined for every time interval, with rank order 1 representing the highest flow rate. The rank orders are then plotted against the time interval in Figure 3-1. The overall rank order (i.e., for the "all" category, far right on the horizontal axis of each graph) is determined using the total flow for the entire run. The eight largest channels are selected according to this "overall rank order".

Figure 3-2 plots the number and percentage of identical channels against rank order numbers for selected pairs of experimental runs. The rank numbers used for the x-axis are the "overall" rank orders. A data point (n, m) on the upper graph indicates that, between the two runs which are being compared for their respective m largest channels, n channels are identical. For the lower graph, the quantity (n/m x100%) instead of n is used for the y-axis. To clarify, take the comparison between runs C1R1 and C1R2 (square symbols) as an example. From Figure 3-1, the eight largest channels in C1R1 are P34, P30, P36, P35, P33, P10, P2, and P28, whereas the eight largest channels in C1R2 are P34, P30, P15, P35, P33, P10, P36, and P37. Among these two groups there are six identical channels (P34, P30, P36, P35, P33, P10). The result of this comparison is plotted on the upper graph as point (6, 8) and on the lower graph as (75%, 8), where 75% is obtained from 6/8 x 100%. The line designated as "perfect" in the upper graph corresponds to the case where the ranks of the large channels remain unchanged between the two runs compared: the largest, the second largest, the third largest, … flow channels for one run is, respectively, also the largest, the second largest, the third largest, … flow channels for the other run. In Figure 3-2, the closer a line is to the "perfect" line (upper graph) or 100% (lower line), the higher the *channel stability* between the two runs compared.

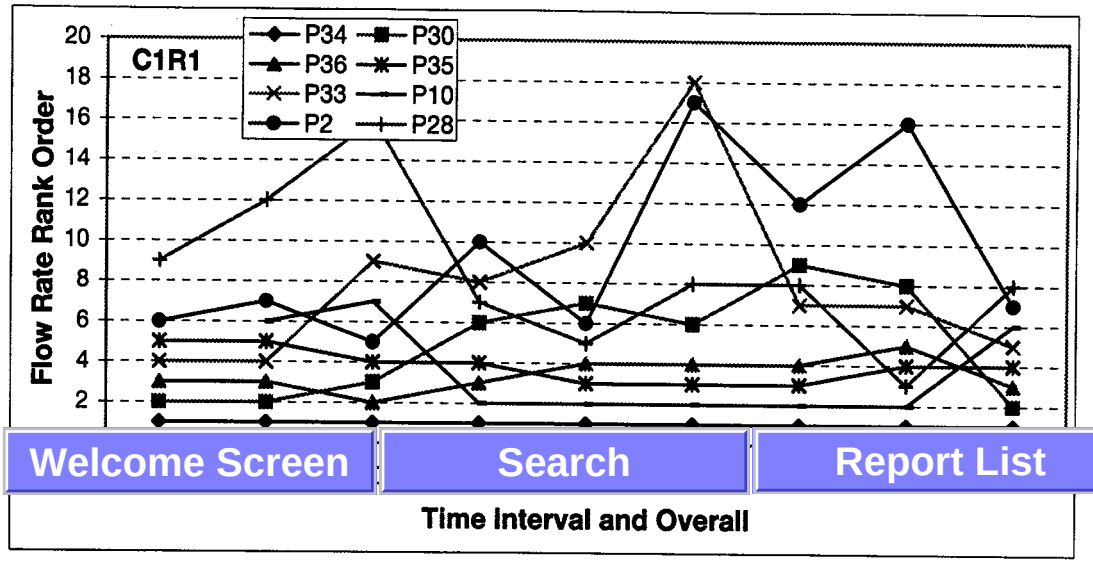

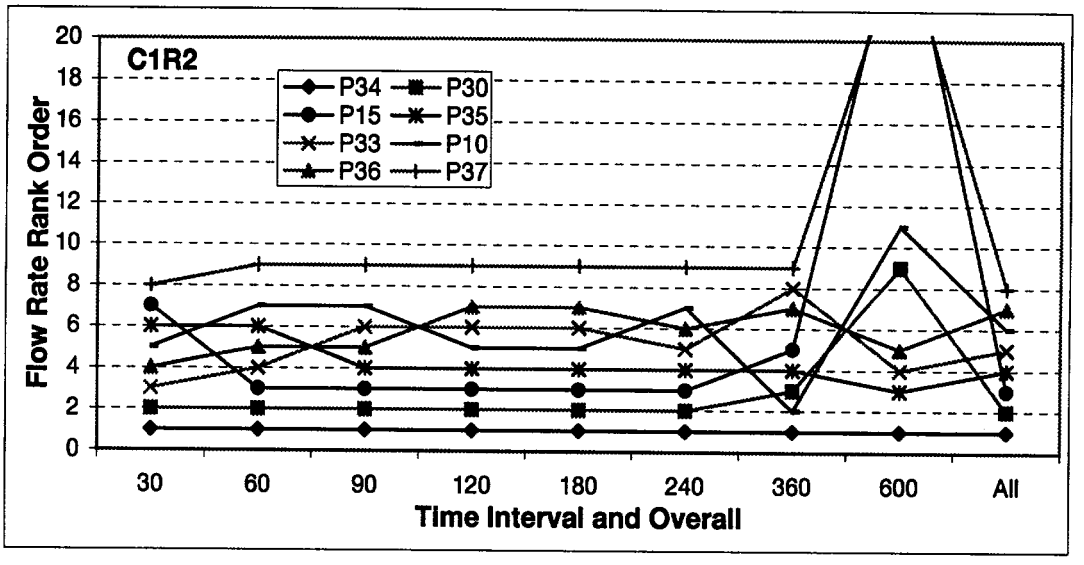

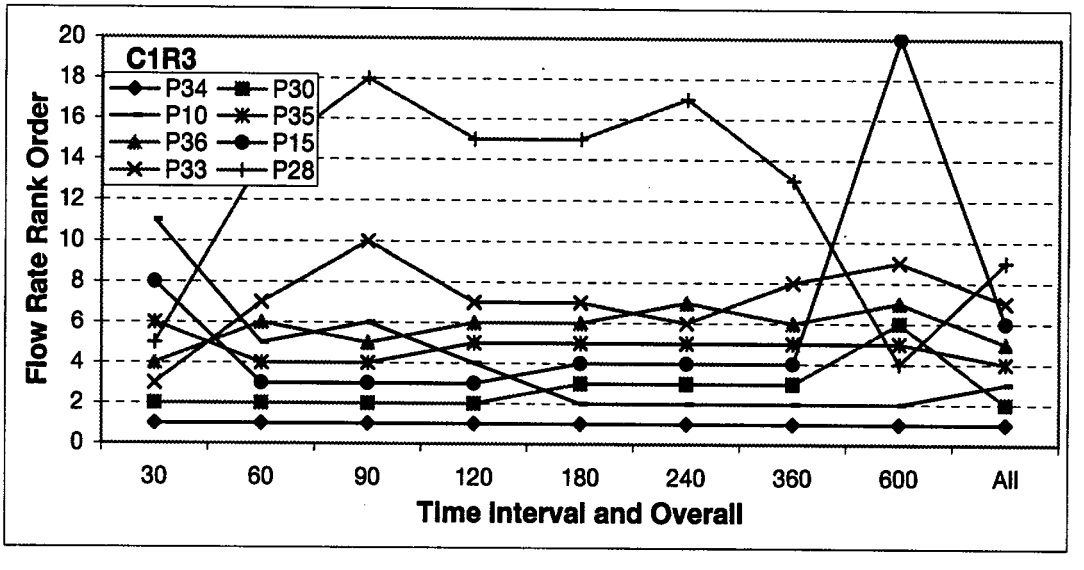

Figure 3-8 Flow Rate Rank Order of 8 Largest Channels vs. Time Intervals

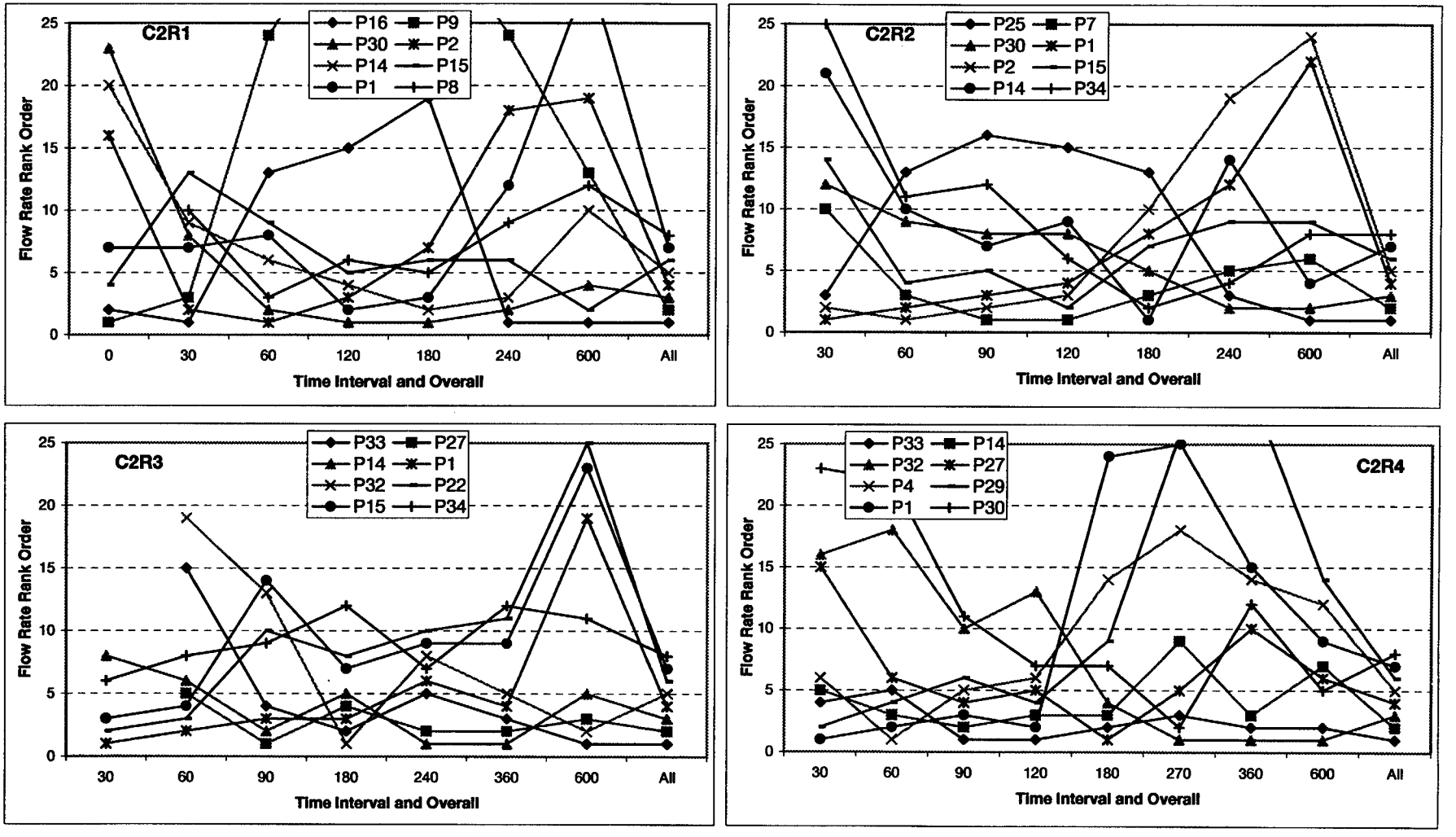

Figure 3-8 Flow Rate Rank Order of 8 Largest Channels vs. Time Intervals (Cont'd)

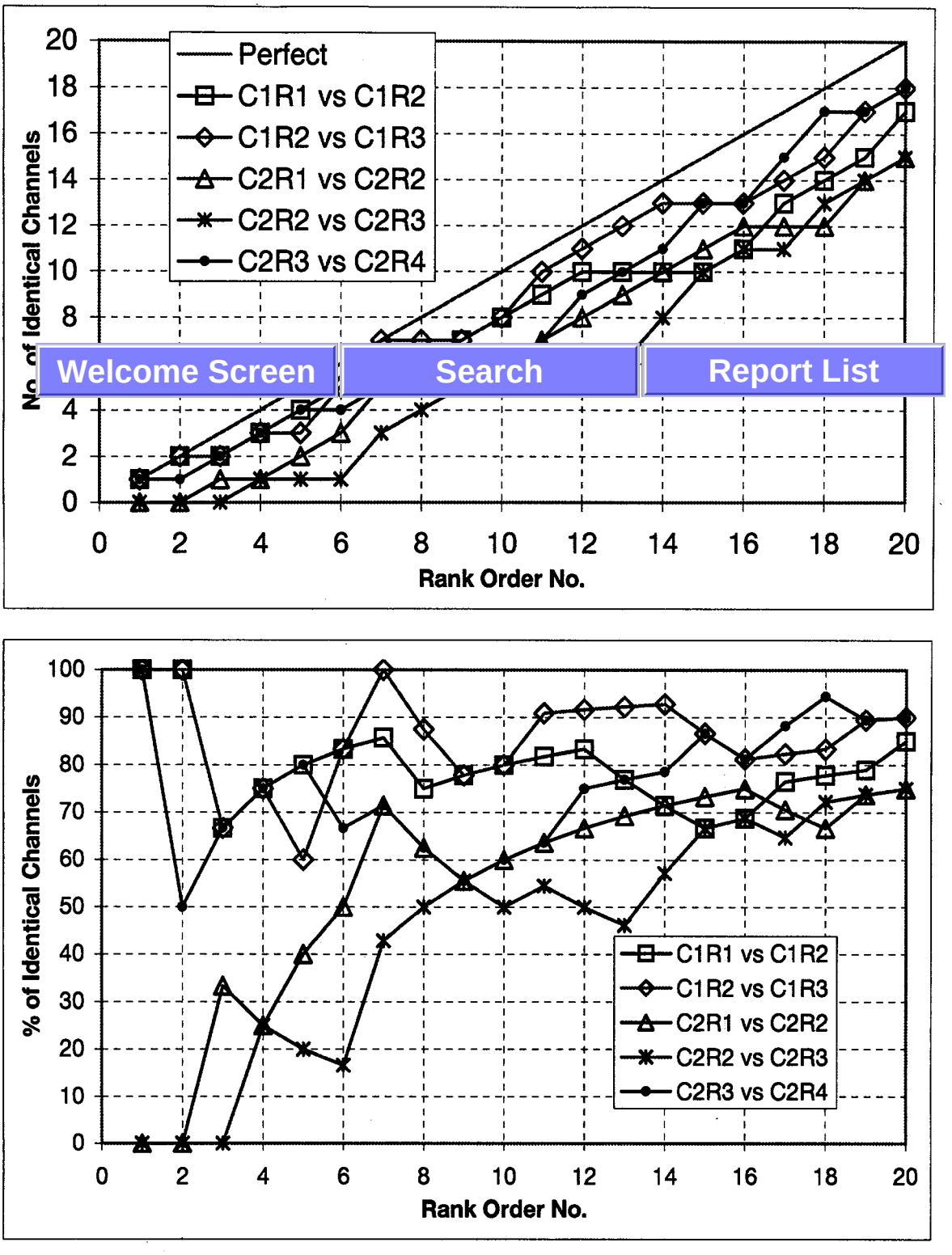

Figure 3-9 No. and % of Identical Channels vs. Rank Order Numbers for Selected Run Pairs

Effects of Rock Bed Height on Channel Stability

Such effects are revealed by comparisons among C2R1 (0.5-m bed), C2R2 (1.0-m bed), and C2R3 (1.5-m bed). Increasing sample bed thickness has a major effect. In Figure 3-2, this is reflected by the large deviations of the data points from the "perfect line" in the upper graph or from 100% in the lower graph. For example, Figure 3-2 shows that only one of the four (25%) highest-flow channels in C2R1 remained in the top four channels in C2R2. The two biggest flow channels in C2R2 - P25 and P7 - were newly created; they ranked 29th and 14th, respectively, in C2R1, and thus were insignificant in terms of channelling. Channel stability is even worse from C2R2 to C2R3 than from C2R1 to C2R2 (Figure 3-2, the lowest line): in C2R3 the top three channels were all newly-created, and only 50% of the top eight channels in C2R2 remained in the top eight in C2R3.

The lack of channel stability when rock bed thickness is increased is likely a result of blocking major old channels and creating major new channels. In other words, channels are unstable when new rock is added on top of an existing rock pile.

Another effect of increasing rock bed height seems to be that it smoothes out the variation in the rank orders of the most important channels at different times of the same run. That is, increasing the rock bed height has the effect of increasing the *internal channel stability*. This is seen by comparing C2R1, C2R2 and C2R3 in Figure 3-1.

Effects of Initial Moisture on Channel Stability

Such effects are revealed by comparisons between C1R1and C1R2 and between C2R3 and C2R4. Figure 3-2 shows that the two curves (open square and dot symbols) are not far from the "perfect" line (upper graph) or 100% (lower graph), indicating that the effects of initial moisture on channel stability are small - certainly much smaller than the effects of rock bed height. Figure 3-1 indicates that higher initial moisture tends to increase the *internal stability* of the large channels.

Effects of Rain Duration on Channel Stability

It can probably be inferred that the effects of a longer rain duration applied to a rock mass with a lower initial moisture are similar to the effects of a shorter rain duration applied to a rock mass with a higher initial moisture. This is because a certain amount of the rain is used to replenish the moisture in the rock. If this inference is correct, the effects of longer rain duration versus a shorter one on the channel stability would have been small. Longer rain would also increase the internal channel stability.

Effects of Rain Intensity on Channel Stability

Comparison of C1R2 with C1R3 reveals that the effects of reducing the simulated rain intensity on channel stability are quite small. Figure 3-2 shows that the line representing C1R2 versus C1R3 is very close to the "perfect" line. Figure 3-1 suggests that reducing the rain intensity tends to decrease the internal channel stability within a drainage event.

Column to Column Variations in Channel Stability

The differences between C1 and C2 are analogous to the differences between different regions of a waste rock pile in the field. Comparisons between C1 runs and C2 runs indicate the following:

- The responses to changes in conditions such as rock bed height, initial moisture content, rain duration, and rain intensity are similar.
- Channel stability is higher in C1 than in C2.
- The internal channel stability is consistent for different runs of the same column, but is much higher in C1 runs than in C2 runs.

Flow per Unit Mass and Internal Channel Stability

A common observation derived from the above discussion seems be this: the greater the flow of water conducted per unit rock mass, the greater the internal channel stability. The flow conducted per unit rock mass can be increased via various avenues: increases in rain duration, rain intensity, or initial moisture, and decreases in rock bed height. Internal channel stability is important in the consideration of solute transport, which will be discussed later.

3.3.3 Flows Conducted by Channels

During a drainage event, how much water is conducted by channels, and how much water is conducted by non-channel regions? The answers to these questions would provide important clues as to how fast rain infiltration flows through a waste rock pile and, more importantly, how much contaminants are transported out of the waste structure during the event.

Total Column Flows

The discharge flow rate of a column (or a rock mass) varies with time during a drainage event. A graph plotting the column discharge flow rate against time is called a column discharge hydrograph. The integration of the hydrograph curve equals the total volume of discharge. The column discharge hydrographs for the ten experimental runs are presented in APPENDIX II.

A typical drainage hydrograph normally consists of a rising limb, followed by a falling limb, and ending with a long tail, as illustrated by column discharge hydrographs of C2R1, C2R2, and C2R4 in APPENDIX II.

A drainage hydrograph is preferably constructed from “instantaneous” flow rates - flow rates that are measured in very short time intervals. The hydrographs in APPENDIX II, however, are created using average flow rates, measured over intervals spanning 30 minutes to a couple of hours. They should be considered as approximate hydrographs. The use of these time-averaged flow rates makes it impossible to accurately define the initial rising limb (especially when the rising limb has a

steep slope) and the ending tail. This is why the hydrographs of C1R1,C1R2, C1R3, C3R1, C3R2, and C3R3 do not show their rising limbs. In addition, the positions of the tails in all the hydrographs are very rough, since the last data point of each hydrograph is an average over a long time period.

The special shape of the C2R3 hydrograph is caused by a discontinuity in the simulated rain. The second simulated rain application was not planned, but was added at the time when the experiment was conducted because the originally-planned simulated rain duration was found insufficient to cause the required drainage flow.

Channel Flows

Figure 3-1 plots the individual port flow as a percentage of the whole-column flow for a given time interval. On the x-axis, the drainage port numbers are arranged in the order of decreasing overall flow rate. The inset shows the whole-column hydrograph for the run plotted. Figure 3-2 shows how the flow in each of the eight largest channels vary with time. In Figure 3-2, for any given time interval, the individual port flows on the vertical scale are expressed as a percentage of the whole-column flow for that time interval. The column hydrographs (using the right scale) are also depicted for comparison.

If the infiltration flows were distributed homogeneously on the plane of the base of the rock bed, at any moment or through any time interval during a drainage event, each drainage port would receive approximately 1/37 (37 being the number of drainage ports), or 2.7%, of the total flow crossing the base plane. Ports receiving flows much higher than 2.7% of the total flow are intercepting flow channels.

Figure 3-1 shows that there are two major channels in C1R1 to C1R3, corresponding to P34 and P30, that conduct more than 10% of the total flow for at least one time interval. There are seven or eight channels that conduct more than 5% of the total flow for at least one time interval. On the other hand, there are about ten drainage ports that conduct virtually no flow. If the eight channels of which each conducts more than 5% of the total flow for at least one time interval are considered to represent the majority of the channel flows, they would represent 8/37=21.6% of the rock bed base area.

Figure 3-2 shows that the flows in the eight largest channels as percentages of the whole-column interval flows change with time during a drainage event. The largest channel, corresponding to P34, is outstanding in that it carries a much higher percentage of the whole-column flow than each of the remaining channels for all time intervals.

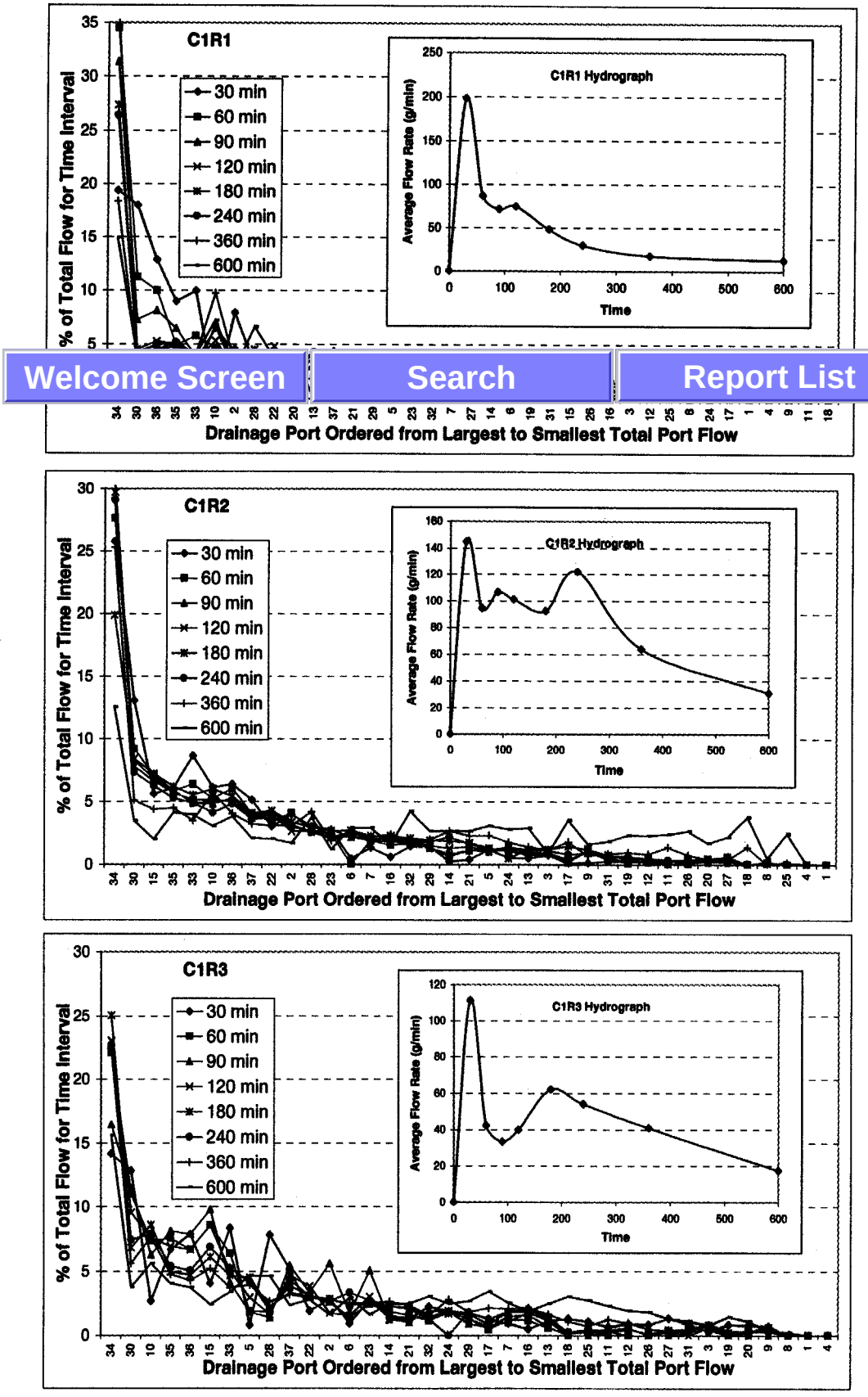

Figure 3-10 % of Total Interval Flows Conducted by Various Channels for C1

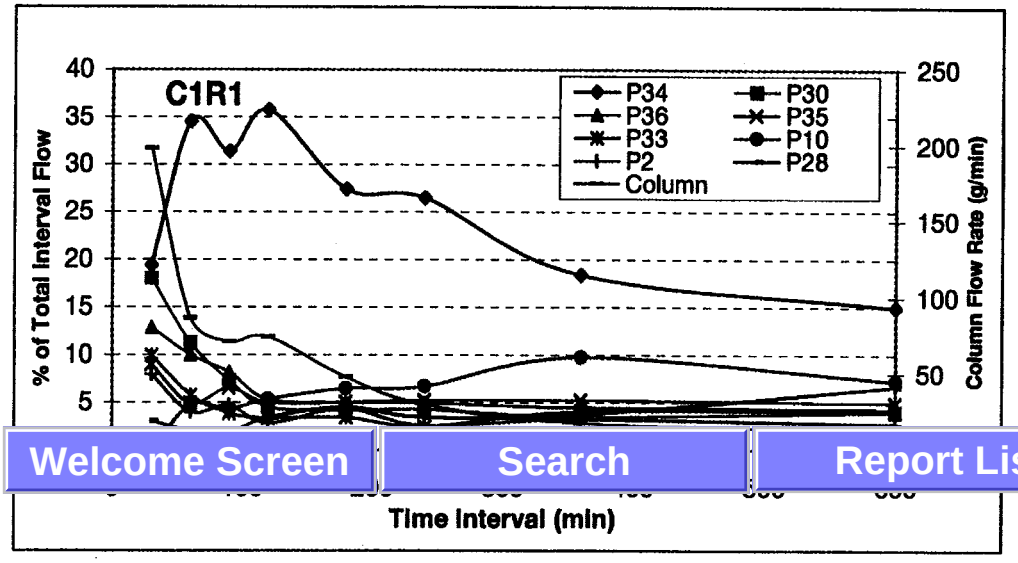

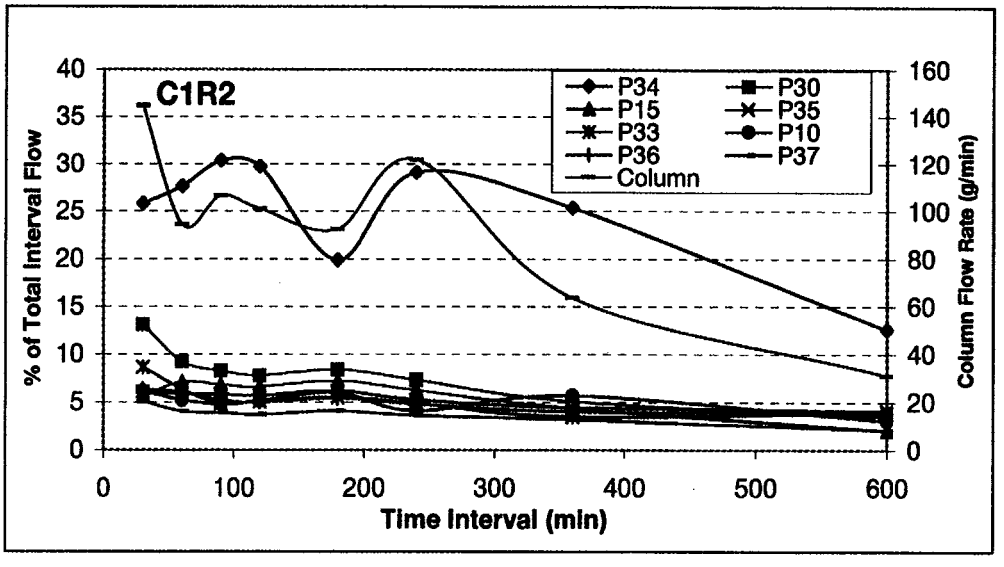

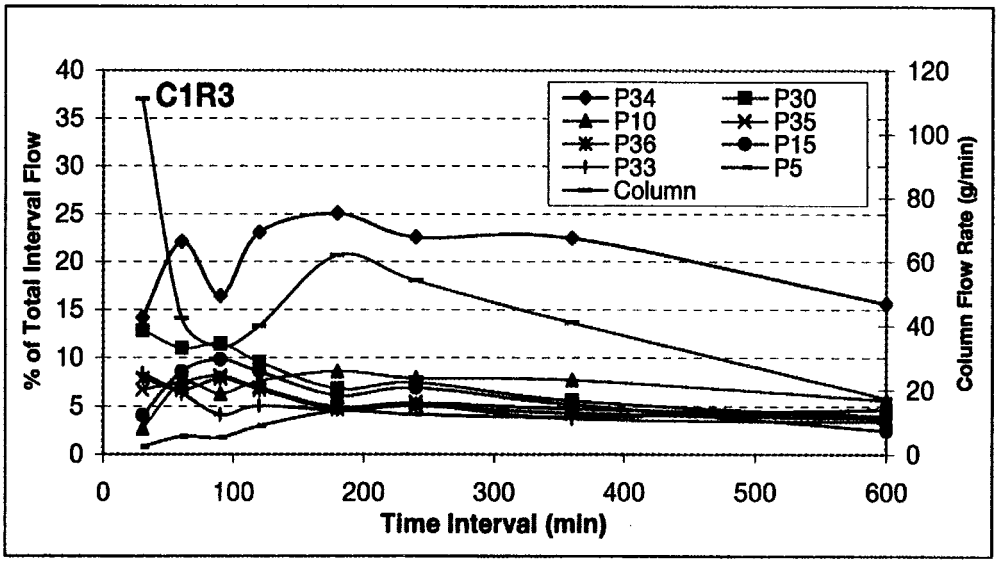

Figure 3-11 % of Interval Flows Conducted by 8 Largest Channels vs. Time for C1

With the exception of the largest channel (P34), the channelling effects are most pronounced at the beginning of the drainage event and diminish with the progress of the drainage event. For P34, the flow seems to be positively correlated with the whole-column flow except the initial data point at the 30 min interval.

In Figure 3-3, the three experimental runs of C1 are compared. The horizontal axis, drainage port rank number, increases with decreasing channel size. The vertical axis, % of total flow, is the individual port flow during the experimental run calculated as a percentage of the whole-column drainage flow for the same duration.

Figure 3-3 shows that the largest difference among the three runs is exhibited by the largest channel (rank number 1): approximately from 19 to 27%. The difference between R1 and R2 is slightly smaller than that between R2 and R3. Recall that R1 and R2 differ in initial moisture whereas R2 and R3 differ in simulated rain intensity. It appears that the effects of rain intensity on the largest channel flow is slightly more pronounced that those of initial moisture.

The experimental observations from the three runs conducted on C1 are summarised as follows:

- One large outstanding channel representing a very small percentage (~3.7%) of the total base drainage area conducts a significant percentage (~19 to 27%) of the whole-column drainage flow, and it remains active throughout the drainage event. The flow conducted by this channel appears to correlate positively with the whole-column flow (i.e., the hydrograph) over time.

- Several intermediate channels representing ~20% of the total base drainage area carry approximately 40% of the whole-column drainage flow. The channelling effects of these channels appear to diminish as the drainage event progresses.

- About 50% of all the drainage ports carry the remaining 30-40% of the total flow. This can probably be described as “background flows” or “matrix flows”.

- About 30% of all the drainage ports conduct virtually no flow.

- The channelling effects are influenced by changes in experimental variables such as rock bed thickness, initial moisture content, and simulated rain intensity.

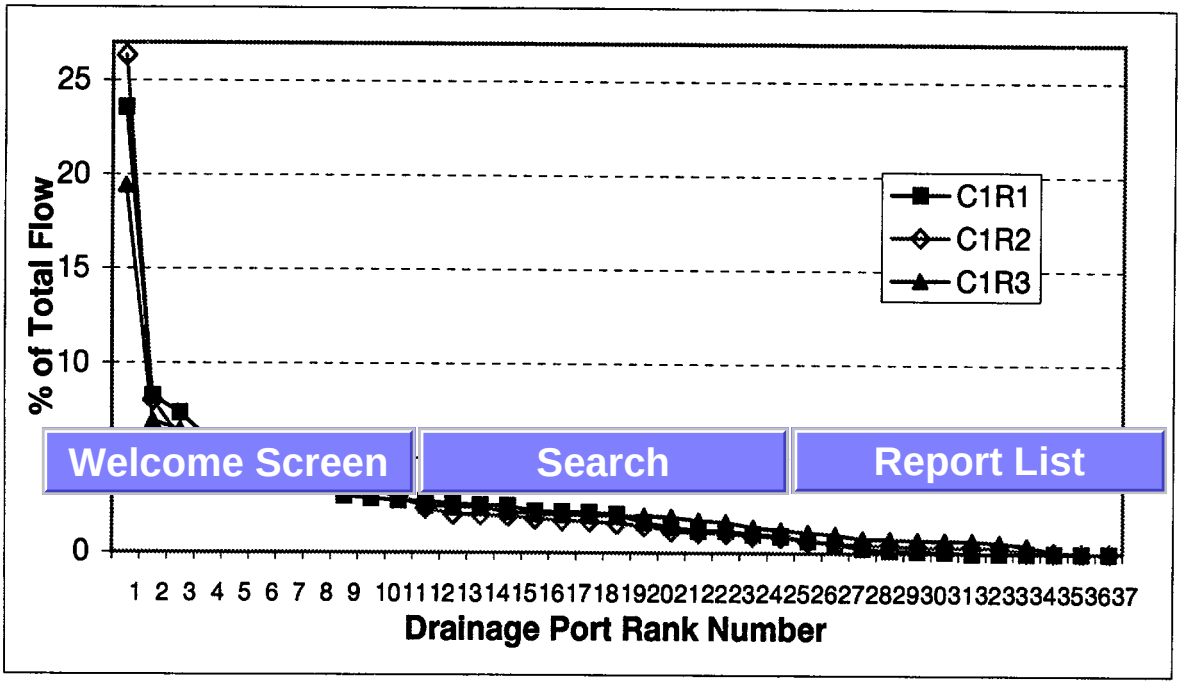

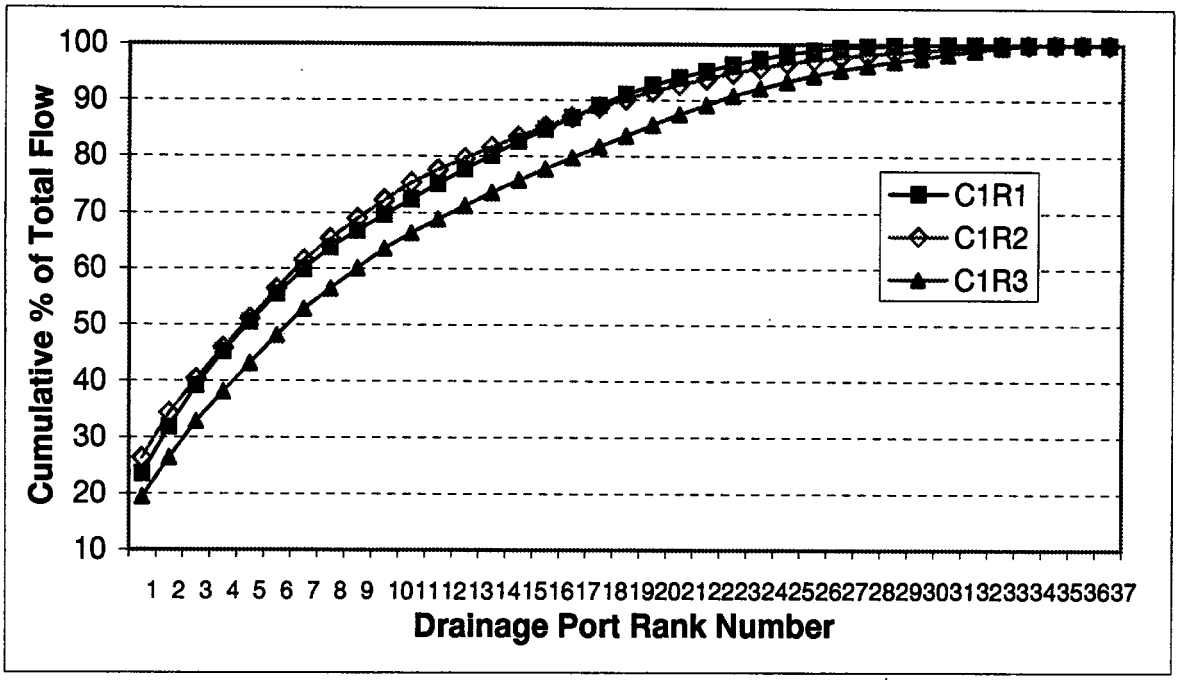

Figure 3-12 % and Cumulative % of Total Run Flows in Individual Ports for C1

3.3.4 Areas Conducting Channelled Flows

In Figure 3-1, cumulative percentages of flows (relative to the whole-column flow for a given time interval) is plotted against the cumulative percentages of the rock bed base drainage area (relative to the total base drainage area) receiving these flows. The drainage ports have been sorted from the largest to the smallest flow. The straight line labelled as "uniform" corresponds to an ideal, homogeneous flow where the % total cumulative flow is equal to the % cumulative drainage area receiving this flow. To illustrate, for C1R1 in the time interval of 30 to 60 min (empty square symbol, top graph), 20% of the bottom drainage area received 77% of the whole-column flow collected in this time interval. Note that this 20% of the base drainage area is not a random 20%, but one intercepting the largest channel flows. The closer an experimental curve is to the "uniform" curve, the more homogeneous is the flow regime, and thus the less channelling effects there are.

Examination of Figure 3-1 reveals the following:

- All runs start with highly heterogeneous flows (with strong channelling) and tend towards homogeneous flows. But homogeneous flows are never attained.

- The percentage of the whole-column flow carried by the eight largest channels (representing ~22% of the base drainage area) change from one interval to another, from one run to another, and from one column to another. For C1 and C2, they range from 70 to 90% for the early stages of the drainage events.

- For C1 and C2 where simulated rain was applied, 20-50% of the total base drainage area does not conduct any flow during the early stages of the drainage events.

- For C3 where feed water is applied at one central location on the rock bed surface, 20-60% of the base drainage area does not conduct flow.

It is worth pointing out that the above interpretations are based on the assumption that each channel occupies the same area as the drainage partition that intercepts it. Realistically, the cross-sectional area of a channel is probably much smaller than the area of the partition intercepting the channel. If this is taken into consideration, the percentages of flows would be conducted by much smaller percentages of the base drainage area than shown in Figure 3-1. This would shift all the curves towards the left and make their initial slopes steeper. Unfortunately, a more accurate channelling analysis such as this is impossible due to the limitations imposed by the fixed resolution of the base partitions.

For a real waste rock pile in the field, because rain is intermittent instead of continuous and because rain intensity changes instead of being constant, there is little chance for field seepage to approach uniform flow. For a typical waste rock pile, highly heterogeneous channelled flows would be the dominant mode of infiltration flow in the interior of the pile during and following rainstorms.

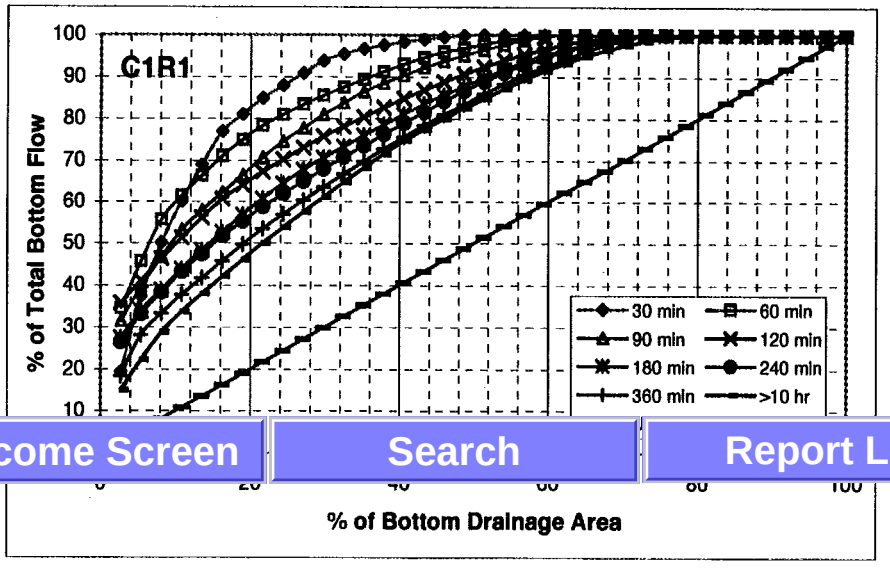

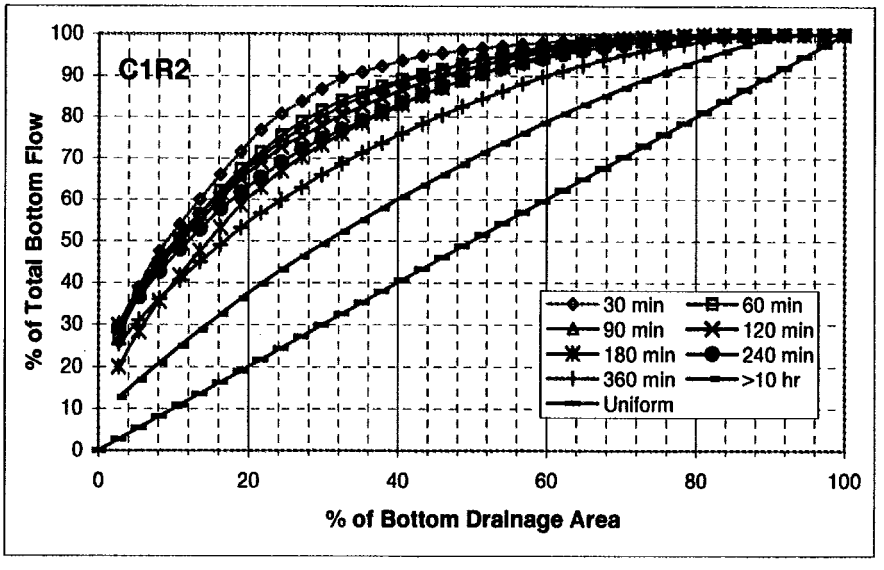

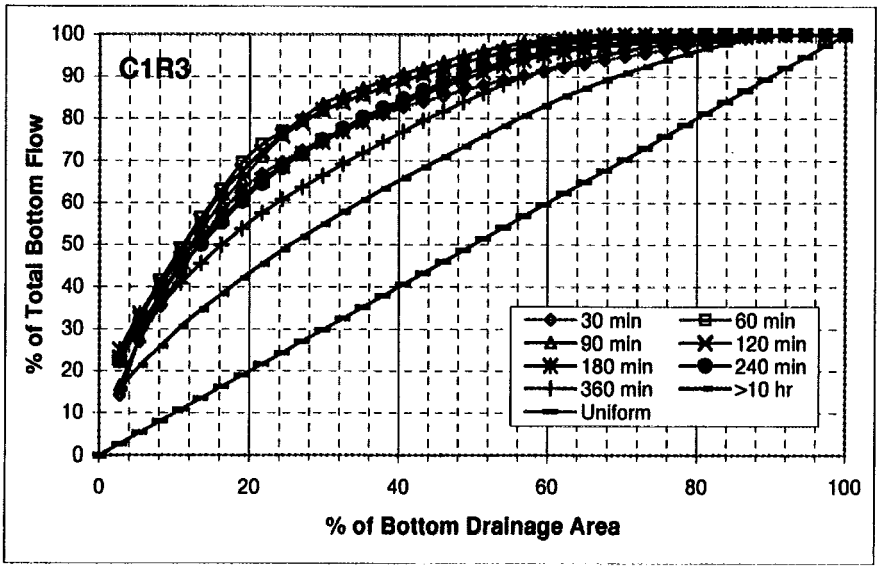

Figure 3-13 % of Flows vs. % of Bottom Drainage Areas Conducting These Flows

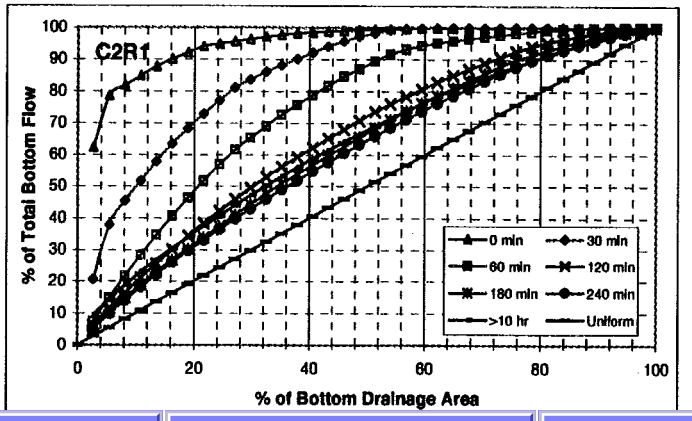

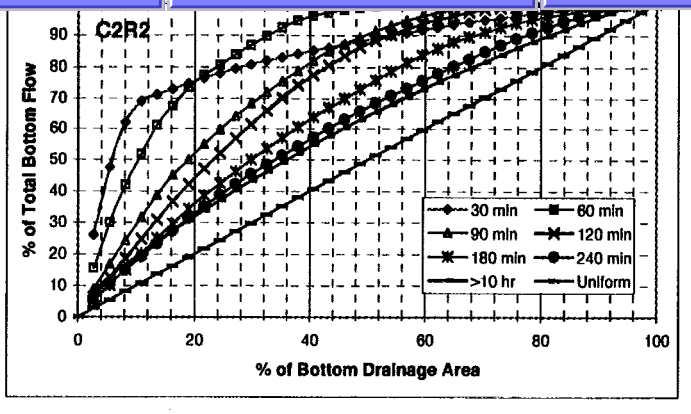

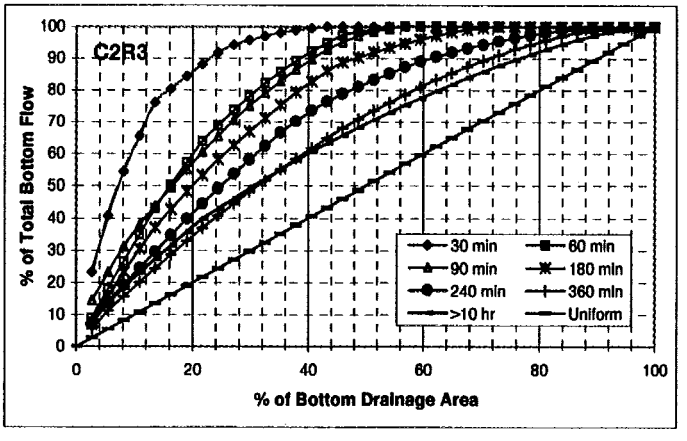

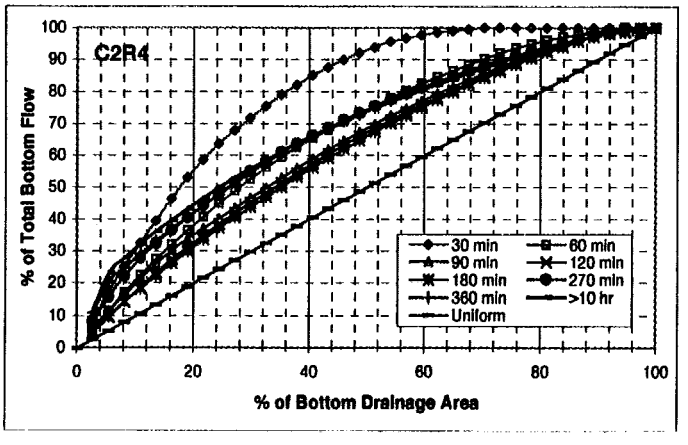

Figure 3-13 % of Flows vs. % of Bottom Drainage Areas Conducting These Flows (Cont'd)

Welcome Screen Search Report List

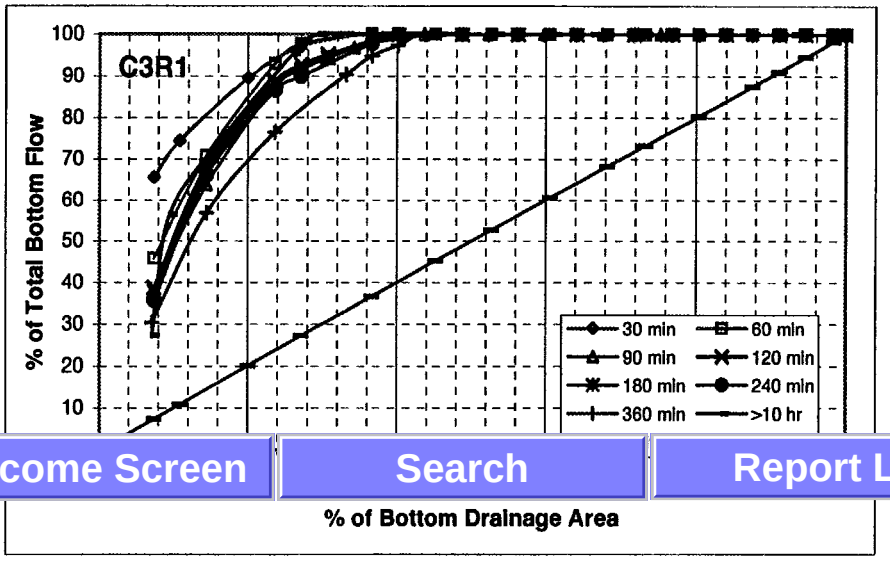

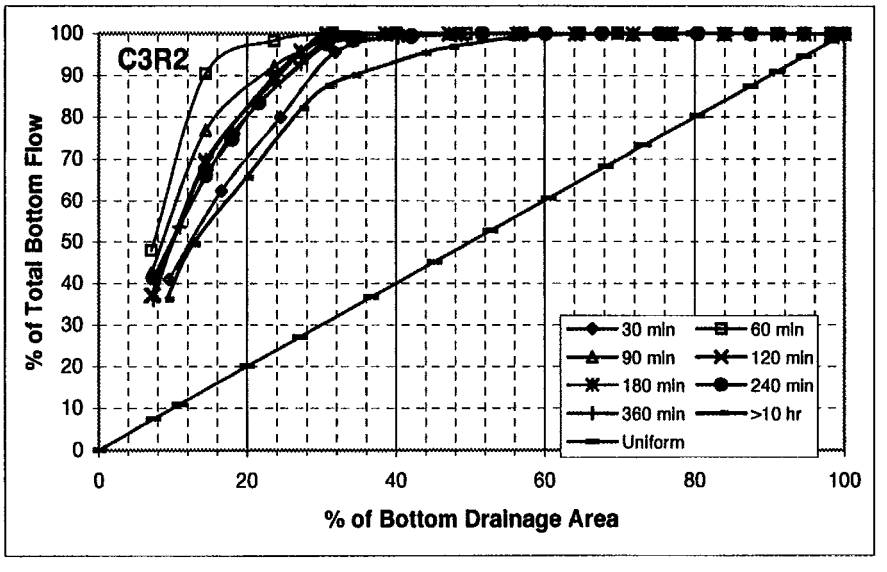

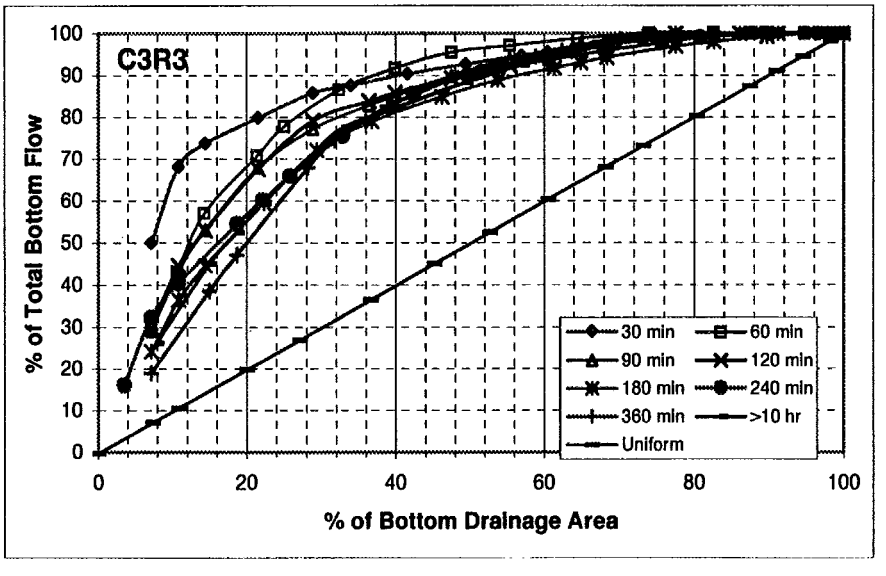

Figure 3-13 % of Flows vs. % of Bottom Drainage Areas Conducting These Flows (Cont'd)

3.3.5 Summary

The large column experiments have demonstrated that channelling is an ubiquitous phenomena in the waste rock studied. Large channels representing a very small fraction (< 5%) of the total drainage area at the base of the rock mass conduct a significant fraction (~ 20-30%) of the total drainage flow. Intermediate channels account for ~20% of the drainage area carry ~ 40% of the total flow. About 50% of the drainage area has background or matrix flows and carry 30-40% of the total flow. About 30% of the column base area does not intercept any flow. Channelling is more pronounced in the earlier stages of drainage events. During a drainage event, the drainage flows are highly heterogeneous at the rock bed base at the beginning of the drainage event, but they tend towards more homogeneous flows as the drainage process progresses.

Channel stability is the persistence of large channels when conditions change. Internal channel stability is the ability of large channels to maintain their ranks during a drainage event.

The experimental observations on the effects of several rock bed variables and simulated rain variables are summarised in Table 3-1.

Table 3-4 Observed Effects of Several Variables on Channelling Phenomena

Variable	Observed Effects
Rock bed height	• Addition of new material on existing rock bed changes channel locations, perhaps by blocking old channels. • Channel stability is lost when rock bed height changes. • Thicker rock bed has higher internal channel stability. • Greater bed height/thickness tends to lead to more uniform flow distribution.
Initial moisture	• Higher initial moisture in the rock mass means shorter drainage arrival time at the base. • Effects of higher initial moisture are similar to those of longer rain duration. • Effects of initial moisture on channel stability are small. • Higher initial moisture increases internal channel stability.
Simulated rain duration	• Effects of longer rain duration are similar to those of higher initial moisture. • Effects of rain duration are small on channel stability. • Longer rain duration increases internal channel stability.
Intensity of simulated rain	• Effects of rain intensity are small on channel stability. • Higher rain intensity increases internal channel stability. • Lower rain intensity causes smaller drainage flow rates in the same channels.

3.4 DRAINAGE SOLUTE TRANSPORT

3.4.1 Inferences from Zn Mass Balance

Zinc mass balance has been calculated for the three runs of C1 using parameter values given previously (Table 3-1).Treating the column as a single reactor, a hypothetical zinc output has been calculated for each run of C1. Three hypothetical reactor types were used: plug flow reactor, mixed batch reactor, and continuously stirred tank reactor (CSTR). By comparing the measured zinc outputs with hypothetical zinc outputs, inferences can be made regarding the solute transport phenomena within the waste rock.

Table 3-5 Calculated Zn Mass Balance for Three Runs of C1

	C1R1	C1R2	C1R3
Start moisture (%)	5.70	7.38	7.40
Start moist rock weight (kg)	3700	3767	3768
Start water weight (kg)	211	278	279
Start pore water Zn (g/kg)	16.0	11.1	9.70
Start Zn mass (g)	3376	3093	2707
Water input (kg)	92.5	50.0	36.0
Water output (kg)	25.6	48.7	27.0
Zn output (g)	283	386	176
End moisture (%)	7.38	7.40	7.63
End moist rock weight (kg)	3767	3768	3777
End water weight (kg)	278	279	288
End pore water Zn (g/kg)	11.1	9.70	8.79
End Zn mass (g)	3093	2707	2531
% of Zn mass removed	8.4	12.5	6.5
Drainage as % of end water weight	9.2	17.4	9.4
% Zn removed per kg drainage	0.33	0.26	0.24

Notes:
1. Zn mass refers to that of dissolved Zn in pore water.
2. Evaporation is ignored in the mass balance calculation.
3. Pore water Zn concentration is a bulk average except the initial one.

It has been shown in Section 3.2 that Zn in the dissolved drainage comes from the pore water in the waste rock and there is negligible mineral dissolution involved. Now if we assume that the flow within the pores of the waste rock mass is via pore water displacement (equivalent to a plug flow reactor), that is, the original pore water is pushed out by the infiltrating water without mixing or dispersion, the Zn output from the rock mass would be the product of the drainage volume and the initial pore water Zn concentration, until all the initial pore water (211 kg) is displaced. Since the total drainage water amounts only to 101 kg, the Zn output in the drainage can be calculated by this method, which gives 410 g, 779 g, and 432 g, respectively, for R1, R2 and R3.

If we assume the column to be a batch reactor, with each run treated as a batch reaction in which the original pore water and infiltrating water are fully mixed, the Zn outputs can be calculated as the product of drainage volume and the Zn concentration after through mixing. The results are 285 g, 459 g, and 232 g, respectively.

Finally if we assume the column to be a CSTR to which the infiltrating water is continuously added and from which the well-mixed solution is continuously discharged, at a steady-state the Zn outputs can be approximated by the formula

$$M = V_0 C_0 \left[1 - \exp\left(-\frac{V_{out}}{V_0} \right) \right]$$

where V_0 and C_0 are, respectively, the total volume of water and the Zn concentration of the well-mixed solution at the time when drainage starts to flow at the base; and V_{out} is the total volume of drainage collected in a run. The Zn output calculated with this formula is 297, 495, and 242 g, respectively.

The various Zn outputs are compared in Figure 3-1. The measured Zn output is far less than that expected from the pore water displacement mechanism. This rules out pore water displacement as a possible flow model. This result indicates that most of the original pore water is probably stagnant during an infiltration event.

The measured Zn loading is also less than that expected for a CSTR or a mixed batch reactor. What is surprising is that the measured efficiencies of Zn removal come so close to the efficiencies of a mixed batch reactor (within 76-99% of the measured efficiencies) and the efficiencies of a CSTR (within 73-95% of the measured efficiencies). Although the waste rock mass cannot be likened to a fully-mixed batch reactor or a CSTR in terms of conceptual structures, the data nevertheless suggest that, in a practical sense, the leaching of Zn from the waste rock mass can be approximated by leaching taking place in a well mixed system. This may seem like a paradox, but the finding is practically important. The implication is that, even if we do not understand the true mechanism, a simple model can be applied to estimate the leaching of dissolved mass from a waste rock pile that behaves like the large columns. A critical question of course remains: What are the characteristics of a waste rock pile that make it behave as if it were a well mixed system? Some aspects related to this question will be briefly touched on in Chapter 4.0 .

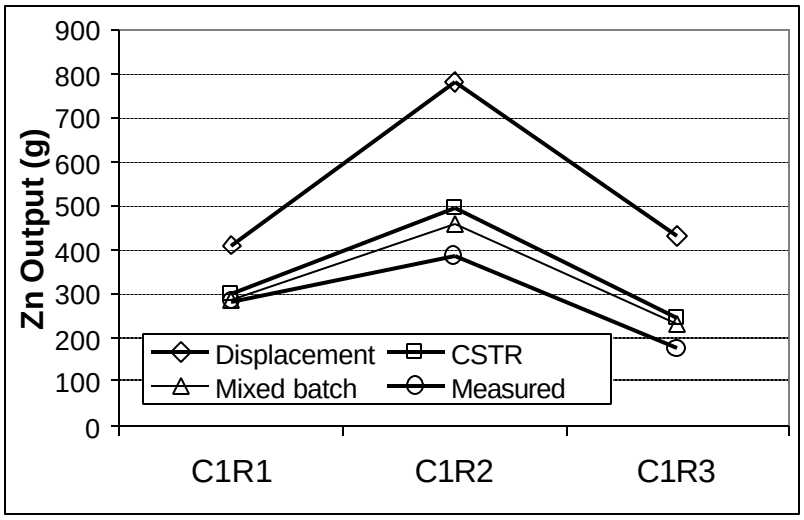

Figure 3-14 Comparison of Measured Zn Output with Those for Hypothetical Reactors

3.4.2 Conceptual Flow and Solute Transport Model

In Section 3.2.5 it was shown that there is no simple correlation between flow rates and concentrations of dissolved Zn and SO_4^{2-}. Despite the large variations in the flow rates, the Zn and SO_4^{2-} concentrations stay in a relatively narrow range. For example, In Figure 3-1, the flow rate for C1R1 ranges from 0.2 to 40 g/min/port, a range factor of 200, whereas the Zn concentration is from 6000 to 15000 mg/L, a range factor of only 2.5.

This observation suggests that high-flow channels are not formed at the surface and channels do not run the entire rock bed depth. In other words, the model shown in case (a) of Figure 3-1 is inappropriate. This is because if case (a) were a correct model, the flow in a large channel, having originated at or near the surface and flowing quickly to the base, would have little chance to mix with the original pore water. This would cause highly dilute solutions to be discharged in large channels. As this phenomenon has not been observed in the large column experiments, the model represented by case (a) must be dismissed.

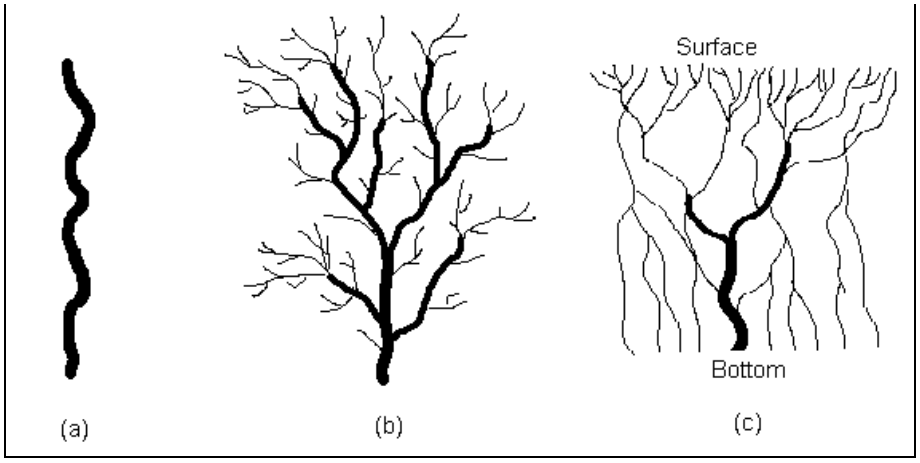

Figure 3-15 Possible Configurations of Channel Formation

(a) Single top-to-bottom main channel (b) Dendritic model for formation of rivers and streams (c) Dendritic-reticulate model for channelled flow in waste rock

To explain the narrow concentration ranges despite wide flow rate variations, one needs to find a model in which all flows, whether in large channels, small channels, or matrix flows, have sufficient contact and mixing with the pore water. In search of an proper model, one can make an analogy to the formation of rivers, as shown in (b) of Figure 3-1. Rivers are formed from branches at tributaries; branches are formed by joining of streams; and streams are formed from collection of overland flows and ground water discharges. An adaptation of the river system configuration to the infiltrating flow within a waste rock mass is show in (c) of Figure 3-1. From its structure, this model is named a “dendritic-reticulate channelling flow model”.

In this model, there is no large flows originating at the surface. Major channels are formed from successive amalgamation of smaller flows; each of the smaller flows can trace its origin to surface infiltration from precipitation. Every pocket of water ultimately appearing in major flow channels has had plenty of contacts with the original pore water before it joins a main channel. As a result, the Zn and S concentrations in large flow channels do not differ appreciably from those in small channels or matrix flows. In this model, the Zn and S concentrations of an infinitesimally pocket of water in the drainage are dependent primarily of three variables: the total path length (varying with the tortuosity of the path), the total residence time (a function of flow velocity and total path length), and the degree of mixing (which determines the mass of solute transferred between the pore water and the flowing water). Since none of these three variables is deterministic, it follows that the Zn and S concentrations in the drainage would be *random dependent variables* with their distribution functions determined mainly by stochastic processes. The path length, residence time, and degree of mixing mentioned above are the *independent random variables*.

Another feature of the dendritic-reticulate model that differs from the river system configuration is the coexistence of fine flow channels and major flow channels. The so called “fine flow channels” cover both true small flow channels and matrix flows (if present). The idea stems from the experimental observation that flows occur not only in major channels, which are relatively few, but also

as scattered flows at most parts of the rock bed base. Except for the initial stage when only large channels issued drainage, a majority of the drainage ports received flows when the drainage event is well in progress. The dividing line between “large channels” and “fine channels” is artificial, because the flow rate in each channel fluctuates widely during a drainage event.

The fine flows featured in the dendritic-reticulate model also help explain the relatively high efficiency of Zn removal from the original pore water. If the fine flows were absent, all the drainage would be discharged at the column base by relatively few major channels. This would imply that only a fraction of the lower waste rock bed would be contacted by the major channels, resulting in an inefficient Zn removal from the pore water in this region. This appears inconsistent with the removal efficiency observed.

The conceptual dendritic-reticulate channel flow model proposed here appears to be able to qualitatively explain the experimental observations. This model is therefore our recommended flow model in this report. We have adopted it so far to explain the observed flow phenomena and will use it later to support our conclusions from the kinematic wave modelling exercise (Chapter 4.0).

3.4.3 Changes in Dilution Factors

Suppose the initial pore water Zn concentration is C_0 (previously estimated at 16 000 mg/L) and that the mass-weighted average Zn concentration of all column base flows for the interval ending at time t is C_t. The ratio C_t/C_0 is defined as the “dilution factor” f. Dilution factor f is numerically equal to the fraction of the original pore water in the drainage water for the time interval considered. For pure simulated rain water that has not mixed at all with the pore water, f = 0. For pure pore water, f = 1. In the large column experiments f varies between 0 and 1.

In Figure 3-1, the dilution factor for the three successive runs of C1 is plotted against the cumulative total volume of water passed through the column as simulated rain. Figure 3-1 shows some interesting patterns:

- The dilution factors show a continuous decline from R1 to R3.
- The beginning dilution factors for C1R2 and C1R3 are approximately equal to the ending dilutions factors of C1R1 and C1R2, respectively. In other words, there is a continuity in dilution factor between two consecutive runs.
- The decrease in the simulated rain intensity from R2 to R3 did not increase the dilution factor, as one would expect intuitively.
- The dilution factor trend in each run is different: in R1 it is a continuous, nearly linear decline; in R2 a decline followed by a plateau; and in R3 a irregular wave.
- There is temporary upsurge in dilution factor half way through R3.

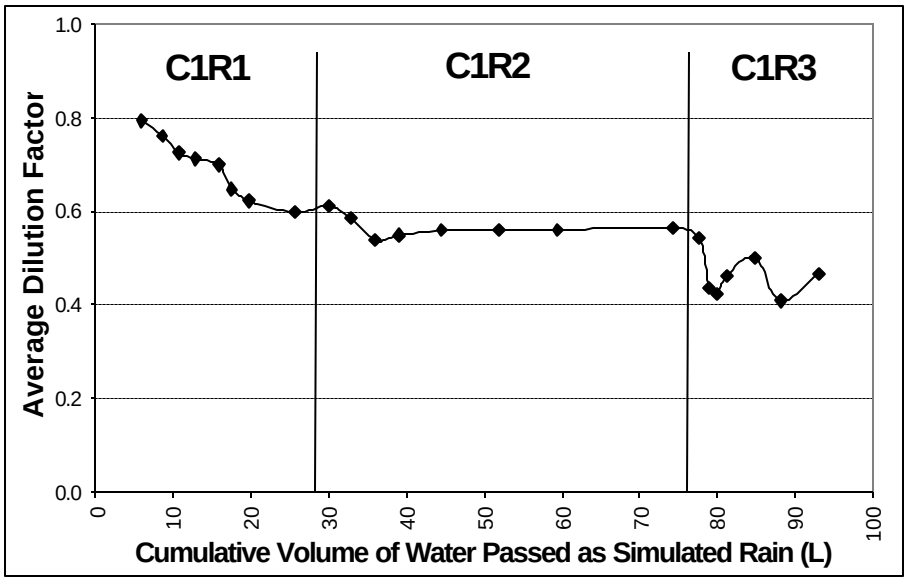

Figure 3-16 Changes in Dilution Factors for Three Consecutive Runs of Column 1

It is impossible to use the dilution factor changes to infer the solute transport controlling mechanisms even with the help of the conceptual dendritic-reticulate channelling model. However, it may be possible to use the dilution factor information in a backward direction through parameter optimisation to probe the solute transport controls. For example, one could follow the steps below to select a model that best describes the dilution factor data:

- First, establish several mathematical models that have a potential to describe the solute transport phenomena adequately.
- Second, by using known input parameters and adjusting model parameters, attempt to reproduce the dilution factor patterns.
- Third, select the model that best reproduces the observed dilution factor changes as the best model.

The model selected by this procedure does not necessarily reflect the true solute transport controlling processes. It must be validated independently before application to new cases.

3.4.4 Summary

Zn mass balance calculations show that the measured efficiencies of Zn removal from the waste rock pore water are comparable to those of a well-mixed reactor. The transport of solute is shown not to take place by pore water displacement. Experimental observations lead to the proposition of a conceptual model - the dendritic-reticulate channelling model. The variation in dilution factors in three consecutive runs is shown to possess certain patterns.

3.5 STATISTICAL ANALYSIS

In this section the statistical distributions of three variables are examined: flow rate, Zn concentration, and Zn loading. The stochastic processes possibly underlying these distributions are briefly discussed.

3.5.1 Flow Rate Distribution

To investigate the statistical distribution of individual port flow rates, the flow rates in all the drainage ports with non-zero flows are used to construct a histogram. One histogram is produced for each time interval (there are six to eight intervals in each run) in all the experimental runs of C1 and C2. The resulting histograms are presented in APPENDIX IX.

An examination of the histograms reveals a predominant feature: they are highly unsymmetrical and skewed to the right. This reflects the experimental observation that the total flow is conducted by relatively few large channels and a large number of intermediate and fine channels.

This leads one to suspect that the flow rates may obey a lognormal distribution. To verify this, the flow rate data are transformed by taking their natural logarithm. The re-plotted histograms are also shown in APPENDIX IX. With a few exceptions, the new histograms are now symmetrical and have the bell shape characteristic of the normal distribution.

Lognormal distribution is one in which the log-transformed data distributes normally. If we use x to represent the untransformed variable (e.g., flow rates), the distribution of x is described by the probability density function

$$f(x) = \frac{1}{\sqrt{2p}\, s\, x} e^{-\frac{1}{2}\left(\frac{\ln x - m}{s}\right)^2}$$

where μ is the population mean and σ the population standard deviation of the log-transformed variable $y = \ln x$. The maximum likelihood estimates (MLE) for μ and σ from a sample are given by

$$\hat{m} = \frac{1}{n}\sum_{i=1}^{n} \ln x_i$$

$$\hat{s}^2 = \frac{1}{n}\sum_{i=1}^{n} (\ln x_i - \hat{m})^2$$

where x_i, i = 1, …, n, are observed values in a sample of size n.

To test whether the flow rate data obey lognormal distribution, the last two formulae are used to compute the MLE's of μ and σ, which are used to calculate the lognormal density function f(x). The f(x) is then superimposed on the histograms in Figure 3-1.

The histograms agree with the f(x) of the lognormal distribution reasonably well. The deviation of some histograms is most probably a result of insufficient data used to plot the histograms. This is a constraint imposed by the experimental design because there are only 37 drainage ports. Thus the maximum number of flow rate data for any given time interval is 37. From Figure 3-1, it is concluded that the lognormal distribution appropriately describes the flow rate data.

Figure 3-1 reveals that, as the drainage event progresses, the lognormal distribution shows increased peakedness, whereas the location of the mean shifts to the left. This means that both the range and the mean of flow rates decrease as the drainage event proceeds. The lognormal distributions fitted to the experimental data at various time intervals for C1R1 are compared in Figure 3-2. For a discussion of lognormal distribution and random processes the reader is referred to Ott, 1995.

What random process underlies the observed lognormal distribution of flow rates is unclear. To clarify this requires further theoretical and experimental work. Generally speaking, the lognormal distribution characterises a random variable that shows very few occurrences of very high values. This seems to fit the profile of the individual port flow rates when channelling is present.

3.5.2 Zinc Concentration Distribution

As pointed out earlier, all zinc concentrations are interval-averaged. In examining the statistical distributions, all zinc concentrations have been normalised to the initial pore water zinc concentration of 16000 mg/L. The relative Zn concentration so obtained is termed “dilution factor”.

The dilution factor data have been subjected to the same scrutiny as that applied to the flow rate data. Figure 3-3 exhibits the comparison between the histograms constructed using standardised dilution factors and the fitted standard normal distribution for C1R1. The standardisation of the dilution factors is achieved by the formulae

$$z_i = \frac{x_i - \bar{x}}{s} \qquad \bar{x} = \frac{1}{n}\sum_{i=1}^{n} x_i \qquad s = \frac{1}{n-1}\sum_{i=1}^{n}(x_i - \bar{x})^2$$

where n is the number of concentration samples for any given time interval; x_i is the concentrations; $\bar{x}$ is the mean of concentrations; and s is the sample standard deviation.

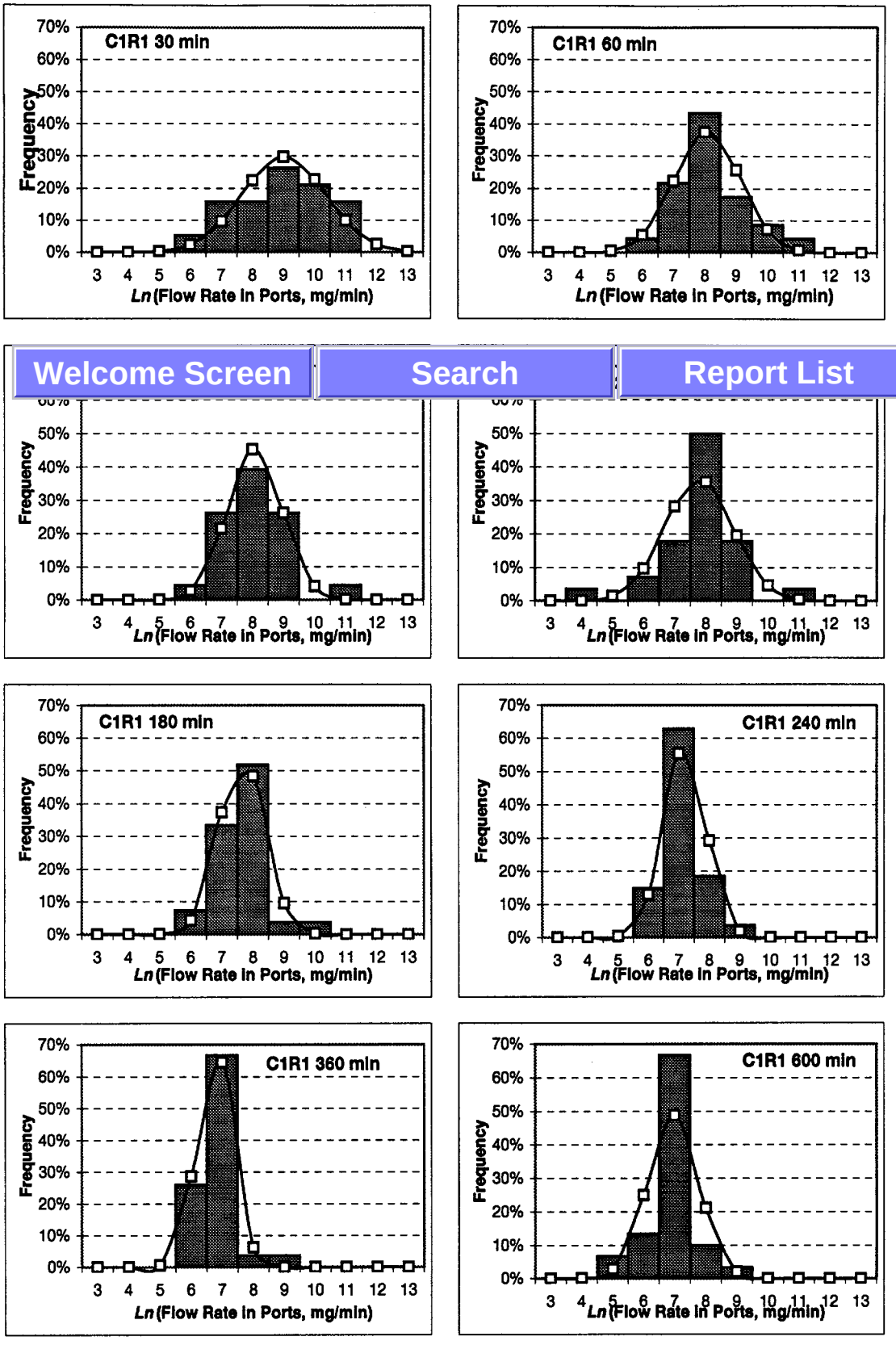

Figure 3-17 Experimental Flow Histograms vs. Lognormal Distribution for C1R1

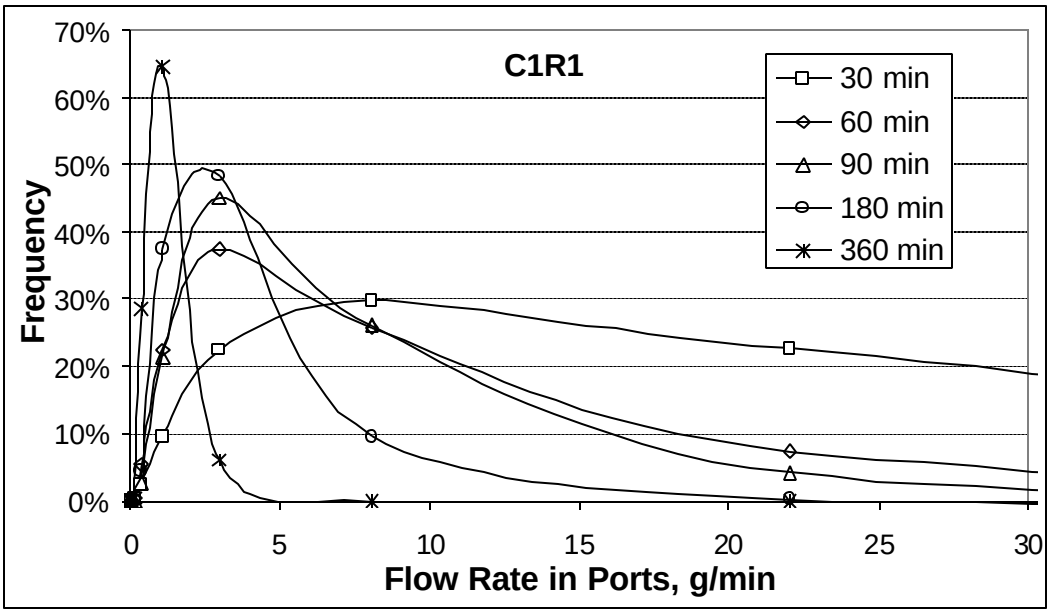

Figure 3-18 Lognormal Distributions Fitted to Experimental Data for C1R1

Figure 3-3 shows that, unlike the flow rates which distribute lognormally, the standardised dilution factor histograms agree well with the standard normal distribution. It is therefore concluded that the zinc concentrations obey a normal distribution. In comparison, Morin et al. (1995) found that the dissolved copper concentrations recorded over 10 years at the now-closed Bell Mine, Noranda Inc. display a lognormal distribution.

As with the case of flow rates, the construction of the dilution factor histograms is subject to the constraint of the experimental design.

Figure 3-4 illustrates how the dilution factor (non-standardised in this case) distribution varies within one run (C1R1) and among three runs (C1R1, C1R2, C1R3). Within one run, with the progress of a drainage event, the distribution tends to shift towards the left (more dilution of the initial pore water) whereas the standard deviation decreases (narrower dilution factor ranges). For successive runs, the dilution factor distributions for a given time interval also shift to the left but, unlike within one run, the distribution becomes more widespread.

The central limit theorem states that the distribution of the mean of samples with n observations, $\overline{X}_n$, which itself is a random variable, approaches normal distribution as n $\rightarrow \infty$, regardless of the distribution of the parent population. More generally, a normal distribution can be produced by random sum processes. The sum of n mutually independent random variables (called a random sum) will have a normal distribution when n $\rightarrow \infty$, regardless of the kinds of distributions of the n independent random variables.

The random sum process may be the stochastic process underlying the observed normal distribution of zinc concentrations. To verify this, however, requires further experimental and theoretical work.

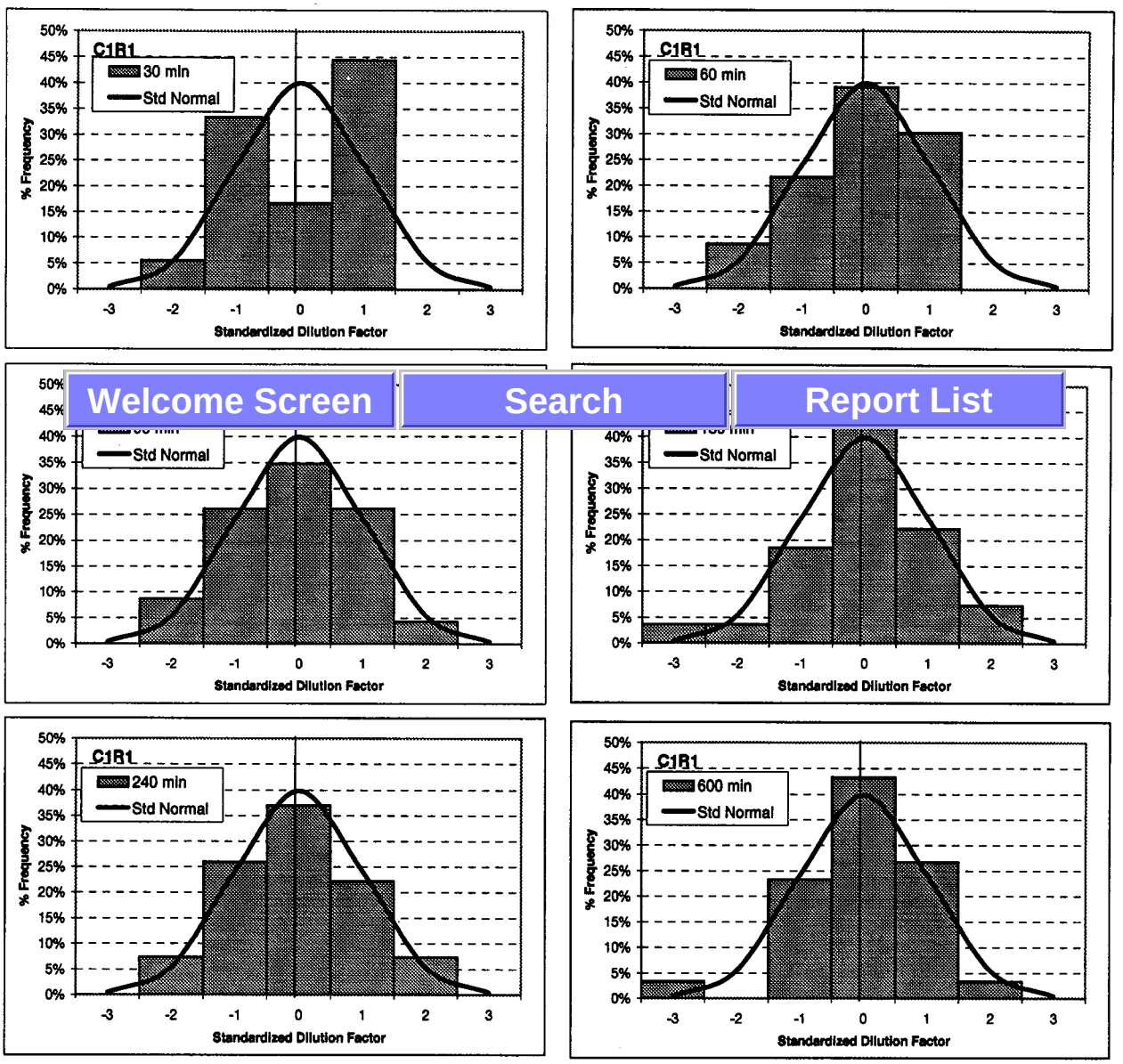

Figure 3-19 Experimental Dilution Factor Histograms vs. Standard Normal Distribution

Welcome Screen Search Report List

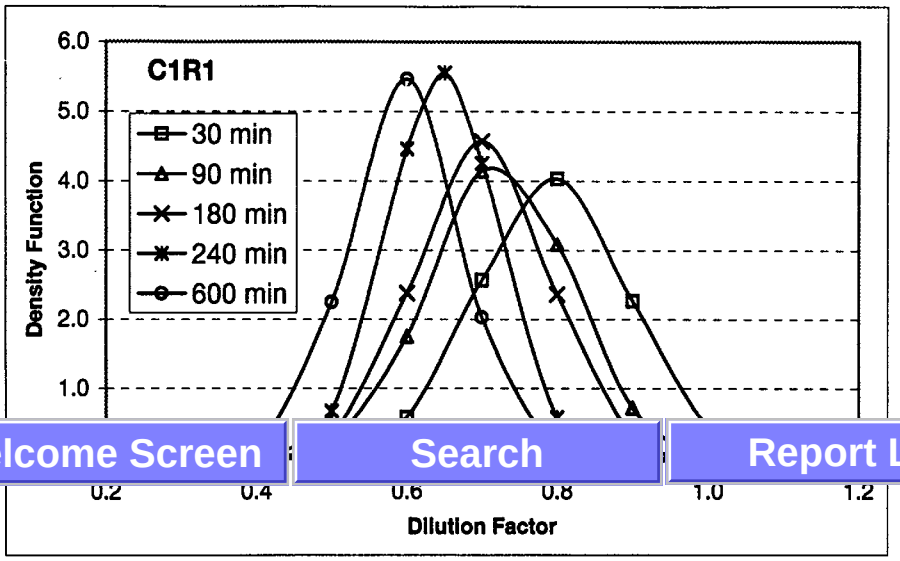

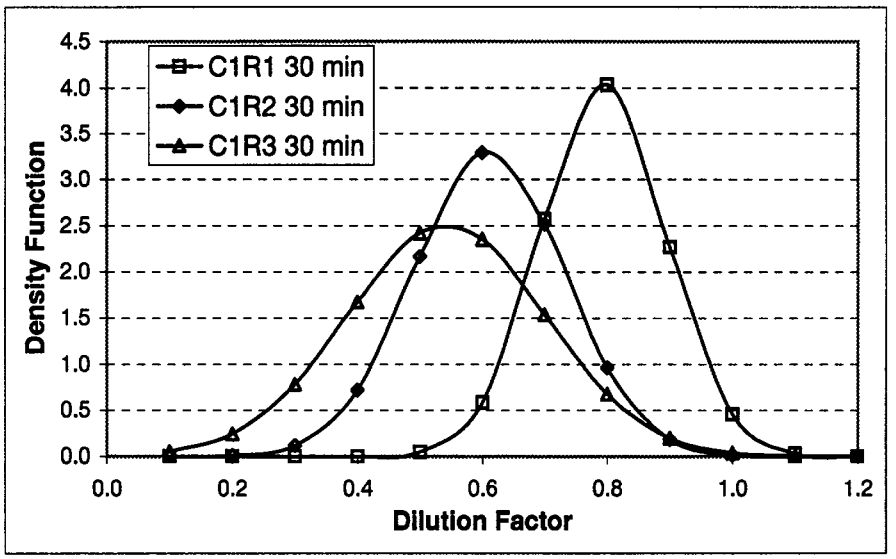

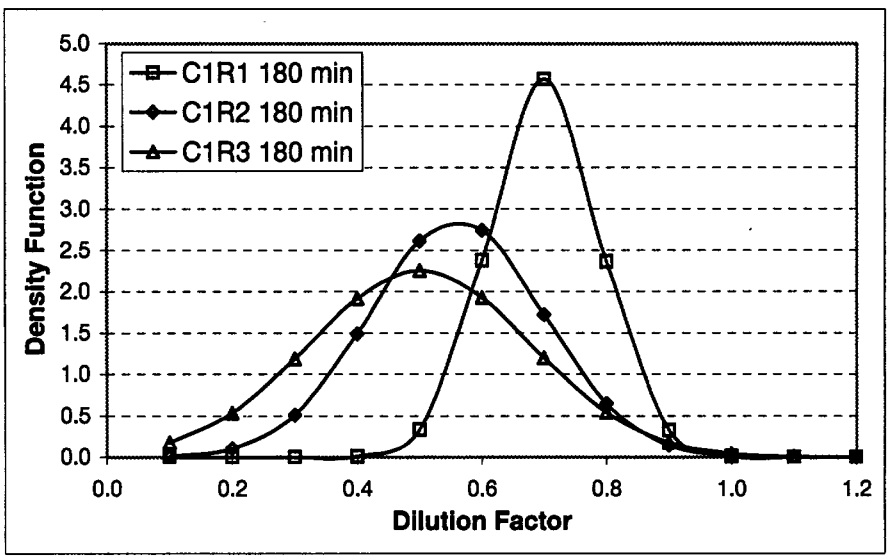

Figure 3-20 Variations of Dilution Factor Distribution within One Run and between Runs

3.5.3 Loading Distribution

In the previous two sections flow rate and zinc concentration are found to be appropriately described by the lognormal and the normal distribution, respectively. Since zinc loading is the product of flow rate and zinc concentration, can the relationship between the distribution of Zn loading and those of flow rate and Zn concentration be deduced? The answer is negative. According to the probability theory, if **X** and **Y** are two independent variables obeying two different distributions, the distribution of a third random variable **Z** = **X**x**Y** cannot be obtained from the distributions of **X** and **Y**.

To find the distribution of Zn loadings in different drainage ports, the same analytical techniques as those used for flow rates and Zn concentrations are applied. The resulting histograms and fitted distributions are shown in Figure 3-1. It turns out that the Zn loading distribution is also approximately lognormal.

Since the flow rate range is much wider than the zinc concentration range, the loading distribution is dominated by the distribution of flow rates, which is lognormal. This can be understood through the following analysis. Let **X** be the random variable representing the flow rate and Y the random variable representing the Zn concentration, and assume they are independent of each other (as is probably the case in this study). Then **Z** = **X**x**Y** is the new random variable representing the Zn loading. Since the variation in **X** is far greater than that in **Y**, **Y** can be approximately treated as a constant and instead of a random variable. **Z** then becomes a product of a random variable and a constant and has the same distribution as **X**, which is lognormal.

Figure 3-2 shows the variation of the lognormal distributions fitted to the experimental Zn loading data. Understandably, the pattern of variation is similar to that for the lognormal distributions fitted to the flow rate data.

3.5.4 Summary

The flow rates and the zinc loadings in individual drainage ports were found to be approximated adequately by the lognormal distribution. The individual port Zn concentrations are however distributed approximately normally. Zn loading is a product of flow rate and Zn concentration. As such the loading distribution is dominated by the flow rate distribution since flow rates vary much more widely than Zn concentrations.

The distributions of flow rates, Zn concentrations, and Zn loadings can be treated as either deterministic distributions (like a particle size distribution) or probabilistic distributions (like the distribution of a random variable). Which approach to take depends on the circumstances. Generally speaking, since the large number of individual flow rates under a field waste rock pile are impossible to measure, treating these distributions probabilistically makes the most sense.

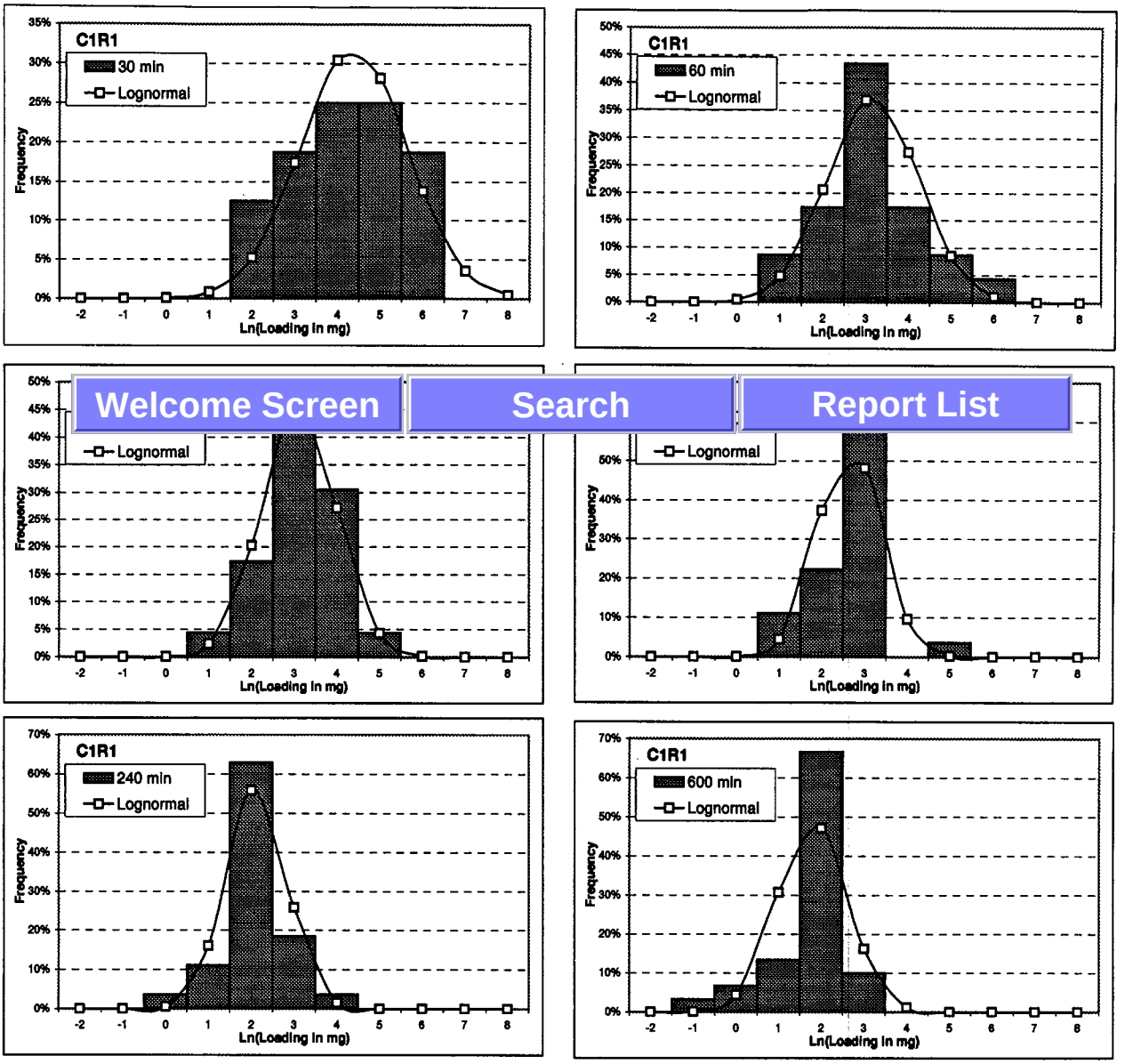

Figure 3-21 Experimental Zinc Loading Histograms vs. Lognormal Distribution

Welcome Screen Search Report List

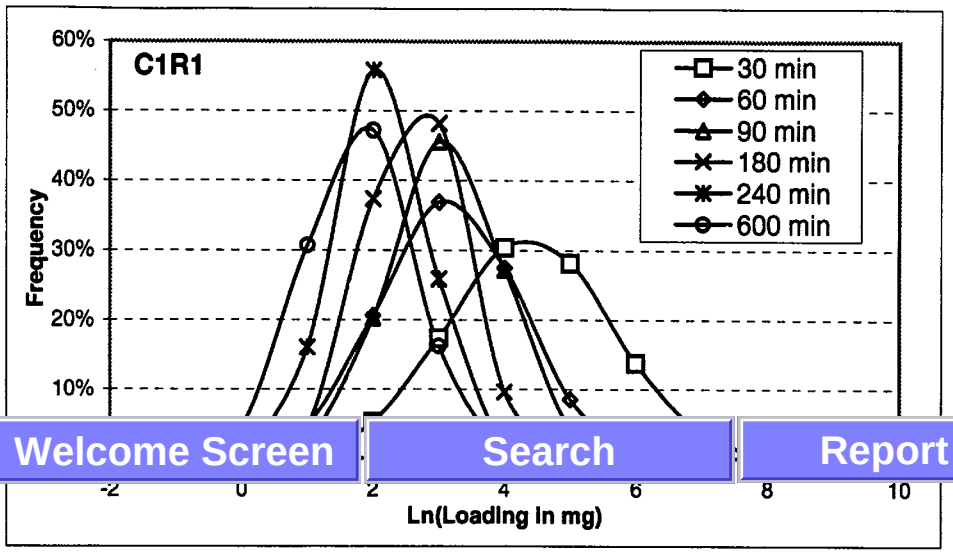

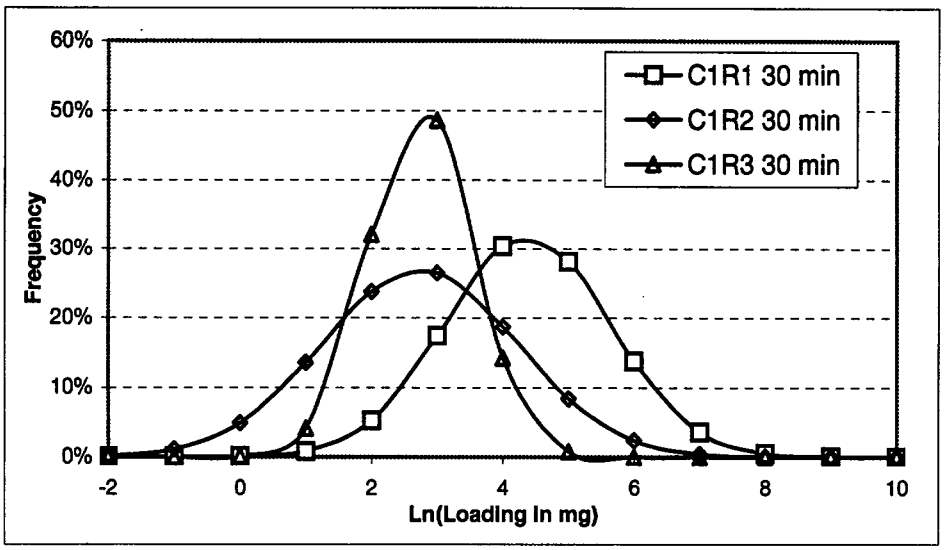

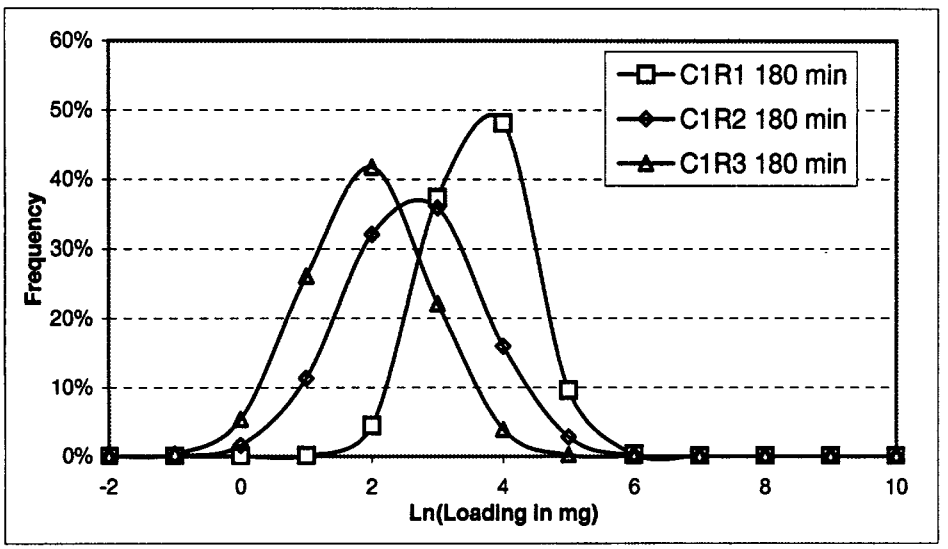

Figure 3-22 Variations of Zinc Loading Distribution within One Run and between Runs

3.6 CONCLUSIONS

Geochemistry

The emphasis of data analysis was placed on the mechanisms controlling the concentrations of dissolved constituents in the drainage. Experimental results suggest that the concentrations of Ca, Pb, and Al are solubility-controlled by gypsum, anglesite, and jurbanite, respectively. Solubility control does not exist for dissolved Zn, Fe, and SO_4^{2-}. Rather, the variations in Zn, Fe, and SO_4^{2-} concentrations can be satisfactorily explained by a dilution hypothesis. The hypothesis states that these concentrations and the pH in the drainage are a result of successive dilutions and/or intermixing of various-stage dilutions of the original pore water, subject to the regulation by redox reactions and goethite precipitation. All soluble zinc seems to be stored in the pore water, and dissolution of zinc-containing minerals does not contribute significant zinc to the drainage. The zinc loading in the drainage is primarily determined by the Zn mass transfer that occurs in the dilution and mixing processes.

Hydrology

Channelling is an ubiquitous phenomena in the waste rock studied. Large channels representing a very small fraction (< 5%) of the total drainage area at the base of the rock mass conduct a significant fraction (~ 20-30%) of the total drainage flow. Intermediate channels account for 20% of the base drainage area and carry ~ 40% of the total flow. About 50% of the drainage area has background or matrix flows and carry 30-40% of the total flow. Nearly 30% of the base area does not intercept any flow. Channelling is more pronounced in the earlier stages of drainage events. During a drainage event, the drainage flow distribution is highly heterogeneous at the beginning of the drainage event, but tend to become more homogeneous as the draining process progresses. Channel stability and internal channel stability are defined and found to be influenced by several variables related to the rock bed properties and simulated rain properties.

Solute Transport

Zn mass balance calculations show that the efficiencies of Zn removal from the pore water are comparable to those of well-mixed systems. The transport of solute is unlikely to take place by pore water displacement. Experimental observations lead to the proposition of a conceptual model - the dendritic-reticulate channelling model.

Statistical Analysis

The individual port flow rates and the zinc loadings were found to approximately obey the lognormal distribution. The individual port zinc concentrations are however distributed approximately normally. The distribution of zinc loadings is dominated by the distribution of flow rates, since the flow rate vary much more widely that the zinc concentration.

3.7 POTENTIAL BENEFITS AND FUTURE WORK

3.7.1 Potential Benefits

The observations and findings in this chapter are specific to the partially oxidised Stratmat waste rock sample used in the experiments. Nevertheless, the following benefits can be envisaged.

- The results can be used to help understand how channelling phenomena influence water quality and contaminant loadings from field waste rock piles. This may lead to improvement in ARD prediction for waste rock piles.

- The results may be useful in deriving theoretical representation and performing mathematical modelling of channelling phenomena in similar materials, as will be discussed in Chapter 4.0 .

- The rock sample used in the experiments is similar to materials in heap leach piles. The findings in this study may be used to understand and optimise heap leaching operations.

- The results may be used to help understand and model the responses of leached heaps to decommissioning methods based on rinsing, Such information is valuable in evaluation, selection, and design of decommissioning measures.

- The results may be helpful in evaluating the practicality of passivation of acid generating wastes by application of solutions bearing passivating agents.

3.7.2 Potential Future Work

Waste rock piles are complex structures consisting of different parts of vastly differing hydraulic (flow) properties. The present understanding of the hydrology and solute transport in waste rock piles is poor. Better understanding of a field waste rock pile requires better understanding of its components. The present large column study examined but one kind (hydraulically speaking) of rock material that may exist in a field waste rock pile. The findings would be applicable to the regions of a waste rock pile consisting of a hydraulically similar material. More studies using other types of rock materials found in field rock piles are needed. Once one understands the behaviour of many kinds of rock materials that comprise a field rock pile, he can develop models to predict the flow and transport behaviour of the field pile, provided that the composition of the field pile is known, either deterministically or probabilistically.

3.8 SUGGESTIONS FOR FUTURE EXPERIMENTERS

Based on our experience in conducting the large column experiments, the following suggestions for improvements are offered to researchers who are interested in carrying on similar experiments. It is realised that these improvements requires investments of great financial and human resources, which have to be justifiable by the research objectives.

- First, the time resolution of the experiment may be increased. As mentioned in Section 2.6 , the present experiments were carried out in a "batch mode" and consequently generated "batch data". However, from the point of view of quantifying the internal geochemical, hydrologic, and solute transport processes and of modelling these processes, instantaneous data would be preferred. Examples of instantaneous data are instantaneous flow rates, instantaneous elemental concentrations, instantaneous pH, etc., which are measured on the drainage at the moment of exiting the waste rock bed. It is recognised that truly instantaneous measurements are impossible to make; the word "instantaneous" as used in this context is taken to mean measurements made in very short time intervals, such as seconds, instead of the 30 min to several hours used in this study. Collection of instantaneous data would require elaborate instrumentation and experimental design which enable the measurements of physicochemical parameters on tiny quantities of solution. The benefits of better time resolution are more accurate hydrographs and chemographs for both individual port and the whole-column, which provide the basic data for mathematical modelling.

- Second, the spatial resolution of the experiment may be improved. The drainage partitions at the base of the rock bed may be made smaller. The benefit of this is a more accurate measurement of the cross-sections intercepting flow channels and better resolution in differentiating closely-spaced flow channels.

- Third, the scale of the experiment may be enlarged. The benefit of this is to increase the experiment's representativity of the REV.

- Fourth, the method for identifying "breakthrough time" may be refined. The identification of drainage breakthrough in the present study had a degree of arbitrariness and only one breakthrough time was designated for all drainage ports. To improve the accuracy of individual port hydrographs and chemographs, the drainage breakthrough should be identified separately for each individual drainage port as the time when solution starts to flow in that port. The identification of these individual breakthrough times would require instrumentation capable of monitoring flow continuously in every drainage port.

4.0 HYDROLOGIC AND SOLUTE TRANSPORT MODELING

4.1 INTERNAL STRUCTURE OF WASTE ROCK PILES

Discussions of the internal structure of waste rock piles are available elsewhere (e.g., Morin et al., 1991; Smith et al., 1995) and will not be repeated here. The purpose of this section is to discuss the basic component structures of waste rock piles.

4.1.1 Channelling Flow Rock and Porous Media Flow Rock

4.1.1.1 Clarifications and Explanations

In this report, waste rock is classified into two categories according to the driving force for the flows in them: (1) channelling flow rock, in which the dominant driving force is gravitational potential alone, and (2) porous media flow rock, in which the dominant driving forces are gravitational potential and capillary potential. What driving force dominates is predicted from the properties of the waste rock. In this sense, the waste rock classification is made entirely on the properties of the waste rock.

It is recognised that the flow regime (i.e., channelling flow or porous media flow) in a given waste rock may be determined by factors other than the properties of the waste rock alone, such as the flow flux. For example, the flow regime in a given waste rock may be channelling flow at a low flow flux, but it may become porous media flow when the flow flux is greatly increased. This argument implies that the classification method proposed here may not be deterministic. To rectify this situation, we limit the scope of applicability of this classification scheme to the conditions of unsaturated flows in waste rock structures, such as those that prevail in typical mining waste rock piles and dumps.

The term “porous media flow” used in this report is defined as the flow that is governed by Richards’ equation (see Section 4.1.1.3). It is relative to the term “channelling flow”, which cannot be described by Richards’ equation at all.

Under unsaturated flow conditions prevailing in typical field waste rock piles, a “channelling flow rock” would conduct infiltrating water by means of channel flows, whereas a “porous media flow rock” would conduct infiltrating water by means of “porous media flows” as governed by Richards’ equation. This is the whole intention of the waste rock classification proposed here.

4.1.1.2 Channelling Flow Rock

Channelling flow rock (CFR) is defined as a broken rock aggregate material in which unsaturated water flows are driven by gravity alone and are not subject to capillary forces.

It is impossible to predict the unsaturated flow of water within CFR at the microscopic (particle) level from fundamental principles of physics, mainly due to the complexity of the many forces resisting the flow (for proof see APPENDIX X). On the macroscopic (particle aggregate) level, today's science has not found an empirical law (analogous to Richards' equation in unsaturated porous media flows) that governs the unsaturated flow of water within CFR. Consequently, the study of unsaturated flows in CFR is without the help of quantitative laws. At the present time, quantification of such flows must rely on stochastic approaches.

The modes of water flows and water retention on individual CFR particles have not been studied extensively. They are probably similar to those on the particles in a trickle bed reactor, depicted in Figure 4-1 (Ng and Chu, 1987). Apparently, which mode of flow dictates on a specific rock particle would depend on a suite of parameters, including the particle size, particle shape, surface roughness, surface slope, flow rate, recent wetting history, and ways of contact with neighbouring particles. The relationship between different flow modes and water retention modes on individual CFR particles and the macroscopic phenomenon of channelling has not been addressed in the literature.

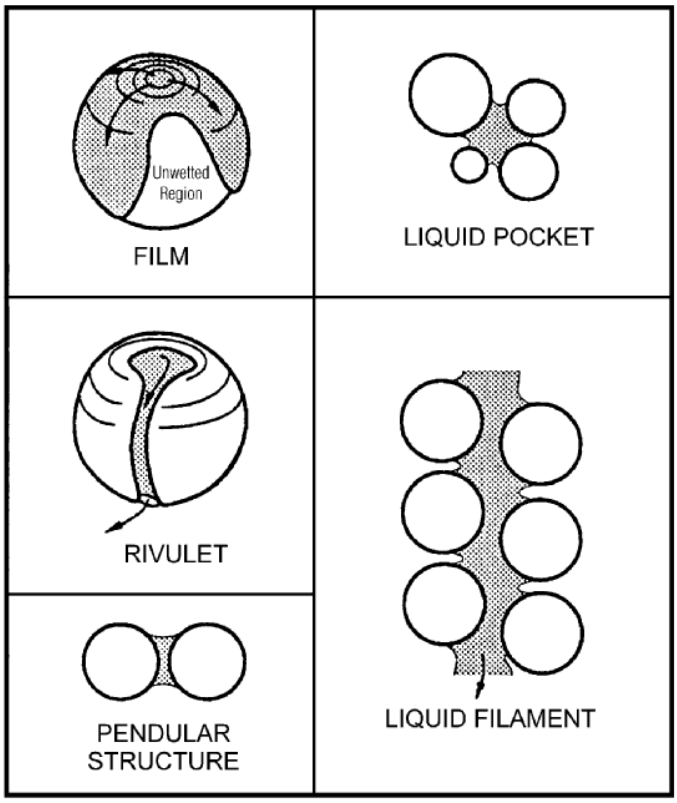

Figure 4-32 Modes of Water Flow and Retention in Trickle-Bed Reactors

(after Ng, 1987)

4.1.1.3 Porous Media Flow Rock

Porous media flow rock (PMFR) is defined as the broken rock aggregate material in which the unsaturated flow of water is driven by soil-water potential and is governed by Richards' equation:

$$\frac{\partial}{\partial x}\left[K_x(y)\frac{\partial y}{\partial x}\right]+\frac{\partial}{\partial y}\left[K_y(y)\frac{\partial y}{\partial y}\right]+\frac{\partial}{\partial z}\left[K_z(y)\left(1+\frac{\partial y}{\partial z}\right)\right]=C(y)\frac{\partial y}{\partial t}$$

where

x, y, z, t are spatial and time co-ordinates,
$K_x(y), K_y(y), K_z(y)$ are directional hydraulic conductivity as a function of capillary pressure ψ, and
$C(\psi) = \partial\theta/\partial\psi$ is the specific moisture capacity.

Since soil-water potential consists of gravitational potential and capillary potential, unsaturated flows in PMFR are driven by both gravitational forces and capillary forces.

Due to the presence of a quantitative law, it is much easier to model flows in PMFR than to model flows in CFR. Channelling effects in a predominantly PMFR are weak and can often be neglected.

4.1.2 Particle Size Boundary between CFR and PMFR

Particle size is used to differentiate channelling flow rock (CFR) from porous media flow rock (PMFR) as defined previously. For the simple case of single-size rock particle aggregates, the boundary that separates CFR from PMFR is the particle size greater than which the capillary potential becomes negligible. Interpretation of the results of Elboushi (1975) indicates that capillary water retention starts to take effect at a size of about 10 mm and becomes fully effective at about 0.2 mm. “Fully effective” here means that water would not flow before the moisture content of the rock particle bed reaches its water retention capacity. Therefore, his work suggests that the grain size boundary for single-size rock particle aggregates could be 10 mm.

The particle size boundary of 10 mm derived for single-sized particles can probably be safely extended to multi grain size aggregates as follows: rock particle aggregates with a minimum grain size of about 10 mm are CFR; rock particle aggregates with a maximum grain size of about 10 mm are PMFR.

In realistic broken rock materials whose particle size ranges from well below 10 mm to well-above 10 mm, the differentiation between CFR and PMFR becomes difficult. The CFR and PMFR can

probably be taken as having similar meanings as the “rock-like” and “soil-like” materials referred to by Smith et al. (1995). Their literature survey results indicate that the boundary between “rock-like” and “soil-like” materials is 10-30% sand (-2 mm) content. Unfortunately, this “boundary” itself encompasses a fairly wide range into which many rock materials fall into, and thus cannot be classified as either category.

To extend the 10-30% sand content criteria for differentiating CFR and PMFR, one can apply the following rules:

- Rock materials with less than 10% sand content are CFR.
- Rock materials with greater than 30% sand content are PMFR.
- Rock materials with sand content between 10-30% cannot be classified as either.

The Stratmat waste rock used in the large column study has an overall sand content of 20%, which unfortunately makes it an unclassifiable material according to the above rules. From the evident channelling effects observed in the experiments, the author is inclined to classify this material as a channelling flow rock, although it may be only marginally so.

The classification rules above are meant for well-blended rock materials, not materials that are segregated. In addition, other physical properties of rock materials may affect their classification, thus these rules are not absolute and should be applied with discretion.

4.1.3 Basic Component Structures of Waste Rock Piles

Field waste rock piles are complex structures, and are normally macroheterogeneous. In this section, we attempt to show that all waste rock piles may be partitioned into regions having one of the five basic rock structures illustrated in Figure 4-1:

a. Continuous channelling flow rock (CCFR), which is a well mixed CFR.

b. Porous media flow rock pocket suspended in continuous channelling flow rock, or PMFRP/CCFR, where the CFR has continuity whereas the PMFR pockets are isolated.

c. Channelling flow rock pocket suspended in continuous porous media flow rock, or CFRP/CPMFR, where the PMFR has continuity whereas the CFR pockets are isolated.

d. Continuous porous media flow rock (CPMFR), which is a well-mixed PMFR.

e. Low permeability plate or pan (LPP), which is a laterally-spreading thin strata with a very low hydraulic conductivity.

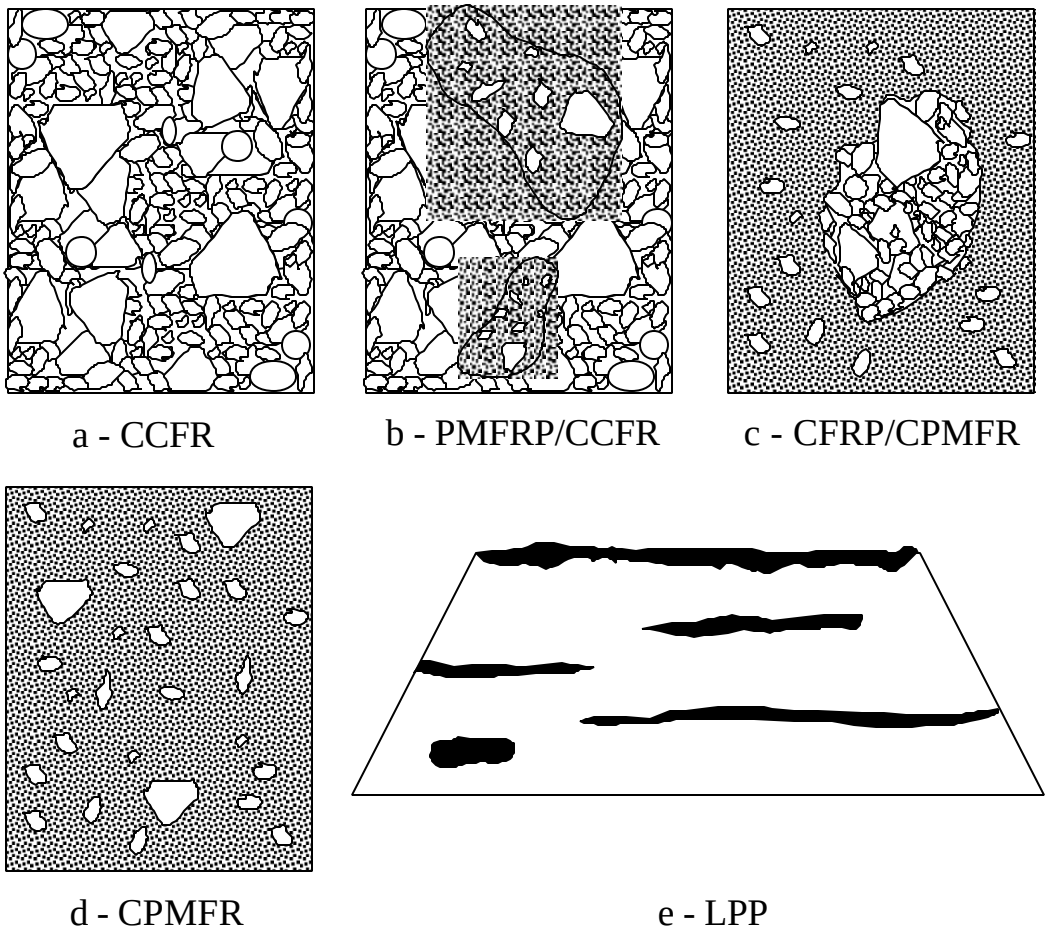

Figure 4-23 Five Basic Component Structures of Waste Rock Piles

Of these five basic component structures, CCFR and CPMFR are mesoheterogeneous, whereas PMFRP/CCFR, CFRP/CPMFR, and LPP are macroheterogeneous. Various combinations of the five basic component structures can occur in field waste rock piles. In some cases one or two may be dominant; in other cases all five may coexist in different regions.

PMFRP/CCFR is actually a small CPMFR dispersed in background CCFR, whereas CFRP/CPMFR is a small CCFR dispersed in background CPMFR. When the pockets become large in extent, they should be treated as CPMFR and CCFR, respectively.

CCFR structures are normally formed in one of two ways: direct deposit of CFR and size segregation when waste rock is constructed. PMFRP/CCFR and CFRP/CPMFR structures could result from load-to-load or blast-to-blast variations of the waste rock material and lack of blending. CPMFR normally results from direct dumping of well blended fine rock. It could also be the upper layer product of size segregation.

LPP is usually a result of mining traffic compaction at successive lift surfaces and access ramps. It could also be due to other causes such as rapid physical and chemical weathering of surface rock,

chemical precipitation, and cementation (hardpans). LPP's are normally horizontal structures but can also be angled and bulky. For a rock material to qualify as LPP, its saturated hydraulic conductivity should be smaller than 10^{-4} - 10^{-5} cm/s. In other words, if on surface it should be able to cause ponding or runoff for a precipitation such as a 24-hour, 100-mm rainstorm. Without heavy compaction, chemical precipitation, or cementation, normal blasted waste rock originating from open-pit mining usually cannot meet the threshold of LPP, and this is true even for the segregated fines.

4.1.4 Factors and Processes Influencing Flows in Component Rock Structures

4.1.4.1 Continuous Channelling Flow Rock

In CCFR, flow heterogeneity in the form of channelling would be a main feature. Quantitative laws describing flows in CCFR have not been established. Hence channelling is normally studied empirically with statistical or stochastic approaches. The main reasons causing channelling probably include, deterministically,

- uneven rain water distribution at the surface,
- the tendency of water flow to follow the lowest resistance route,
- the tendency of fluid to form “rivulet” or “filament” flows rather than “film” and homogeneous bulk flows due to the surface tension of water and hydrophobicity of some rock particles,

and stochastically,

- “random walk” due to the random arrangements and random contacts among channelling flow rock particles,
- “random umbrella effects” (Figure 4-1) due to the presence and random locations of large rock particles (boulders and large pebbles).

Important factors influencing the flow in CCFR include its shape, orientation, spatial extent, size distribution, size segregation, etc.

Presently, flows in CCFR are principally modelled with the following approaches:

- kinematic wave approximation
- stochastic processes
- chemical engineering approaches (reactor in series, reactor in series with dead spaces and/or recirculation, Turner's flow structure, etc.)
- others

4.1.4.2 Continuous Porous Media Flow Rock

Unsaturated flows in CPMFR belongs to the well-established domain of unsaturated flows in soils, which is quantitatively described by Richards' equation, with the addition of “umbrella effects” (Figure 4-1) due to the presence of isolated large rock particles. The study of this rock relies on the determination of the inter-relationships among moisture content, soil-water potential (or pressure), and hydraulic conductivity.

Important factors influencing unsaturated flows in CPMFR include its shape, orientation, spatial extent, structural heterogeneity due to size segregation and lack of blending.

Modelling of unsaturated flows in CPMFR can be done using the Richards' equation, kinematic wave theory, and others.

4.1.4.3 Porous Media Flow Rock Pockets and Channelling Flow Rock Pockets

PMFRP/CCFR produces the “sponge effect” (Figure 4-1): when flow channels are intercepted by a porous media flow rock pocket, the pocket absorbs water at a rate that can be described by the theory of infiltration developed by Philip (1957). If the total channel flow rate is greater than the infiltration capacity of the pocket, part of the channel flows will run off and around the pocket and carry on as a smaller channel flow underneath the pocket. If the channel flow rate is smaller than the infiltration capacity of the pocket, the entire channel flow would be used to recharge the moisture in the pocket. After that drainage will appear at the bottom of the pocket and continue as a channel flow. Unsaturated flows in PMFRP/CCFR can be modelled as those in CCFR with a provision to deal with the sponge effect.

CFRP/CPMFR causes a “bubble effect” (Figure 4-1). Moisture movement in the continuous porous media flow rock tends to avoid entering the channelling flow rock pocket and migrates around it because the CPMFR is at a lower soil-water potential than the CFRP due to capillary action. This creates a “bubble” devoid of water flows in the pocket. The bubble effect will cause the water flux to rise in the areas surrounding the pocket because of the reduction in the cross-sectional area available to flows. Unsaturated flows in CFRP/CPMFR structures can basically be modelled as those in CPMFR with provisions to deal with the bubble effect.

4.1.4.4 Low Permeability Pans (Plates)

The main effects of LPP’s are as follows:

- On the surface and in the interior of a waste rock pile they cause re-distribution of the rain water or infiltrating water into a much more uneven pattern through “running off”, “blanketing”, “funnelling”, and “day-lighting” (Figure 4-1), contributing to the occurrence of strong channelling

effects.

- LPP's reduce the proportion of total precipitation infiltrating into the waste rock pile by incurring surface runoff and day-lighting, and by increasing evaporation through surface ponding of water.

- Ponding and perched water tables retard the flow of water through the pile (i.e., flattening of the drainage hydrograph).

- LPP's terminate and re-initiate flow channels by blanketing and funnelling.

No modelling efforts have been documented in the literature to account for the presence of LPP's. The difficulty lies in the mapping of LPP's in the waste rock pile, which is practically impossible to do in the field.

The overwhelming feature of LPP's is the redistribution of water on the surface and in the interior of waste rock piles. This must be taken into consideration for realistic modelling of unsaturated flows in field waste rock piles. When detailed mapping of LPP's is unavailble, the appearance of LPP's can probably be treated stochastically.

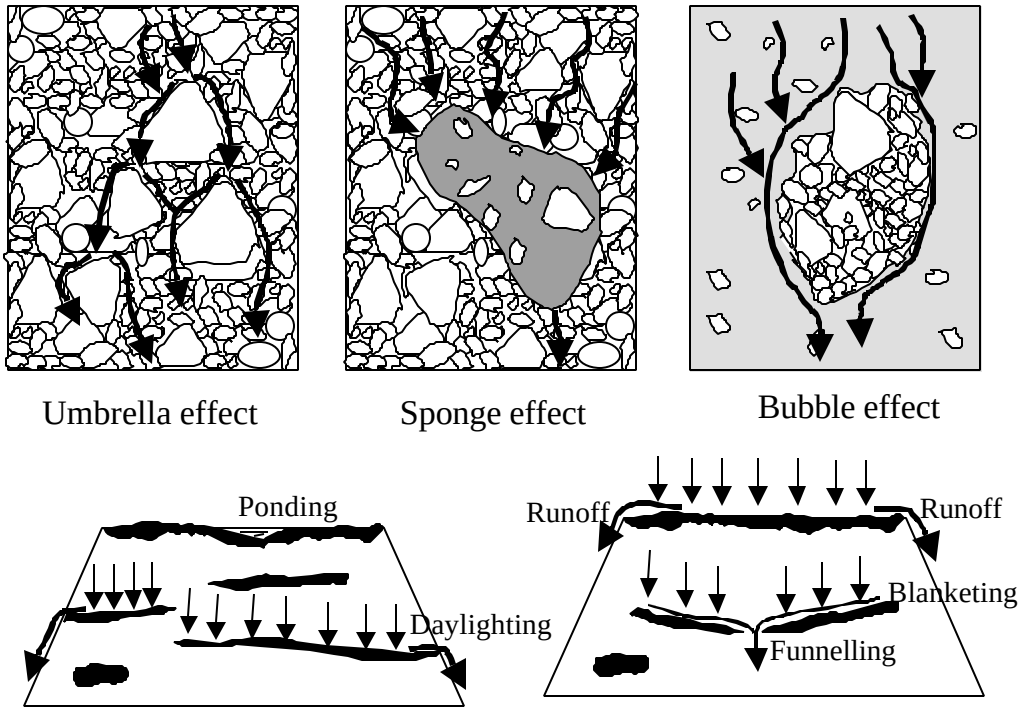

Figure 4-24 Some Flow Processes in Waste Rock

4.1.4.5 Summary

The main factors and processes influencing unsaturated flows in the five basic component structures of waste rock are summarised along with their effects in Table 4-1. Modelling approaches instead of specific models are indicated in the table with representative references.

4.1.5 Field Waste Rock Piles

The number of ways in which the five basic structures are combined in the field to form waste rock piles is unlimited; so are the kinds of waste rock pile configurations in the field. On the other hand, any existing field waste rock pile can be decomposed, theoretically, into uni-structural regions using the five basic component structures. Figure 4-1 shows a two-dimensional example (in practice this would be in 3-D). The difficulty in doing so is usually the lack of necessary data, which can be very expensive to gather for complexly-structured waste piles. An alternative is to lower the accuracy requirement and decompose the waste rock pile approximately with existing information and the help of the mining engineer who has constructed the waste rock pile.

Once a waste rock pile is decomposed, there are a number of ways to proceed with flow modelling and solute transport modelling. If the decomposition shows that the waste rock pile is dominated by one basic structure, the whole pile can be modelled according to the main processes and factors for that basic structure (Table 4-1). If the decomposition shows that the pile is a complex assembly of several basic structures, one can

- Model it using the detailed decomposition. In this case, each basic structure region has to be separately modelled and logically linked. This exercise could become very complicated and the linking between different regions may not always be achievable.

- Simplify the decomposition until an acceptable compromise is reached between the modelling effort and result accuracy or until the complexity is handlable. This can be done by dropping the less important details of the decomposition. Modelling can then proceed with the simplified version of the waste rock decomposition.

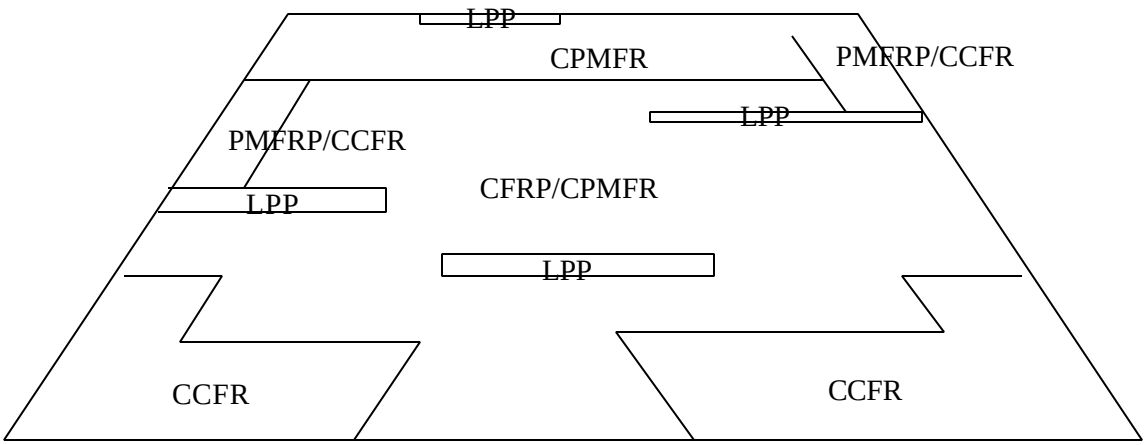

Figure 4-25 Decomposition of a Waste Rock Pile into Basic Component Structure Regions

Table 4-1 Factors and Processes Affecting Flows in Basic Waste Rock Structures

Basic Structure	Main Processes and Factors	Feature Effects	Quantitative Governing Law	Potentially Applicable Modelling Approaches	Modelling Approach Reference
CCFR	Processes: surface and internal water re-distribution, gravity flows by least resistance routing, random walk, umbrella effects Factors: shape, orientation, spatial extent, size distribution, size segregation, rock physical and chemical properties, rain characteristics	Channelling	None	Kinematic wave theory Chemical engineering Stochastic Statistical Geostatistical Fractal	Germann, Smith, Singh Levenspiel, Dixon, Ng Gelhar, Erriksson, Schlitt Gelhar Gelhar
PMFRP/CCFR	Processes: processes for CCFR, processes for CPMFR, sponge effect Factors: factors for CCR and CFR	Channel termination and re-initiation Retardation of flow	Same as for CPMFR	Those for CCFR with provisions for sponge effect	Same as for CCFR
CFRP/ CPMFR	Processes: processes for CPMFR, processes for CCFR, bubble effect Factors: factors for CPMFR and CCFR	Increased flow flux around CFRP	Same as for CPMFR	Those for CPMFR with provisions for bubble effect	Same as for CPMFR
CPMFR	Processes: unsaturated flow in soils, umbrella effect Factors: shape, orientation, special extent, structural heterogeneity, rock physical and chemical properties, rain characteristics	Lack of significant channelling	Richards' equation Philip's infiltration theory	Richards' equation Kinematic wave theory Stochastic Statistical	Soil science textbooks Singh Gelhar Gelhar
LPP	Processes: ponding, runoff, daylighting, blanketing, funnelling Factors: shape, orientation, special extent, position, hydraulic conductivity	Water re-distribution, channel termination and re-initiation	Darcy's law Richards' equation Philp's theory	LPP position mapping Stochastic positioning	None

4.2 MATHEMATICAL REPRESENTATION

4.2.1 Channel Flows

4.2.1.1 Cumulative Distribution Function and Density Function of Flow Density

Suppose a waste rock pile is intercepted by an imaginary horizontal plane at an arbitrary depth z below the pile surface (which is at z = 0, Figure 4-1). Imagine that the plane has on it a pre-drawn square grid defining many equal squares of side lengths Δx, Δy where $\Delta x = \Delta y$, and area $\Delta A = \Delta x \cdot \Delta y$. The area of intersection of the waste rock pile by the plane is A, and the total number of squares in the intersection is $N = A/\Delta A$.

During a drainage event, at time t, the flow rate of water across an arbitrarily selected square on the plane is Q(z,t), and the total flow rate across the entire plane is $Q_T(z, t)$. The *relative flow rate* across the square is $Q_R(z,t) = Q(z,t)/Q_T(z, t)$.

The *volumetric flux*, or *flow density*, of water across the square is defined as $q(z,t) = Q(z,t)/\Delta A = Q(z,t)/(\Delta x \cdot \Delta y)$. The *relative flow density* of water across the same square is defined as $q_R(z,t) = Q_R(z,t)/\Delta A = Q_R(z,t)/(\Delta x \cdot \Delta y)$.

Now for a given value of $q(z,t) \in [q_{min}, q_{max}]$, we count the number of squares across which the flow density is less than or equal to q(z,t) and suppose that number is n[q(z,t)]. It is a function of q(z,t). The function

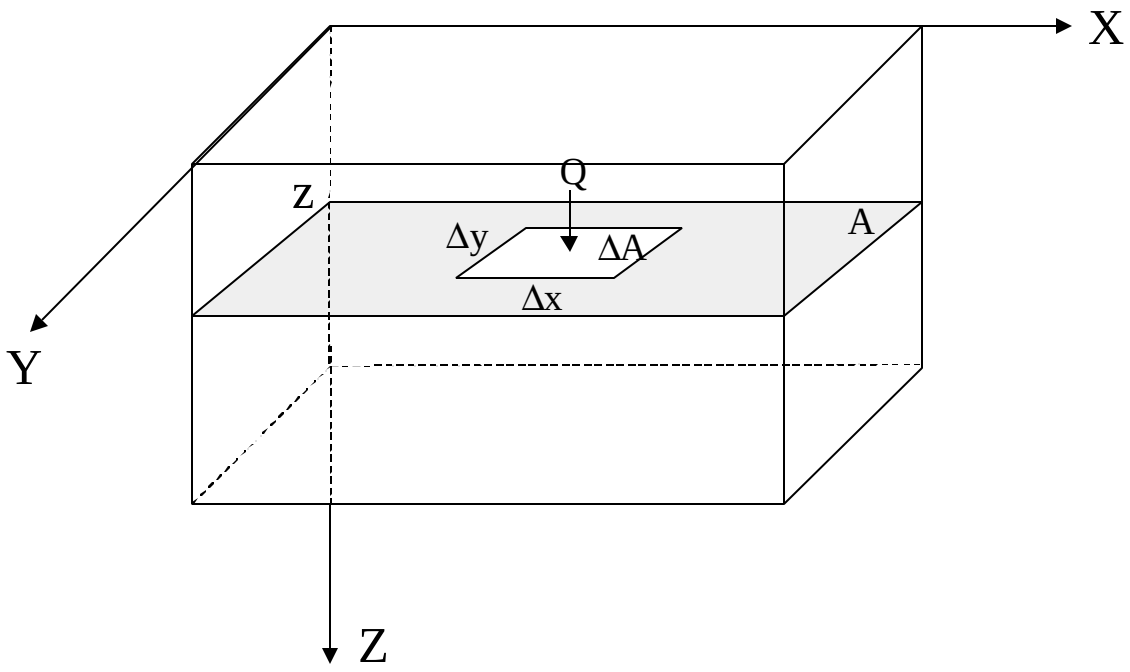

Figure 4-30 Simplified Representation of Waste Rock Dump

$$F(q,z,t)=\lim_{\Delta x\to 0,\Delta y\to 0}\frac{n[q(z,t)]}{N}=\lim_{\Delta A\to 0}\frac{n[q(z,t)]}{N} \qquad \text{Equation 4-1}$$

is defined as the *cumulative flow density distribution function*, or CFDDF. Its interpretation can be stated as one of the following three, which are equivalent:

- It gives, for any value of q = q', the number of squares as a percentage of the total number of squares that carry a flow density less than or equal to q'.
- It gives, for any value of q = q', the area as a percentage of the total area *A* that carries a flow density less than or equal to q'.
- It gives, for any value of q = q', the number of q values as a percentage of the total number of q values that are less than or equal to q'.

Holding z and t constant and solve for q in F(q,z,t), we obtain the inverse function of F with respect to q,

$$q(F,z,t)=F_q^{-1}(q,z,t) \qquad \text{Equation 4-2}$$

The meaning of q(F,z,t) is this: for any given percentage of the total area F, q(F,z,t) gives the flow density such that all the flows that have a flow density less than or equal to that occupy a percentage of the total area equal to F.

The density function of flow density, DFFD is defined as

$$f(q,z,t)=\frac{\partial F(q,z,t)}{\partial q}=\left.\frac{dF}{dq}\right|_{\text{z, t=constant}} \qquad \text{Equation 4-3}$$

Apparently, we have

$$F(q,z,t)=\int_0^q f(t,z,t)dt \qquad \text{Equation 4-4}$$

$$F(q_2,z,t)-F(q_1,z,t)=\int_{q_1}^{q_2} f(q,z,t)dq \qquad q_2>q_1 \qquad \text{Equation 4-5}$$

$$F(q_{\max},z,t)=\int_0^{q_{\max}} f(q,z,t)dq=1 \qquad \text{Equation 4-6}$$

The meaning of f(q,z,t) is that, at time t and depth z, the percentage area across which the flow density is within a very small interval of dq centred around q is f(q,z,t)dq.

It follows that the total flow rate across the plane at depth z and time t carried by flows having flow densities between q_1 and q_2 is

$$Q(q \in [q_1, q_2], z, t) = A\int_{q_1}^{q_2} q\, f(q,z,t)\, dq \qquad \text{Equation 4-7}$$

The total flow rate across the plane at depth z and time t is

$$Q_T(z,t) = A\int_0^{q_{max}} q f(q,z,t)\, dq \qquad \text{Equation 4-8}$$

which for $z = z_{max}$ (the height of the pile) gives the base drainage hydrograph.

The total drainage flow discharged from the waste rock pile during the drainage event is given by

$$V_T = A\int_0^T \int_0^{q_{max}} q f(q, z_{max}, t)\, dq dt \qquad \text{Equation 4-9}$$

where T is the duration of drainage discharge.

The percentage of total drainage flow rate $Q_T(z,t)$ accounted for by all the flows having flow densities less than or equal to q, denoted by $\sigma(q,t)$, is given by

$$s(q,t) = \frac{Q(q \in [0,q], t)}{Q_T(t)} = \frac{\int_0^q t\, f(t,t)\, dt}{\int_0^{q_{max}} q f(q,t)\, dq} \qquad \text{Equation 4-10}$$

where the variable z is dropped because only bottom drainage is considered, $z=z_{max}$=constant. We can plot the function $\sigma(q,t) = \sigma(F_q^{-1}(q,t),t) = \sigma(q(F,t),t) = \sigma(F,t)$ on a σ-F plane as a way of expressing channelling phenomena. This plot shows the percentage of the total flow carried by all flows having a flow density less or equal to q against the percentage of total drainage area carrying flows having flow densities less than or equal to q. Figure 3-1 is a plot of this kind (albeit the flux is arranged in reverse order and the z fluxes are disregarded).

The above discussion shows that the DFFD or CFDDF totally characterise the channelling phenomena during a drainage event.

4.2.1.2 Variables Affecting DFFD

Since channelling is a very complex phenomenon, the density function of flow density (DFFD) is affected by many factors. This can be expressed in the following form:

$$f(q,z,t) = f\left(p(x,y,t), E(x,y,t), RO(x,y,t), PO(x,y,t), R(x,y,z), G, S(x,y,z), F, T, P\right)$$

Equation 4-1

where

- p(x,y,t) is the input function for the precipitation prior to a drainage event. If the rain is spatially homogeneous on the waste rock pile, p(x,y,t) = p(t), which is termed a hyetograph. If the rain is steady over time (i.e. a square pulse hyetograph) such as in the large column tests, p(t) = constant for $t \in [0, t_{max}]$, the duration of the precipitation.
- E(x,y,t) is the evaporation function and can normally be ignored due to its small effects.
- RO(x,y,t) is the runoff function and should be considered when surface LPP's are widespread. Otherwise it can be ignored.
- PO(x,y,t) is the surface water ponding function and should be considered when surface LPP's are widespread. Otherwise it can be ignored.
- R(x,y,z) is the rock property function which lumps together all rock properties influencing channelling effects.
- G is the geometry function of the waste rock pile
- S(x,y,z) is the rock pile structure function that describes the type of basic component structure.
- F is fluid property function and for water the effects of this factor can be disregarded.
- T is the temperature function and is often ignored.
- P is the ambient pressure function and is often ignore.

After ignoring unimportant factors and making some reasonable assumptions, Equation 4-1 can be realistically simplified to

$$f(q,z,t) = f\left(p(t), RO(x,y,t), R(x,y,z), S(x,y,z)\right)$$

Equation 4-2

For an existing waste rock pile, R(x,y,z) and S(x,y,z) are fixed and do not vary within a short period of time, the above equation reduces to

$$f(q,z,t) = f\left(p(t), RO(x,y,t)\right)$$

Equation 4-3

For typical waste rock piles, the surface is permeable and RO is normally zero, then

$$f(q,z,t) = f\left(p(t)\right)$$

Equation 4-4

Rewriting the functional form and consider only bottom drainage,

$$f(q,t) = f\left(p(t), z_{max}\right) \qquad \text{Equation 4-5}$$

That is, the bottom drainage channelling is a function of precipitation. For an existing pile z_{max} is fixed, we have

$$f(q,t) = f\left(p(t)\right) \qquad \text{Equation 4-6}$$

That is to say that the channelling phenomena for an existing dump is primarily a function of precipitation alone.

When we generally study how channelling effects vary from one waste rock pile to another, we must use the functional expression of Equation 4-1.

4.2.1.3 Experimental CFDDF and DFFD

The CFDDF and DFFD are defined on the basis of $\Delta x \rightarrow 0$ and $\Delta y \rightarrow 0$, which is impractical to test experimentally. Experiments must be designed to use finite Δx and Δy and in such a case the CFDDF and DFFD derived from experimental data are approximations. This applies to the large column experiments reported here.

The data for Column 1 Run 2 (C1R2) were selected to derive CFDDF and DFFD. The CFDDF and DFFD are determined for the intervals 30 min, 90 min, and 180 min. The resulting functions are exhibited in Figure 4-1 and Figure 4-2.

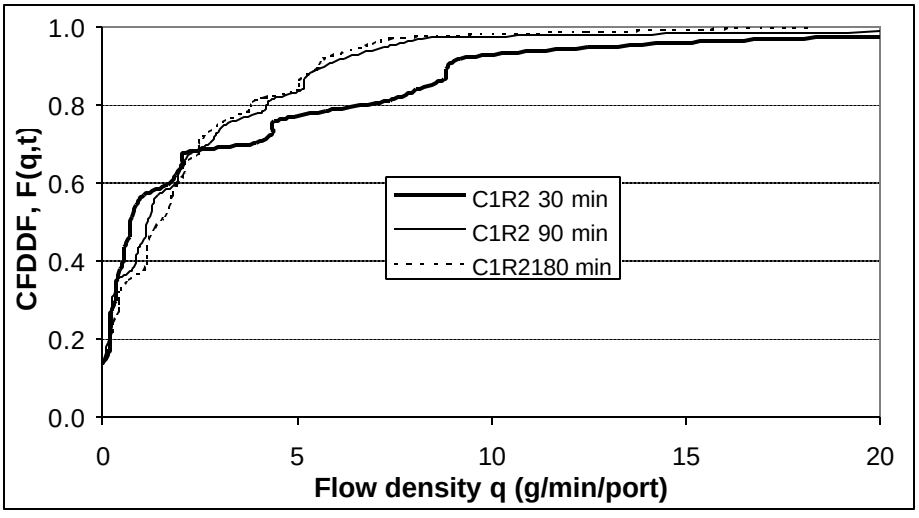

Figure 4-6 Experimental CFDDF Determined Using C1R2 Data

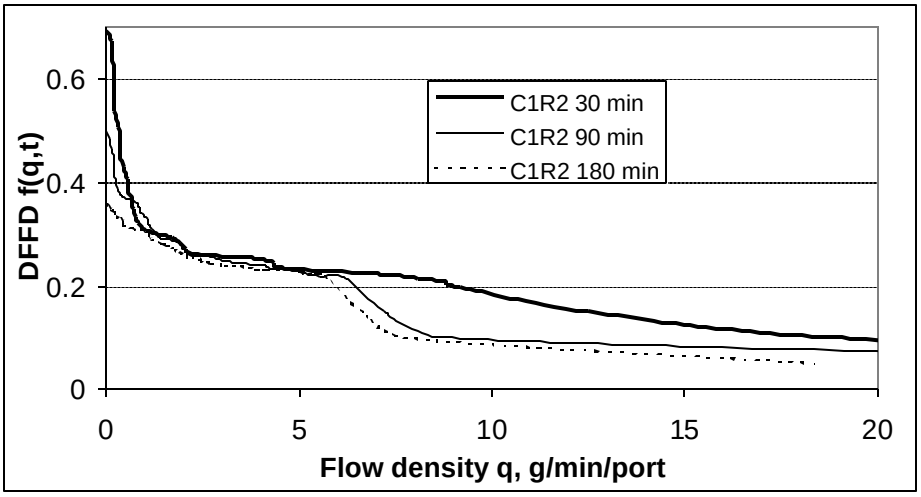

Figure 4-7 Experimental DFFD Determined Using C1R2 Data

The CFDDF shows a "nugget" effect, i.e., at q = 0 it has a non-zero value. For the three curves shown, this value is 0.14, which means that 14% of the total drainage area does not have flow at all. The DFFD function has a steep negative slope at low q's and flattens out at high q's. This means that there are many flows with small flow densities (e.g., q < 1) and much fewer flows with high flow densities (e.g., q >10).

4.2.2 Solute Transport

Let C be the concentration of the solute (e.g., dissolved Zn or SO_4^{2-}). For the simplest case where $C = constant = C_0$, the solute flux J (mass per unit time, e.g., moles per second) as a function of time during a drainage event is

$$J(t) = C_0 Q_T(t) = C_0 A \int_0^{q_{max}} qf(q,t)dq \qquad \text{Equation 4-1}$$

(The variable z is dropped because $z \equiv z_{max}$ for bottom drainage thus no longer a variable. The same argument applies hereafter.)

The total solute loading L_T for the drainage event is given by

$$L_T = C_0 V_T = C_0 A \int_0^T \int_0^{q_{max}} q f(q,t)dqdt \qquad \text{Equation 4-2}$$

For the case where the *solute concentration is a function of q and t*, C=C(q,t), the flux and loading are respectively

$$J(t) = A\int_0^{q_{max}} qf(q,t)C(q,t)dq \qquad \text{Equation 4-3}$$

$$L_T = A\int_0^T \int_0^{q_{max}} q\,f(q,t)C(q,t)dqdt \qquad \text{Equation 4-4}$$

Specifically, if the *solute concentration is inversely proportional to the flux q*, as it may be sometimes, we have C = K/q where K is a constant. Substituting into the above two equations, we obtain the following results:

$$J(t) = A\int_0^{q_{max}} qf(q,t)\frac{K}{q}dq = AK\int_0^{q_{max}} f(q,t)dq = AK \qquad \text{Equation 4-5}$$

$$L_T = A\int_0^T \int_0^{q_{max}} q\,f(q,t)\frac{K}{q}dqdt = AKT \qquad \text{Equation 4-6}$$

That is, the solute flux does not change over time during the drainage event and is simply equal to the product *AK*.

Finally, the solute concentration C sometimes cannot be related to any other variable. In these cases it can be regarded as a *random variable* **C** for any fixed time t. For the duration of the drainage event, t changes from 0 to t_{max}, and the solute concentration becomes a random function **C**(t). The flux also becomes a random function:

$$\mathbf{J}(t) = A\mathbf{C}(t)\int_0^{q_{max}} qf(q,t)dq \qquad \text{Equation 4-7}$$

and the total solute loading becomes a random variable:

$$\mathbf{L}_T = A\int_0^T \mathbf{C}(t)\int_0^{q_{max}} q\,f(q,t)dqdt \qquad \text{Equation 4-8}$$

4.2.3 Application of Mathematics of Channelling to Large Column Data

The mathematics of channelling and solute transport developed in Sections 4.2.1 and 4.2.2 can be applied to the large column data. This would involve investigating the functional forms of f(q,z,t) and how f(q,z,t) is influenced by the variable assemblies shown on the right side of the following

equation:

$$f(q,z,t) = f\left(p(t), RO(x,y,t), R(x,y,z), S(x,y,z)\right) \qquad \text{Equation 4-2}$$

However, this is beyond the scope of this report.

The ultimate goal of the research on channelling and solute transport would be to develop the capability of

- predicting f(q,z,t) from information on waste rock pile properties and precipitation properties,
- predicting the concentration function C(q,t) or the random concentration function, $\mathbf{C}(t)$,
- using the channelling and solute transport mathematics developed above to predict $Q_T(t)$, J(t) and L_T, or in the case of stochastic modelling, $\mathbf{Q}_T(t)$, $\mathbf{J}(t)$, and $\mathbf{L}_T$.

The application of kinematic wave theory to channelling flow, which will be discussed next, can be considered a special case of Equation 4-12 or Equation 4-16 where the f(q,z,t) (or equivalently F(q,z,t)) is expressed as a function of p(t) using the kinematic wave approximation.

4.3 APPLICATION OF KINEMATIC WAVE MODEL TO EXPERIMENTAL DATA

4.3.1 Description of the Model

The kinematic wave theory was introduced by Lighthill and Whitham (1955) who used the theory to describe flood movement in rivers. The conditions for a kinematic wave are very simple: flux is functionally related to concentration. For example, the greater the number of cars there are in a section of the road per unit length (the concentration), the smaller the number of cars that can pass through (the flux). This would generate a kinematic wave of car concentration in the direction opposite to the direction of traffic. In the case of moisture movement in macropores or channels, the flux (volume of water passing across unit area per unit time) is positively related to concentration (the volumetric moisture content, m^3/m^3, in the flowing macropores or channels). This generates a kinematic wave of moisture moving down.

The word "kinematic" is relative to "dynamic" in the study of motion, and means "without consideration of inertia or energy". So the energy balance of the fluid motion is ignored in the kinematic wave theory. The "wave" is unlike a conventional wave such as those seen on the surface of a water body. Rather, the kinematic wave is one that involves a "jump" (a discontinuity) of a quantity such as flow density q, at a position z_{jump}, that is, $q(z^+_{jump}) = 0$ and $q(z^-_{jump}) = q(t)$. The position of the jump continuously travels, giving rise to the notion of a wave.

Since its introduction, kinematic wave theory has been used in many diversified branches of hydrology including flood flows in rivers, surface watershed flows, subsurface soil flows, irrigation flows,

snow melting, moisture movement in soil, and flows in macropores. Two text books have been written on the application of kinematic wave theory in hydrology (Singh, 1997, 1996).

The application of the kinematic wave theory to macropore flows was due to Germann and Beven (1981a, 1981b, 1985, 1986). Smith et al. (1995) applied the approach developed by Germann and Beven to a drainage flow hydrograph measured at Island Copper Mine, B.C. and showed that kinematic wave theory has potential for describing channel flows existing waste rock piles.

Germann and Beven have given detailed account of the mathematical development of their approach in the references mentioned above. A brief mathematical deduction of the kinematic wave model in the form used in this report is given in APPENDIX XI. A schematic representation of the physical set-up of the model is shown in Figure 4-1.

The kinematic wave model presented in APPENDIX XI describes the flow in a single macropore. To apply the model to field soil that has many macropores of different sizes, shapes, depths, conductances, matrix sorbances, etc., German and Beven (1986) assumes that all the macropores can be classified into n groups, each of which has a distinct conductance b_j, j = 1, 2, … n. The sorbance is assumed constant for all macropore groups. They then proceeded to vary the conductance b_j and abundance (described by ΔA_j) of each channel group to obtain a best fit between the hydrograph predicted by the kinematic wave theory and the observed hydrograph. The physical interpretation of ΔA_j is the proportion of the soil surface that are connected to macropores of group j. This approach, which they referred to as "a (discrete) distribution function approach", reveals a b_j-ΔA_j relationship, which tells the aerial extent of each channel group and the conductance associated with each group. The main equation describing this approach is as follows:

$$q(Z,t) = \sum_{j=1}^{n} \Delta A_j q_j(Z,t) \qquad \textit{where} \quad t \le t_I \qquad \text{Equation 4-1}$$

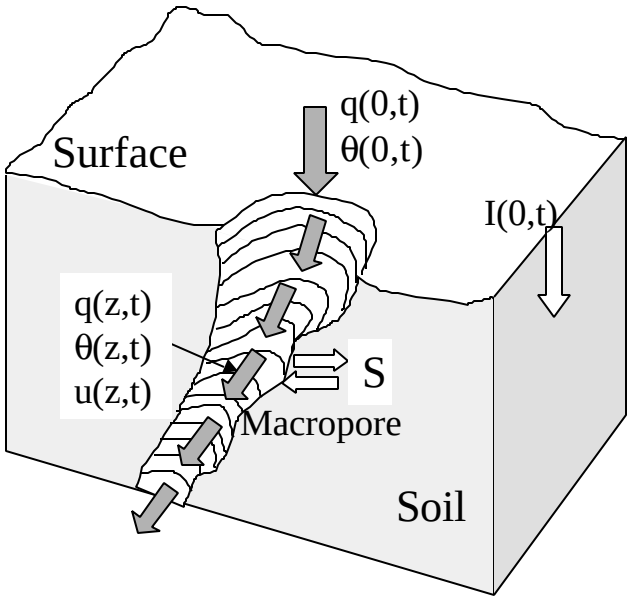

Figure 4-33 Schematic Illustration of Macropore Flow for Kinematic Wave Model

4.3.2 Application to Large Column Data

Smith et al. (1995) used Germann and Beven's approach described above to model drainage flows from a waste rock pile. They treated flow channels in waste rock piles the same way as Germann and Beven treated macropores. According to Smith et al. (1995),

> *In a waste rock pile, there are many different types of channels, rather than a single channel type. The channel system will have a complex pattern of different sizes, shapes, depths, and orientations. Fluid exchange occurs between the different types of channels within the pile. We simplify the complexity of the system by assuming that the pile is formed by multiple independent channels of unknown geometry. In our model, each channel group is characterised by a conductance b_j and a fraction of the surface of surface area of the pile…*

In our application here, we adopt the original approach described in Germann and Beven (1986) and admit the premises of Smith et al. (1995). We attempt here to provide an *independent validation* of the kinematic wave model using the large column results.

The logic for independently validating the kinematic wave model is this: First, the kinematic wave model is applied to a whole-column hydrograph to calibrate the model, that is, to obtain the values of the model parameters specific to the experiment. Second, the calibrated model is used in a predictive mode to calculate CFDDF's for selected points in time. Third, the calculated CFDDF's are compared with experimental CFDDF's for the selected times. Since the model parameters are obtained only from information contained in the whole-column hydrograph and there are an infinite number of CFDDF's that can produce the observed column hydrograph, an agreement between the predicted CFDDF's and the experimentally observed CFDDFs constitutes an independent validation.

The experimental results selected for model validation are those of Column 1 Run 2 (C1R2). The most important reason for its selection is to make the sorbance r = 0. The sorbance r measures the loss of water from flowing channels to the soil matrix. There are many uncertainties associated with r. First, the model assumes r = constant for all channel groups, which is not accurate. Second, it is not measurable. The approach of Germann and Beven, as well as that of Smith et al., is to assume various values of r spanning orders of magnitude, and select the one that produces the most meaningful results. This seriously compromises the validity of the modelling results. The drawback is avoided by making r = 0.

We consider r = 0 for C1R2 because the total water input to the column during this run, 49.7 L, is almost equal to the total amount of water drained for this run, 48.7 L. When water is not retained in the rock bed, it should be reasonable to assume that there is no absorbance of water by the soil

matrix. In addition, C1R2 was run only two days after C1R2. This short period of rest does not allow significant evaporation from the rock bed.

With r = 0, the kinematic wave model equations are greatly simplified. The simplified equations can be obtained by taking limits as r→0 (please consult APPENDIX XI for the meanings of symbols), as follows:

$$z^* = \lim_{r\to 0} \frac{abq_0^{a-1}}{(a-1)r} = +\infty \qquad \text{Equation 4-1}$$

(Because there is no absorbance of the water, the water can theoretically flow down to a depth of infinity if there were no physical limits.)

$$z_W(t) = \lim_{r\to 0}\left[\frac{abq_0^{a-1}}{(a-1)r}\left(1-\exp\left(-\frac{(a-1)rt}{a}\right)\right)\right] = bq_0^{a-1}t \qquad \text{Equation 4-2}$$

$$t_W(z) = \frac{z}{bq_0^{a-1}} \qquad \text{Equation 4-3}$$

$$z_D(t) = \lim_{r\to 0}\left[\frac{abq_0^{a-1}}{(a-1)r}\left(1-\exp\left(-r(a-1)(t-T)\right)\right)\right] = abq_0^{a-1}(t-T) \qquad \text{Equation 4-4}$$

$$t_D(z) = T + \frac{z}{abq_0^{a-1}} \qquad \text{Equation 4-5}$$

$$z_I = \lim_{r\to 0}\left[\frac{abq_0^{a-1}}{(a-1)r}\left(1-e^{-rT}\right)\right] = \frac{abq_0^{a-1}}{(a-1)}T \qquad \text{Equation 4-6}$$

$$t_I = \frac{a}{a-1}T \qquad \text{Equation 4-7}$$

To compute the drainage flow density at a depth $Z \le z_I < z^*$, the following equations are used:

$$0 \le t \le t_W(Z): \quad q(Z,t) = 0$$
$$t_W(Z) \le t \le t_D(Z): \quad q(Z,t) = bq_0^a = q_0 \qquad \text{Equation 4-8}$$
$$t_D(Z) \le t \le t_I \quad q(Z,t) = \left(\frac{Z}{ab^{1/a}(t-T)}\right)^{\frac{a}{a-1}}$$

where q_0 is the precipitation expressed in the same way as flow density q(z,t). Knowing $t_W(z)$ at z and q_0, the conductance b can be solved for:

$$t_W(Z) \le t \le t_D(Z): \qquad b = \left(\frac{Z}{t_W(Z)}\right)^a q_0^{1-a} \qquad \text{Equation 4-9}$$

An important note on the application of the kinematic wave model to observed data is that the experimental hydrograph must be unimodal, and relatively smooth. Since our experimental data show rugged patterns, we fitted the data to some functions that meet these requirements. After testing several functions, we found that two worked well on our data. One is a two-piece quadratic function (one piece for the rising limb and one for falling limb) and the other is a two-parameter gamma distribution:

$$f(x) = \frac{1}{b^a \Gamma(a)} x^{a-1} e^{-\frac{x}{b}} \qquad \text{Equation 4-10}$$

where α, β are function parameters and $\Gamma(\alpha)$ is the gamma function with one parameter, α.

In order to fit the data, the arrival time of the column hydrograph is needed. It was estimated at 120 min. To make the kinematic wave modelling easy to handle, the time t = 0 should correspond to the beginning of the simulated rain application. After the shifting of the time axis, the time shown in the result graphs below is equal to the time used in previous presentations plus 170 min.

The specific data used for the kinematic wave modelling are as follows:

1. q_0 = 1.406E-4 $m^3min^{-1}m^{-2}$ (or m/min).
2. Z = 1.5 m
3. T = 420 min
4. a = 2.5 as recommended by Germann and Beven (1986).
5. t_I = 701 min as calculated by Equation 4-32.
6. t_A = 120 min (the time of arrival on the column hydrograph)
7. Intervals of modelling Δt_1 = 5 min, Δt_2 = 15 min, Δt_j = 30 min for j = 3, 4, …, 20, giving t_1 = 125 min, t_2 = 140 min, t_3 = 170 min, …, t_{20} = 680 min.

4.3.3 Results and Discussion

The results for the decomposition of the observed whole-column hydrograph using the kinematic wave model are shown in Figure 4-1. The experimental data (represented by empty squares) are fitted to a two-piece quadratic function and a gamma function. The gamma function curve was used for decomposition. The two-piece quadratic function curve gives similar but less prefe rable results.

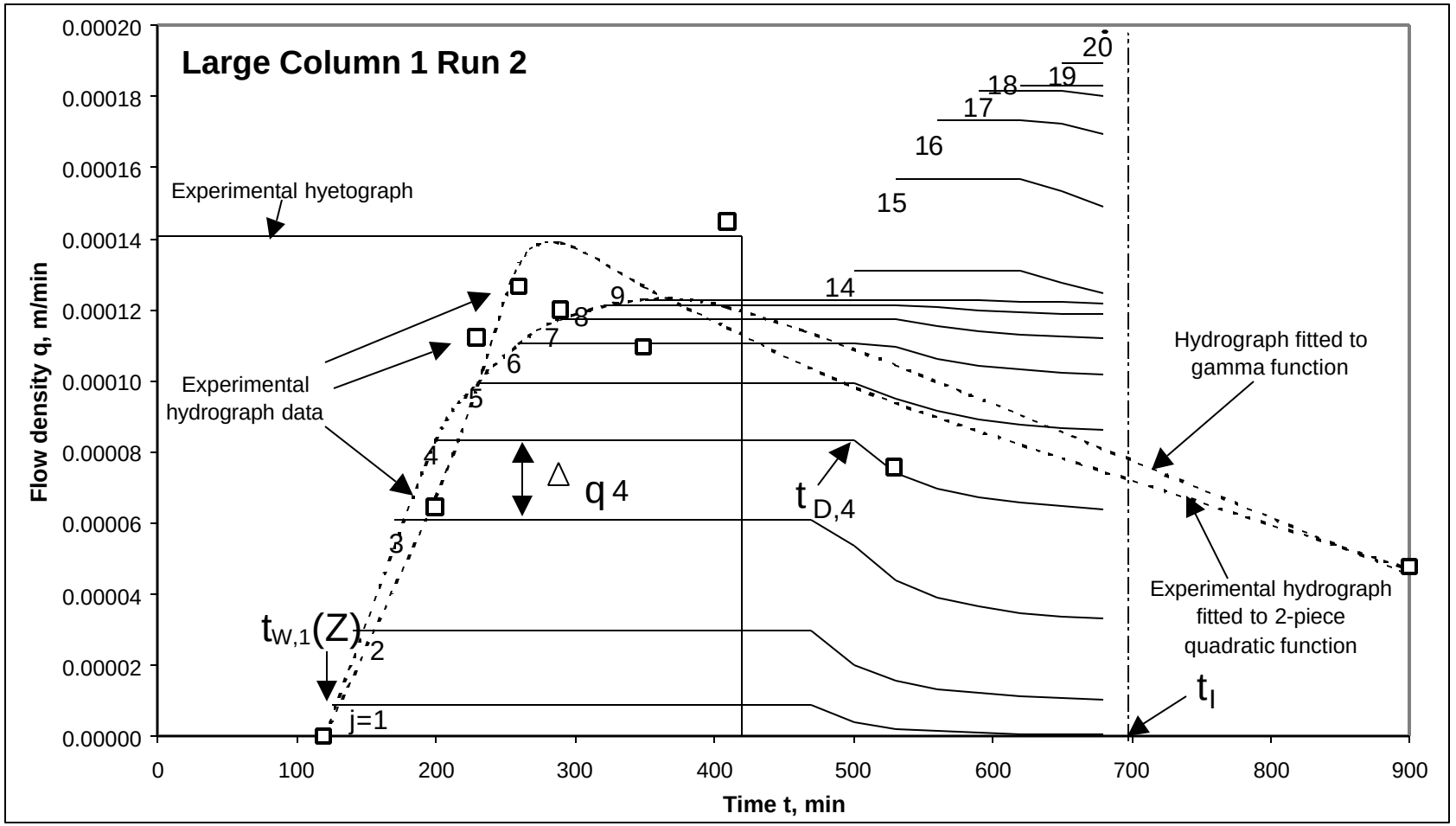

Figure 4-11 Results for Decomposition of Column Hydrograph Using Kinematic Wave Model

The contribution to the total column flow density by each of the 20 component channel groups is represented by a channel group hydrograph, which has a characteristic shape of a flat portion followed by a falling tail. The time of arrival of water in jth channel group is $t_{W,j}(Z)$ and the flow density in this channel group starts to decline at $t_{D,j}(Z)$. The time of interception of the wetting front by the draining front is the same for all channel groups, $t_I \approx 700$ min. The channel group hydrographs are shown additively. The decomposition is such that the sum of all component channel hydrographs is exactly equal to the whole-column hydrograph represented by the gamma function curve.

The distribution of channel conductance b_j given by the kinematic wave model is shown in Figure 4-2. Each point (x,y) on the curve indicates the percentage of the total surface area, y, which is connected to channels with conductances not exceeding x. The graph shows that there is a fairly high percentage (~40%) of the rock bed surface connected to channels with very low conductivity (< 0.2 m/min). About 45% of the surface is connected to channels with a conductivity between 1 and 4.5 m/min. The remaining 15% of the surface are connected to highly conductive channels with b > 5 m/min.

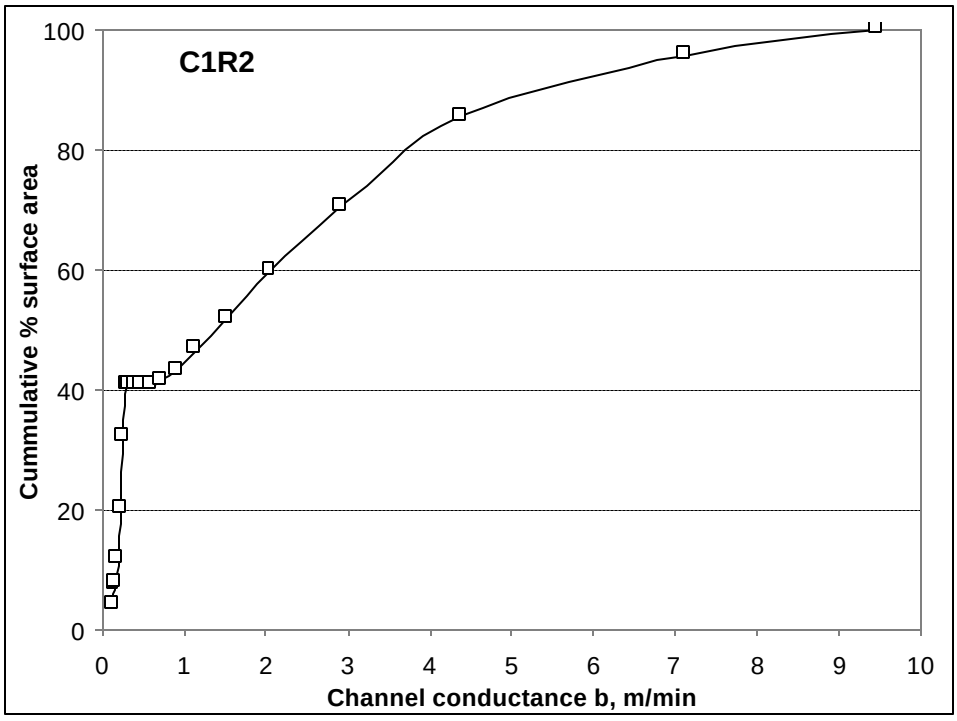

Figure 4-28 Distribution of Channel Conductance from Kinematic Wave Modelling

From the modelling results the CFDDF (cumulative flow density distribution function, see Section 4.2.1.1) was calculated for two selected times, 350 min and 500 min (180 min and 360 min in the old time notation). These are compared with experimental CFDDF's in Figure 4-3.

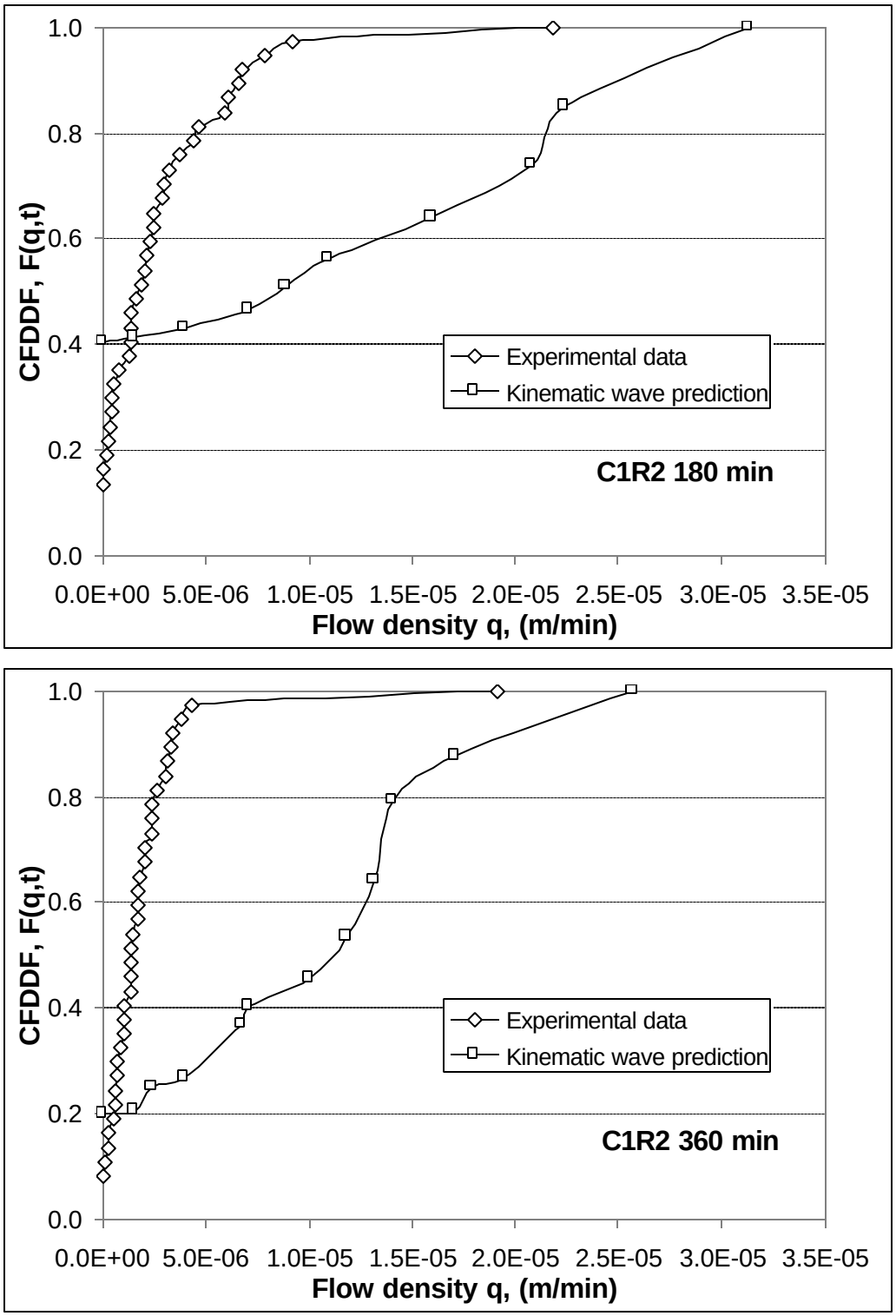

Figure 4-28 Comparison of Experimental and Model-Predicted CFDDF's

Apparently, the CFFDF's predicted by the kinematic wave model do not agree with the experimental CFFDF's very well. For example, at 180 min, the model predicts that 40% of the drainage area should show no flow, whereas the experimental results show that only 14% of the drainage

area has no flow. The predicted maximum flow density is 1.44 times greater than that experimentally observed. More generally, the kinematic wave model predicts much more bigger channels than experimentally observed. The same analysis applies to the 360 min comparison as well.

One possible reason for the discrepancy is the experimental resolution. If the bottom drainage grid were finer, one would expect the maximum flow density to be greater and the percentage of base drainage area receiving zero flow to be higher. To correct for this, the experimental data were adjusted as follows: Suppose we divided the bottom drainage area into 1.44 times more drainage partitions (37 x 1.44 ≈ 53 partitions). Suppose all the 16 new partitions (53 - 37 = 16) receive zero flow and all the flows are accommodated within the same number of partitions as before the increase in partition numbers (each new partition has a smaller area than the old partition). The experimental CFDDF's can be recalculated under these assumption. This recalculation has the effect of forcing the (recalculated) experimental maximum flow density equal to that predicted by the model. The recalculated CFDDF's are compared with the model-predicted CFDDF's in Figure 4-4.

The recalculated experimental percentage of drainage area receiving zero flow now agrees with the model predictions quite well, but the distributions of flow densities are still far apart. The discrepancy in the shapes of the experimental curve and the model-predicted curve cannot be resolved by increasing partition resolution. It is therefore concluded that the kinematic wave model is not appropriate to describe the channelling phenomena observed in our experiment. It must be point out that this conclusion is made on the basis of our experiment using the Stratmat waste rock. This conclusion may be reasonably extended to flows within similar rocks - those containing ~20% sand-size material and having a macrohomogeneous structure. This conclusion, however, should certainly not be extended to flows within other structures (e.g., CCFR or CPMFR). The applicability of the kinematic wave model to other structures need further validation studies to clarify.

The kinematic wave model, which conceptually precludes merges and splits of flows, is fundamentally inconsistent with the conceptual dendritic-reticulate model we proposed earlier based on experimental observations of flow and drainage chemistry. As a matter of fact, the kinematic wave model is based on the type of channel shown in (a) of Figure 3-1, which we particularly concluded to be absent. This makes the lack of applicability of the kinematic wave model to our experiment understandable. The kinematic wave model is probably more applicable to situations where merges and splits of channel flows are not pronounced. Imaginably, this could be the case with coarse waste rock piles in which the sand content is far less than 10%, that is, CCFR structures.

The dendritic-reticulate flow model, on the other hand, allows merges and splits of flows to take place. This feature allows the explanation of the experimentally-observed higher area extent of small flows that the kinematic wave model fails to account for. Nevertheless, the dendritic-reticulate model is only a conceptual one, it needs to be developed into a quantitative form if it were to be used for flow modelling.

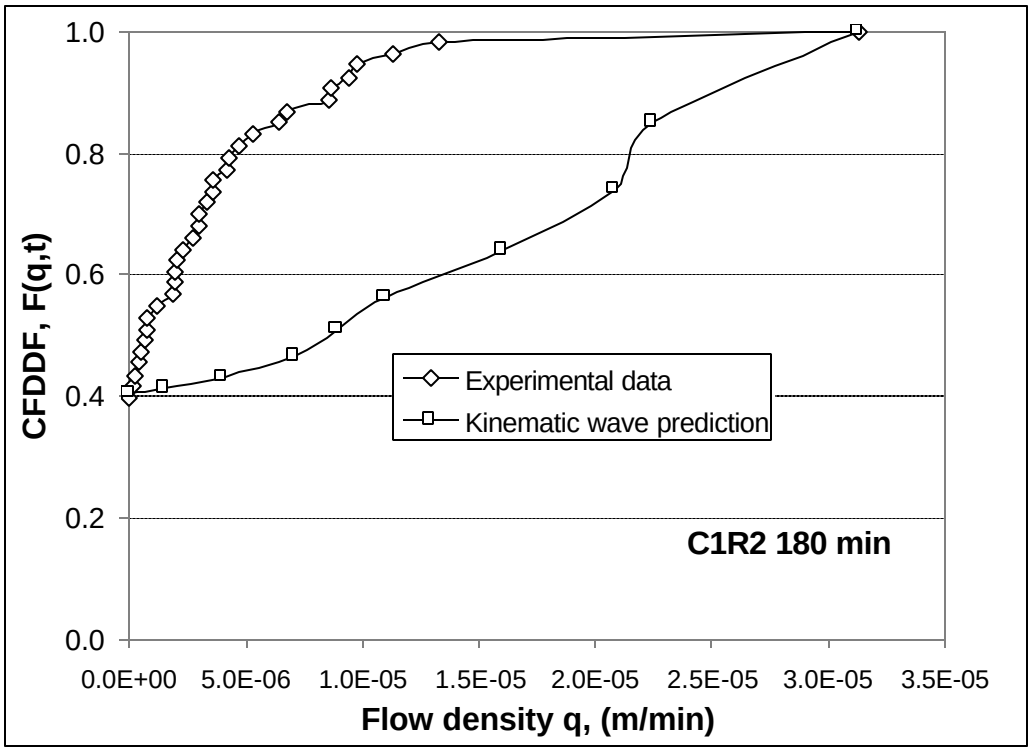

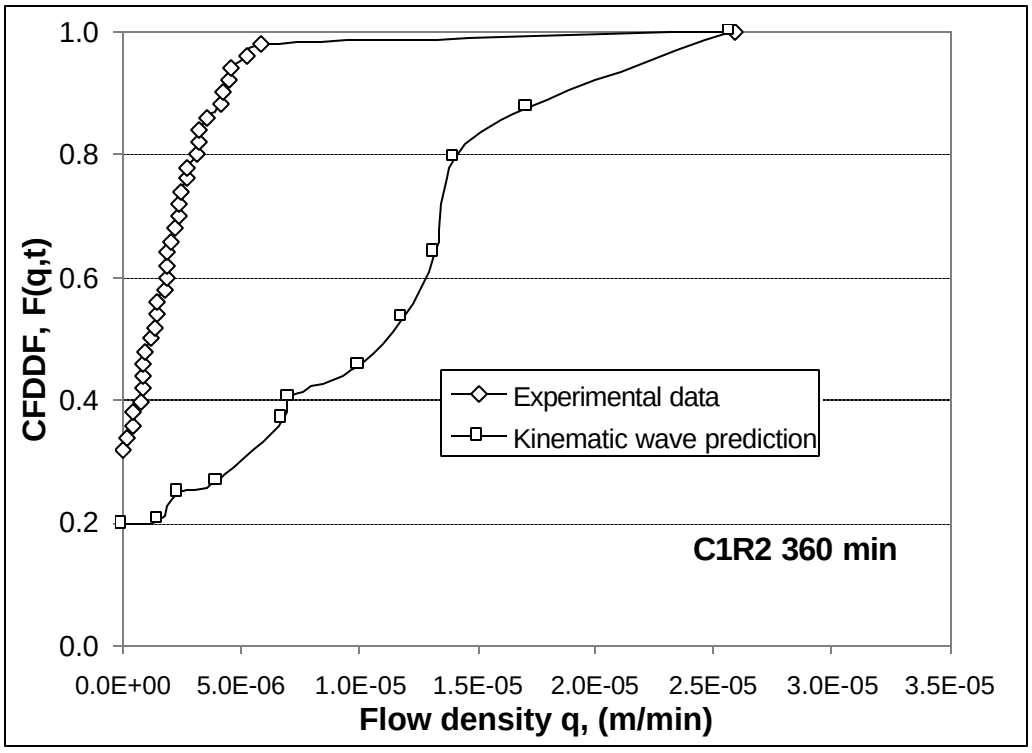

Figure 4-14 Comparison of Recalculated Experimental with Model-Predicted CFDDF's

4.4 CONCLUSIONS

Flow and solute transport modelling has important applications in ARD prediction, prevention, control and treatment. The main challenges are channelling and interactions between flows and geochemical factors. Studies on internal flows within waste rock are noticeably scarce in the literature. It is hoped that the work presented in this chapter can fill some of that gap. The following conclusions have been reached:

- Waste rock can be roughly classified into porous media flow rock (PMFR) and channelling flow rock (CFR) according to their size distribution characteristics. The two differ both hydraulically and in terms of solute transport.

- Five basic component rock structures can be identified within waste rock piles. Continuous channelling flow rock (CCFR) is a well-mixed aggregate of channelling flow rock particles. Continuous porous media flow rock (CPMFR) is a well-mixed aggregate of porous media flow rock particles. Porous media flow rock pockets suspended in continuous channelling flow rock (PMFRP/CCFR) are structures where the channelling flow rock has continuity whereas the porous media flow rock pockets are isolated. Channelling flow rock pockets suspended in continuous porous media flow rock (CFRP/CPMFR) are structures where the porous media flow rock has continuity whereas the channelling flow rock pockets are isolated. Low permeability plates or pans (LPP) are laterally-spreading thin rock strata with a very low hydraulic conductivity.

- Each of the five basic component structures has a set of distinct characteristics and should be modelled with different approaches. Factors that influence the flow of water within waste rock piles are discussed. Flow phenomena contributing to flow heterogeneity in waste rock piles, including the umbrella effects, the sponge effects, the bubble effects, ponding, day-lighting, blanketing, and funnelling, are identified.

- Channelling phenomena can be characterised mathematically by the use of cumulative flow density distribution functions (CFDDF's) or density functions of flow densities (DFFD's). These functions are jointly determined by many factors including the rock properties, rock structures, and precipitation characteristics. The DFFD can be coupled with relationships between solute concentrations and flow rates to model solute transport, either deterministically or probabilistically.

- The kinematic wave model did not adequately describe the channelling flows observed for the partially oxidised Stratmat waste rock, which appears to be, marginally, a continuous channelling flow rock. It over-predicted the extent of larger channel flows at the price of smaller channel flows. The main reason for the lack of applicability probably lies in the fact that the model conceptually precludes merges and splits of flows within waste rock. The kinematic wave model may potentially be more suitable to describe flows in other types of rocks such as CCFR, which contains less than 10% of sand and silt.

5.0 ACKNOWLEDGMENT

Many individuals at Noranda have participated in this project. The experimental work was conducted by K. Shikatani, S. Payant, and K. Faubert. L. Bernier helped with many of the graphing tasks. L. St-Arnaud provided consultation in project management and technical planning. M. Patterson was responsible for site management and site support.

The final report has benefited greatly from the technical reviews by R. Nicholson, C. Weatherell, and L. St-Arnaud. Valuable comments from M. Patterson and D. Scott of Heath Steele Division, Noranda Inc. are also appreciated.

6.0 REFERENCES

Beven, K. and Germann, P. (1981). "Water Flow in Soil Macropores II, A Combined Flow Model," *Journal of Soil Science*, 32, pp. 15-29.

Catalan, L.J.J. and Li, M.G. (1999). "Decommissioning of Heap-Leach Piles", manuscript submitted to *Environmental Science and Technology*.

Catalan, L.J.J., M.G. Li, and G. Comeau. (1998). "Rinsing Copper Oxide Heaps Leached with Sulphuric Acid: A Pilot Study," in *Proceedings of the Fifth International Conference on Tailings and Mine Wastes '98*, January 26-29, 1998, Fort Collins, Colorado, USA, Published by A.A. Balkema, Rotterdam, 1998.

Cathles, L.M. (1981). "Attempts to Model the Industrial-Scale Leaching of Copper-Bearing Mine Waste", In Alpers, C.N. and Blowes, D.W. (eds.), *Environmental Geochemistry of Sulphide Oxidation*, ACS Symposium Series 550, American Chemical Society, Washington, DC.

Courant, R. and Hilbert, D. (1973a). *Methods of Mathematical Physics, Volume I*, Interscience Publishers, Inc., New York.

Courant, R. and Hilbert, D. (1973b). *Methods of Mathematical Physics, Volume II*, Interscience Publishers, Inc., New York.

Dixon, D.G. (1993). "A Mathematical Model for Rinsing of Reagents from Spent Heaps," in Hager, J. et al. (eds.), *Extraction and Processing for the Treatment and Minimisation of Wastes*, The Minerals, Metals, and Materials Society.

Elboushi, I. M. (1975). "Amount of Water Needed to Initiate Flow in Rubbly Rock Particles", *Journal of Hydrology*, 27, pp. 275-284.

Eriksson N. and Destouni, G. (1994). "Modelling Field-Scale Transport of Weathering Products in Mining Waste Rock Dumps," *Proceedings of the Third International Conference on the Abatement of Acidic Drainage*, Pittsburgh, PA, April 24-29.

Farlow, S.J. (1993). *Partial Differential Equations for Scientists and Engineers*, General Publishing Company, Toronto.

Funk, G.A., Harold, M.P., and Ng, K.M. (1990). "A Novel Model for Reaction in Trickle Beds with Flow Maldistribution," *Ind. Eng. Chem. Res.*, 29, pp. 738-748.

Gelhar, L.W. (1993). *Stochastic Subsurface Hydrology*, Prentice-Hall, Englewood Cliffs.

Germann, P. and Beven, K. (1981a). "Water Flow in Soil Macropores I, An Experimental Approach," *Journal of Soil Science*, 32, pp. 1-13.

Germann, P. and Beven, K. (1981b). "Water Flow in Soil Macropores III, A Statistical Approach," *Journal of Soil Science*, 32, pp. 31-39.

Germann, P. and Beven, K. (1985). "Kinematic Wave Approximation to Infiltration into Soils with Sorbing Macropores," *Water Resources Research*, Vol. 21, No. 7, pp. 990-996.

Germann, P. and Beven, K. (1986). "A Distribution Function Approach to Water Flow in Soil Macropores Based on Kinematic Wave Theory," *Journal of Hydrology*, 83, pp. 173-183.

Herasymuik, G.M., Wilson, G.W., Barbour, S.L., and Smith, T. (1995). "The Characterisation of Hydrologic Properties and Moisture Migration Pathways of a Waste Rock Pile," in *Proceedings of the 19th Annual British Columbia Mine Reclamation Symposium*, Held at Dawson Creek, B.C., Canada, June 19-23.

Levenspiel, O. (1972). *Chemical Reaction Engineering*, 2nd edn., John Wiley & Sons, New York.

Li, M. (1999). *Hydrogeochemistry of Oxidised Waste Rock from Stratmat Site, N.B.*, Final Report by Noranda Inc., Technology Centre to MEND2000 (Canmet), March.

Li, M., C. Jacob, and G. Comeau (1995). "Decommissioning of Sulphuric Acid-Leached Heap by Rinsing", *Tailings and Mine Waste 1996*, Balkema, Rotterdam.

Lighthill, M.J. and Whitham, G.B. (1955). "On Kinematic Waves I, Flood Movement in Long Rivers", *Proc. R. Soc. London*, Ser. A, 229, pp. 281-316.

Morin, K.A., Hutt, N.M. and McArthur, R. (1995). "Statistical Assessment of Past Water Chemistry to Predict Future Chemistry at Noranda Minerals' Bell Mine," in *Proceedings of Sudbury '95*, held May 28 - June 1, Sudbury, Ontario, Canada.

Morin, K.A., Horne, I.A., and Riehm, D. (1994). *High-Frequency Geochemical Monitoring of Toe Seepage from Mine-Rock Dumps, BHP Minerals' Island Copper Mine, British Columbia.* In: Proceedings of the Third International Conference on the Abatement of Acidic Drainage, Pittsburgh, PA, USA, April 24-29, Vol. 1, pp. 346-254.

Morin, K., Gerencher, E., Jones, C.E., and Konasewich, D.E. (1991). *Critical Literature Review of Acid Drainage from Waste Rock*, MEND Report 1.11.1.

Murr, L.E., Schlitt, W.J., and Cathles, L.M. (1981). "Experimental Observations of Solution Flow in the Leaching of Copper-Bearing Waste, " in Schlitt, W.J. and Hiskey J.B. (eds.), *Interfacing Technologies in Solution Mining, Proceedings of the Second SME-SPE International Solution Mining Symposium*, Dever, Colorado, November 18-20.

Ng, K.M., Chu, C.F. (1987). "Trickle-Bed Reactors, " *Chem. Eng. Prog.*, 38 (11), pp. 55-63.

Ott, W.R. (1995). *Environmental Statistics and Data Analysis*, CRC Press, Inc., Boca Raton.

Parkhurst, D.L., (1995). *User's Guide to PHREEQC - A Computer Program for Speciation, Reaction-Path, Advective-Transport, and Inverse Geochemical Calculations*, U.S. Geological Survey, Water-Resources Investigations Report 95-4227, Lakewood, Colorado, USA.

Perkins, E.H., H.W. Nesbitt, W.D. Gunter, L.C. St-Arnaud, and J.R. Mycroft, 1995. *Critical Literature Review of Geochemical Processes and Geochemical Models Adaptable for Prediction of Acidic Drainage from Waste Rock*, MEND Report 1.42.1.

Perry, R.H. and Green, D.W. eds. (1997). *Perry's Chemical Engineers' Handbook*, 7th edn., McGraw-Hill, Toronto.

Philip, J.R. (1957). "The Theory of Infiltration, 4, Sorptivity and Algebraic Infiltration Equations, " *Soil Science*, 84, pp. 257-264.

Sanchez-Chacon, A.E. and Lapidus, G.T. (1997). "Model for Heap Leaching of Gold Ores by Cyanidation, " Hydrometallurgy, 44, pp. 1-20.

Satterfield, C.N. (1975). "Trickle-Bed Reactors, " *AIChE Journal*, Vol. 21, No. 2, pp. 209-228.

Schlitt, W.J. and Nocolai, L.F. (1987). "Nonvertical Solution Flow and Its Applications in Heap and Dump Leaching, " *Minerals and Metallurgical Processing*, February, pp. 1-7.

Singh, V.P. (1997). *Kinematic Wave Modelling in Water Resources: Environmental Hydrology*, John Wiley & Sons, New York.

Singh, V.P. (1996). *Kinematic Wave Modelling in Water Resources: Surface Water Hydrology*, John Wiley & Sons, New York.

Smith, L., Lopez, D.L., Beckie, R., Morin, K., Dawson, R., and Price, W. (1995). *Hydrology of Waste Rock Dumps*, Report to Natural Resources Canada.

SRK (Steffen Robertson and Kirsten (Canada) Inc.), (1995). *Modelling Acidic Drainage from Waste Rock Piles*, Draft Report to Ministry of Energy, Mines and Petroleum Resources (B.C.) and Environment Canada.

Stumm, W. and J.J. Morgan (1996). *Aquatic Chemistry - Chemical Equilibria and Rates in Natural Waters*, 3rd edn., John Wiley & Sons, New York.

Synergetic Technology (1996). *Physical Mechanisms in Acid Mind Drainage Waste Rock Piles,* Phase I Part I, Draft Report to MEND and Environment Canada.

APPENDIX I EXPERIMENTAL CONDITIONS AND PROCEDURES

COLUMN 1

Test Conditions

Column 1 Run 1 feed rate = 3.2 mL/min/channel; feed duration = 13 hours; rain simulator position = -22.5°; rock bed thickness = 1.5 m; number of sampling rounds = 8; sampling duration = 6 hours (excluding the last round which was the next morning); number of sampling rounds submitted for ICP analysis = 6; tracer (NaCl) concentration in feed water = 1000 mg/L Na^+; rain simulator turn-on time = 2:15 am; rain simulator turn-off time = 3:15 pm.

Column 1 Run 2 feed rate = 3.2 mL/min/channel; feed duration = 7 hours; rain simulator position = -22.5°; rock bed thickness = 1.5 m; number of sampling rounds = 8; sampling duration = 6 hours (excluding the last round); number of sampling rounds submitted for ICP analysis = 5; tracer (KNO_3) concentration in feed water = 500 mg/L K^+; rain simulator turn-on time = 6:10 am; rain simulator turn-off time = 1:10 pm.

Column 1 Run 3 feed rate = 1.6 mL/min/channel; feed duration = 10 hours; rain simulator position = -22.5°; rock bed thickness = 1.5 m; number of sampling rounds = 8; sampling duration = 6 hours (excluding the last round); number of sampling rounds submitted for ICP analysis = 6; tracer (LiCl) concentration in feed water = 500 mg/L Li^+; rain simulator turn-on time = 2:03 am; rain simulator turn-off time = 12:03 pm.

Test Procedure

Column 1 Run 1

1. The feed water reservoir was refilled with fresh tap water to the 100-L mark. Then NaCl was dissolved to make a 1000 mg/L Na^+ concentration in the feed water.
2. The timer was programmed to turn on the feed pumps at 2:15 am and to turn it off at 3:15 pm on the same day.
3. The drainage breakthrough took place at 2:30 pm, and this was set as time zero for sampling purpose. Drainage breakthrough is arbitrarily defined as the time when water has Ended flowing in about half of the sample bottles.
4. At the time intervals of 30 min., 60 min., 90 min., 120 min., 180 min., 240 min., 360 min., and the next morning (about 1080 min.), each of the 37 drainage bottles underwent the following treatment: sample weight, pH, and conductivity were measured; for selected time intervals (see the next step), a sub-sample (unfiltered) was taken and preserved with pure nitric acid for ICP analysis. Then the sample was discarded.
5. The preserved sub-samples for the following time intervals were submitted for ICP analysis for dissolved S, Fe, Zn, Na, K, Li: 30 min., 60 min., 90 min., 180 min., 240 min., and 1080 min.

Column 1 Run 2

1. The feed water reservoir was emptied, washed, and refilled with tap water to the 100-L mark. KNO_3 was dissolved in the water to make a 500 mg/L K^+ concentration.
2. The timer was programmed to turn on the feed pumps at 6:10 am and to turn it off at 1:10 pm on

the same day.

3. The drainage breakthrough took place at 9:00 am, and this time was set as time zero for sampling purpose.
4. At the time intervals of 30 min., 60 min., 90 min., 120 min., 180 min., 240 min., 360 min., and the next morning (about 1440 min.), each of the 37 drainage bottles underwent the following treatment: sample weight, pH, and conductivity were measured; for selected time intervals (see the next step), a sub-sample (unfiltered) was taken and preserved with pure nitric acid for ICP analysis. Then the sample was discarded.
5. The preserved sub-samples for the following time intervals were submitted for ICP analysis for dissolved S, Fe, Zn, Na, K, Li: 30 min., 60 min., 90 min., 180 min., and 1380 min.

Column 1 Run 3

1. The feed water reservoir was emptied, washed, and refilled with fresh tap water to the 60-L mark (Note: 60 L instead of 100 L, to save reagent cost). LiCl was dissolved in the water to make a 500 mg/L Li^+ concentration.
2. The timer was programmed to turn on the feed pumps at 2:03 am and to turn it off at 12:03 pm on the same day.
3. The drainage breakthrough took place at 8:00 am, and this time was set as time zero for sampling purpose.
4. At the time intervals of 30 min., 60 min., 90 min., 120 min., 180 min., 240 min., 360 min., and the next morning (about 1440 min.), each of the 37 drainage bottles underwent the following treatment: sample weight, pH, and conductivity were measured; for selected time intervals (see the next step), a sub-sample (unfiltered) was taken and preserved with pure nitric acid for ICP analysis. Then the sample was discarded.
5. The preserved sub-samples for the following time intervals were submitted for ICP analysis for dissolved S, Fe, Zn, Na, K, Li: 30 min., 60 min., 90 min., 180 min., 240 min., and 360 min.

Column 2

Test Conditions

Column 2 Run 1 feed rate = 3.2 mL/min/channel; feed duration = 5 hours; rain simulator position = -22.5°; rock bed thickness = 0.5 m; number of sampling rounds = 7; sampling duration = 4 hours (excluding the last round); number of sampling rounds submitted for ICP analysis = 7; rain simulator turn-on time = 1:45 pm; rain simulator turn-off time = 6:45 pm.

Column 2 Run 2 feed rate = 3.2 mL/min/channel; feed duration = 6 hours; rain simulator position = -22.5°; rock bed thickness = 1.0 m; number of sampling rounds = 7; sampling duration = 4 hours (excluding the last round); number of sampling rounds submitted for ICP analysis = 7; rain simulator turn-on time = 6:30 am; rain simulator turn-off time = 12:30 pm.

Column 2 Run 3 feed rate = 3.2 mL/min/channel; feed duration = 10.77 hours; rain simulator position = -

22.5°; rock bed thickness = 1.5 m; number of sampling rounds = 7; sampling duration = 6 hours (excluding the last round); number of sampling rounds submitted for ICP analysis = 6; rain simulator turn-on time = 2:12 am; rain simulator turn-off time = 9:12 am; rain simulator restarted = 10:20 am and re-stopped = 2:06 pm.

Column 2 Run 4 This is a repeat of Column2 Run 3. feed rate = 3.2 mL/min/channel; feed duration = 5.1 hours; rain simulator position = -22.5°; rock bed thickness = 1.5 m; number of sampling rounds = 8; sampling duration = 6 hours (excluding the last round); number of sampling rounds submitted for ICP analysis = 5; rain simulator turn-on time = 4:30 am; rain simulator turn-off time = 9:37 am.

Test Procedures

Column 2 Run 1

1. The feed water reservoir was refilled with fresh tap water to the 100-L mark.
2. The timer was programmed to turn on the feed pumps at 1:45 pm and to turn it off at 6:45 pm on the same day.
3. The drainage breakthrough took place at 4:15 pm, and this was set as time zero for sampling purpose
4. At the time intervals of 0 min., 30 min., 60 min., 120 min., 180 min., 240 min., and the next morning (about 960 min.), each of the 37 drainage bottles underwent the following treatment: sample weight, pH, and conductivity were measured; a sub-sample (unfiltered) was taken and preserved with pure nitric acid for ICP analysis of dissolved S, Fe, Zn. Then the sample was discarded.

Column 2 Run 2

1. The feed water reservoir Ended at the 64-L mark.
2. The timer was programmed to turn on the feed pumps at 6:30 am and to turn it off at 12:30 pm on the same day.
3. The drainage breakthrough took place at 10:30 am, and this was set as time zero for sampling purpose.
4. At the time intervals of 30 min., 60 min., 90 min.,120 min., 180 min., 240 min., and the next morning (about 1320 min.), each of the 37 drainage bottles underwent the following treatment: sample weight, pH, and conductivity were measured; a sub-sample (unfiltered) was taken and preserved with pure nitric acid for ICP analysis of dissolved S, Fe, Zn.

Column 2 Run 3

1. The feed water reservoir was emptied, washed, and refilled with fresh tap water to the 100-L mark.
2. The timer was programmed to turn on the feed pumps at 2:12 am and to turn it off at 9:12 am on the same day. The feed pumps were restarted at 10:20 am and turned off at 2:06 pm to apply additional water.
3. The drainage breakthrough took place at 8:30 am, and this time was set as time zero for sampling purpose.

4. At the time intervals of 30 min., 60 min., 90 min., 180 min., 240 min., 360 min., and the next morning (about 1440 min.), each of the 37 drainage bottles underwent the following treatment: sample weight, pH, and conductivity were measured; for selected time intervals (see the next step), a sub-sample (unfiltered) was taken and preserved with pure nitric acid for ICP analysis. Then the sample was discarded.
5. The preserved sub-samples for the following time intervals were submitted for ICP analysis for dissolved S, Fe, Zn: 30 min., 60 min., 90 min., 180 min., and 1440 min.

Column 2 Run 4

1. The feed water reservoir was emptied, washed, and refilled with fresh tap water to the 100-L mark.
2. The timer was programmed to turn on the feed pumps at 4:30 am and to turn it off at 9:37 am on the same day.
3. The drainage breakthrough took place at 7:15 am, and this time was set as time zero for sampling purpose.
4. At the time intervals of 30 min., 60 min., 90 min., 120 min., 180 min., 240 min., 360 min., and the next morning (about 1500 min.), each of the 37 drainage bottles underwent the following treatment: sample weight, pH, and conductivity were measured; for selected time intervals (see the next step), a sub-sample (unfiltered) was taken and preserved with pure nitric acid for ICP analysis. Then the sample was discarded.
5. The preserved sub-samples for the following time intervals were submitted for ICP analysis for dissolved S, Fe, Zn: 30 min., 60 min., 90 min., 180 min., 360 min.

Column 3

Test Conditions

Column 3 Run 1 Water was fed at one point (centre of the sample bed surface). feed rate = 35 mL/min; feed duration = 10 hours; rain simulator position = -22.5°; rock bed thickness = 0.5 m; number of sampling rounds = 8; sampling duration = 6 hours (excluding the last round); number of sampling rounds submitted for ICP analysis = 6; rain simulator turn-on time = 2:11 am; rain simulator turn-off time = 12:11 pm.

Column 3 Run 2 Water was fed at one point (centre of the sample bed surface). feed rate = 35 mL/min; feed duration = 13 hours; rain simulator position = -22.5°; rock bed thickness = 1.0 m; number of sampling rounds = 8; sampling duration = 6 hours (excluding the last round); number of sampling rounds submitted for ICP analysis = 7; rain simulator turn-on time = 10:02 pm (previous evening); rain simulator turn-off time = 11:02 pm.

Column 3 Run 3 Water was fed at one point (centre of the sample bed surface). feed rate = 35 mL/min; feed duration = 12 hours; rain simulator position = -22.5°; rock bed thickness = 1.5 m; number of sampling rounds = 8; sampling duration = 6 hours (excluding the last round); number of sampling rounds submitted for ICP analysis = 6; rain simulator turn-on time = 2:00 am; rain simulator turn-off time = 4:00 pm.

Test Procedures

Column 3 Run 1

1. The feed water reservoir was refilled with fresh tap water to the 50-L mark. NaCl was dissolved in the water to make a concentration of 1000 mg/L Na^+.
2. The timer was programmed to turn on the feed pump at 2:11 am and to turn it off at 12:11 pm on the same day.
3. The drainage breakthrough took place at 8:00 am, and this was set as time zero for sampling purpose.
4. At the time intervals of 30 min., 60 min., 90 min., 120 min., 180 min., 240 min., 360 min., and the next morning (about 1440 min.), each of the 37 drainage bottles underwent the following treatment: sample weight, pH, and conductivity were measured; for selected time intervals (see next step), a sub-sample (unfiltered) was taken and preserved with pure nitric acid for ICP analysis of dissolved S, Fe, Zn, Na, K, and Li. Then the sample was discarded.
5. The preserved sub-samples for the following time intervals were submitted for ICP analysis: 30 min., 60 min., 90 min., 180 min., 240 min., and 360 min.

Column 3 Run 2

1. The feed water reservoir was emptied, washed, and refilled with fresh tap water to the 50-L mark. KNO_3 was dissolved in the water to make a concentration of 1000 mg/L K^+.
2. The timer was programmed to turn on the feed pumps at 10:02 pm (previous evening) and to turn it off at 11:02 am.
3. The drainage breakthrough took place at 7:00 am, and this was set as time zero for sampling purpose.
4. At the time intervals of 30 min., 60 min., 90 min.,120 min., 180 min., 240 min., 360 min., and the next morning (about 1500 min.), each of the 37 drainage bottles underwent the following treatment: sample weight, pH, and conductivity were measured; and for selected time intervals (see next step), a sub-sample (unfiltered) was taken and preserved with pure nitric acid for ICP analysis of dissolved S, Fe, Zn, Na, K, and Li.
5. The preserved sub-samples for the following time intervals were submitted for ICP analysis: 30 min., 60 min., 90 min., 180 min., 240 min., 360 min., and 1500 min.

Column 3 Run 3

1. The feed water reservoir was emptied, washed, and refilled with fresh tap water to the 50-L mark. LiCl was dissolved in the water to make a concentration of 500 mg/L Li^+.
2. The timer was programmed to turn on the feed pumps at 2:00 am and to turn it off at 4:00 pm on the same day.
3. The drainage breakthrough took place at 4:30 pm, and this time was set as time zero for sampling purpose.
4. At the time intervals of 30 min., 60 min., 90 min., 120 min., 180 min., 260 min., 360 min., and the next morning (about 960 min.), each of the 37 drainage bottles underwent the following treatment:

sample weight, pH, and conductivity were measured; for selected time intervals (see the next step), a sub-sample (unfiltered) was taken and preserved with pure nitric acid for ICP analysis. Then the sample was discarded.

5. The preserved sub-samples for the following time intervals were submitted for ICP analysis for dissolved S, Fe, Zn, Na, K, and Li: 30 min., 60 min., 90 min., 180 min., 360 min. and 960 min.

APPENDIX II DRAINAGE HYDROGRAPHS

Abbreviations

C = Column
R = Run
P = Port of Drainage
SR = Simulated Rain (uniform input at the top of the sample bed)

For example, C1R2 P15 means Column 1, Run 2, Drainage Port No. 15.

Explanations

The rectangle in each column hydrograph represents the simulated rain input on the top of the sample bed; the height of the rectangle is the flow rate of the simulated rain input.

The "flow rate" or "column discharge rate" used in the drainage hydrographs are averages over specific time intervals, calculated by dividing the total volume (mass) of solution collected from a drainage port or for the entire column by the time interval used to collect this volume. For example, the flow rate of C1R1 P10 at 180 minutes is 3.08 g/min, which is obtained by dividing the total volume (mass) of solution collected at Port 10 in Column 1 Run 1 - 184.6 g - by the duration of this collection - 60 minutes (i.e., from 120 to 180 minutes). The column discharge rate is the sum of the flow rates in all 37 drainage ports.

Because the time zero is normally identified with an estimated precision of 0.5 hour and is positively biased, the first data point in all drainage hydrographs is approximate and positively biased. The "true" average flow rate or "true" column discharge rate for the first data point should lie close to 50% of the value plotted on the hydrographs given in this appendix.

Also, because of the very long time interval (overnight) for the last data point in each drainage hydrograph, the value of the last data point is inaccurate and included for illustration purpose only.

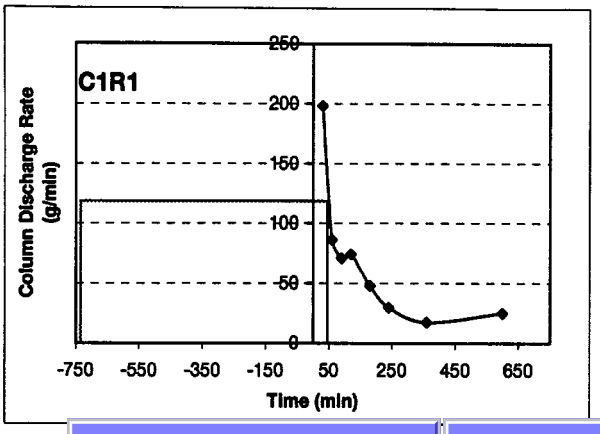

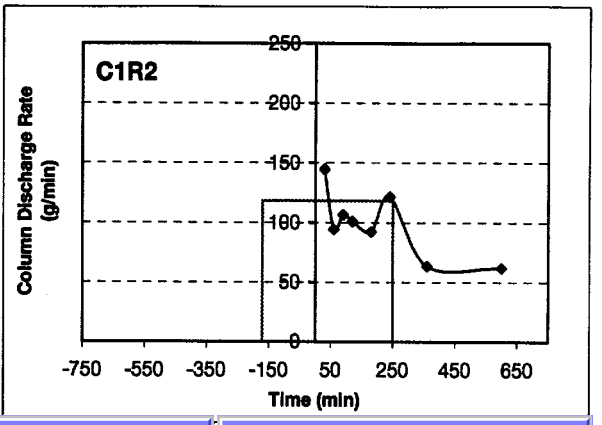

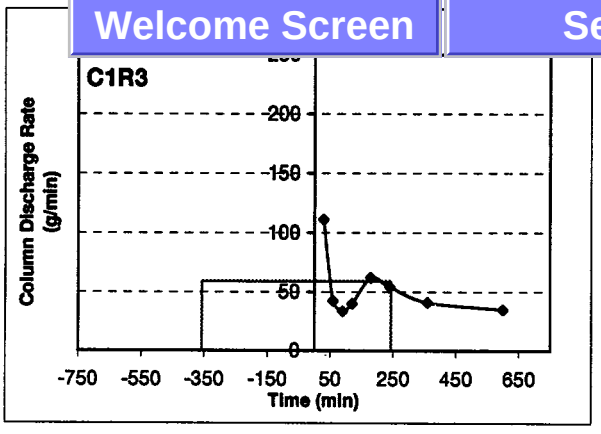

Column 1 Drainage Hydrographs

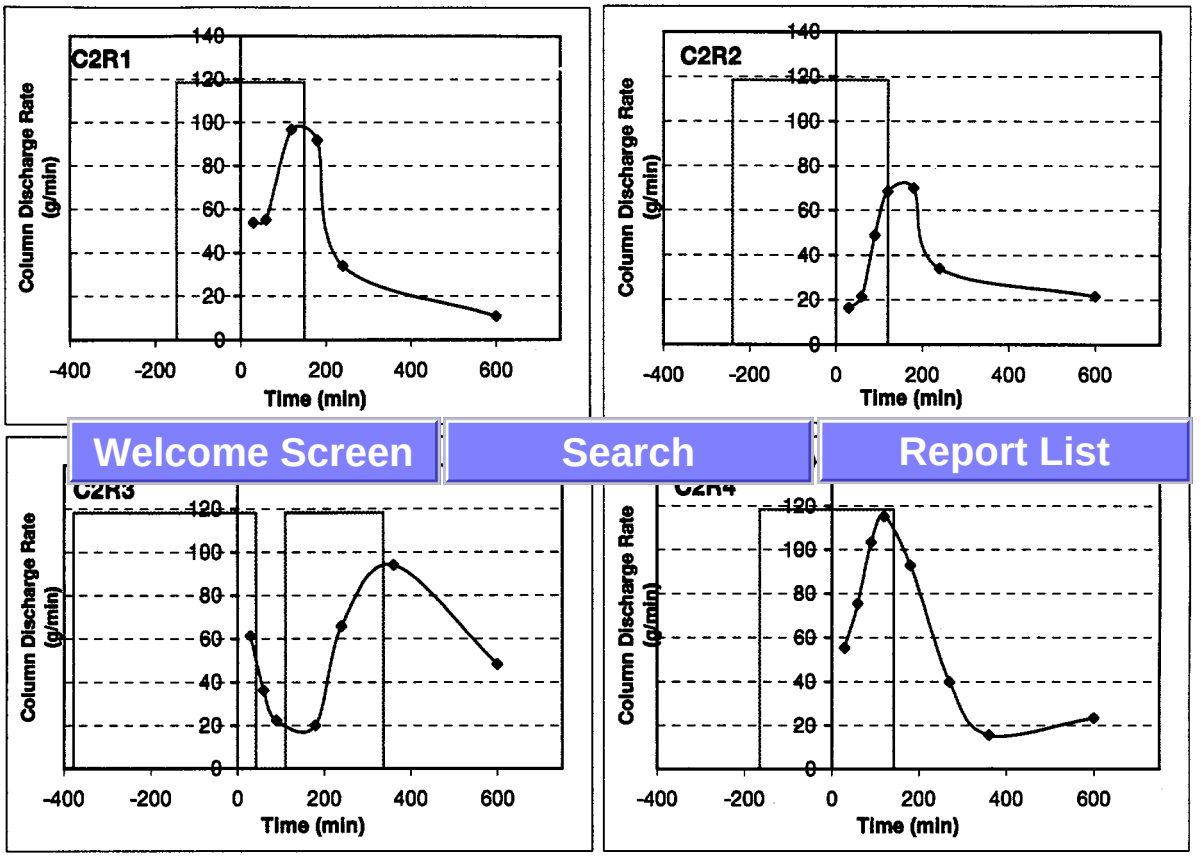

Column 2 Drainage Hydrographs

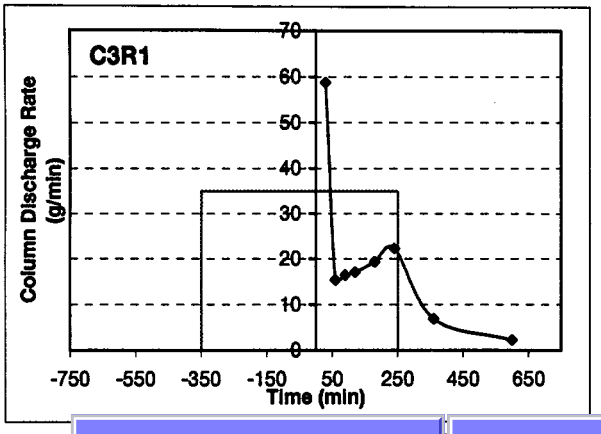

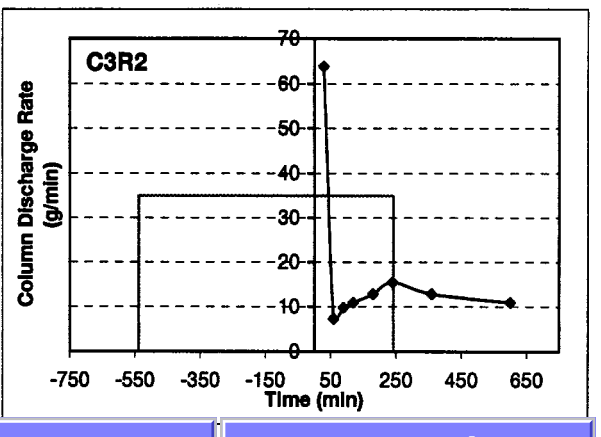

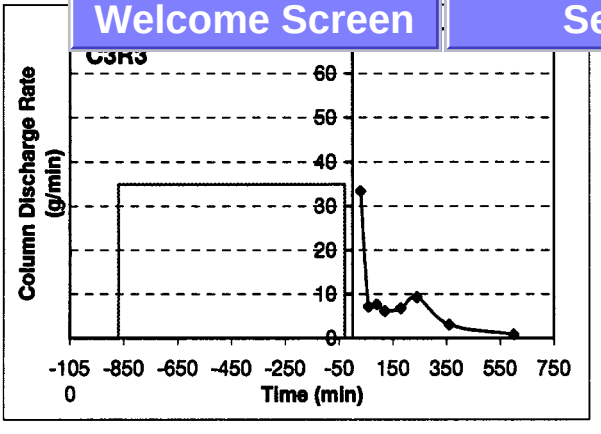

Column 3 Drainage Hydrographs

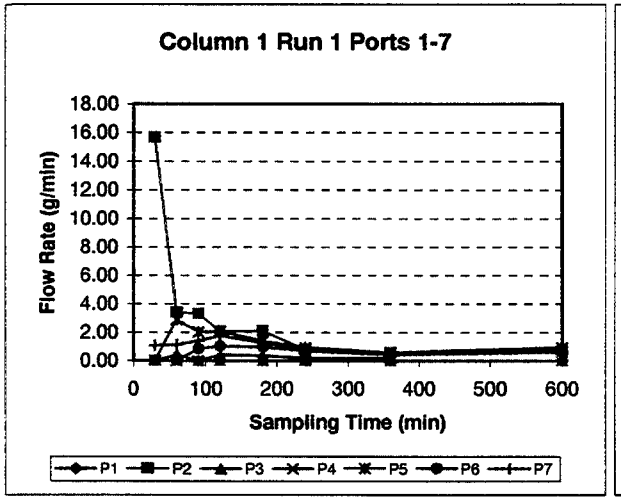
Column 1 Run 1 Ports 1-7
Flow Rate (g/min)
18.00
16.00
14.00
12.00
10.00
8.00
6.00
4.00
2.00
0.00
0
100
200
300
400
500
600
Sampling Time (min)
P1
P2
P3
P4
P5
P6
P7

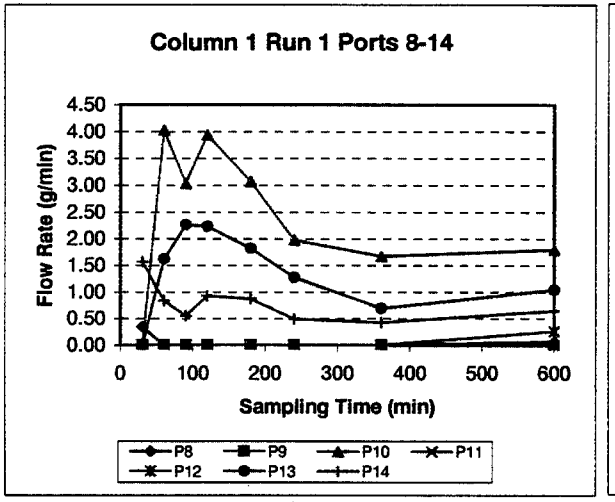
Column 1 Run 1 Ports 8-14
Flow Rate (g/min)
4.50
4.00
3.50
3.00
2.50
2.00
1.50
1.00
0.50
0.00
0
100
200
300
400
500
600
Sampling Time (min)
P8
P9
P10
P11
P12
P13
P14

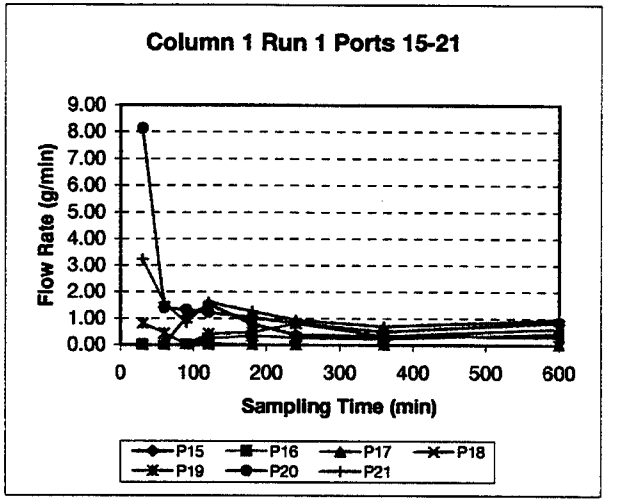
Column 1 Run 1 Ports 15-21
Flow Rate (g/min)
9.00
8.00
7.00
6.00
5.00
4.00
3.00
2.00
1.00
0.00
0
100
200
300
400
500
600
Sampling Time (min)
P15
P16
P17
P18
P19
P20
P21

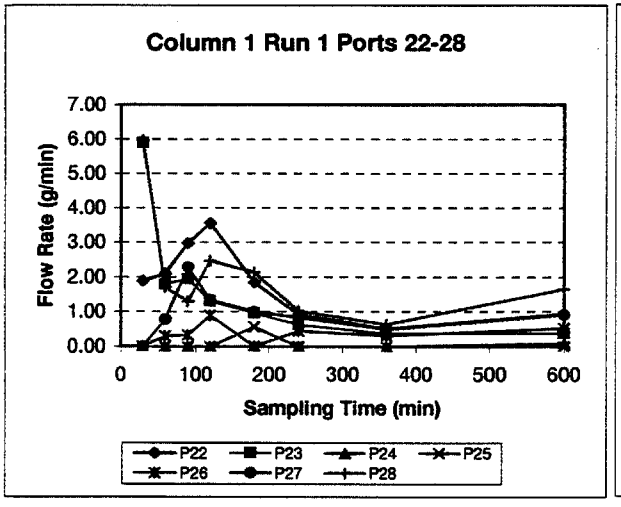
Column 1 Run 1 Ports 22-28
Flow Rate (g/min)
7.00
6.00
5.00
4.00
3.00
2.00
1.00
0.00
0
100
200
300
400
500
600
Sampling Time (min)
P22
P23
P24
P25
P26
P27
P28

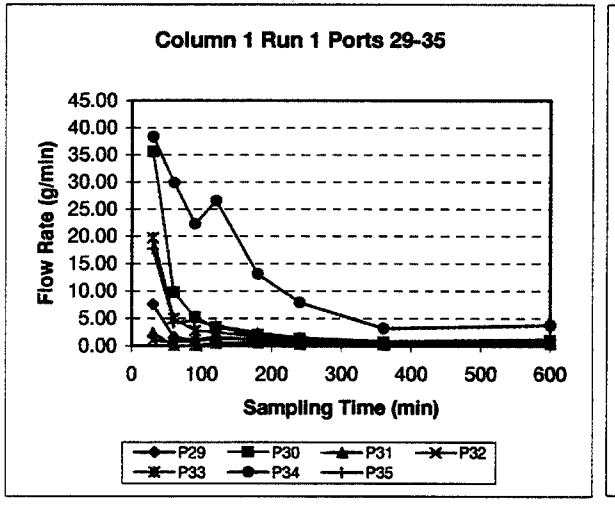
Column 1 Run 1 Ports 29-35
Flow Rate (g/min)
45.00
40.00
35.00
30.00
25.00
20.00
15.00
10.00
5.00
0.00
0
100
200
300
400
500
600
Sampling Time (min)
P29
P30
P31
P32
P33
P34
P35

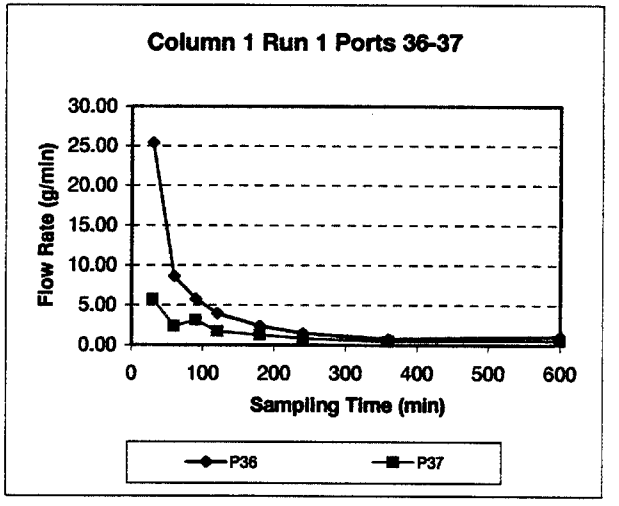
Column 1 Run 1 Ports 36-37
Flow Rate (g/min)
30.00
25.00
20.00
15.00
10.00
5.00
0.00
0
100
200
300
400
500
600
Sampling Time (min)
P36
P37

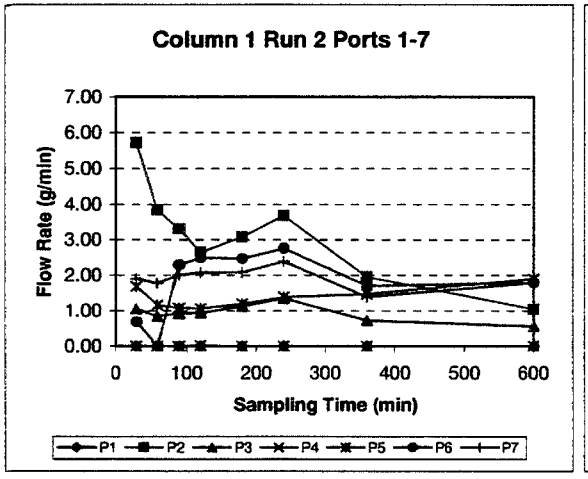
Column 1 Run 2 Ports 1-7
Flow Rate (g/min)
7.00
6.00
5.00
4.00
3.00
2.00
1.00
0.00
0
100
200
300
400
500
600
Sampling Time (min)
P1 P2 P3 P4 P5 P6 P7

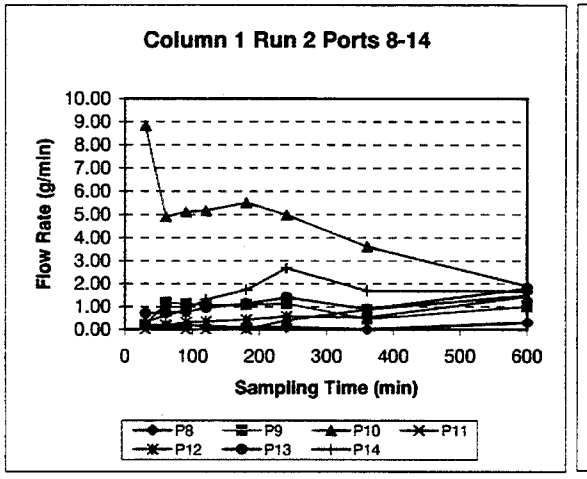
Column 1 Run 2 Ports 8-14
Flow Rate (g/min)
10.00
9.00
8.00
7.00
6.00
5.00
4.00
3.00
2.00
1.00
0.00
0
100
200
300
400
500
600
Sampling Time (min)
P8 P9 P10 P11
P12 P13 P14

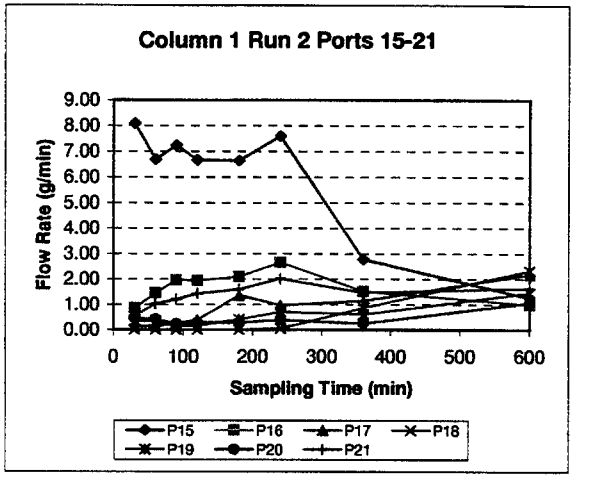
Column 1 Run 2 Ports 15-21
Flow Rate (g/min)
9.00
8.00
7.00
6.00
5.00
4.00
3.00
2.00
1.00
0.00
0
100
200
300
400
500
600
Sampling Time (min)
P15 P16 P17 P18
P19 P20 P21

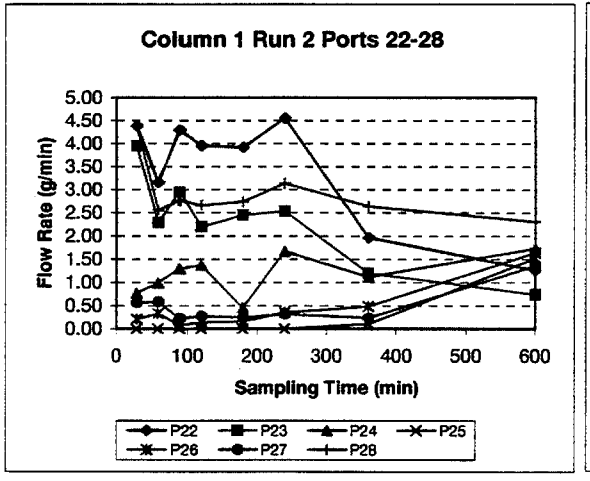
Column 1 Run 2 Ports 22-28
Flow Rate (g/min)
5.00
4.50
4.00
3.50
3.00
2.50
2.00
1.50
1.00
0.50
0.00
0
100
200
300
400
500
600
Sampling Time (min)
P22 P23 P24 P25
P26 P27 P28

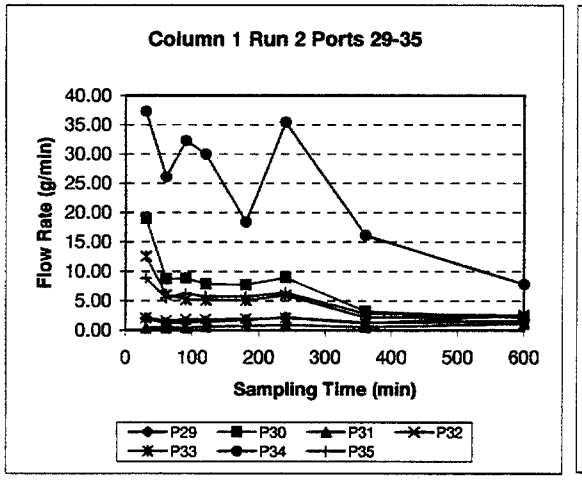
Column 1 Run 2 Ports 29-35
Flow Rate (g/min)
40.00
35.00
30.00
25.00
20.00
15.00
10.00
5.00
0.00
0
100
200
300
400
500
600
Sampling Time (min)
P29 P30 P31 P32
P33 P34 P35

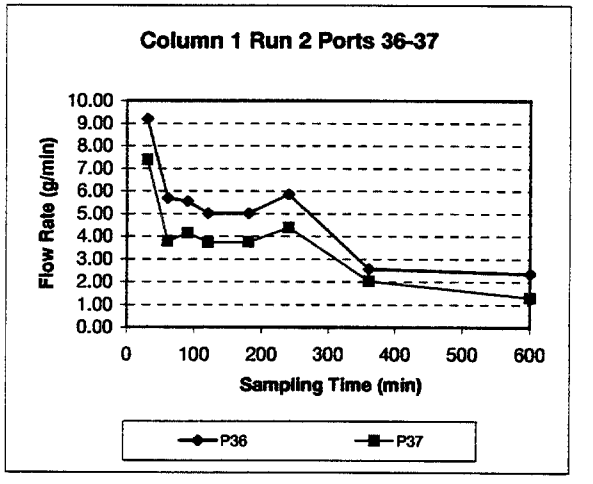
Column 1 Run 2 Ports 36-37
Flow Rate (g/min)
10.00
9.00
8.00
7.00
6.00
5.00
4.00
3.00
2.00
1.00
0.00
0
100
200
300
400
500
600
Sampling Time (min)
P36 P37

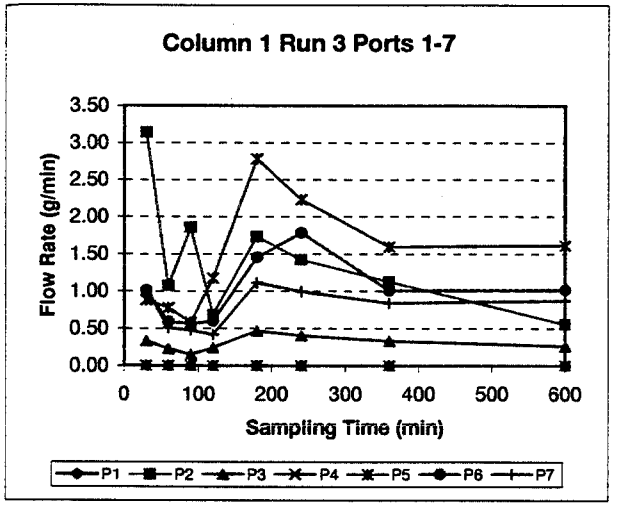
Column 1 Run 3 Ports 1-7
Flow Rate (g/min)
3.50
3.00
2.50
2.00
1.50
1.00
0.50
0.00
0
100
200
300
400
500
600
Sampling Time (min)
P1
P2
P3
P4
P5
P6
P7

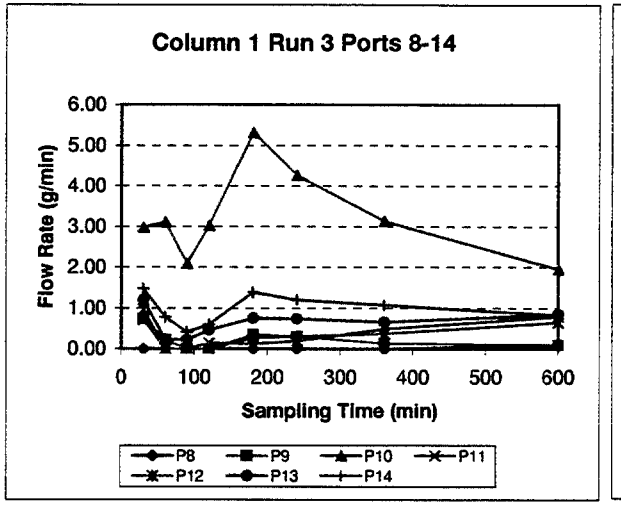
Column 1 Run 3 Ports 8-14
Flow Rate (g/min)
6.00
5.00
4.00
3.00
2.00
1.00
0.00
0
100
200
300
400
500
600
Sampling Time (min)
P8
P9
P10
P11
P12
P13
P14

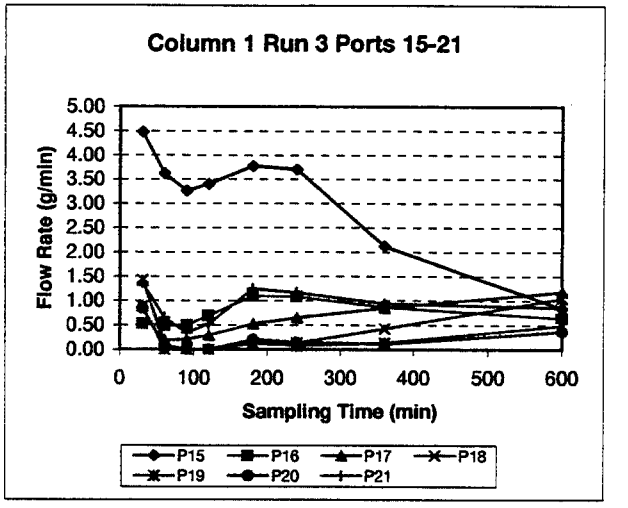
Column 1 Run 3 Ports 15-21
Flow Rate (g/min)
5.00
4.50
4.00
3.50
3.00
2.50
2.00
1.50
1.00
0.50
0.00
0
100
200
300
400
500
600
Sampling Time (min)
P15
P16
P17
P18
P19
P20
P21

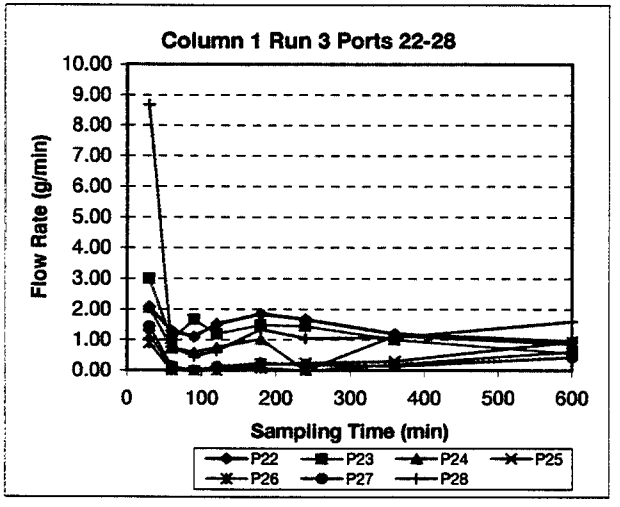
Column 1 Run 3 Ports 22-28
Flow Rate (g/min)
10.00
9.00
8.00
7.00
6.00
5.00
4.00
3.00
2.00
1.00
0.00
0
100
200
300
400
500
600
Sampling Time (min)
P22
P23
P24
P25
P26
P27
P28

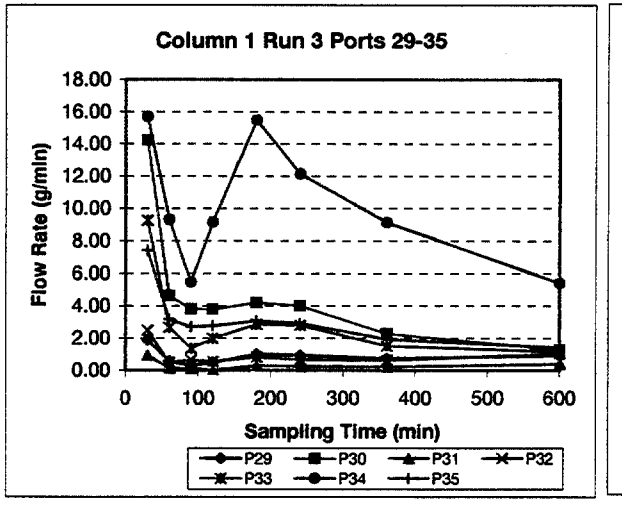
Column 1 Run 3 Ports 29-35
Flow Rate (g/min)
18.00
16.00
14.00
12.00
10.00
8.00
6.00
4.00
2.00
0.00
0
100
200
300
400
500
600
Sampling Time (min)
P29
P30
P31
P32
P33
P34
P35

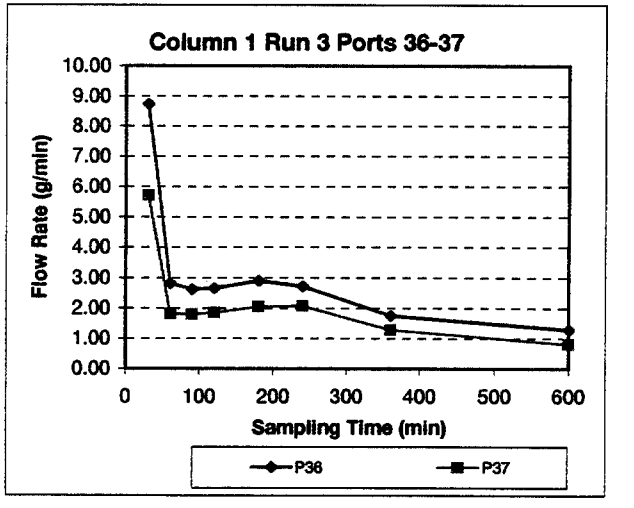
Column 1 Run 3 Ports 36-37
Flow Rate (g/min)
10.00
9.00
8.00
7.00
6.00
5.00
4.00
3.00
2.00
1.00
0.00
0
100
200
300
400
500
600
Sampling Time (min)
P36
P37

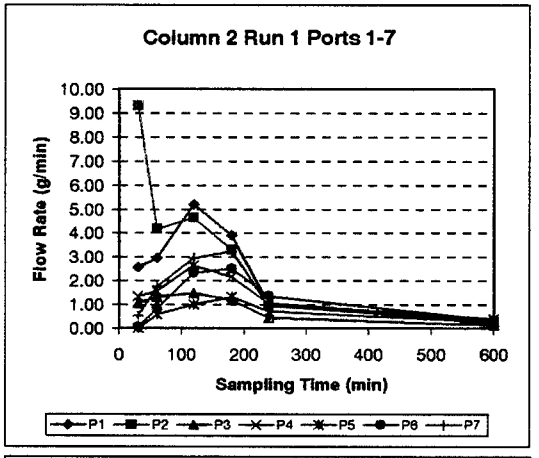
Column 2 Run 1 Ports 1-7
Flow Rate (g/min)
10.00
9.00
8.00
7.00
6.00
5.00
4.00
3.00
2.00
1.00
0.00
0
100
200
300
400
500
600
Sampling Time (min)
P1
P2
P3
P4
P5
P6
P7

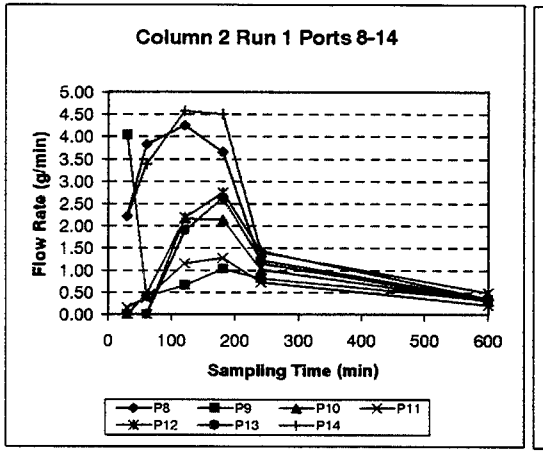
Column 2 Run 1 Ports 8-14
Flow Rate (g/min)
5.00
4.50
4.00
3.50
3.00
2.50
2.00
1.50
1.00
0.50
0.00
0
100
200
300
400
500
600
Sampling Time (min)
P8
P9
P10
P11
P12
P13
P14

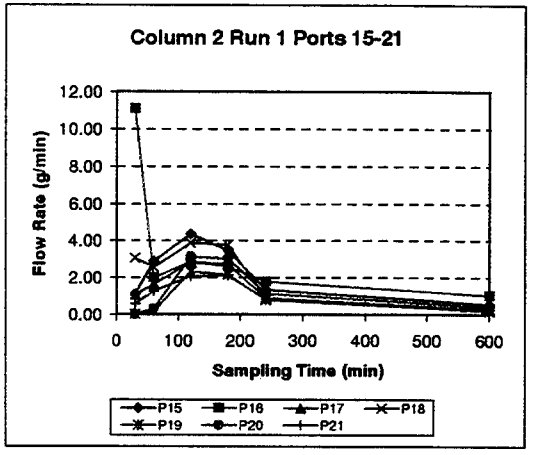
Column 2 Run 1 Ports 15-21
Flow Rate (g/min)
12.00
10.00
8.00
6.00
4.00
2.00
0.00
0
100
200
300
400
500
600
Sampling Time (min)
P15
P16
P17
P18
P19
P20
P21

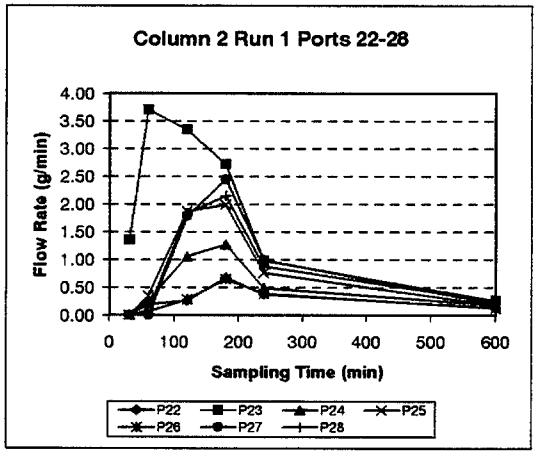
Column 2 Run 1 Ports 22-28
Flow Rate (g/min)
4.00
3.50
3.00
2.50
2.00
1.50
1.00
0.50
0.00
0
100
200
300
400
500
600
Sampling Time (min)
P22
P23
P24
P25
P26
P27
P28

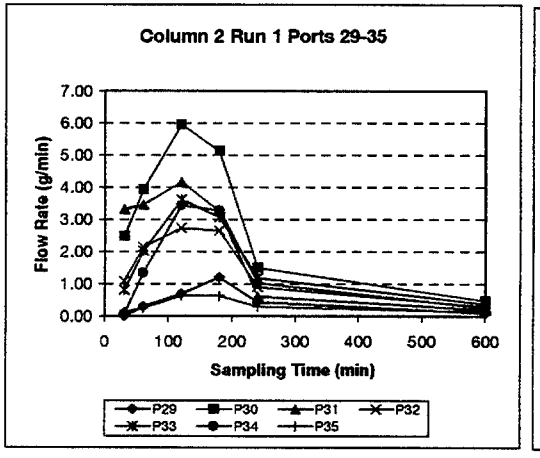
Column 2 Run 1 Ports 29-35
Flow Rate (g/min)
7.00
6.00
5.00
4.00
3.00
2.00
1.00
0.00
0
100
200
300
400
500
600
Sampling Time (min)
P29
P30
P31
P32
P33
P34
P35

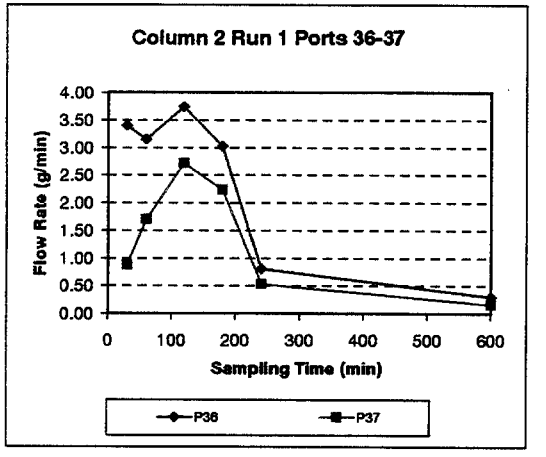
Column 2 Run 1 Ports 36-37
Flow Rate (g/min)
4.00
3.50
3.00
2.50
2.00
1.50
1.00
0.50
0.00
0
100
200
300
400
500
600
Sampling Time (min)
P36
P37

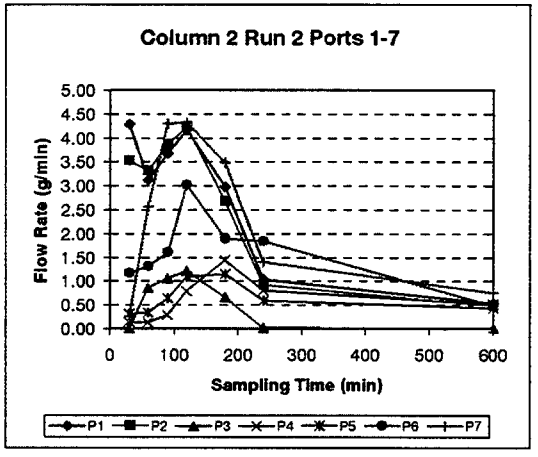
Column 2 Run 2 Ports 1-7
Flow Rate (g/min)
Sampling Time (min)
P1 P2 P3 P4 P5 P6 P7

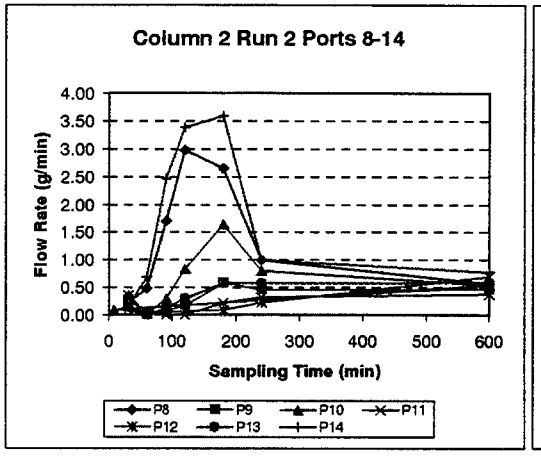
Column 2 Run 2 Ports 8-14
Flow Rate (g/min)
Sampling Time (min)
P8 P9 P10 P11 P12 P13 P14

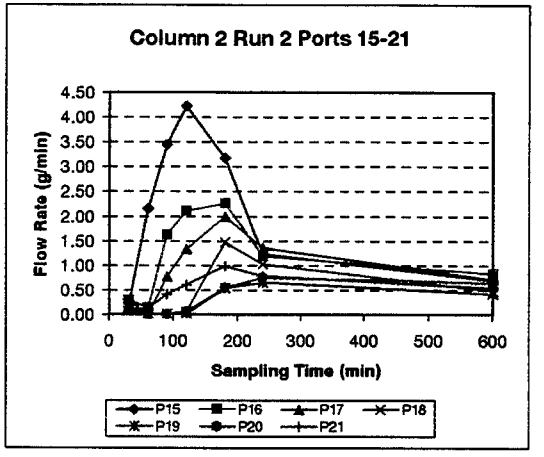
Column 2 Run 2 Ports 15-21
Flow Rate (g/min)
Sampling Time (min)
P15 P16 P17 P18 P19 P20 P21

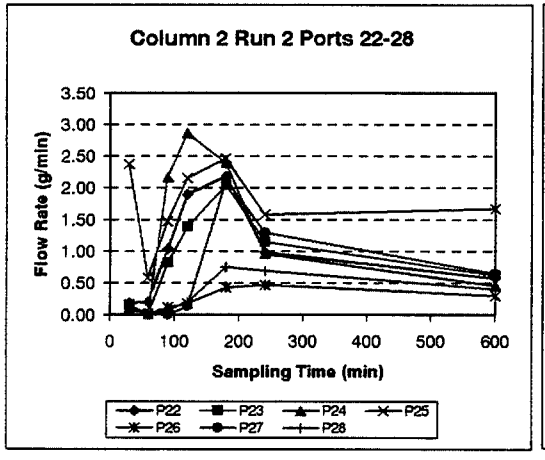
Column 2 Run 2 Ports 22-28
Flow Rate (g/min)
Sampling Time (min)
P22 P23 P24 P25 P26 P27 P28

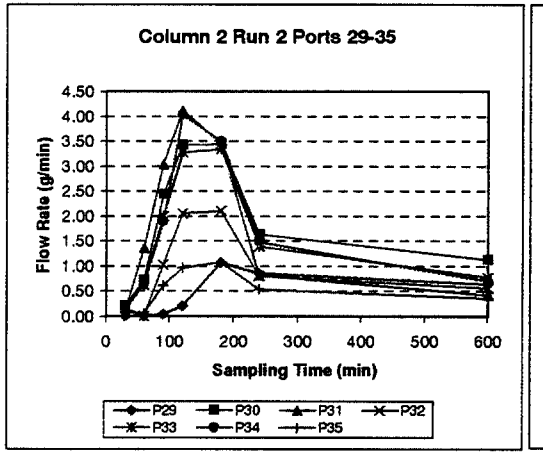
Column 2 Run 2 Ports 29-35
Flow Rate (g/min)
Sampling Time (min)
P29 P30 P31 P32 P33 P34 P35

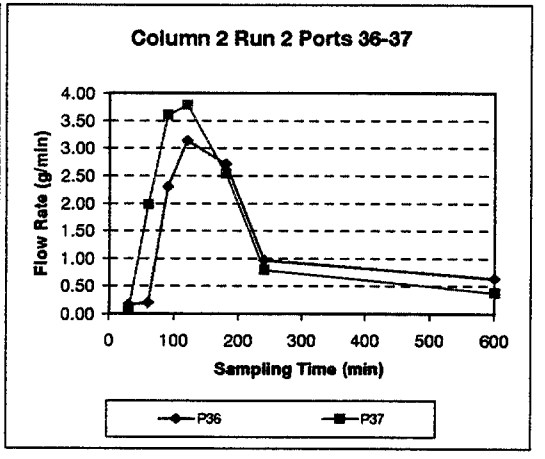
Column 2 Run 2 Ports 36-37
Flow Rate (g/min)
Sampling Time (min)
P36 P37

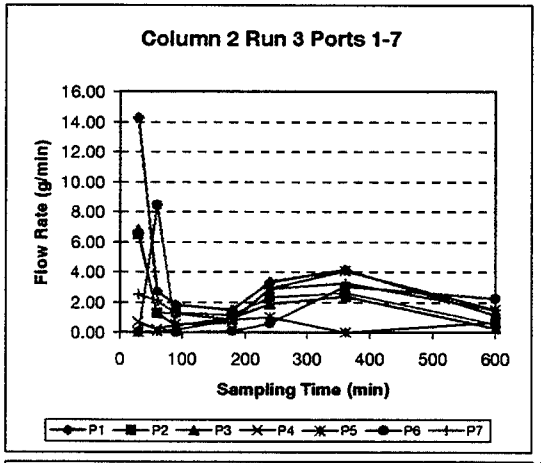
Column 2 Run 3 Ports 1-7
Flow Rate (g/min)
16.00
14.00
12.00
10.00
8.00
6.00
4.00
2.00
0.00
0
100
200
300
400
500
600
Sampling Time (min)
P1
P2
P3
P4
P5
P6
P7

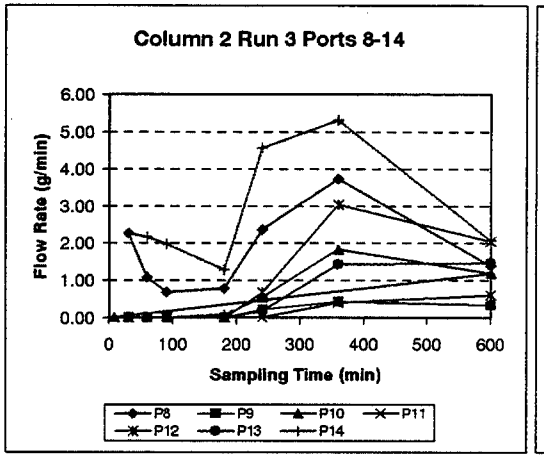
Column 2 Run 3 Ports 8-14
Flow Rate (g/min)
6.00
5.00
4.00
3.00
2.00
1.00
0.00
0
100
200
300
400
500
600
Sampling Time (min)
P8
P9
P10
P11
P12
P13
P14

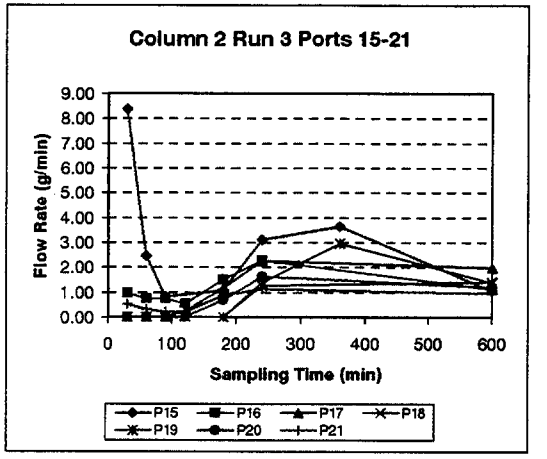
Column 2 Run 3 Ports 15-21
Flow Rate (g/min)
9.00
8.00
7.00
6.00
5.00
4.00
3.00
2.00
1.00
0.00
0
100
200
300
400
500
600
Sampling Time (min)
P15
P16
P17
P18
P19
P20
P21

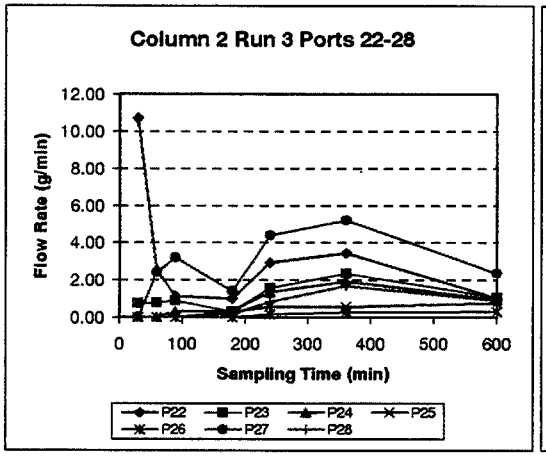
Column 2 Run 3 Ports 22-28
Flow Rate (g/min)
12.00
10.00
8.00
6.00
4.00
2.00
0.00
0
100
200
300
400
500
600
Sampling Time (min)
P22
P23
P24
P25
P26
P27
P28

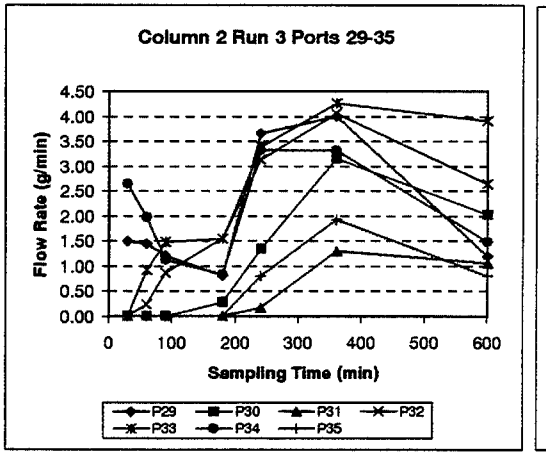
Column 2 Run 3 Ports 29-35
Flow Rate (g/min)
4.50
4.00
3.50
3.00
2.50
2.00
1.50
1.00
0.50
0.00
0
100
200
300
400
500
600
Sampling Time (min)
P29
P30
P31
P32
P33
P34
P35

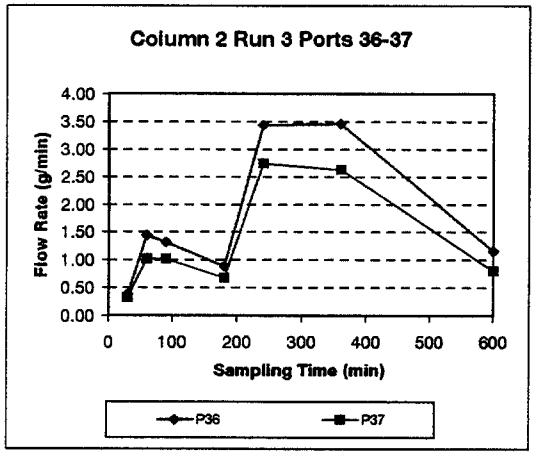
Column 2 Run 3 Ports 36-37
Flow Rate (g/min)
4.00
3.50
3.00
2.50
2.00
1.50
1.00
0.50
0.00
0
100
200
300
400
500
600
Sampling Time (min)
P36
P37

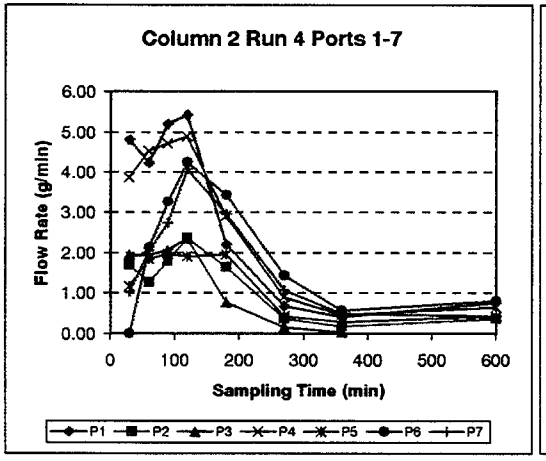
Column 2 Run 4 Ports 1-7
Flow Rate (g/min)
Sampling Time (min)
P1 P2 P3 P4 P5 P6 P7

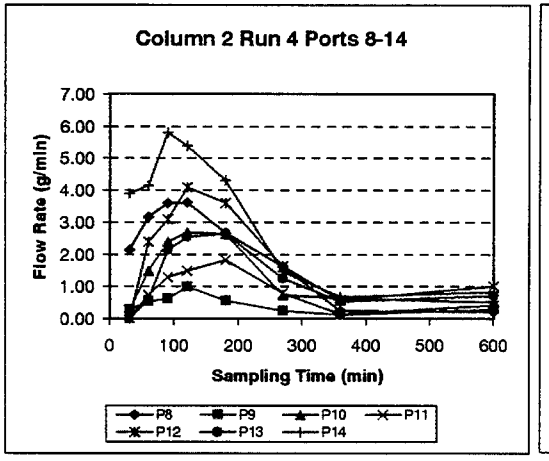
Column 2 Run 4 Ports 8-14
Flow Rate (g/min)
Sampling Time (min)
P8 P9 P10 P11 P12 P13 P14

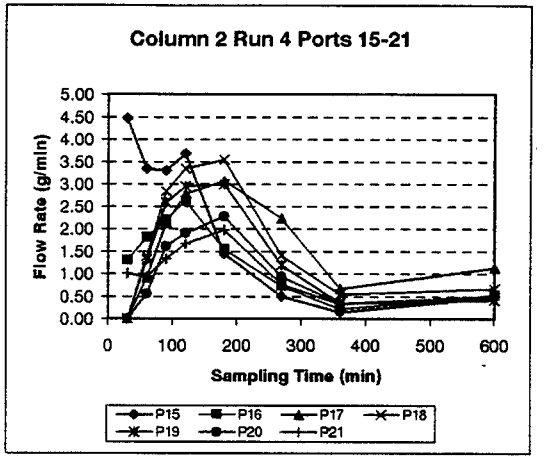
Column 2 Run 4 Ports 15-21
Flow Rate (g/min)
Sampling Time (min)
P15 P16 P17 P18 P19 P20 P21

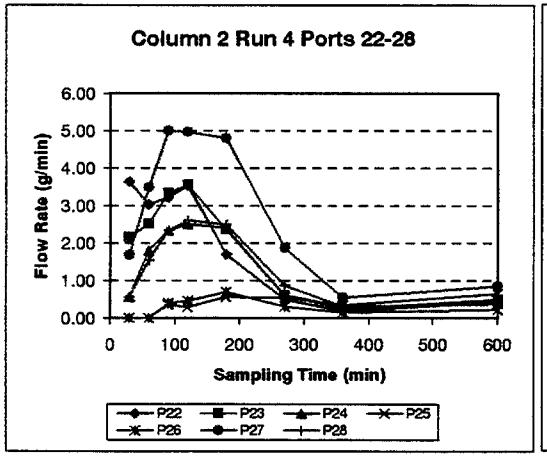
Column 2 Run 4 Ports 22-28
Flow Rate (g/min)
Sampling Time (min)
P22 P23 P24 P25 P26 P27 P28

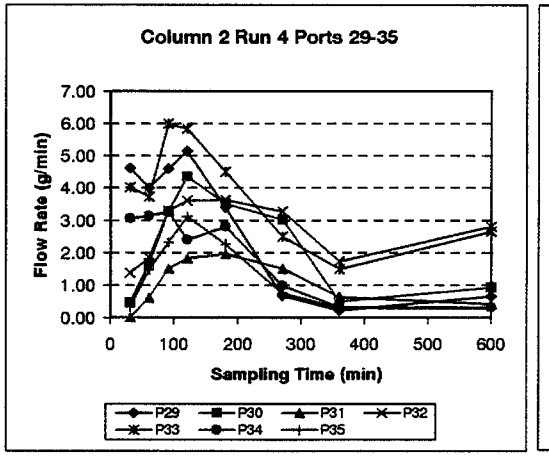
Column 2 Run 4 Ports 29-35
Flow Rate (g/min)
Sampling Time (min)
P29 P30 P31 P32 P33 P34 P35

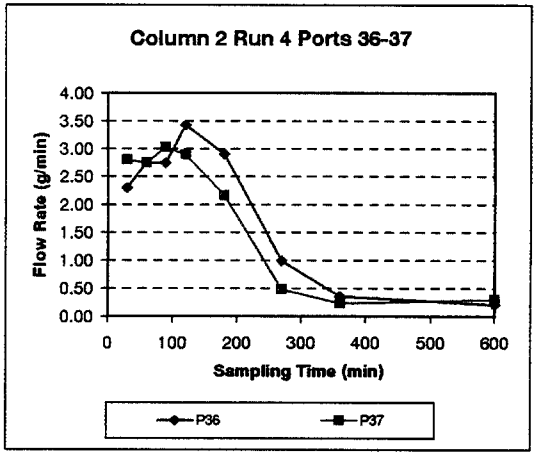
Column 2 Run 4 Ports 36-37
Flow Rate (g/min)
Sampling Time (min)
P36 P37

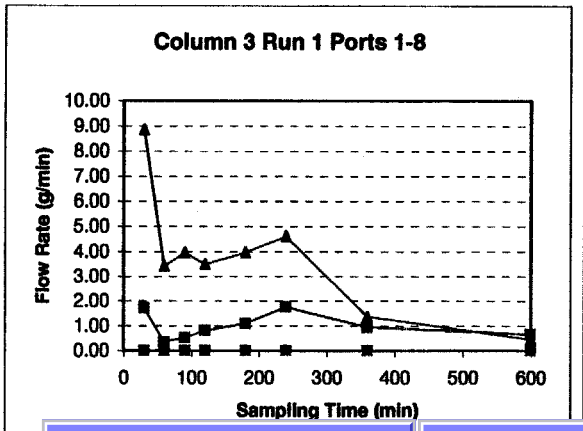

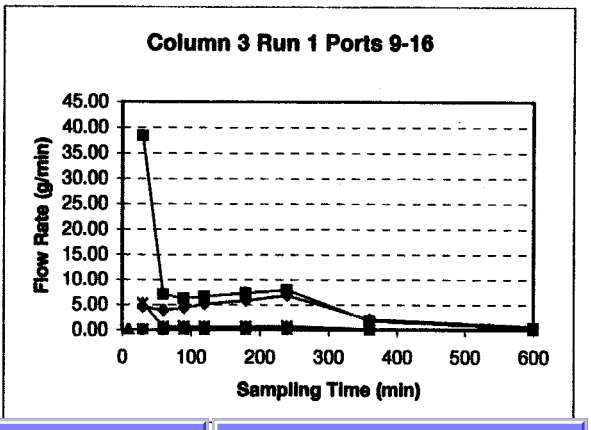

Welcome Screen | Search | Report List

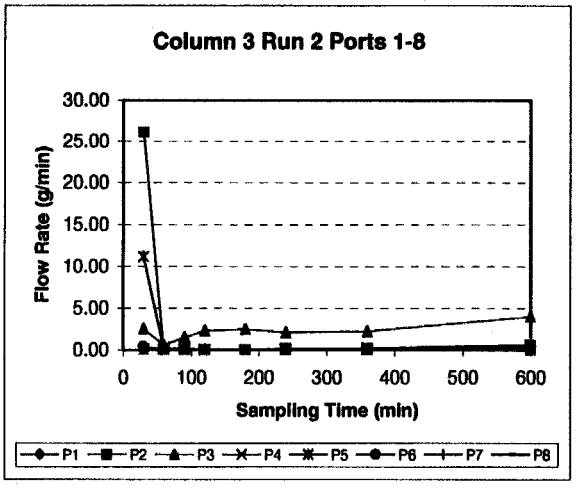

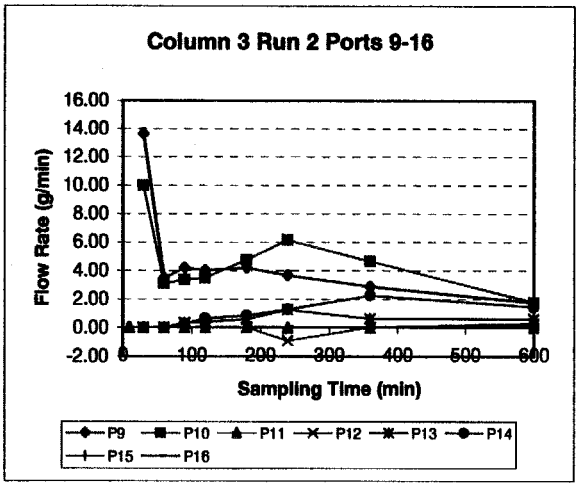

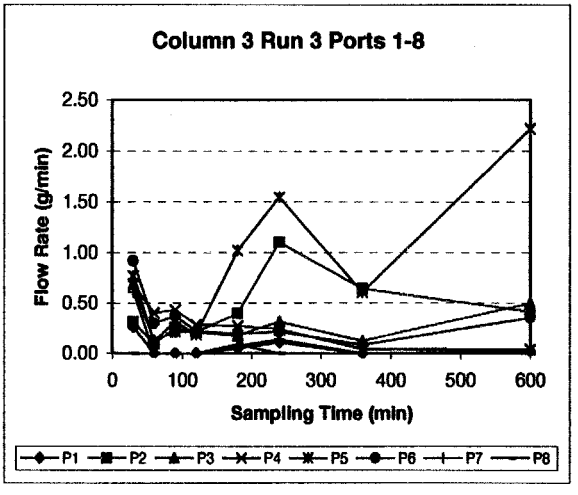

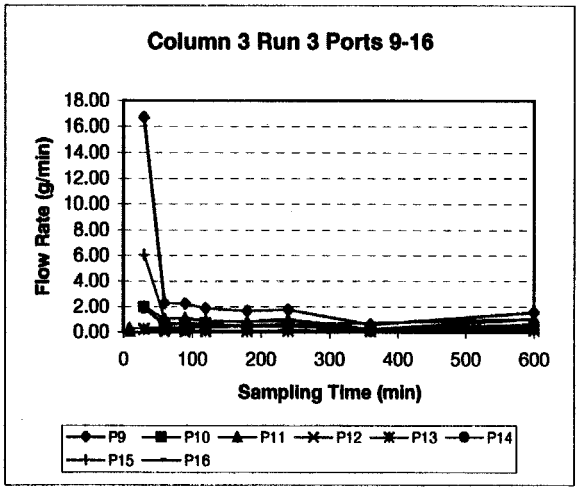

APPENDIX III DRAINAGE CHEMOGRAPHS (ZN)

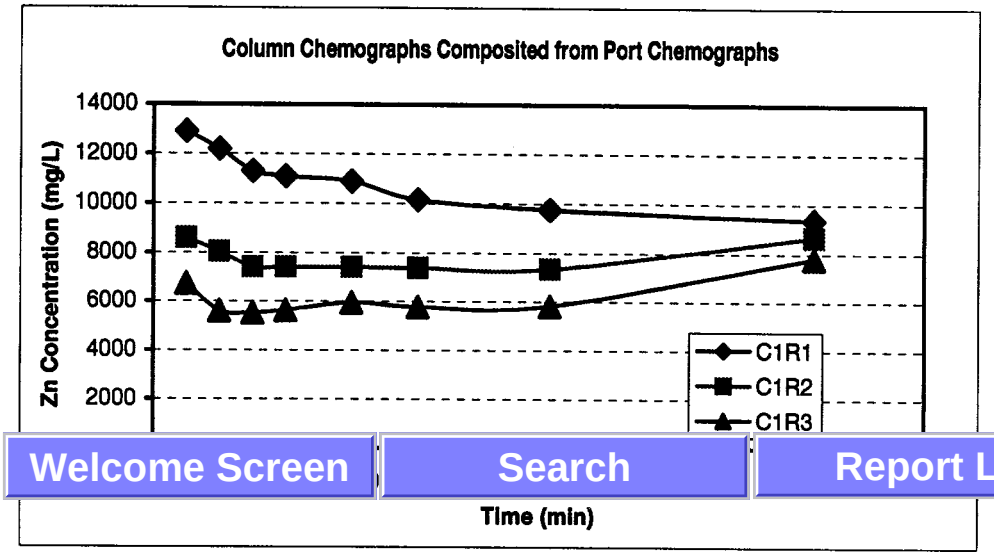
Column Chemographs Composited from Port Chemographs
Zn Concentration (mg/L)
14000
12000
10000
8000
6000
4000
2000
C1R1
C1R2
C1R3
Time (min)

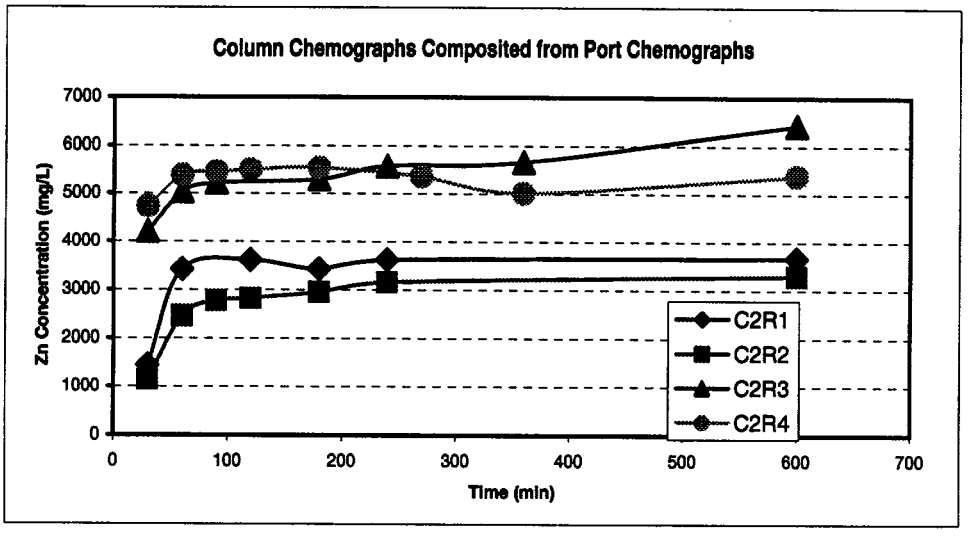
Column Chemographs Composited from Port Chemographs
Zn Concentration (mg/L)
7000
6000
5000
4000
3000
2000
1000
0
0
100
200
300
400
500
600
700
C2R1
C2R2
C2R3
C2R4
Time (min)

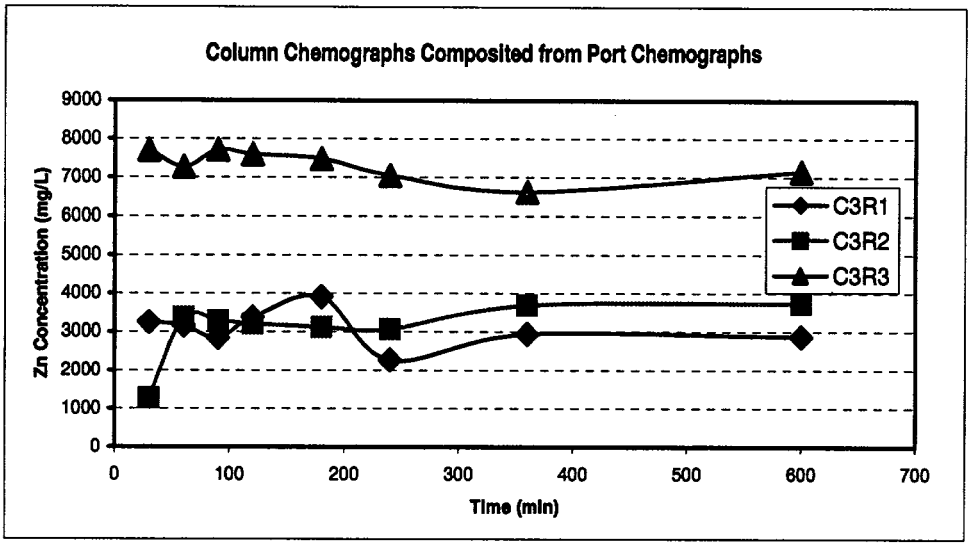
Column Chemographs Composited from Port Chemographs
Zn Concentration (mg/L)
9000
8000
7000
6000
5000
4000
3000
2000
1000
0
0
100
200
300
400
500
600
700
C3R1
C3R2
C3R3
Time (min)

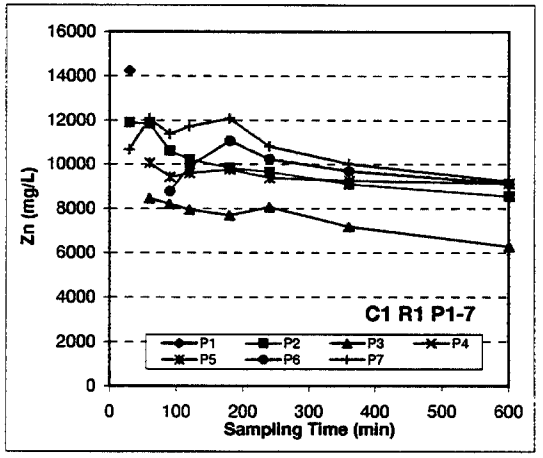
Zn (mg/L)
Sampling Time (min)
C1 R1 P1-7
P1 P2 P3 P4
P5 P6 P7

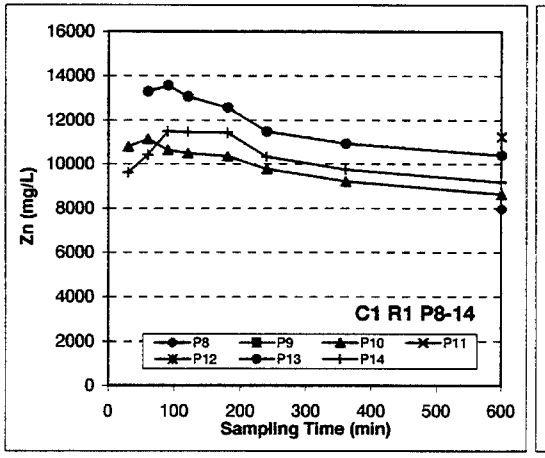
Zn (mg/L)
Sampling Time (min)
C1 R1 P8-14
P8 P9 P10 P11
P12 P13 P14

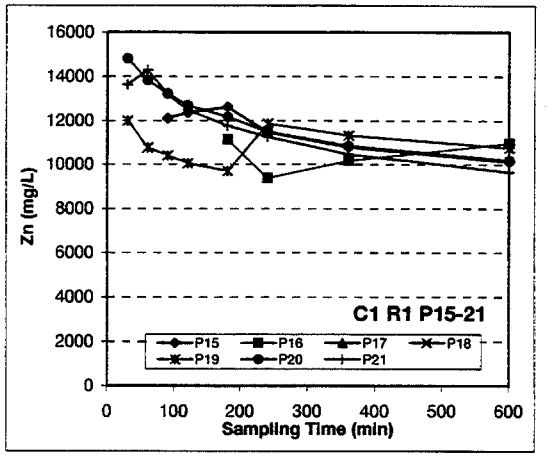
Zn (mg/L)
Sampling Time (min)
C1 R1 P15-21
P15 P16 P17 P18
P19 P20 P21

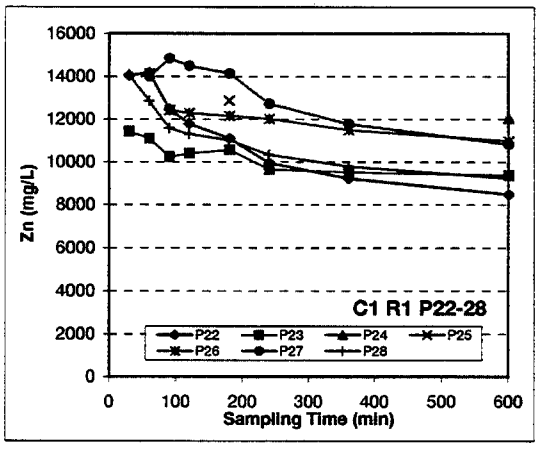
Zn (mg/L)
Sampling Time (min)
C1 R1 P22-28
P22 P23 P24 P25
P26 P27 P28

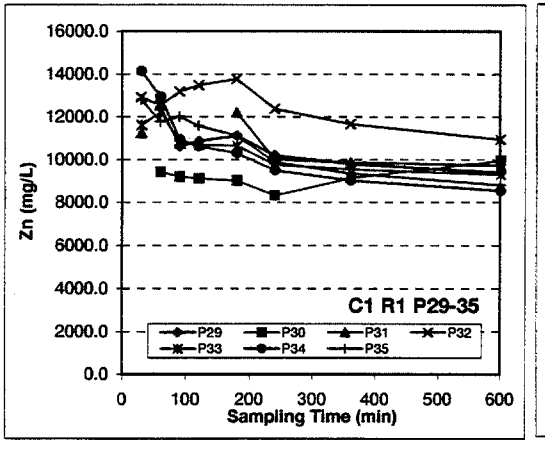
Zn (mg/L)
Sampling Time (min)
C1 R1 P29-35
P29 P30 P31 P32
P33 P34 P35

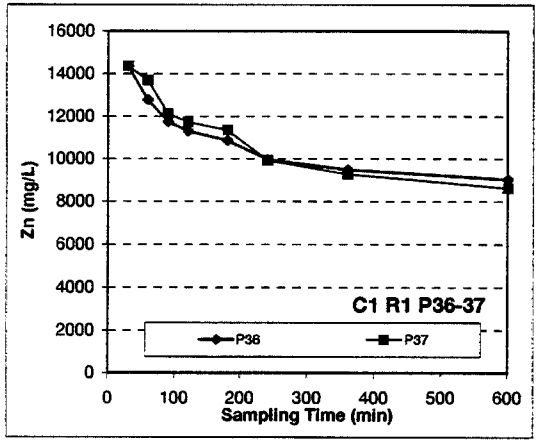
Zn (mg/L)
Sampling Time (min)
C1 R1 P36-37
P36 P37

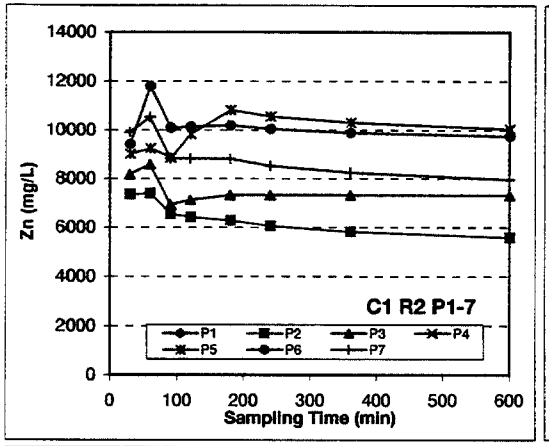
C1 R2 P1-7
P1 P2 P3 P4 P5 P6 P7
Zn (mg/L)
Sampling Time (min)

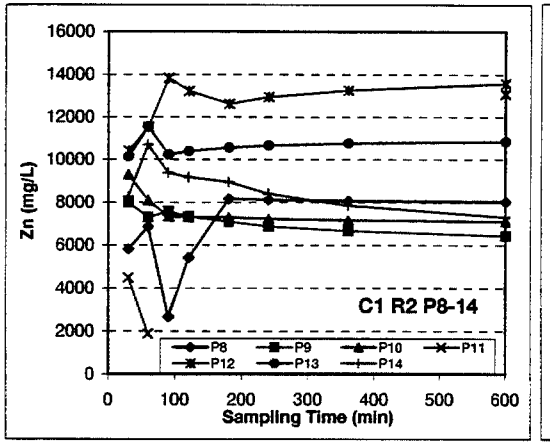
C1 R2 P8-14
P8 P9 P10 P11 P12 P13 P14
Zn (mg/L)
Sampling Time (min)

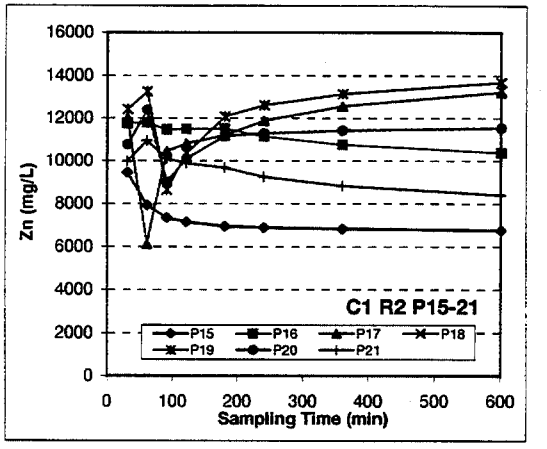
C1 R2 P15-21
P15 P16 P17 P18 P19 P20 P21
Zn (mg/L)
Sampling Time (min)

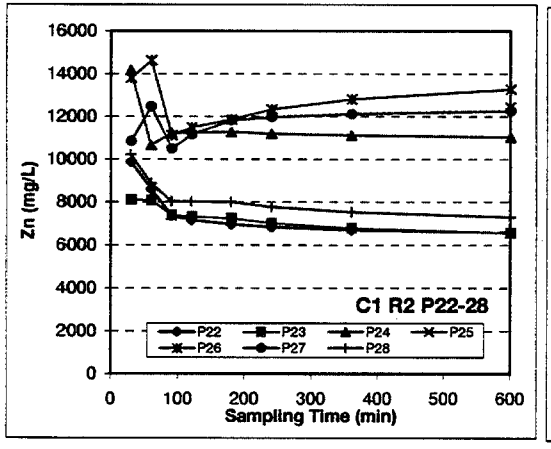
C1 R2 P22-28
P22 P23 P24 P25 P26 P27 P28
Zn (mg/L)
Sampling Time (min)

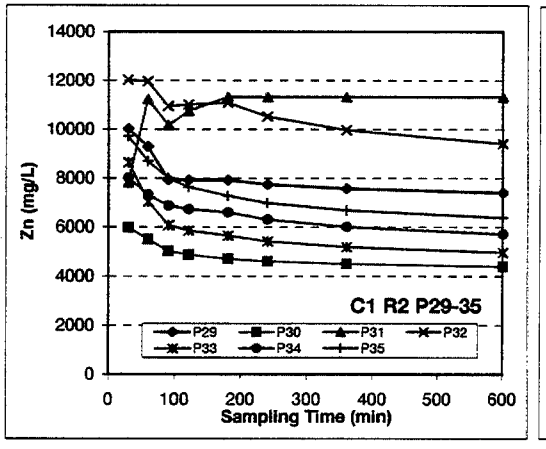
C1 R2 P29-35
P29 P30 P31 P32 P33 P34 P35
Zn (mg/L)
Sampling Time (min)

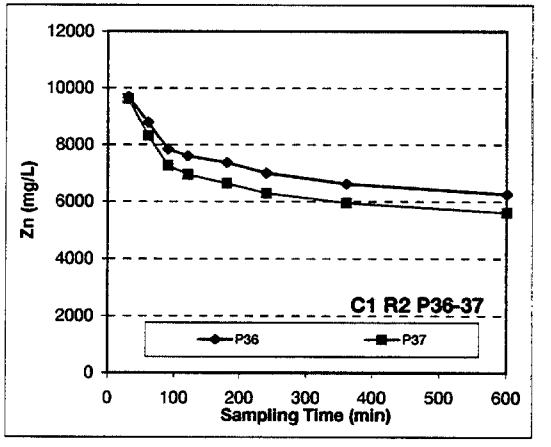
C1 R2 P36-37
P36 P37
Zn (mg/L)
Sampling Time (min)

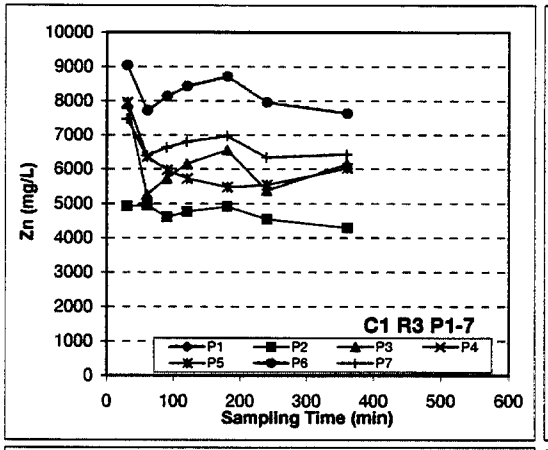
Zn (mg/L)
Sampling Time (min)
C1 R3 P1-7
P1 P2 P3 P4
P5 P6 P7

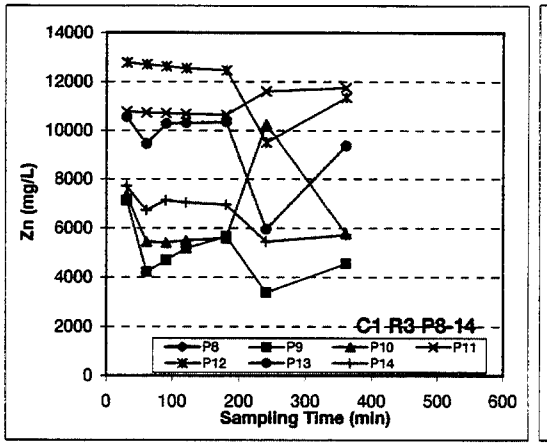
Zn (mg/L)
Sampling Time (min)
C1 R3 P8-14
P8 P9 P10 P11
P12 P13 P14

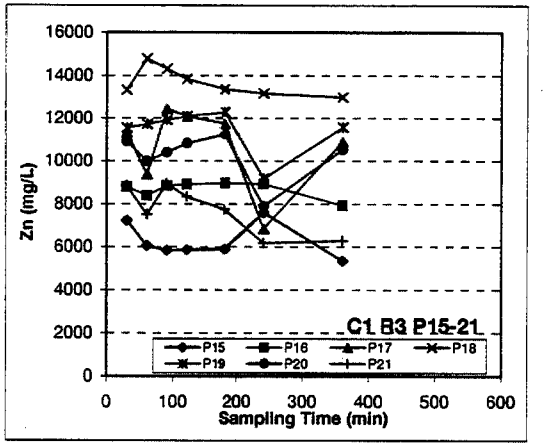
Zn (mg/L)
Sampling Time (min)
C1 R3 P15-21
P15 P16 P17 P18
P19 P20 P21

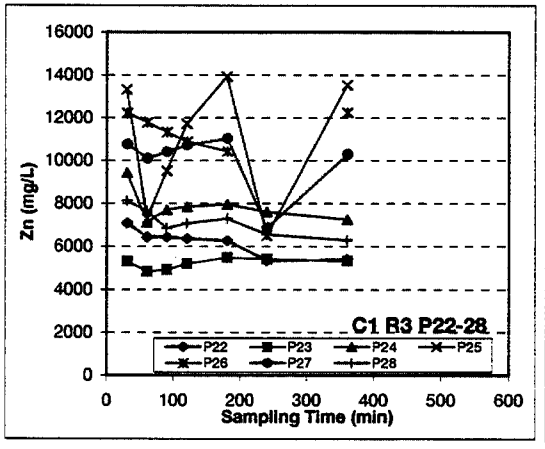
Zn (mg/L)
Sampling Time (min)
C1 R3 P22-28
P22 P23 P24 P25
P26 P27 P28

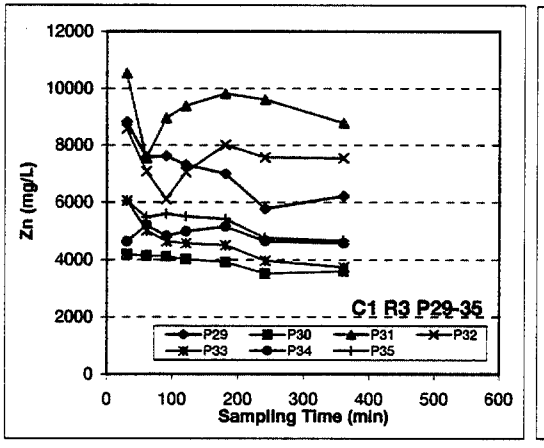
Zn (mg/L)
Sampling Time (min)
C1 R3 P29-35
P29 P30 P31 P32
P33 P34 P35

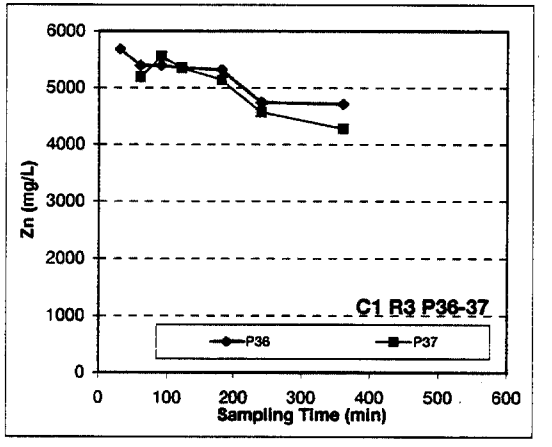
Zn (mg/L)
Sampling Time (min)
C1 R3 P36-37
P36 P37

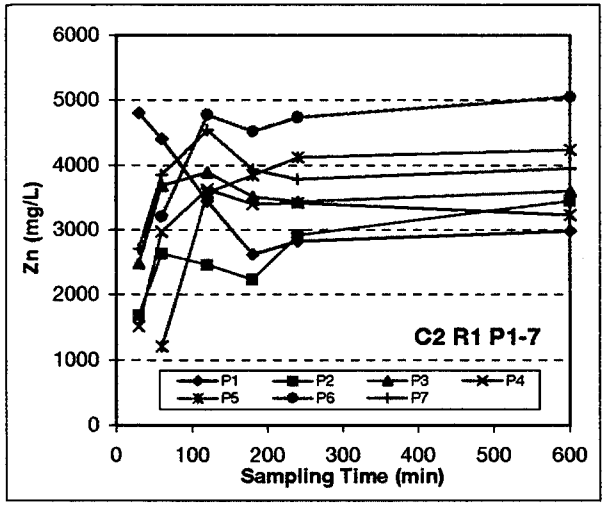
Zn (mg/L)
Sampling Time (min)
C2 R1 P1-7
P1 P2 P3 P4
P5 P6 P7

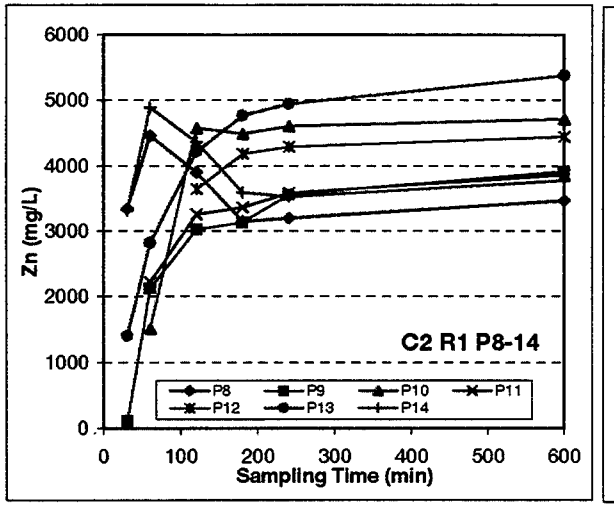
Zn (mg/L)
Sampling Time (min)
C2 R1 P8-14
P8 P9 P10 P11
P12 P13 P14

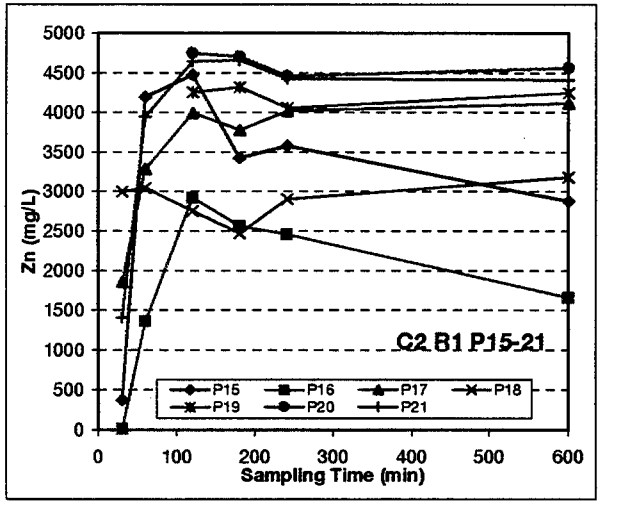
Zn (mg/L)
Sampling Time (min)
C2 B1 P15-21
P15 P16 P17 P18
P19 P20 P21

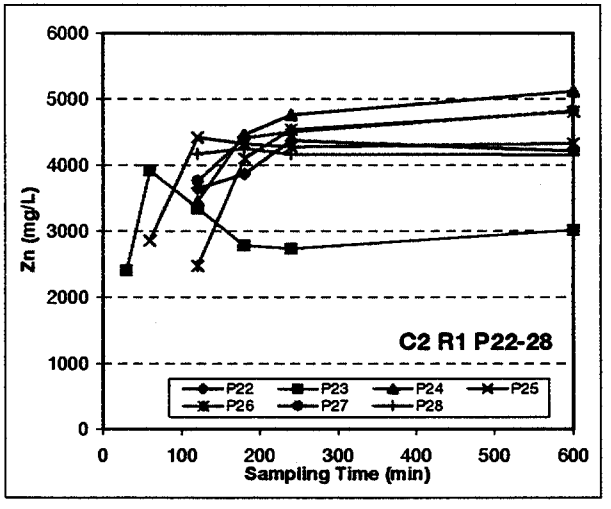
Zn (mg/L)
Sampling Time (min)
C2 R1 P22-28
P22 P23 P24 P25
P26 P27 P28

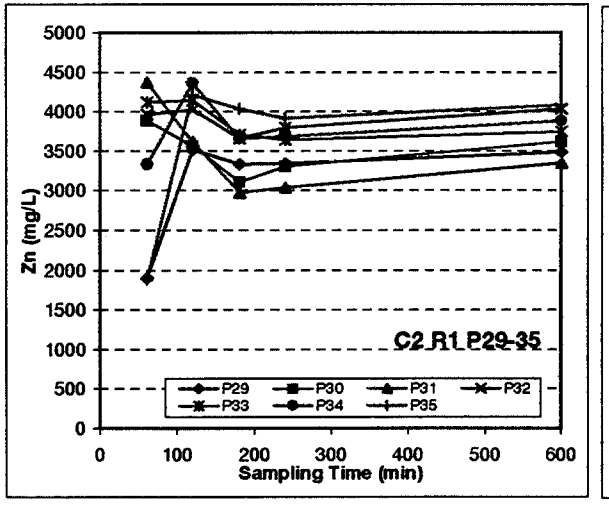
Zn (mg/L)
Sampling Time (min)
C2 R1 P29-35
P29 P30 P31 P32
P33 P34 P35

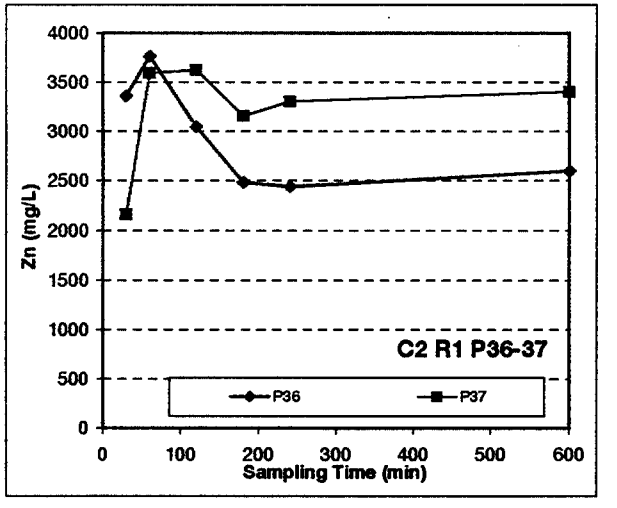
Zn (mg/L)
Sampling Time (min)
C2 R1 P36-37
P36 P37

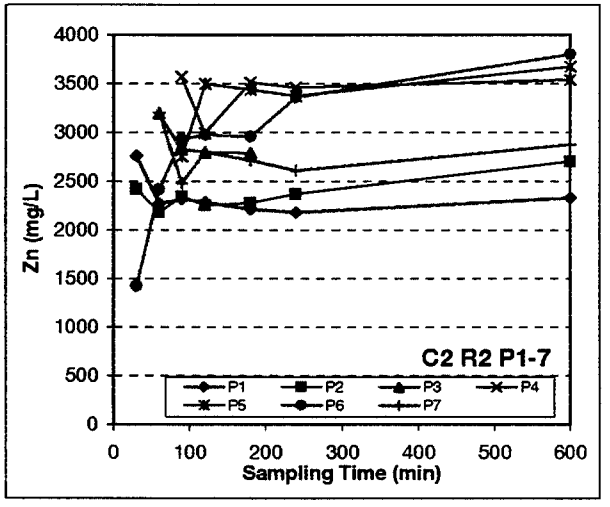
Zn (mg/L)
Sampling Time (min)
C2 R2 P1-7
P1 P2 P3 P4
P5 P6 P7

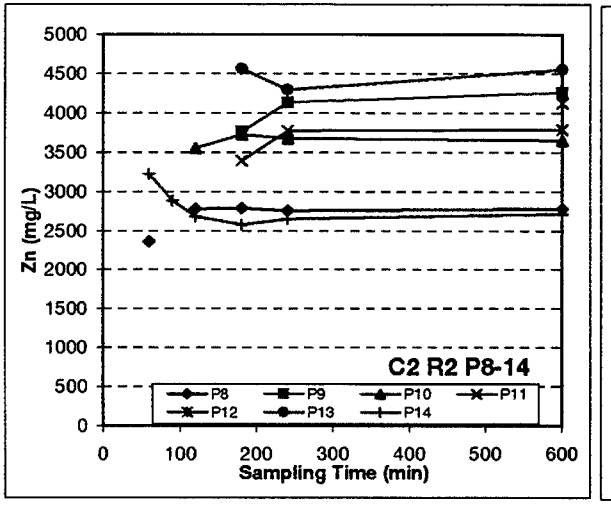
Zn (mg/L)
Sampling Time (min)
C2 R2 P8-14
P8 P9 P10 P11
P12 P13 P14

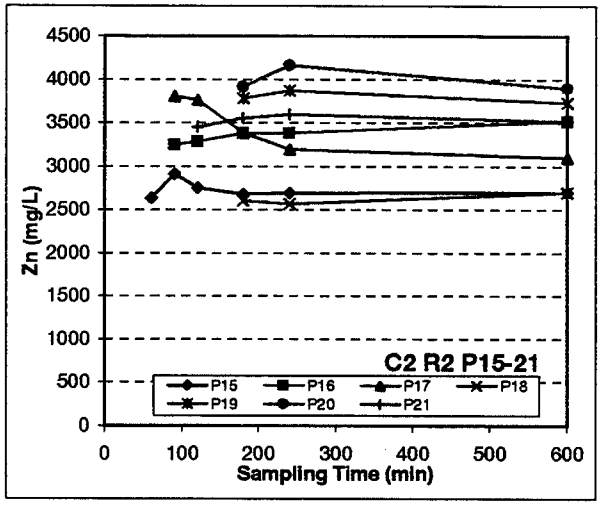
Zn (mg/L)
Sampling Time (min)
C2 R2 P15-21
P15 P16 P17 P18
P19 P20 P21

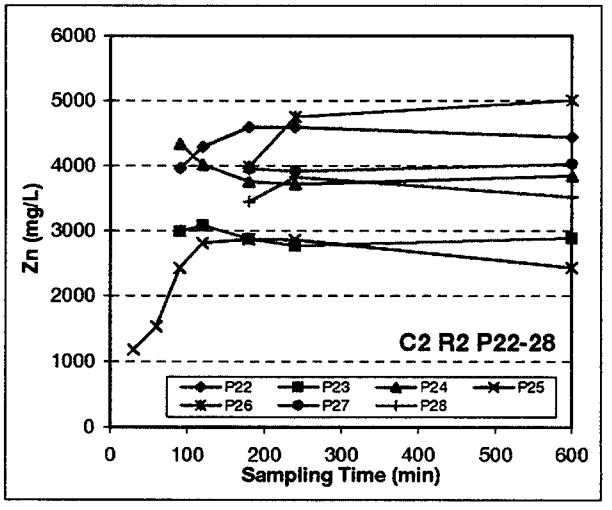
Zn (mg/L)
Sampling Time (min)
C2 R2 P22-28
P22 P23 P24 P25
P26 P27 P28

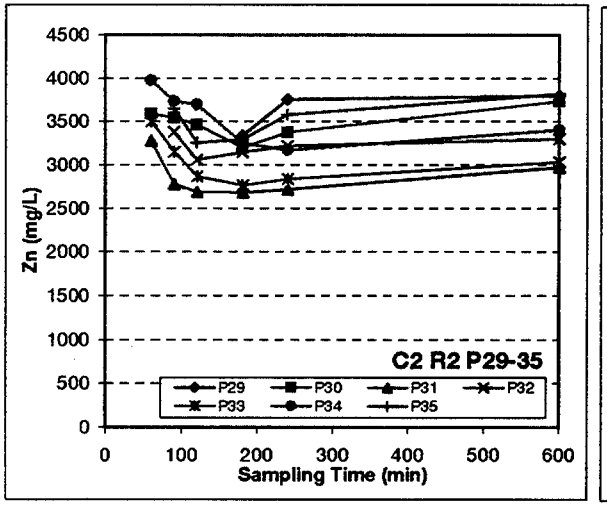
Zn (mg/L)
Sampling Time (min)
C2 R2 P29-35
P29 P30 P31 P32
P33 P34 P35

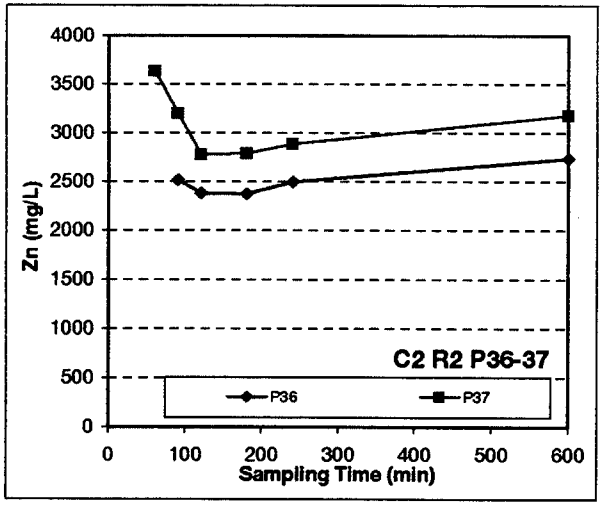
Zn (mg/L)
Sampling Time (min)
C2 R2 P36-37
P36 P37

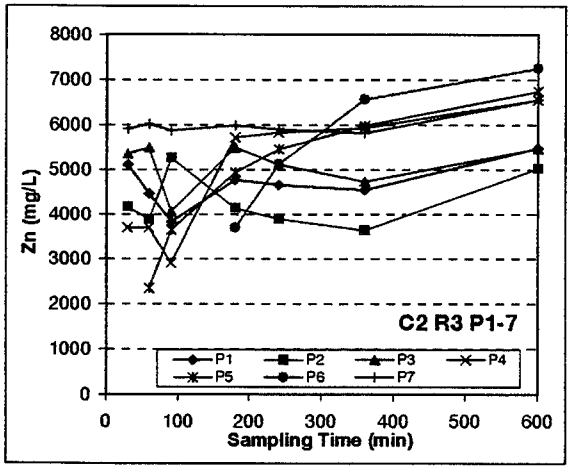
C2 R3 P1-7
Zn (mg/L)
Sampling Time (min)
P1 P2 P3 P4 P5 P6 P7

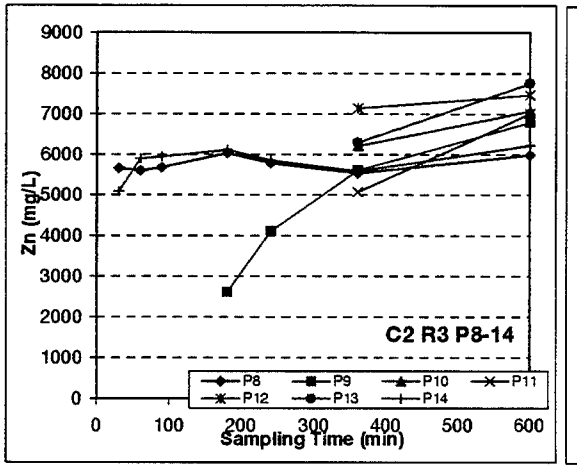
C2 R3 P8-14
Zn (mg/L)
Sampling Time (min)
P8 P9 P10 P11 P12 P13 P14

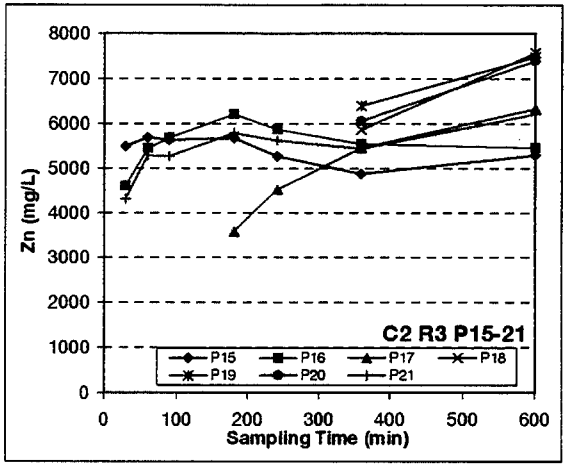
C2 R3 P15-21
Zn (mg/L)
Sampling Time (min)
P15 P16 P17 P18 P19 P20 P21

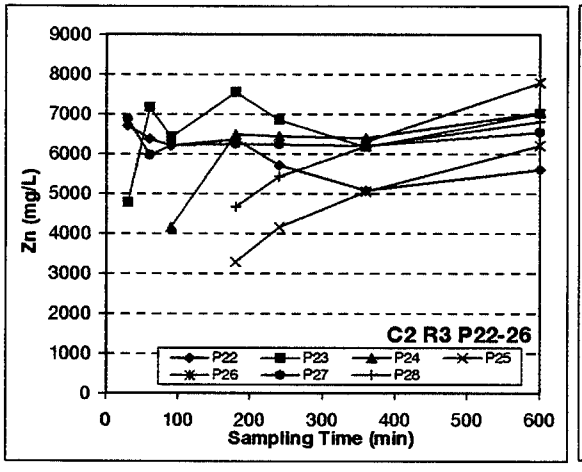
C2 R3 P22-26
Zn (mg/L)
Sampling Time (min)
P22 P23 P24 P25 P26 P27 P28

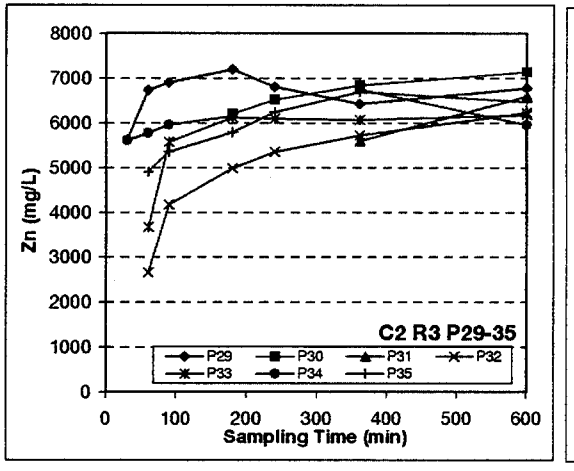
C2 R3 P29-35
Zn (mg/L)
Sampling Time (min)
P29 P30 P31 P32 P33 P34 P35

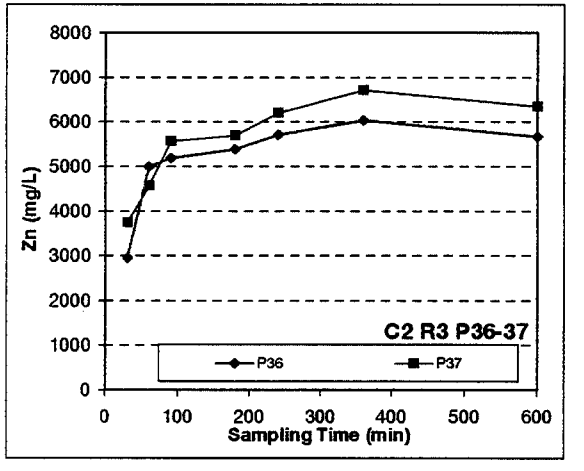
C2 R3 P36-37
Zn (mg/L)
Sampling Time (min)
P36 P37

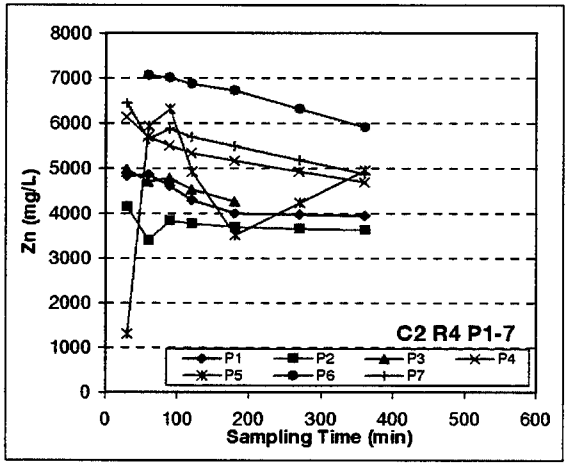
C2 R4 P1-7
P1 P2 P3 P4 P5 P6 P7
Zn (mg/L)
Sampling Time (min)

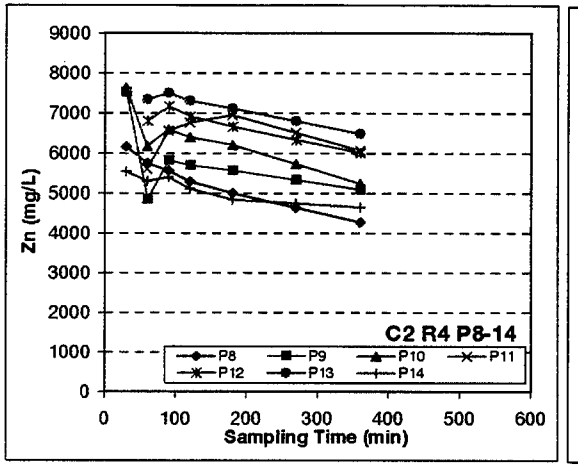
C2 R4 P8-14
P8 P9 P10 P11 P12 P13 P14
Zn (mg/L)
Sampling Time (min)

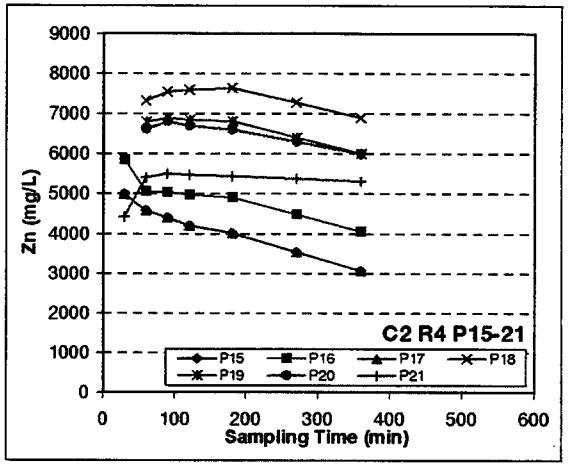
C2 R4 P15-21
P15 P16 P17 P18 P19 P20 P21
Zn (mg/L)
Sampling Time (min)

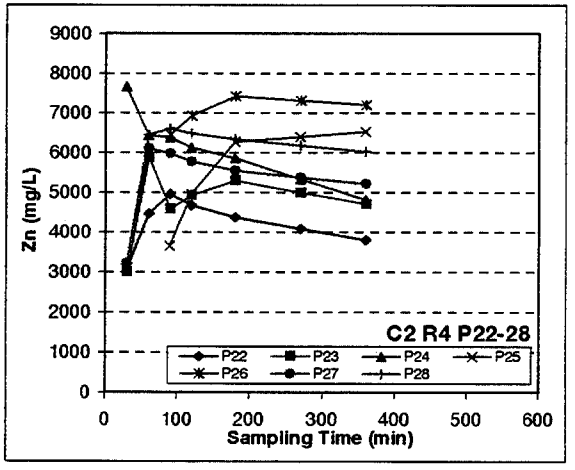
C2 R4 P22-28
P22 P23 P24 P25 P26 P27 P28
Zn (mg/L)
Sampling Time (min)

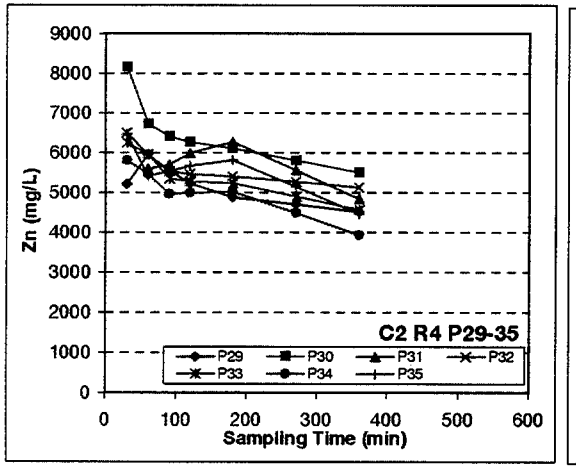
C2 R4 P29-35
P29 P30 P31 P32 P33 P34 P35
Zn (mg/L)
Sampling Time (min)

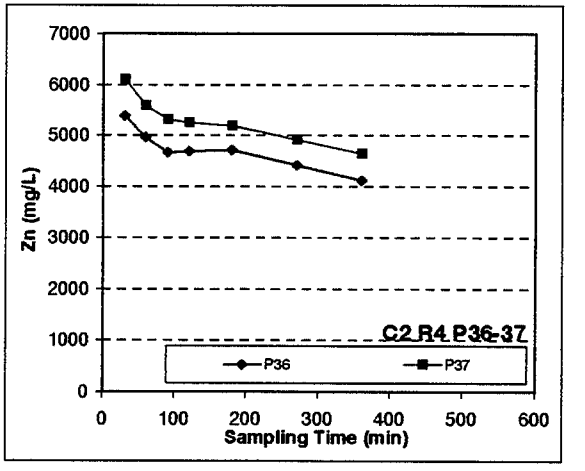
C2 R4 P36-37
P36 P37
Zn (mg/L)
Sampling Time (min)

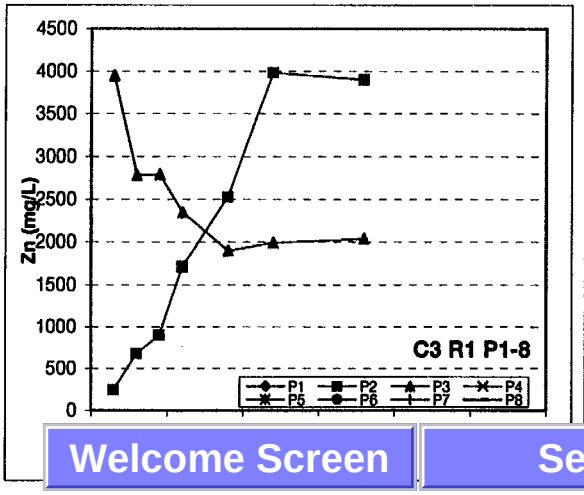

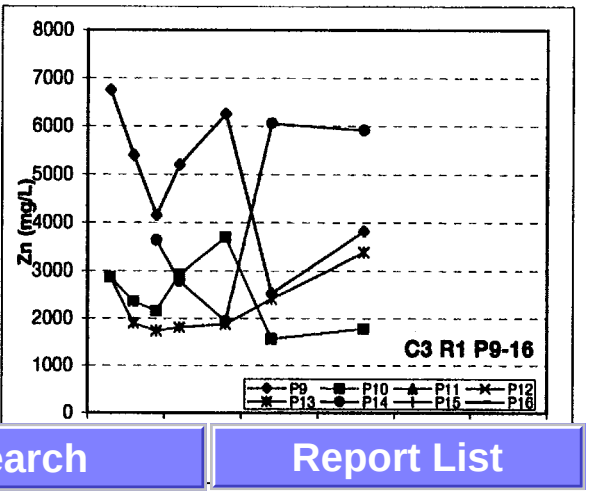

Welcome Screen | Search | Report List

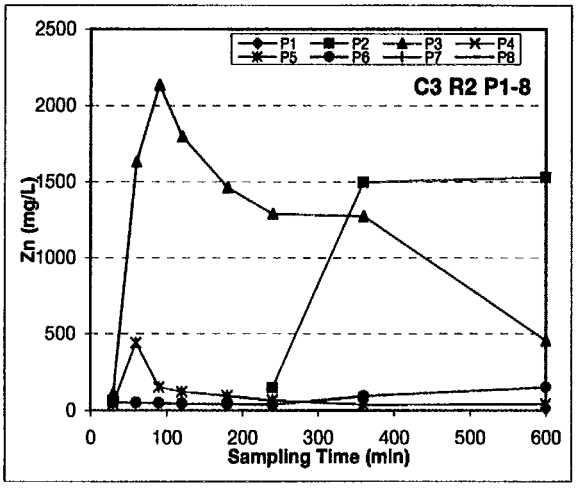

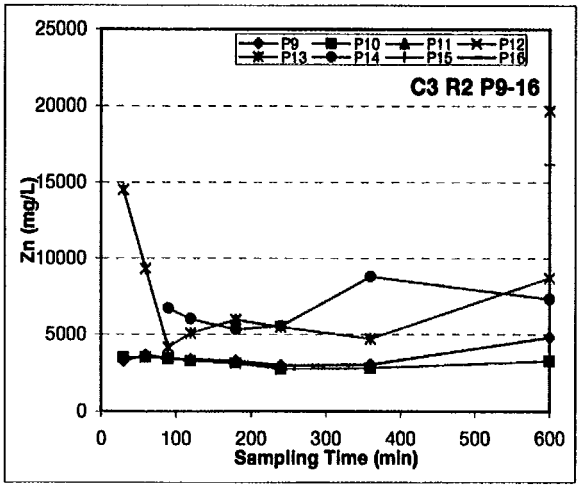

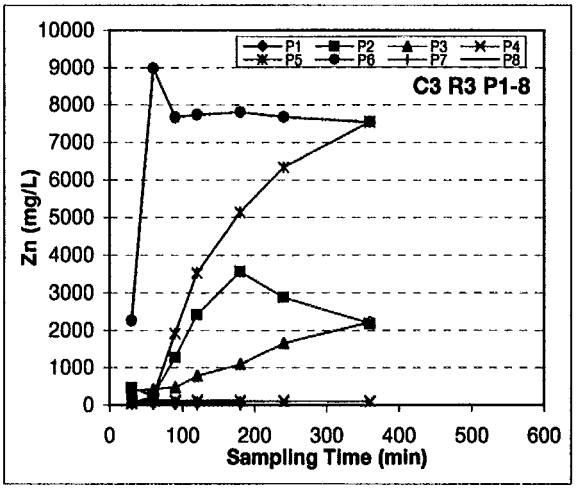

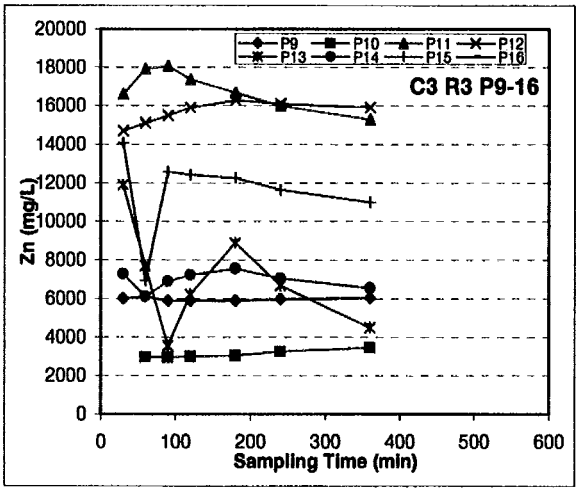

APPENDIX IV DRAINAGE CHEMOGRAPHS (PH)

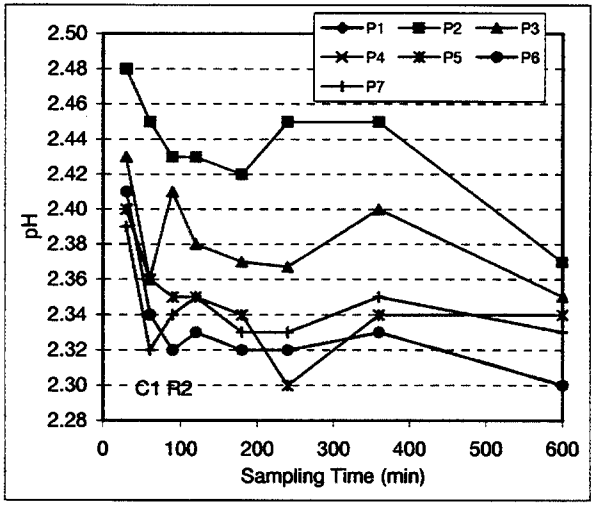
P1 P2 P3
P4 P5 P6
P7
pH
Sampling Time (min)
C1 R2

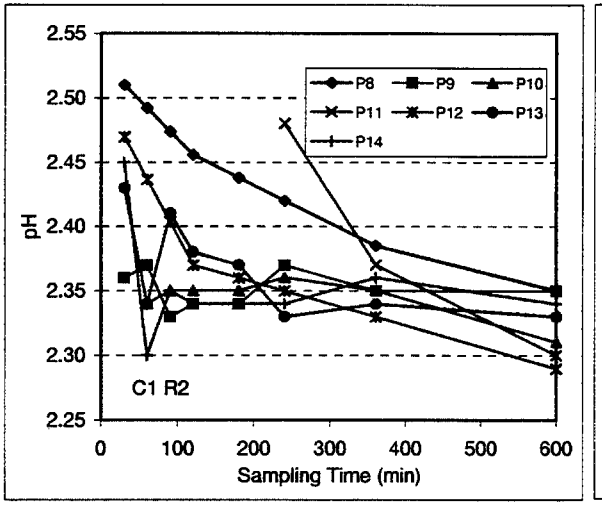
P8 P9 P10
P11 P12 P13
P14
pH
Sampling Time (min)
C1 R2

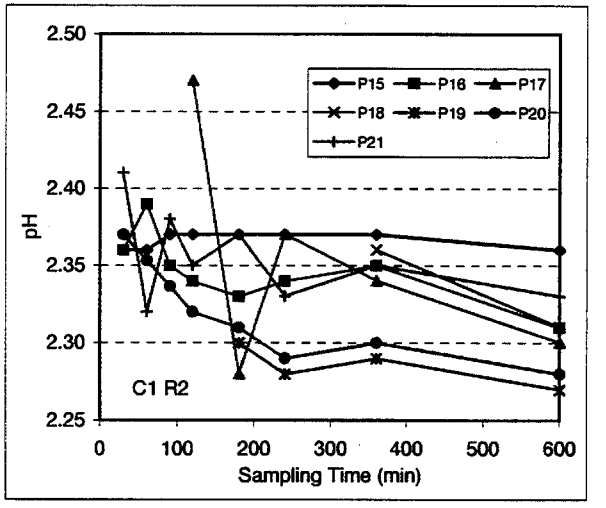
P15 P16 P17
P18 P19 P20
P21
pH
Sampling Time (min)
C1 R2

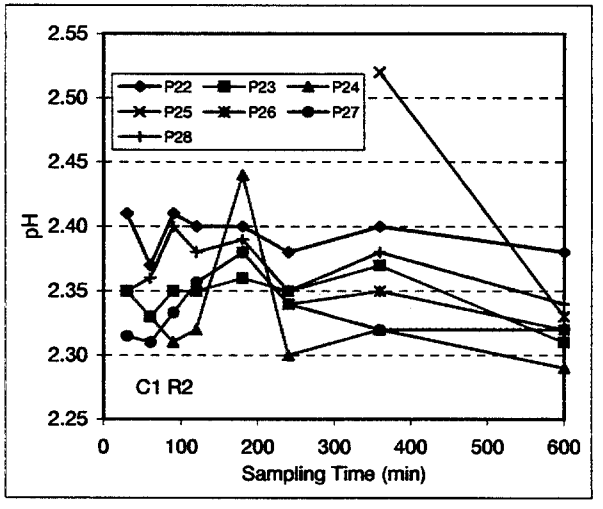
P22 P23 P24
P25 P26 P27
P28
pH
Sampling Time (min)
C1 R2

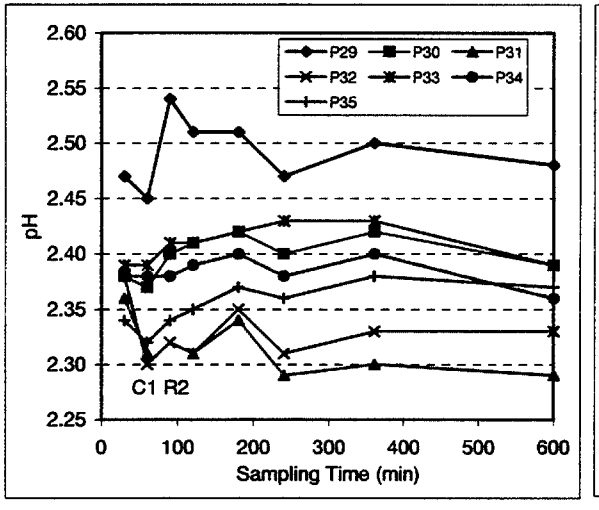
P29 P30 P31
P32 P33 P34
P35
pH
Sampling Time (min)
C1 R2

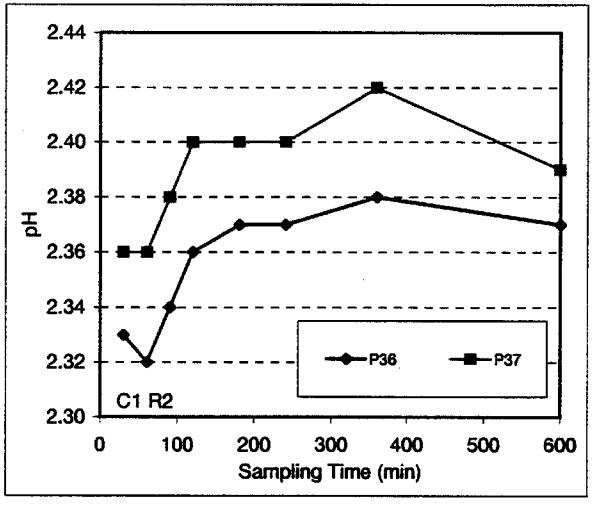
P36 P37
pH
Sampling Time (min)
C1 R2

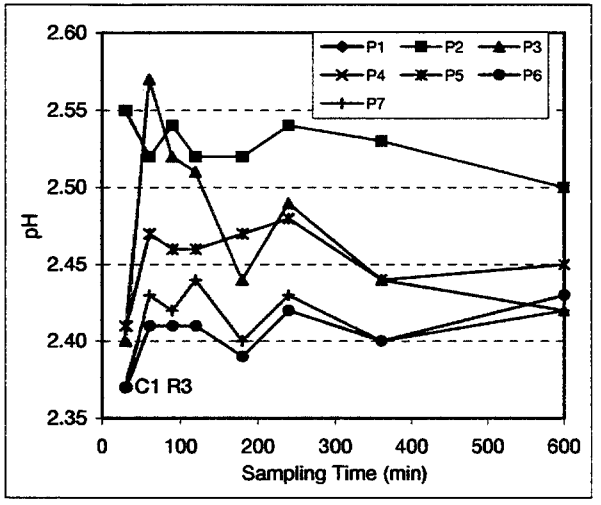
P1 P2 P3
P4 P5 P6
P7
C1 R3
pH
Sampling Time (min)

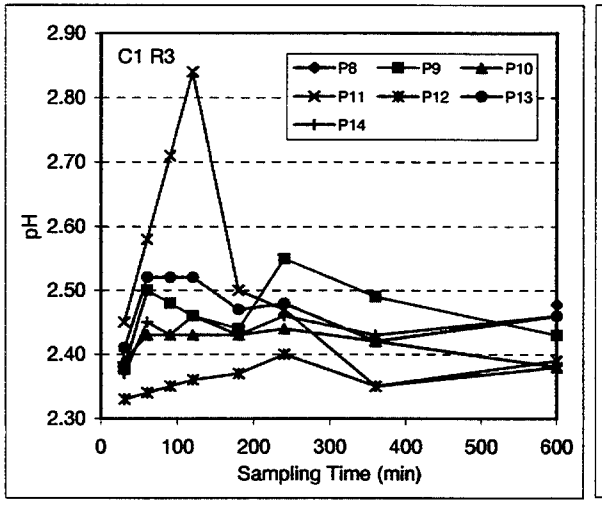
C1 R3
P8 P9 P10
P11 P12 P13
P14
pH
Sampling Time (min)

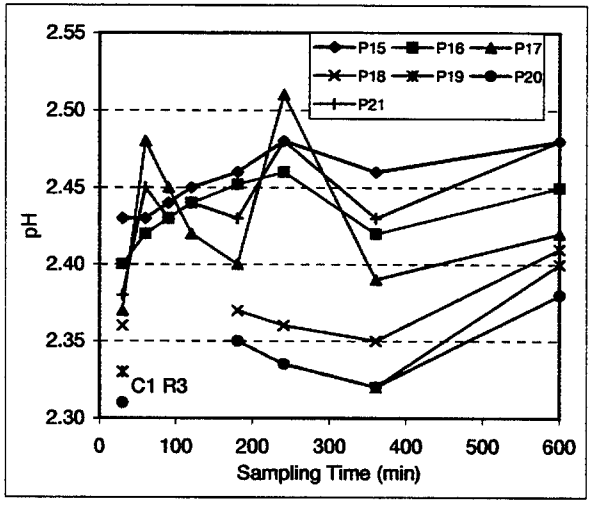
P15 P16 P17
P18 P19 P20
P21
C1 R3
pH
Sampling Time (min)

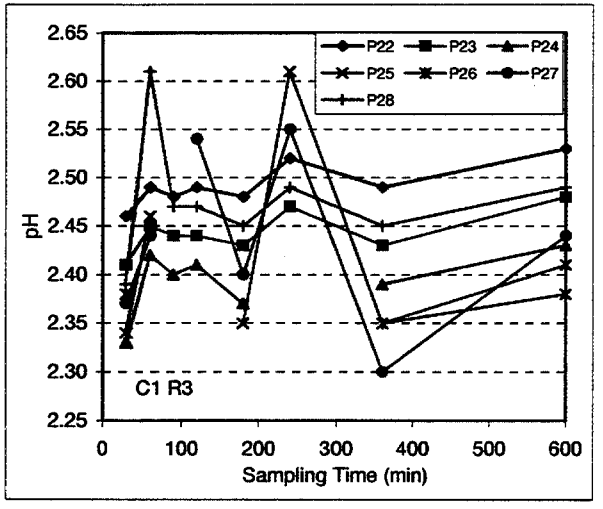
P22 P23 P24
P25 P26 P27
P28
C1 R3
pH
Sampling Time (min)

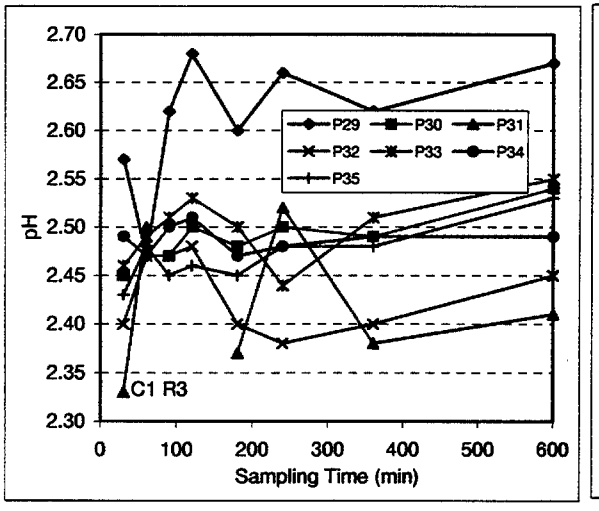
P29 P30 P31
P32 P33 P34
P35
C1 R3
pH
Sampling Time (min)

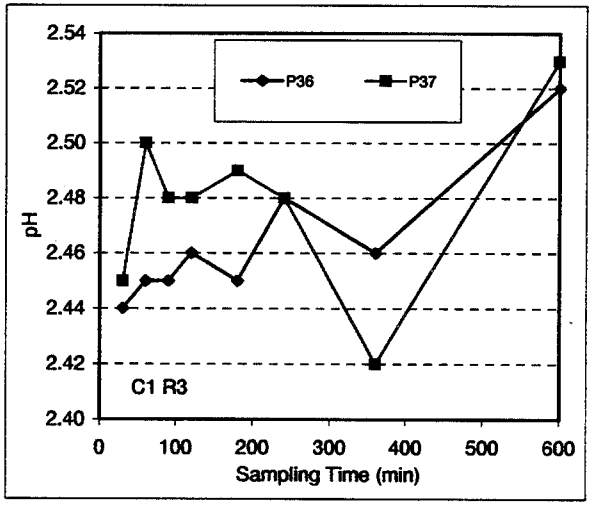
P36 P37
C1 R3
pH
Sampling Time (min)

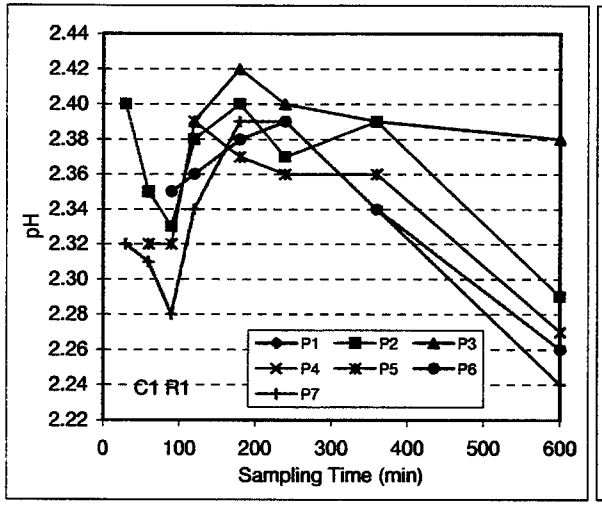
pH
Sampling Time (min)
C1 R1
P1 P2 P3
P4 P5 P6
P7

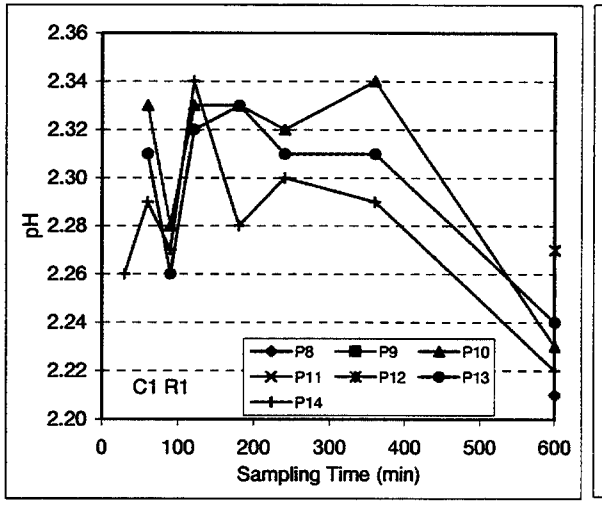
pH
Sampling Time (min)
C1 R1
P8 P9 P10
P11 P12 P13
P14

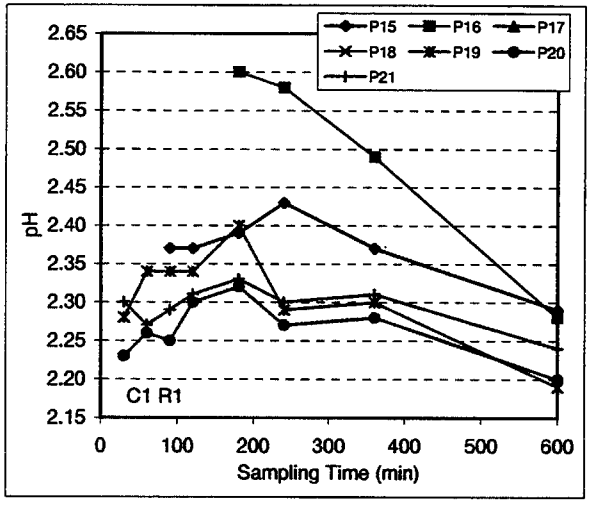
pH
Sampling Time (min)
C1 R1
P15 P16 P17
P18 P19 P20
P21

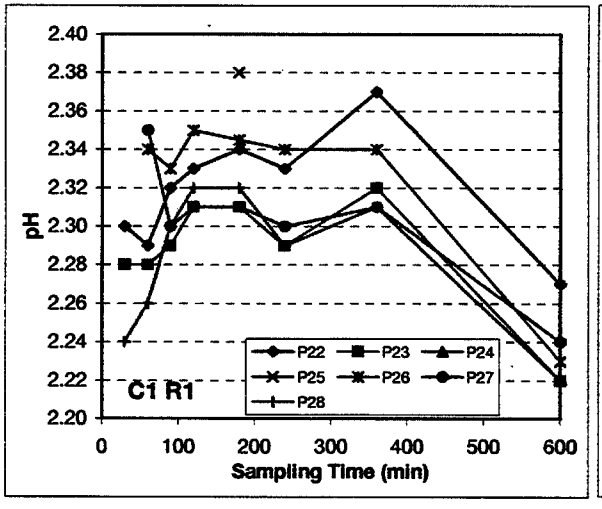
pH
Sampling Time (min)
C1 R1
P22 P23 P24
P25 P26 P27
P28

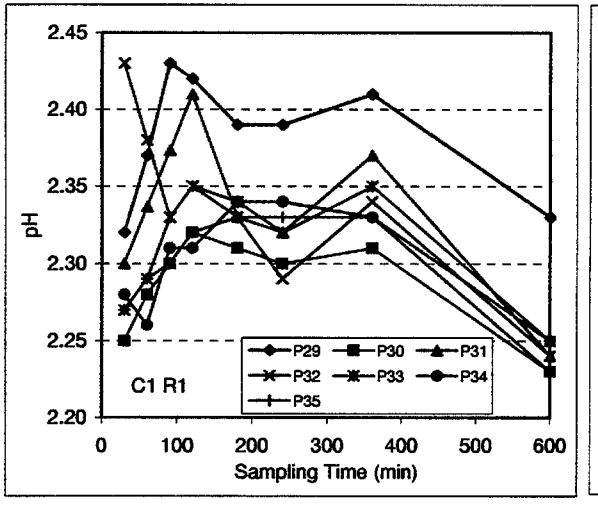
pH
Sampling Time (min)
C1 R1
P29 P30 P31
P32 P33 P34
P35

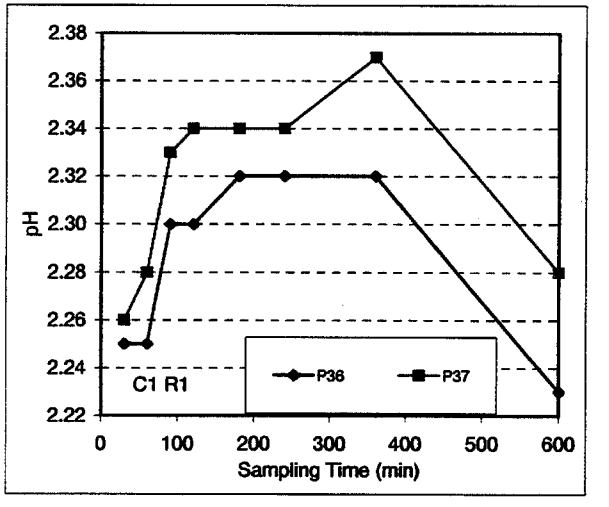
pH
Sampling Time (min)
C1 R1
P36 P37

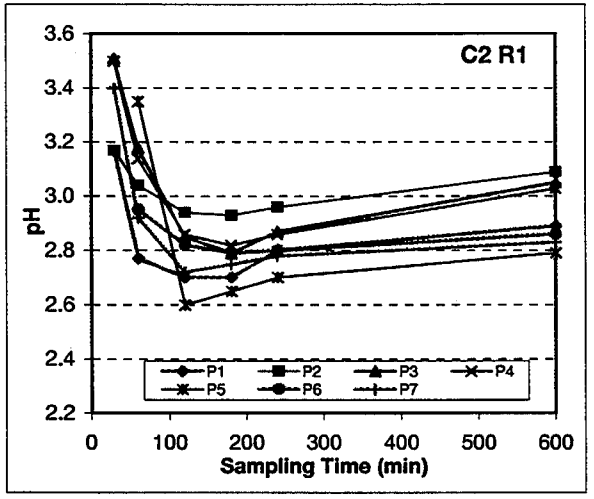
C2 R1
pH
Sampling Time (min)
P1 P2 P3 P4
P5 P6 P7

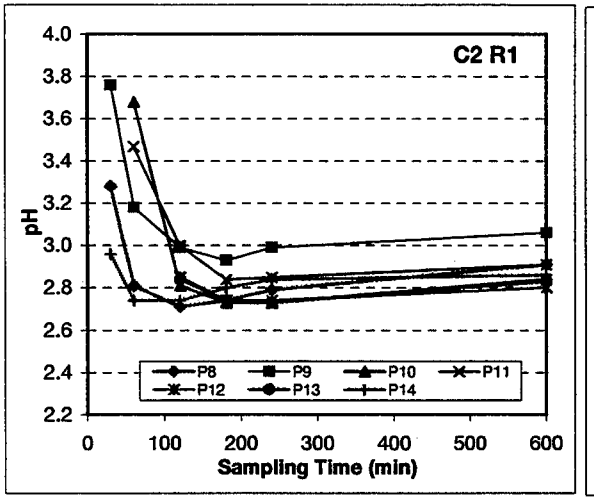
C2 R1
pH
Sampling Time (min)
P8 P9 P10 P11
P12 P13 P14

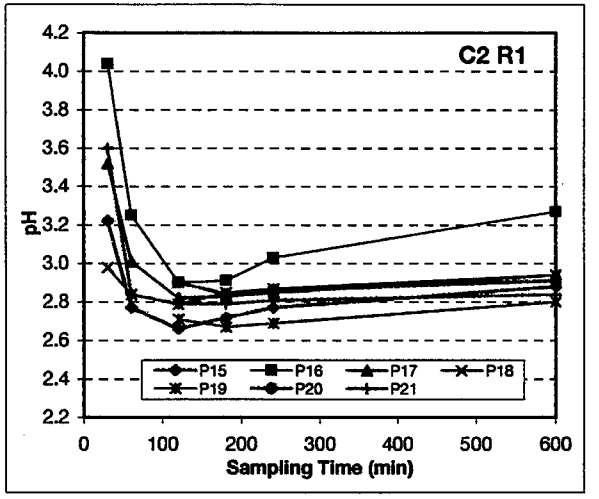
C2 R1
pH
Sampling Time (min)
P15 P16 P17 P18
P19 P20 P21

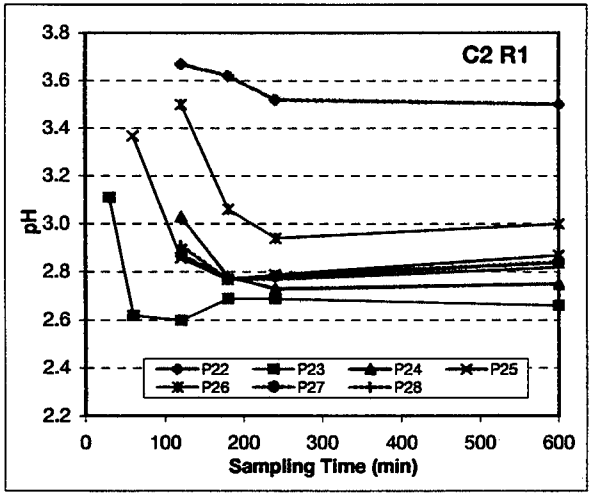
C2 R1
pH
Sampling Time (min)
P22 P23 P24 P25
P26 P27 P28

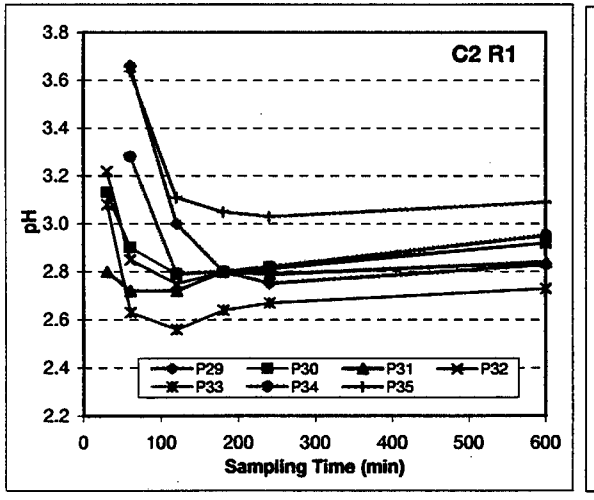
C2 R1
pH
Sampling Time (min)
P29 P30 P31 P32
P33 P34 P35

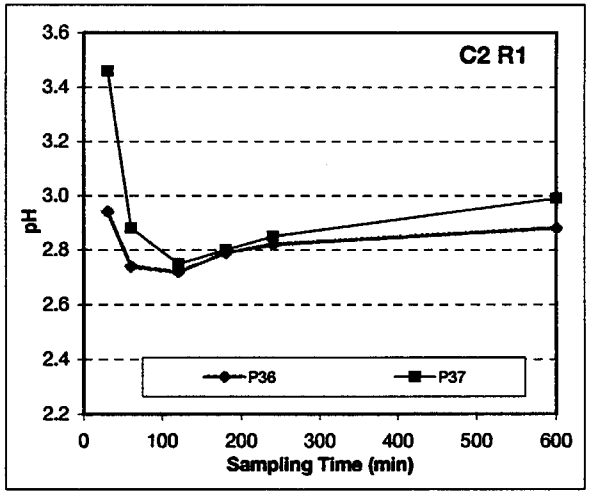
C2 R1
pH
Sampling Time (min)
P36 P37

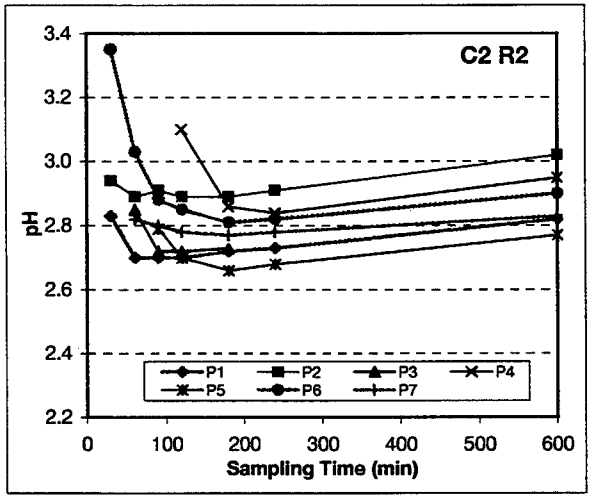
C2 R2
pH
Sampling Time (min)
P1 P2 P3 P4
P5 P6 P7

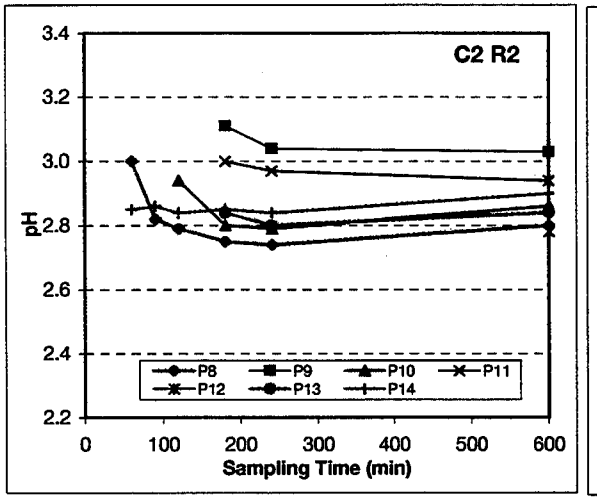
C2 R2
pH
Sampling Time (min)
P8 P9 P10 P11
P12 P13 P14

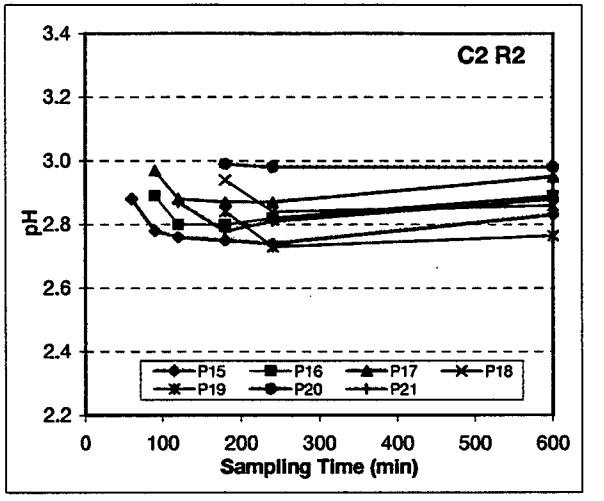
C2 R2
pH
Sampling Time (min)
P15 P16 P17 P18
P19 P20 P21

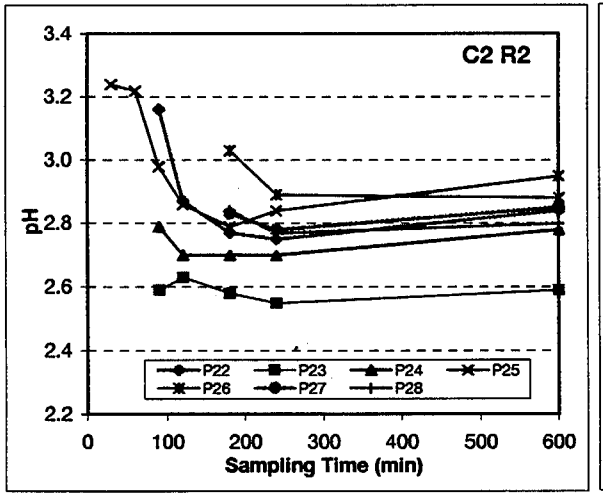
C2 R2
pH
Sampling Time (min)
P22 P23 P24 P25
P26 P27 P28

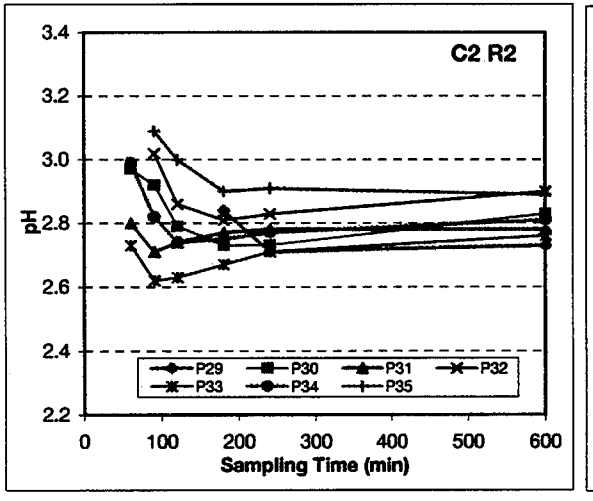
C2 R2
pH
Sampling Time (min)
P29 P30 P31 P32
P33 P34 P35

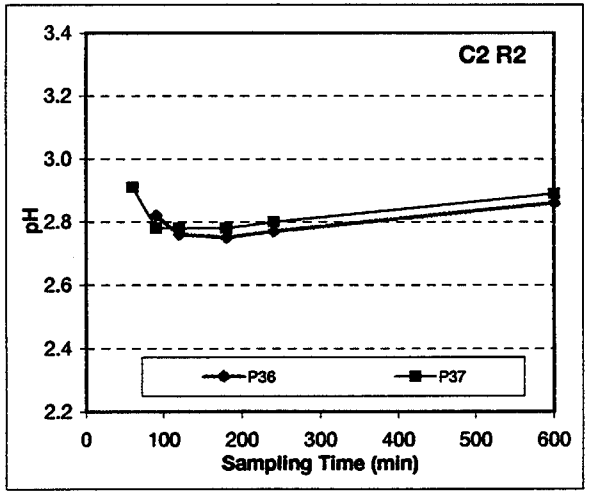
C2 R2
pH
Sampling Time (min)
P36 P37

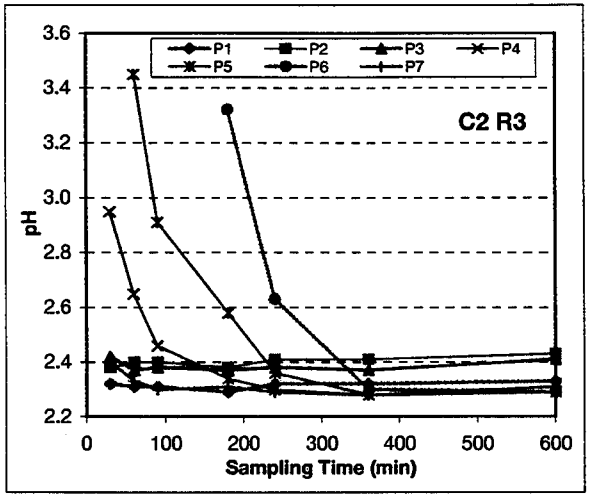
P1 P2 P3 P4
P5 P6 P7
C2 R3
pH
Sampling Time (min)

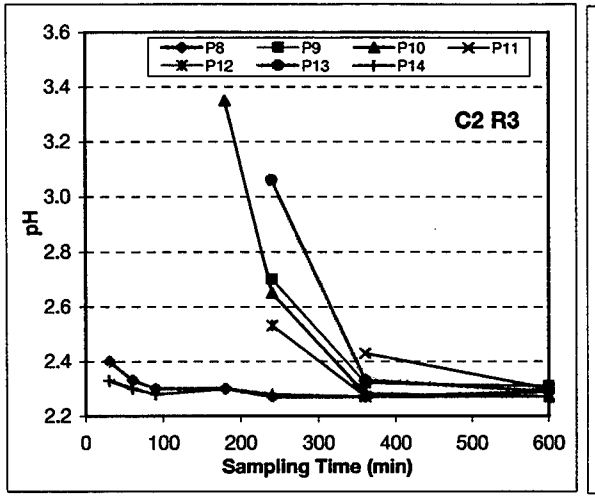
P8 P9 P10 P11
P12 P13 P14
C2 R3
pH
Sampling Time (min)

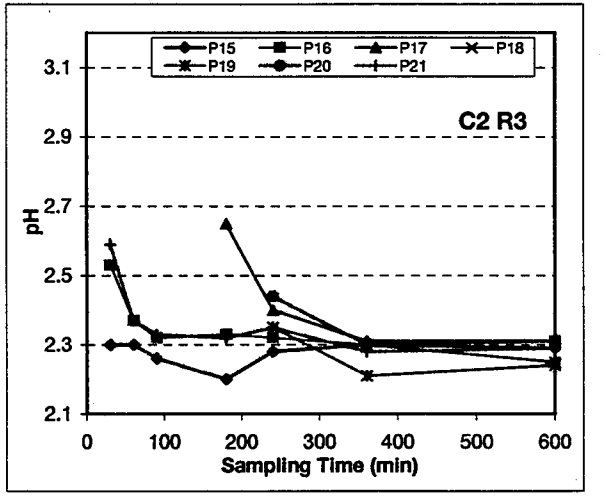
P15 P16 P17 P18
P19 P20 P21
C2 R3
pH
Sampling Time (min)

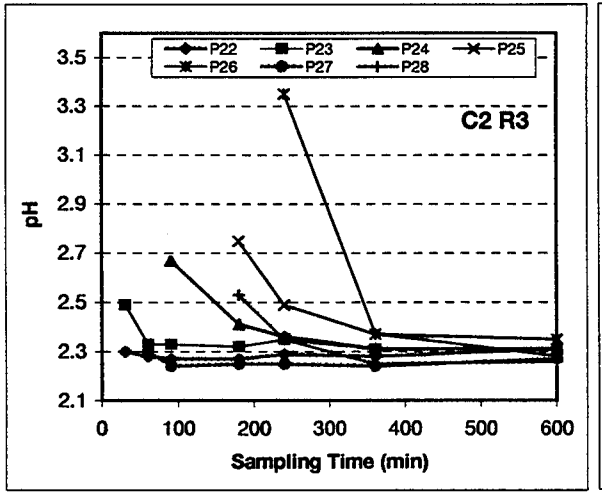
P22 P23 P24 P25
P26 P27 P28
C2 R3
pH
Sampling Time (min)

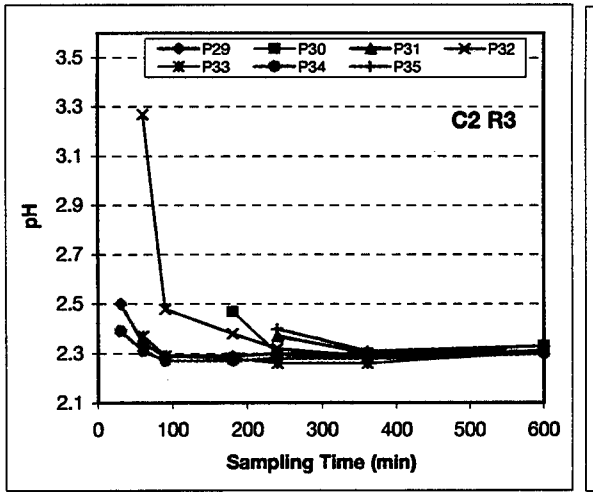
P29 P30 P31 P32
P33 P34 P35
C2 R3
pH
Sampling Time (min)

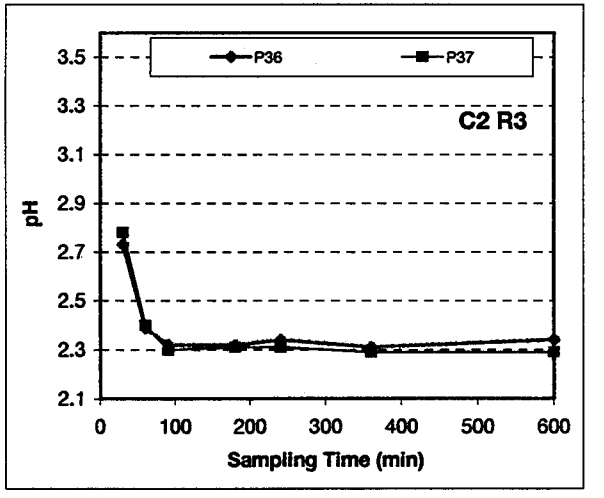
P36 P37
C2 R3
pH
Sampling Time (min)

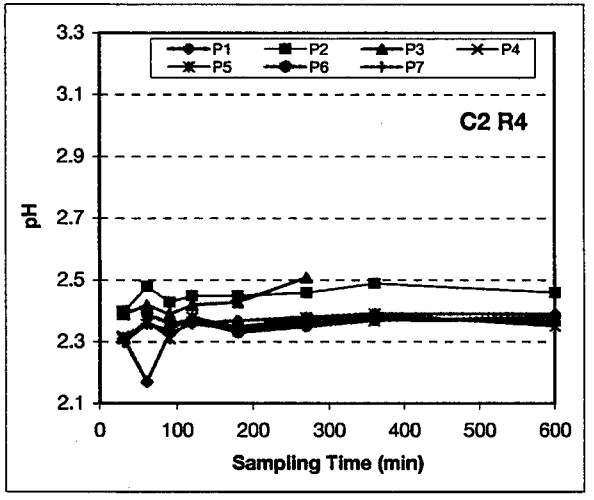
P1 P2 P3 P4
P5 P6 P7
C2 R4
pH
3.3
3.1
2.9
2.7
2.5
2.3
2.1
0 100 200 300 400 500 600
Sampling Time (min)

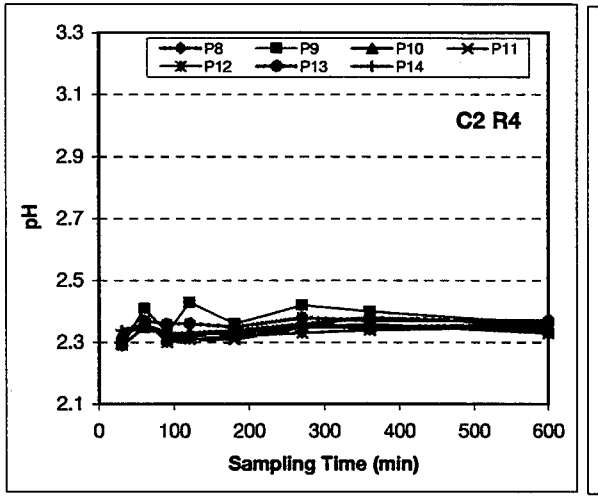
P8 P9 P10 P11
P12 P13 P14
C2 R4
pH
3.3
3.1
2.9
2.7
2.5
2.3
2.1
0 100 200 300 400 500 600
Sampling Time (min)

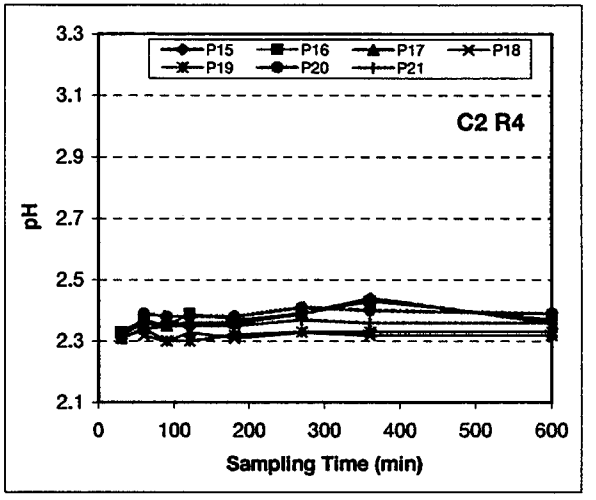
P15 P16 P17 P18
P19 P20 P21
C2 R4
pH
3.3
3.1
2.9
2.7
2.5
2.3
2.1
0 100 200 300 400 500 600
Sampling Time (min)

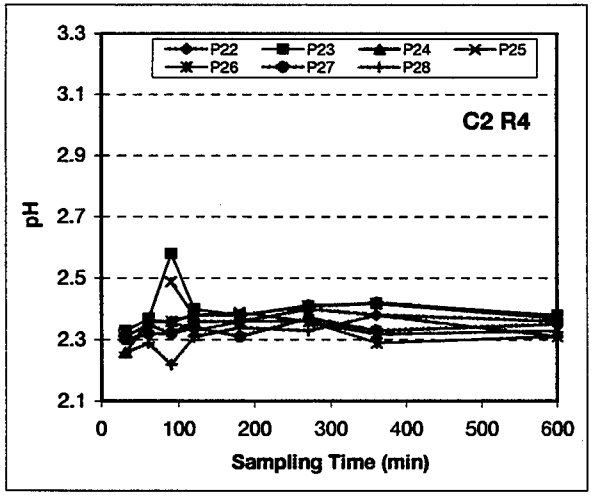
P22 P23 P24 P25
P26 P27 P28
C2 R4
pH
3.3
3.1
2.9
2.7
2.5
2.3
2.1
0 100 200 300 400 500 600
Sampling Time (min)

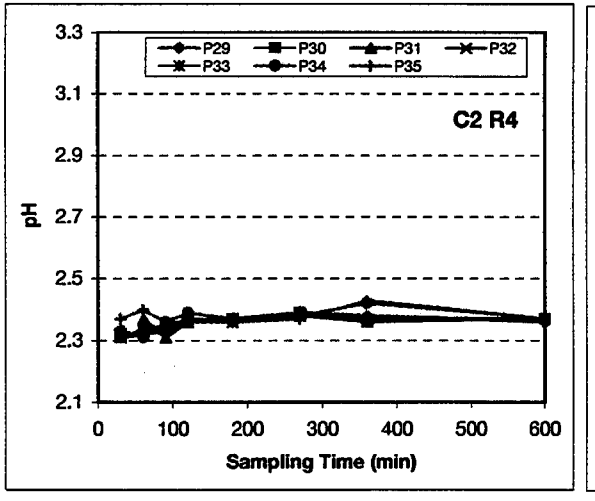
P29 P30 P31 P32
P33 P34 P35
C2 R4
pH
3.3
3.1
2.9
2.7
2.5
2.3
2.1
0 100 200 300 400 500 600
Sampling Time (min)

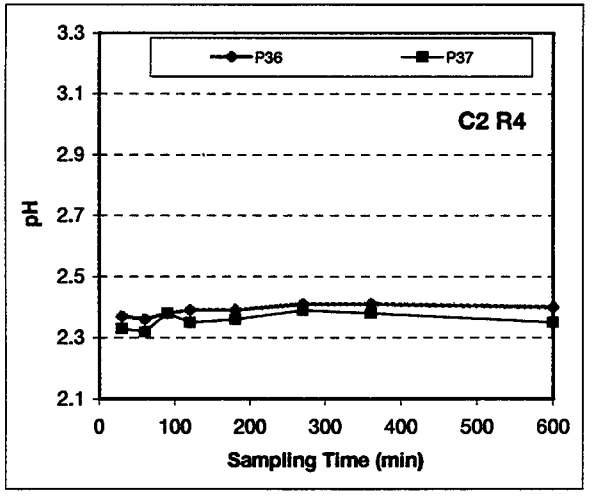
P36 P37
C2 R4
pH
3.3
3.1
2.9
2.7
2.5
2.3
2.1
0 100 200 300 400 500 600
Sampling Time (min)

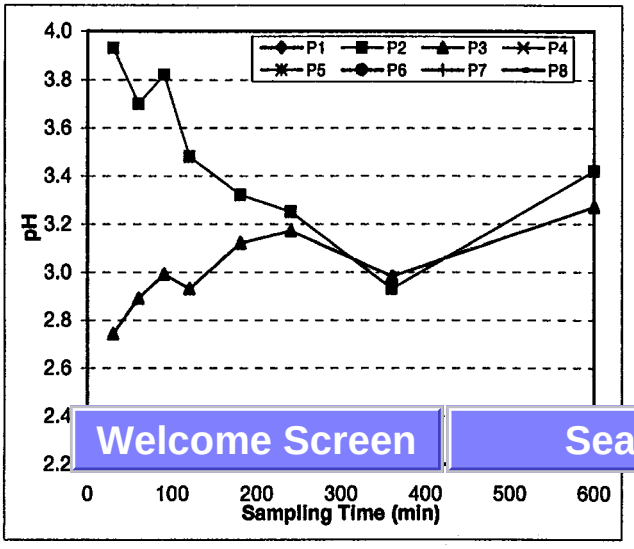
P1 P2 P3 P4
P5 P6 P7 P8
pH
Sampling Time (min)

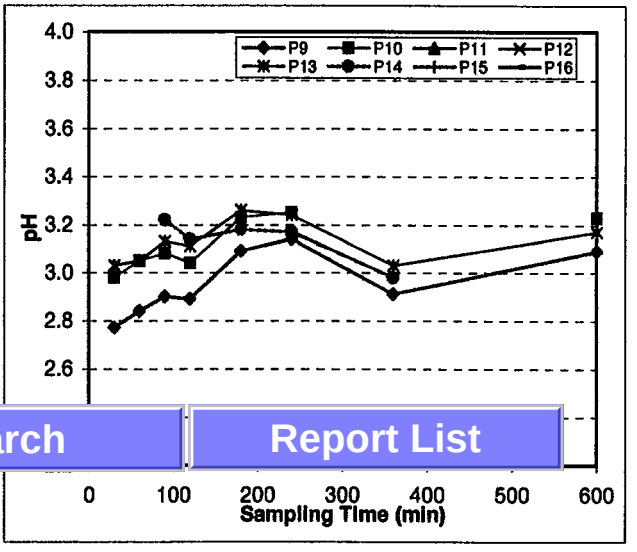
P9 P10 P11 P12
P13 P14 P15 P16
pH
Sampling Time (min)

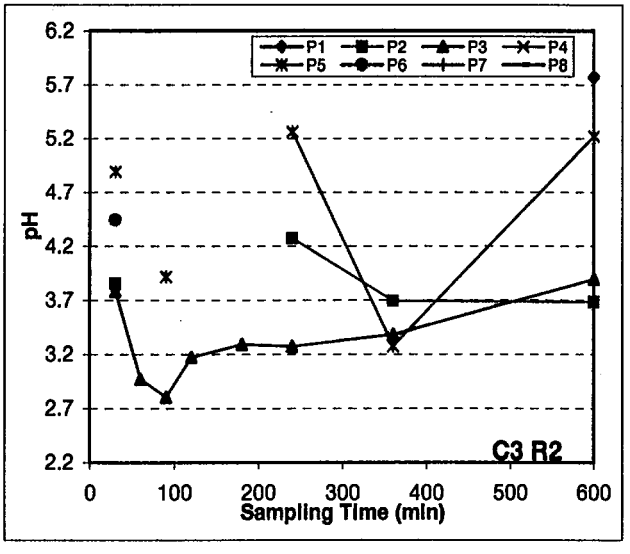
P1 P2 P3 P4
P5 P6 P7 P8
C3 R2
pH
Sampling Time (min)

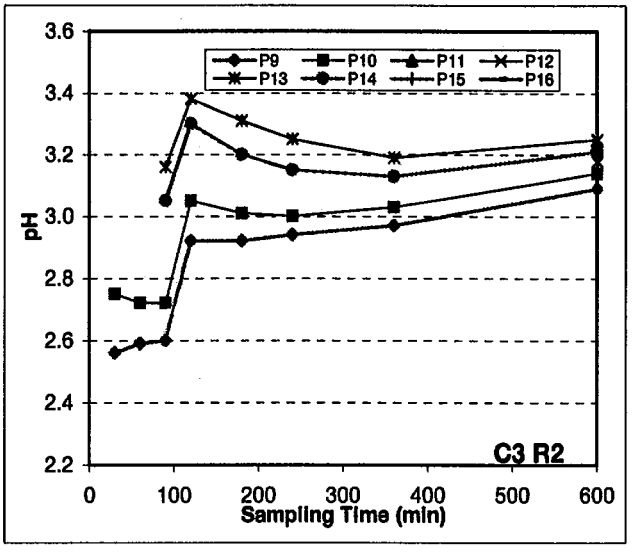
P9 P10 P11 P12
P13 P14 P15 P16
C3 R2
pH
Sampling Time (min)

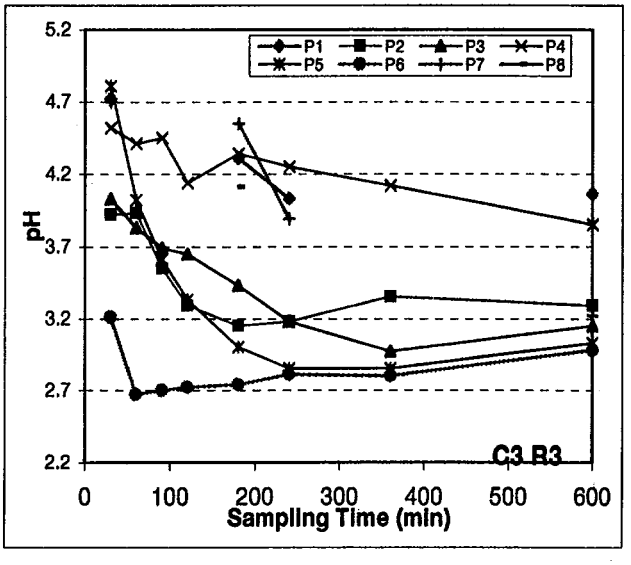
P1 P2 P3 P4
P5 P6 P7 P8
C3 R3
pH
Sampling Time (min)

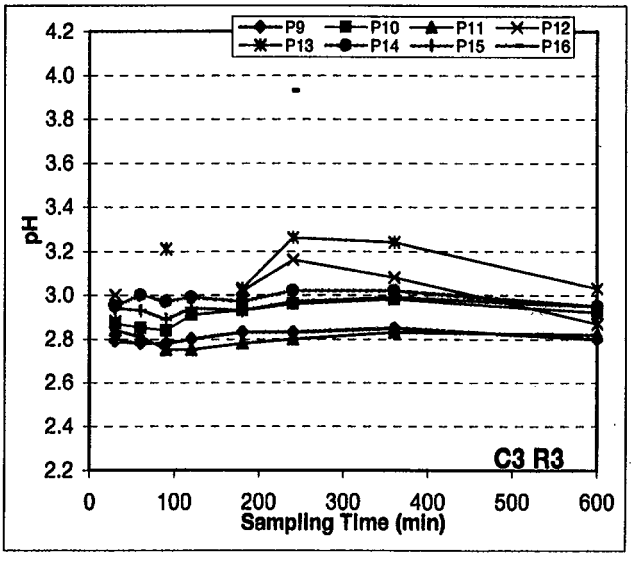
P9 P10 P11 P12
P13 P14 P15 P16
C3 R3
pH
Sampling Time (min)

APPENDIX V TRACER CHEMOGRAPHS

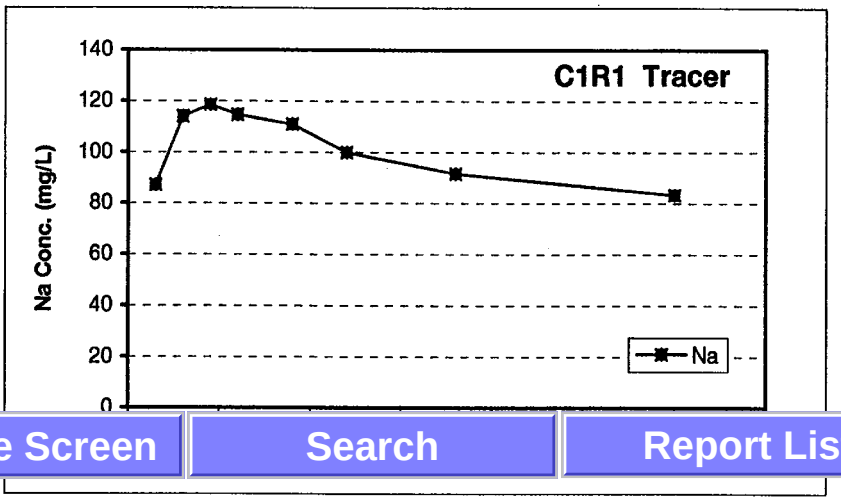
C1R1 Tracer
Na Conc. (mg/L)
140
120
100
80
60
40
20
0
Na

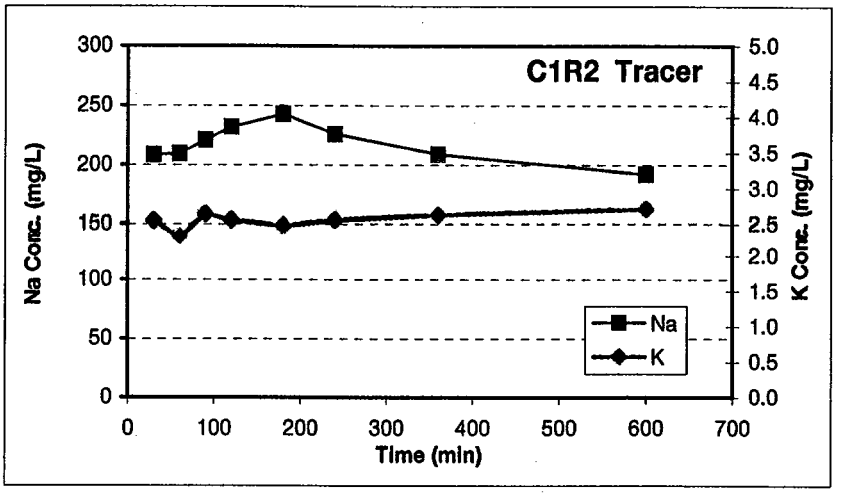
C1R2 Tracer
Na Conc. (mg/L)
K Conc. (mg/L)
Time (min)
300
250
200
150
100
50
0
5.0
4.5
4.0
3.5
3.0
2.5
2.0
1.5
1.0
0.5
0.0
0
100
200
300
400
500
600
700
Na
K

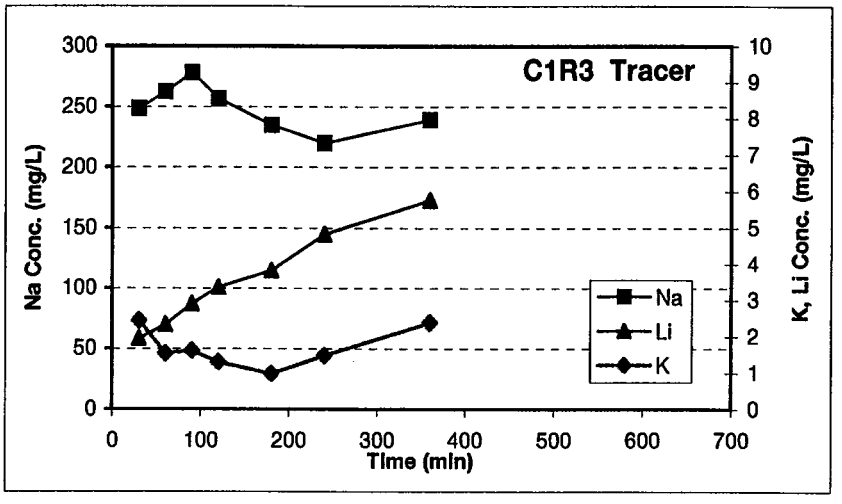
C1R3 Tracer
Na Conc. (mg/L)
K, Li Conc. (mg/L)
Time (min)
300
250
200
150
100
50
0
10
9
8
7
6
5
4
3
2
1
0
0
100
200
300
400
500
600
700
Na
Li
K

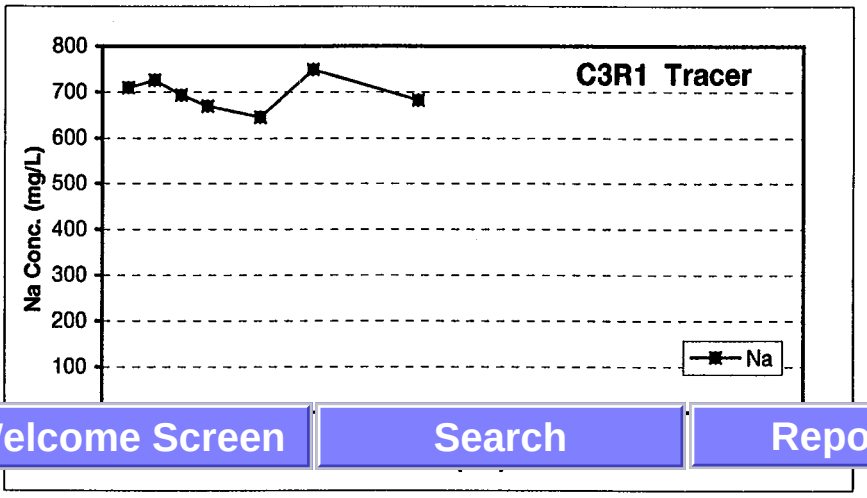
C3R1 Tracer
Na Conc. (mg/L)
800
700
600
500
400
300
200
100
Na

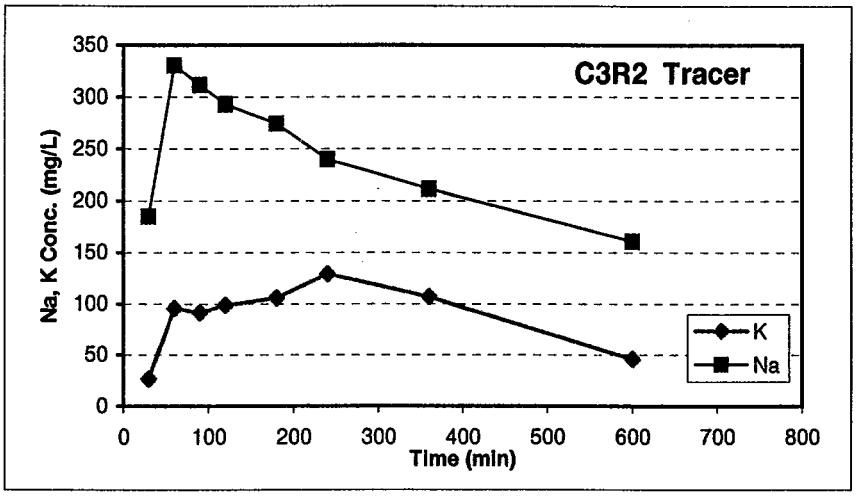
C3R2 Tracer
Na, K Conc. (mg/L)
350
300
250
200
150
100
50
0
0
100
200
300
400
500
600
700
800
Time (min)
K
Na

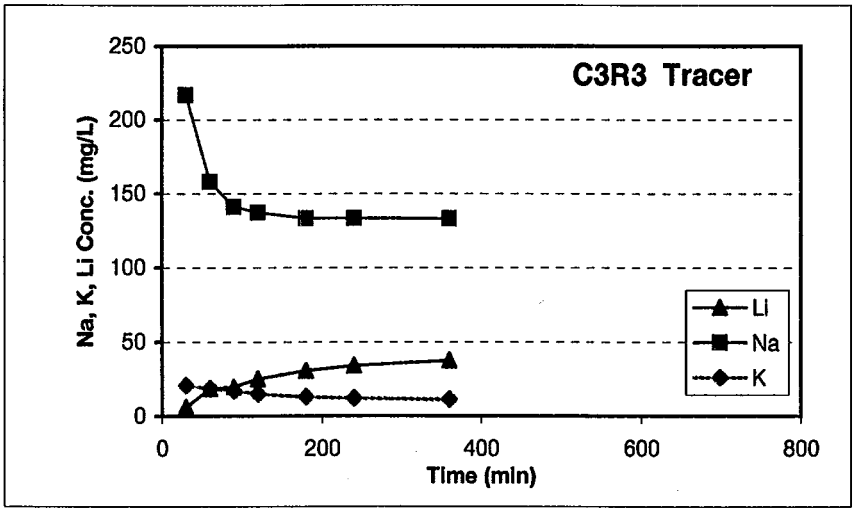
C3R3 Tracer
Na, K, Li Conc. (mg/L)
250
200
150
100
50
0
0
200
400
600
800
Time (min)
Li
Na
K

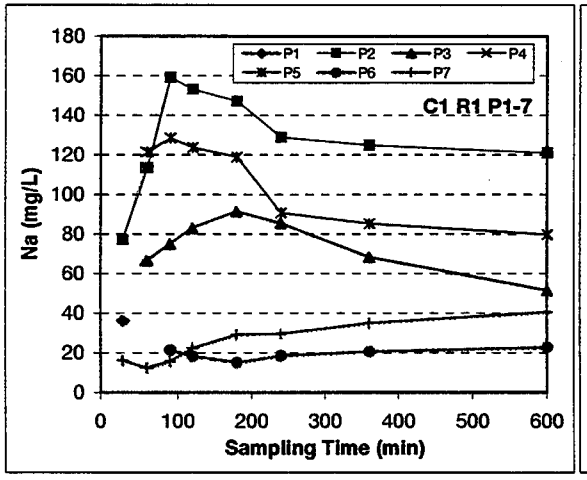
C1 R1 P1-7
P1 P2 P3 P4 P5 P6 P7
Na (mg/L)
Sampling Time (min)

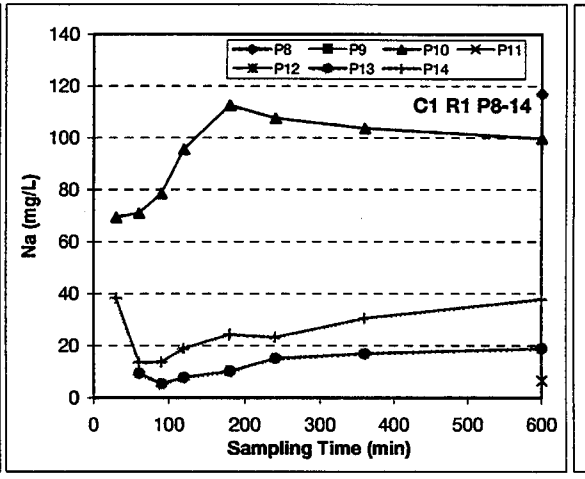
C1 R1 P8-14
P8 P9 P10 P11 P12 P13 P14
Na (mg/L)
Sampling Time (min)

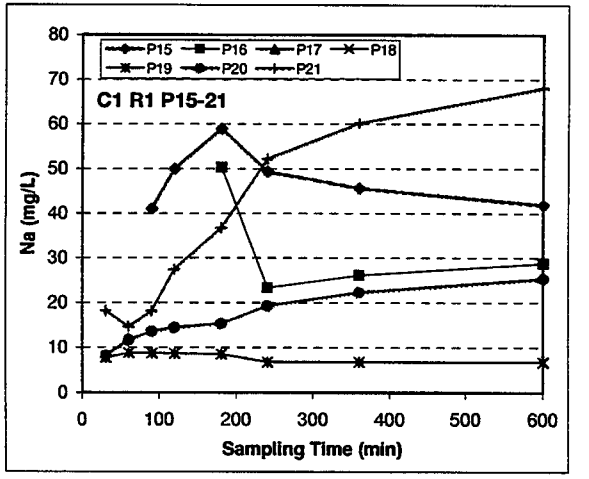
C1 R1 P15-21
P15 P16 P17 P18 P19 P20 P21
Na (mg/L)
Sampling Time (min)

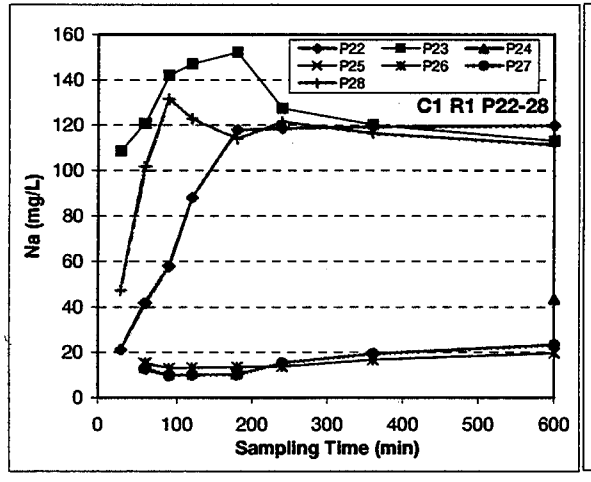
C1 R1 P22-28
P22 P23 P24 P25 P26 P27 P28
Na (mg/L)
Sampling Time (min)

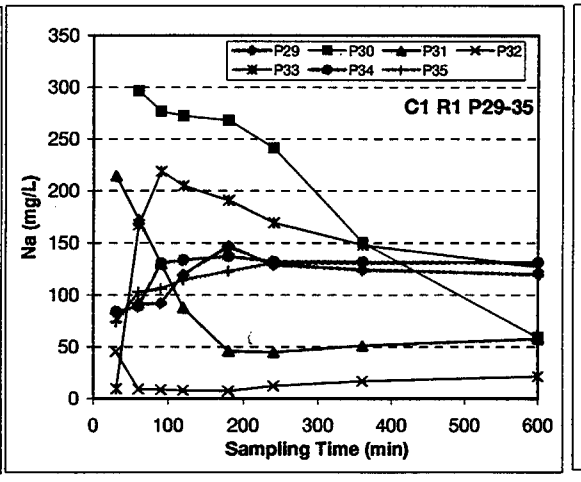
C1 R1 P29-35
P29 P30 P31 P32 P33 P34 P35
Na (mg/L)
Sampling Time (min)

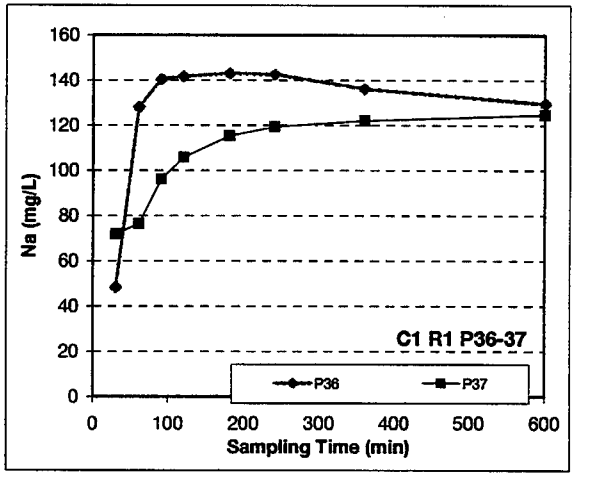
C1 R1 P36-37
P36 P37
Na (mg/L)
Sampling Time (min)

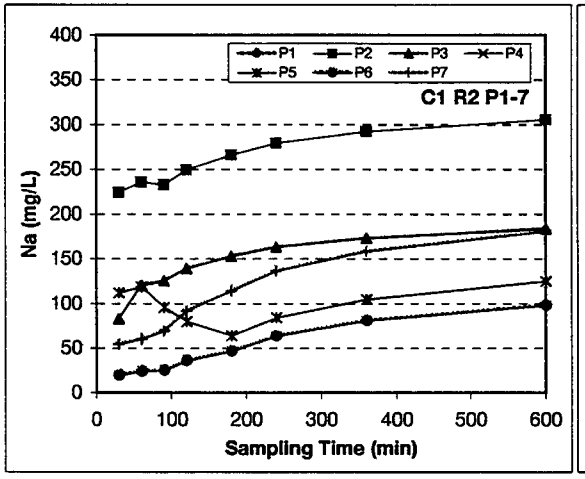
C1 R2 P1-7
P1 P2 P3 P4 P5 P6 P7
Na (mg/L)
Sampling Time (min)

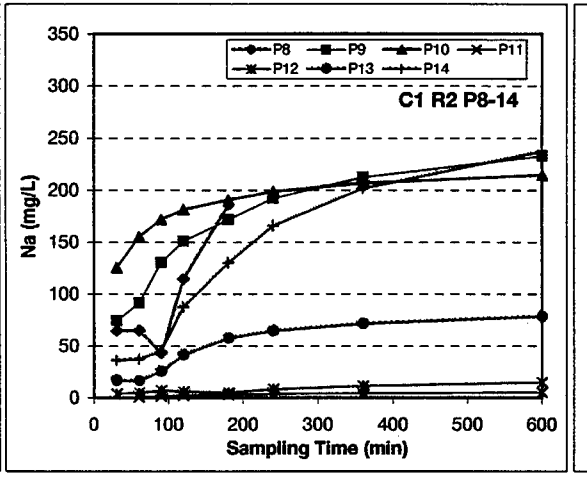
C1 R2 P8-14
P8 P9 P10 P11 P12 P13 P14
Na (mg/L)
Sampling Time (min)

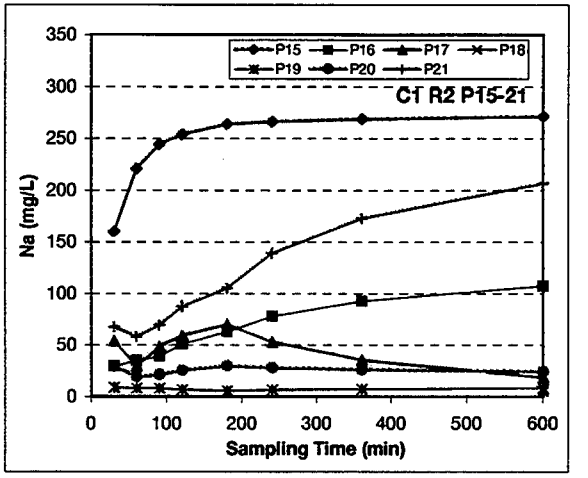
C1 R2 P15-21
P15 P16 P17 P18 P19 P20 P21
Na (mg/L)
Sampling Time (min)

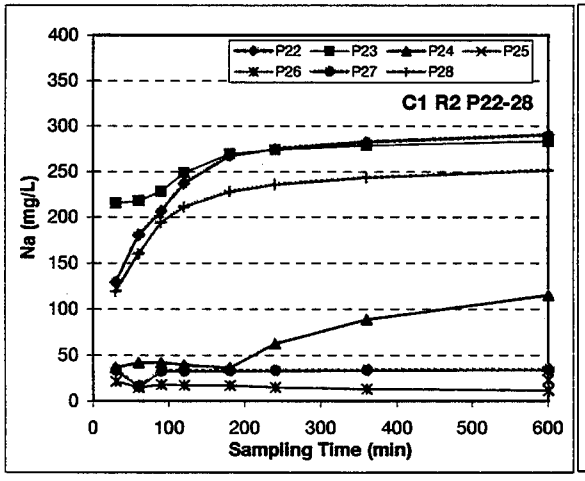
C1 R2 P22-28
P22 P23 P24 P25 P26 P27 P28
Na (mg/L)
Sampling Time (min)

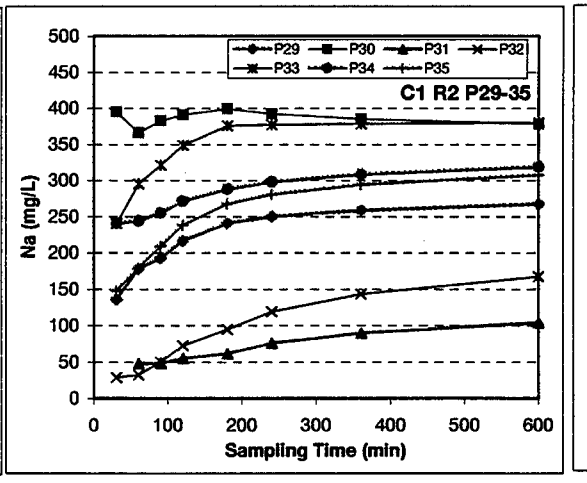
C1 R2 P29-35
P29 P30 P31 P32 P33 P34 P35
Na (mg/L)
Sampling Time (min)

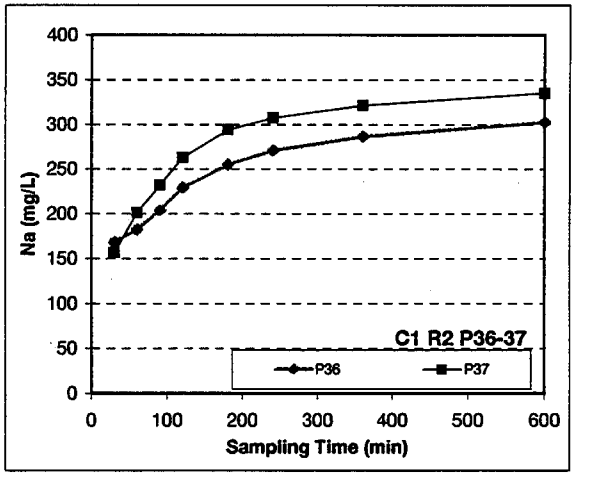
C1 R2 P36-37
P36 P37
Na (mg/L)
Sampling Time (min)

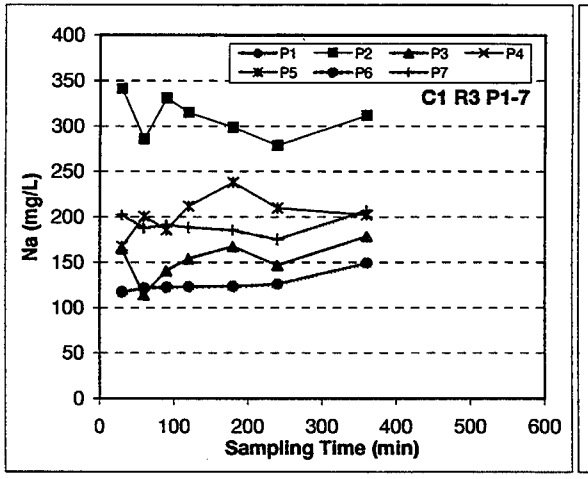
C1 R3 P1-7
P1 P2 P3 P4
P5 P6 P7
Na (mg/L)
Sampling Time (min)

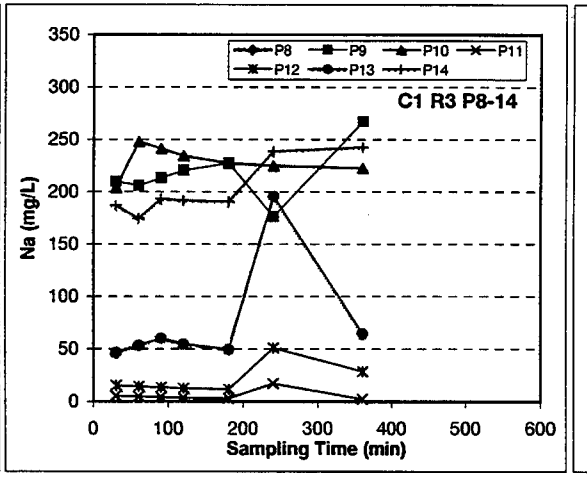
C1 R3 P8-14
P8 P9 P10 P11
P12 P13 P14
Na (mg/L)
Sampling Time (min)

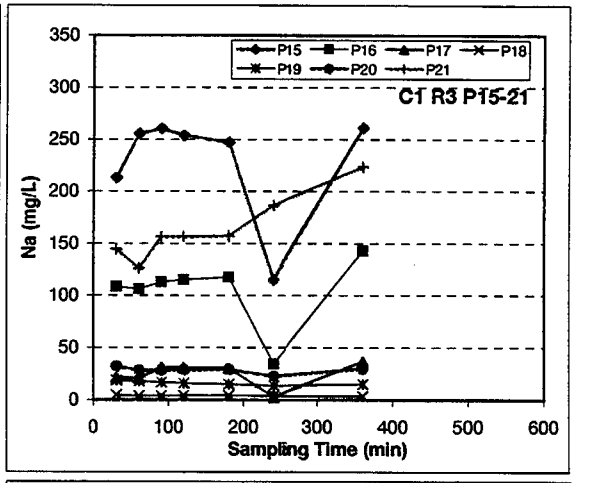
C1 R3 P15-21
P15 P16 P17 P18
P19 P20 P21
Na (mg/L)
Sampling Time (min)

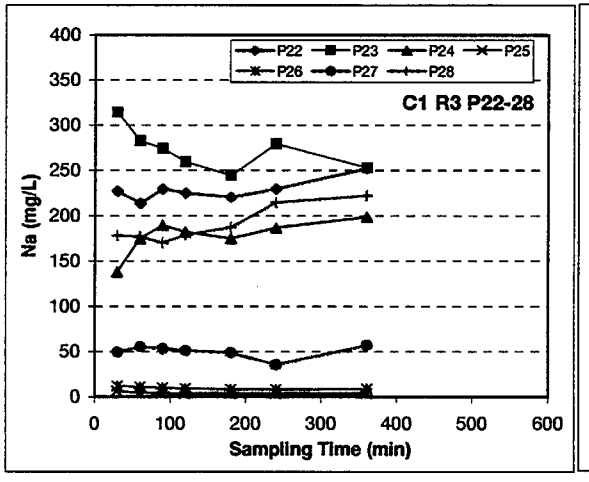
C1 R3 P22-28
P22 P23 P24 P25
P26 P27 P28
Na (mg/L)
Sampling Time (min)

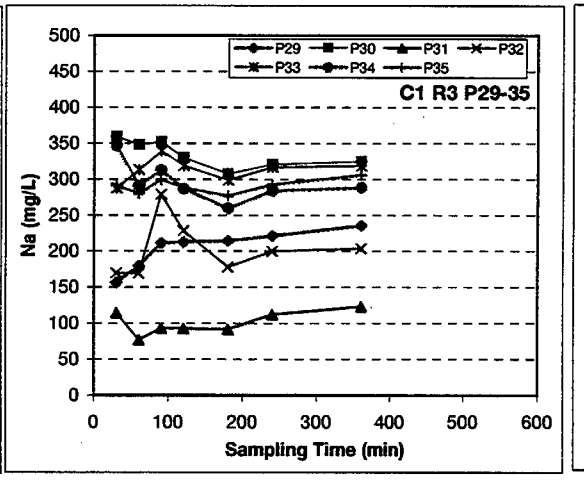
C1 R3 P29-35
P29 P30 P31 P32
P33 P34 P35
Na (mg/L)
Sampling Time (min)

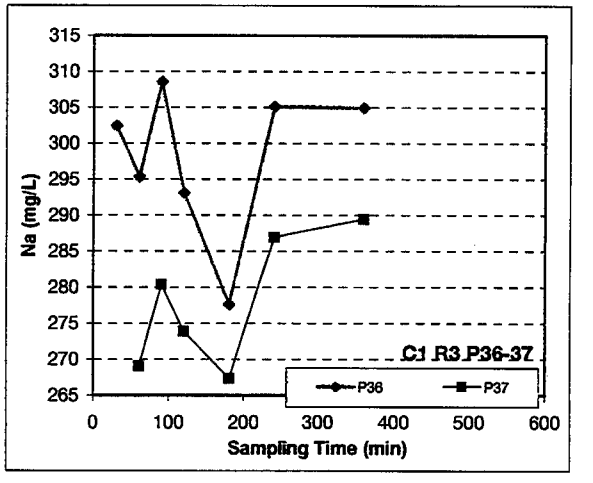
C1 R3 P36-37
P36 P37
Na (mg/L)
Sampling Time (min)

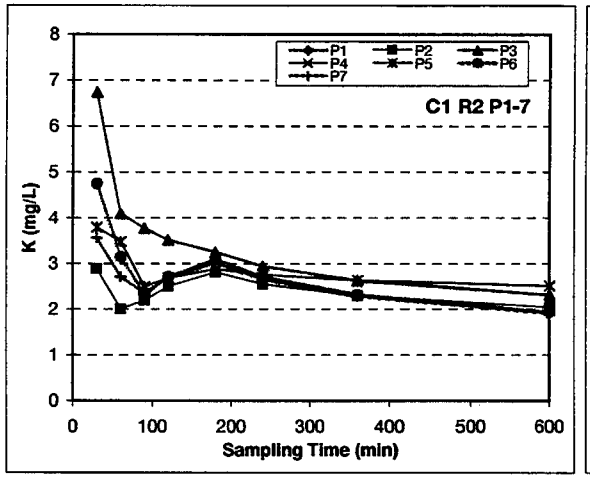
C1 R2 P1-7
P1 P2 P3 P4 P5 P6 P7
K (mg/L)
Sampling Time (min)

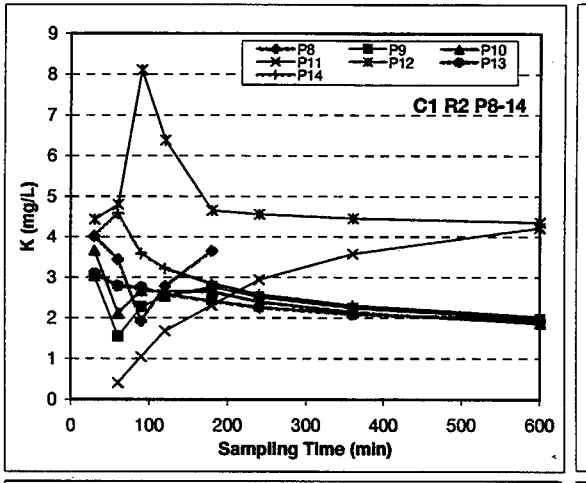
C1 R2 P8-14
P8 P9 P10 P11 P12 P13 P14
K (mg/L)
Sampling Time (min)

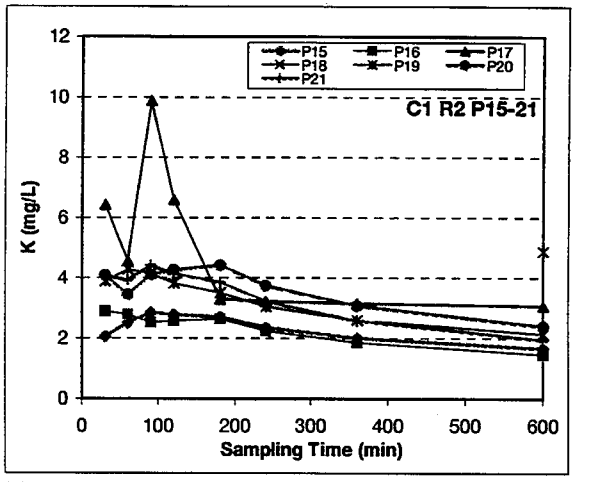
C1 R2 P15-21
P15 P16 P17 P18 P19 P20 P21
K (mg/L)
Sampling Time (min)

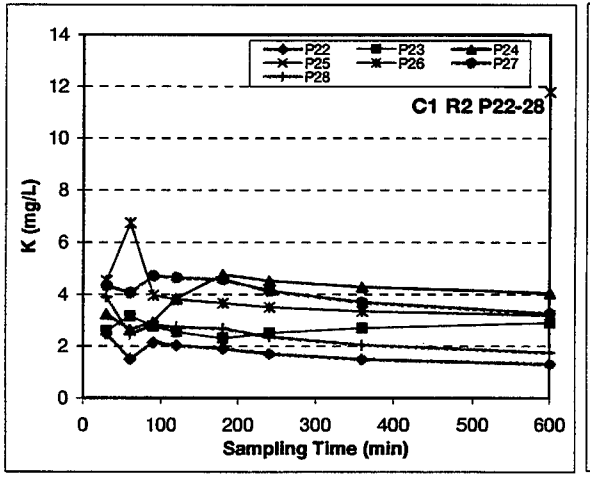
C1 R2 P22-28
P22 P23 P24 P25 P26 P27 P28
K (mg/L)
Sampling Time (min)

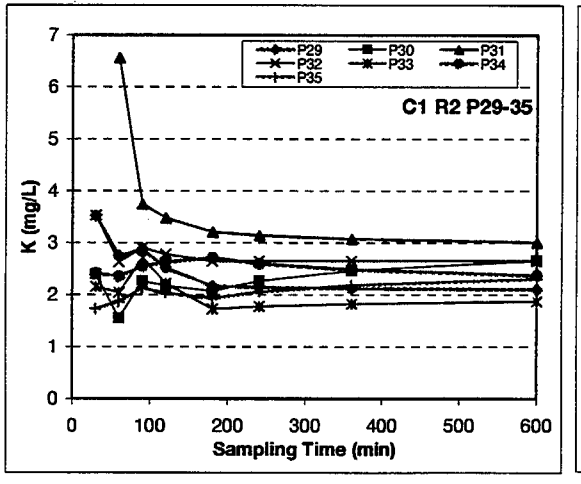
C1 R2 P29-35
P29 P30 P31 P32 P33 P34 P35
K (mg/L)
Sampling Time (min)

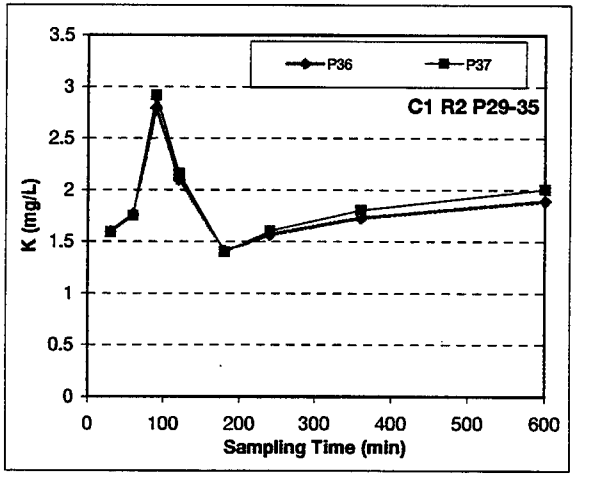
C1 R2 P29-35
P36 P37
K (mg/L)
Sampling Time (min)

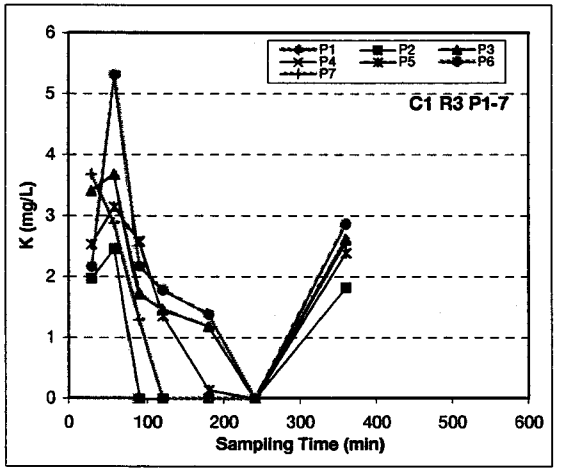
C1 R3 P1-7
P1 P2 P3 P4 P5 P6 P7
K (mg/L)
Sampling Time (min)

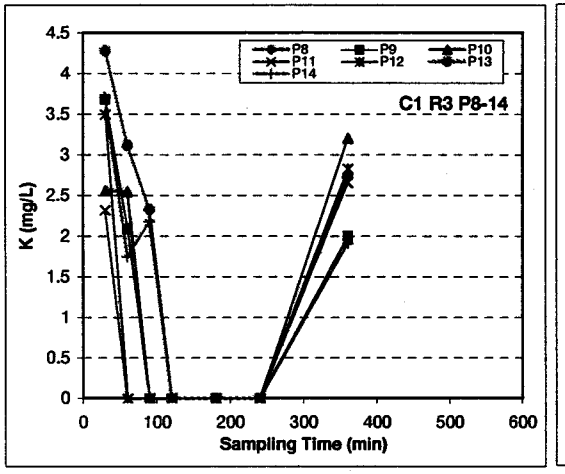
C1 R3 P8-14
P8 P9 P10 P11 P12 P13 P14
K (mg/L)
Sampling Time (min)

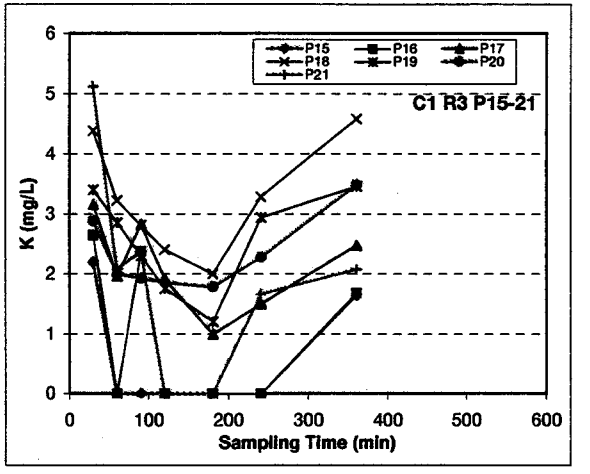
C1 R3 P15-21
P15 P16 P17 P18 P19 P20 P21
K (mg/L)
Sampling Time (min)

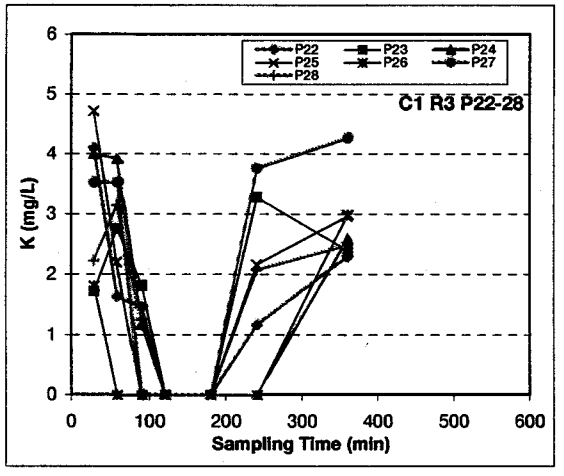
C1 R3 P22-28
P22 P23 P24 P25 P26 P27 P28
K (mg/L)
Sampling Time (min)

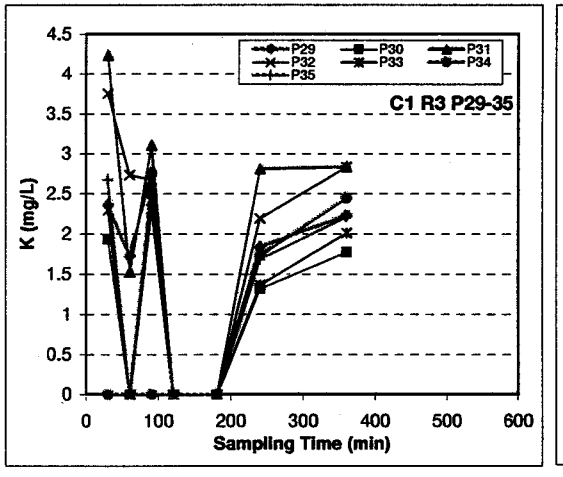
C1 R3 P29-35
P29 P30 P31 P32 P33 P34 P35
K (mg/L)
Sampling Time (min)

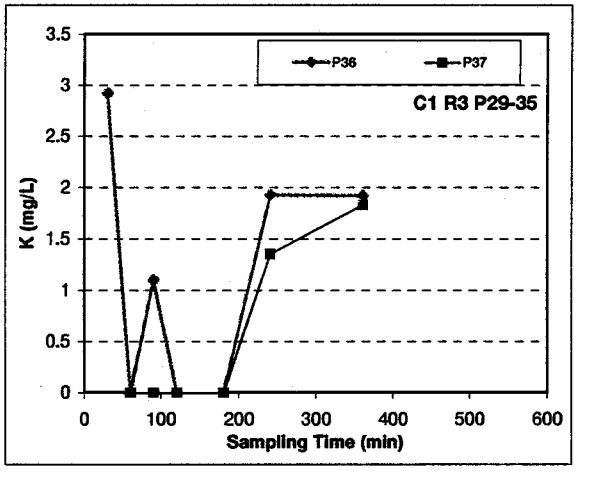
C1 R3 P29-35
P36 P37
K (mg/L)
Sampling Time (min)

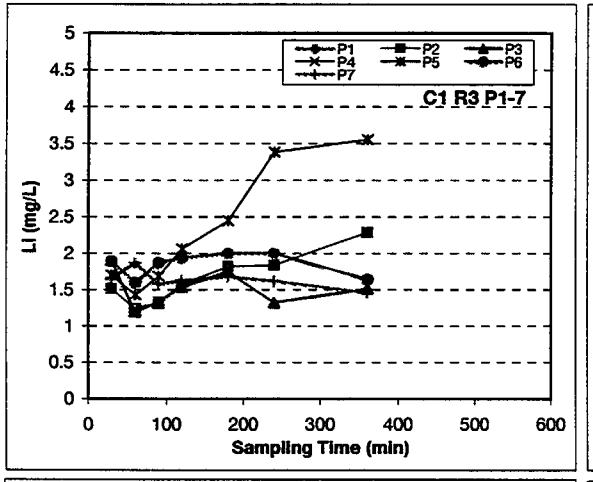
C1 R3 P1-7
P1 P2 P3 P4 P5 P6 P7
LI (mg/L)
Sampling Time (min)

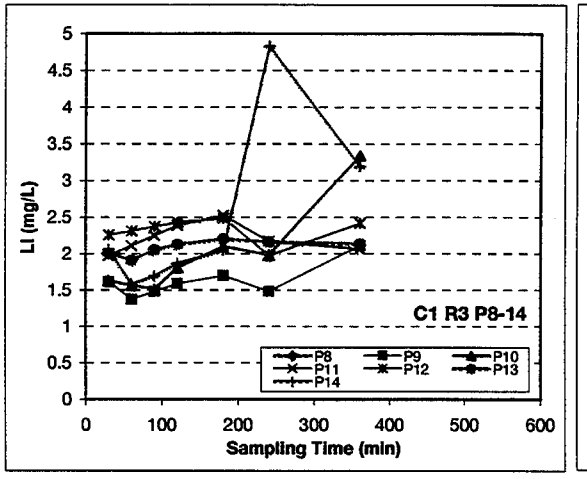
C1 R3 P8-14
P8 P9 P10 P11 P12 P13 P14
LI (mg/L)
Sampling Time (min)

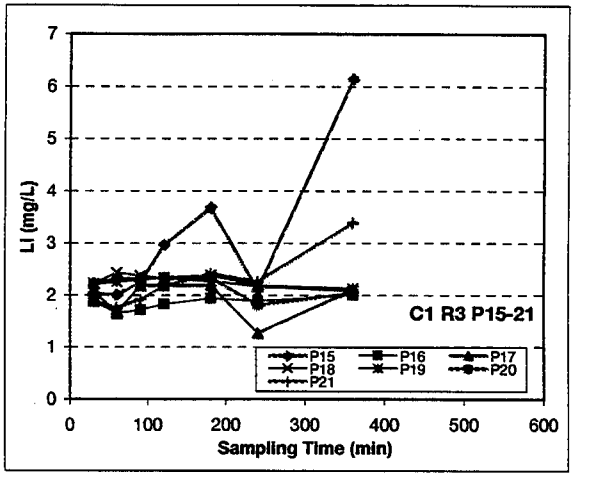
C1 R3 P15-21
P15 P16 P17 P18 P19 P20 P21
LI (mg/L)
Sampling Time (min)

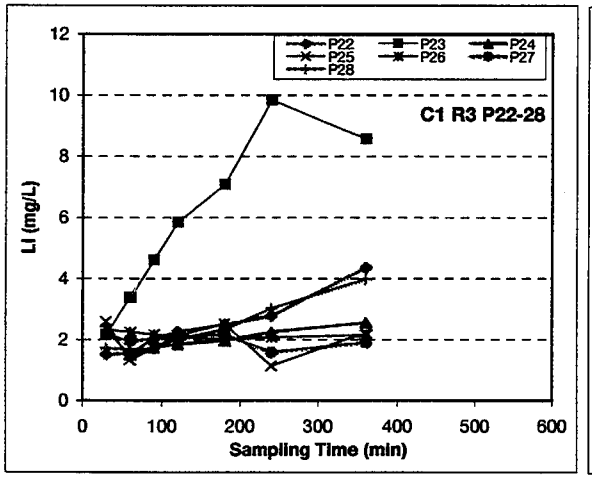
C1 R3 P22-28
P22 P23 P24 P25 P26 P27 P28
LI (mg/L)
Sampling Time (min)

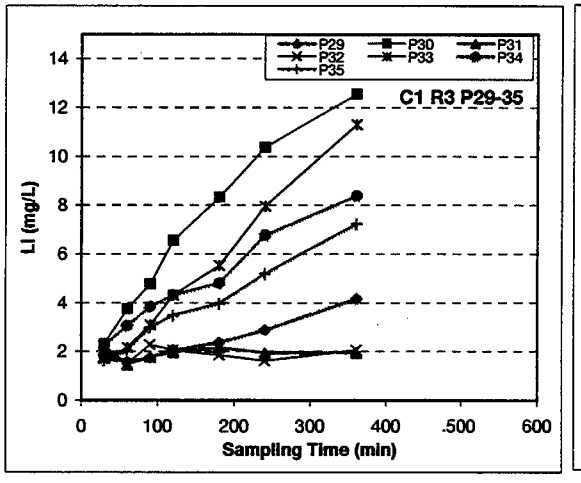
C1 R3 P29-35
P29 P30 P31 P32 P33 P34 P35
LI (mg/L)
Sampling Time (min)

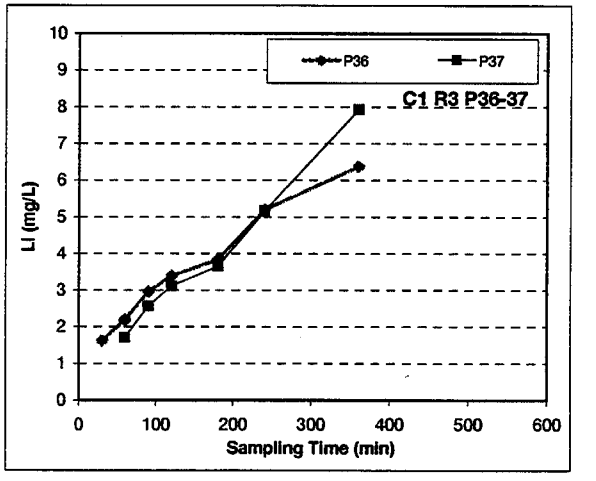
C1 R3 P36-37
P36 P37
LI (mg/L)
Sampling Time (min)

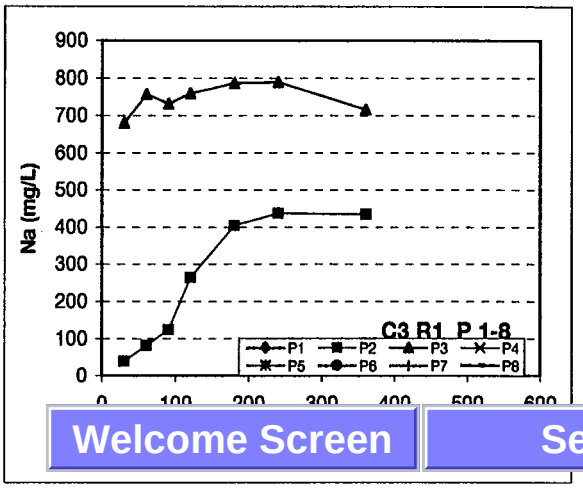

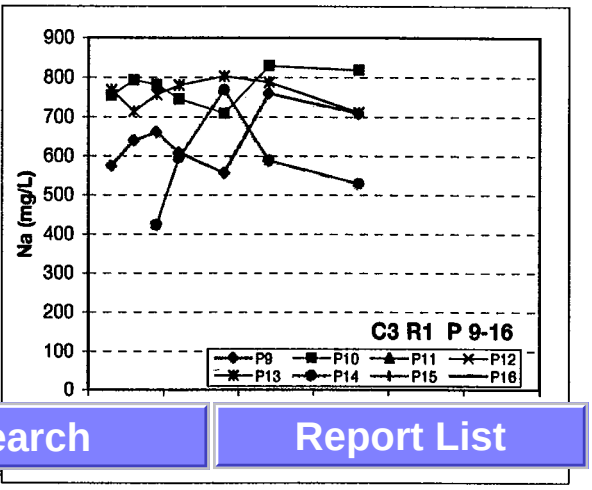

Welcome Screen | Search | Report List

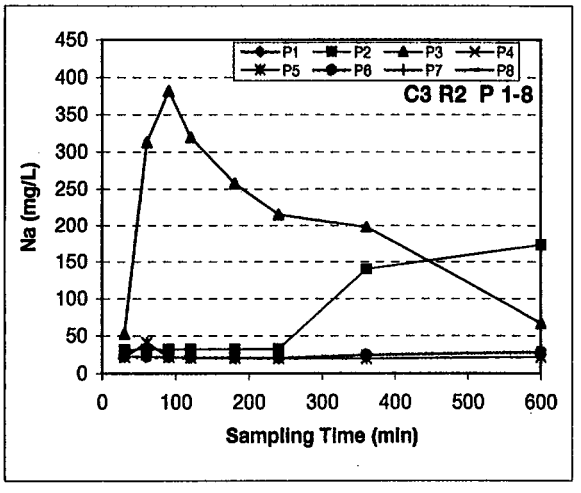

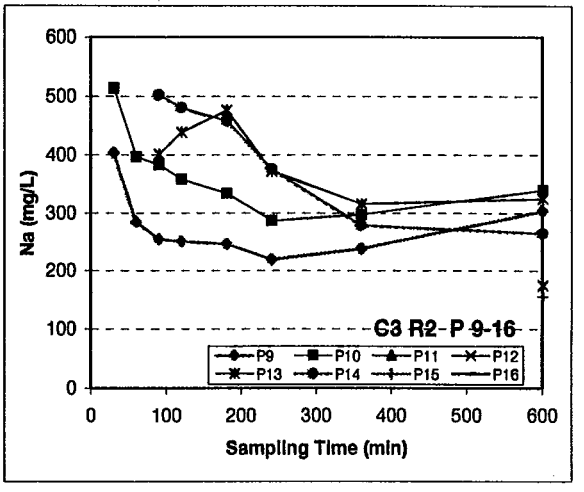

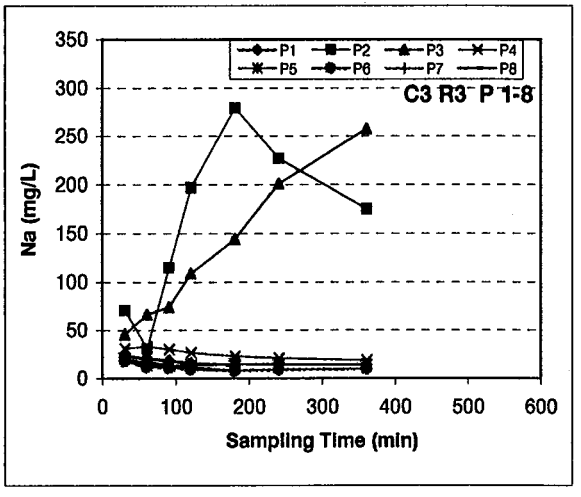

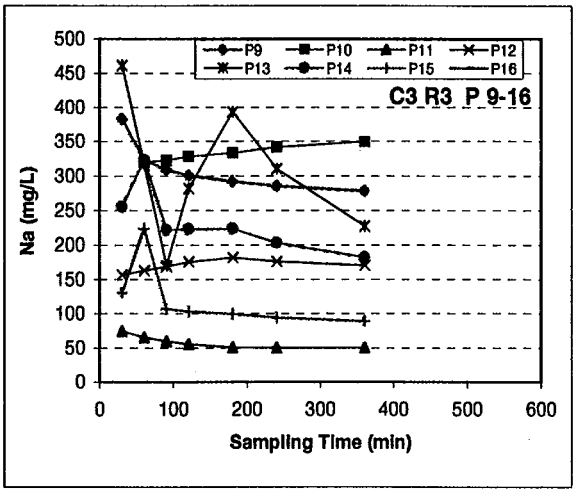

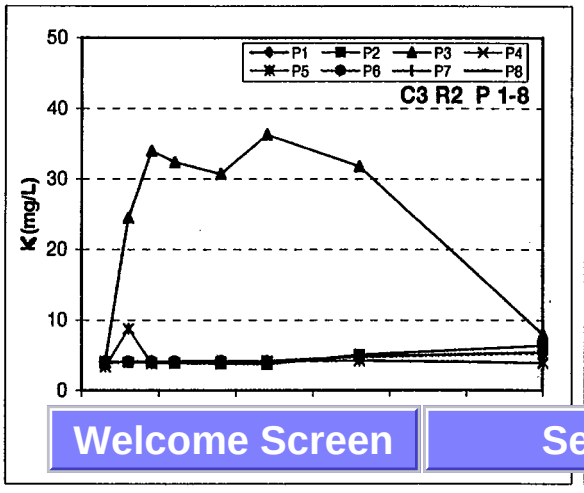

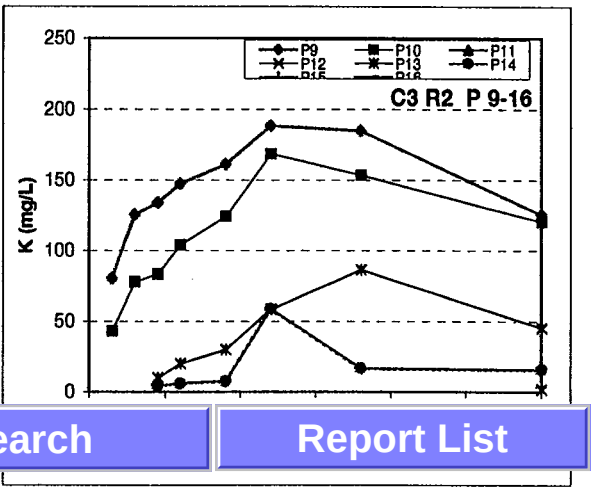

Welcome Screen | Search | Report List

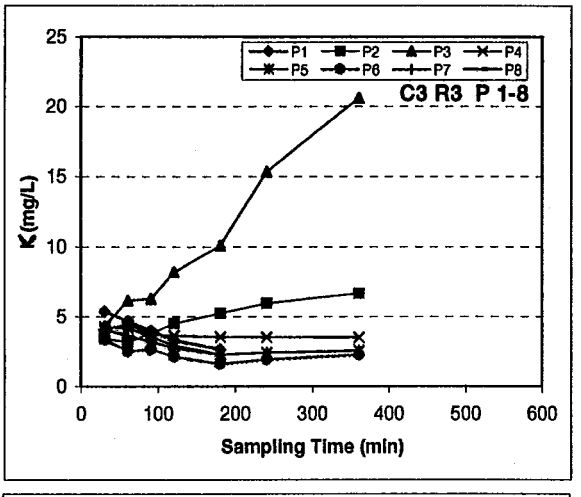

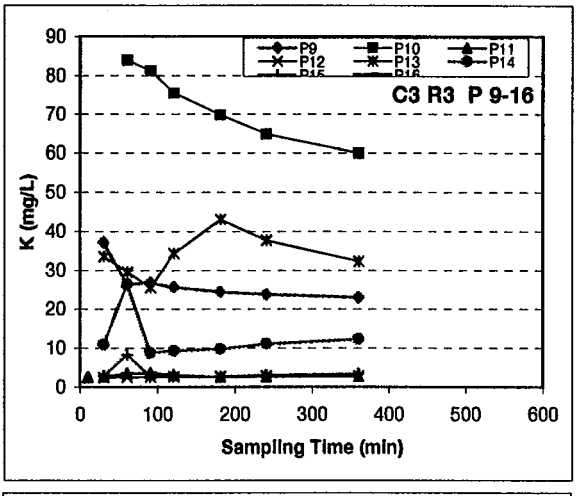

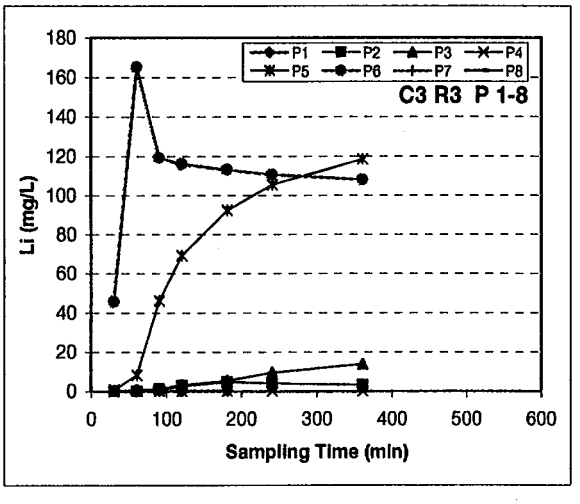

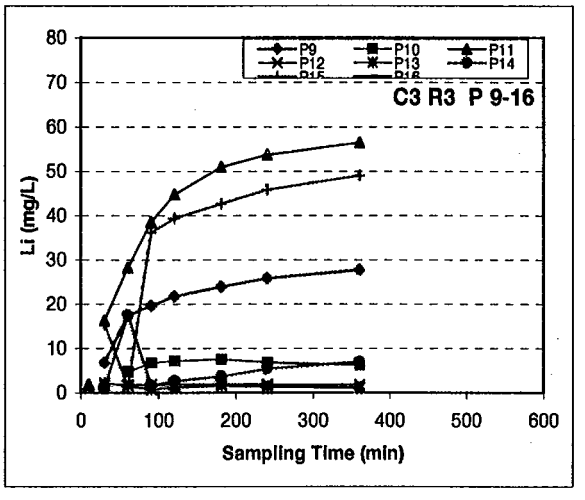

APPENDIX VI RADIAL DISPERSION FLOW GRAPHS

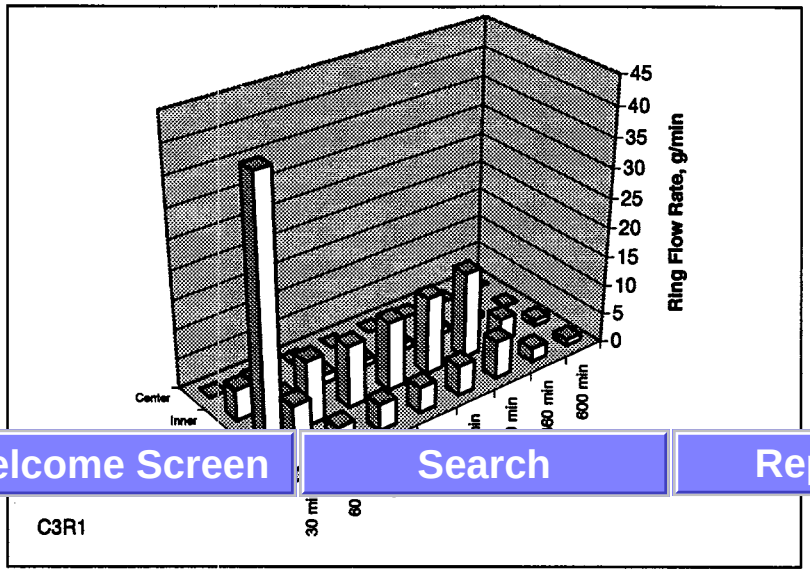
45
40
35
30
25
20
15
10
5
0
Ring Flow Rate, g/min
Center
Inner
600 min
C3R1

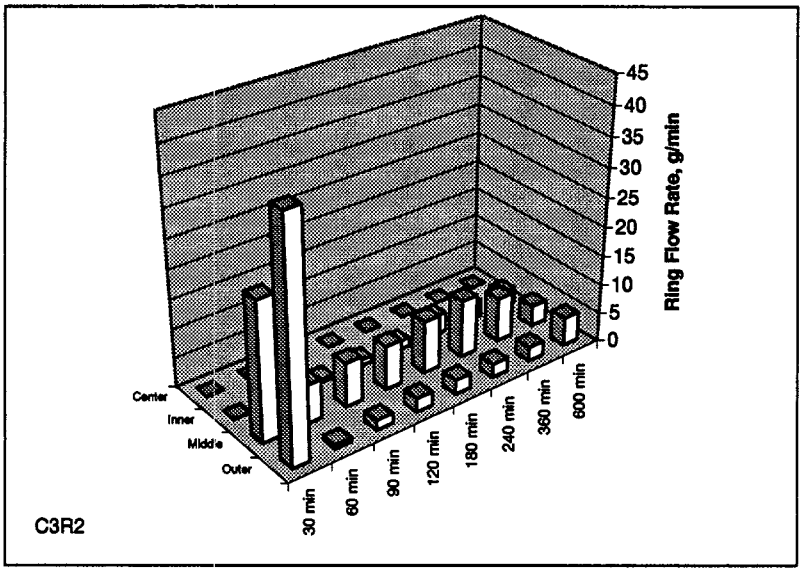
45
40
35
30
25
20
15
10
5
0
Ring Flow Rate, g/min
Center
Inner
Middle
Outer
30 min
60 min
90 min
120 min
180 min
240 min
360 min
600 min
C3R2

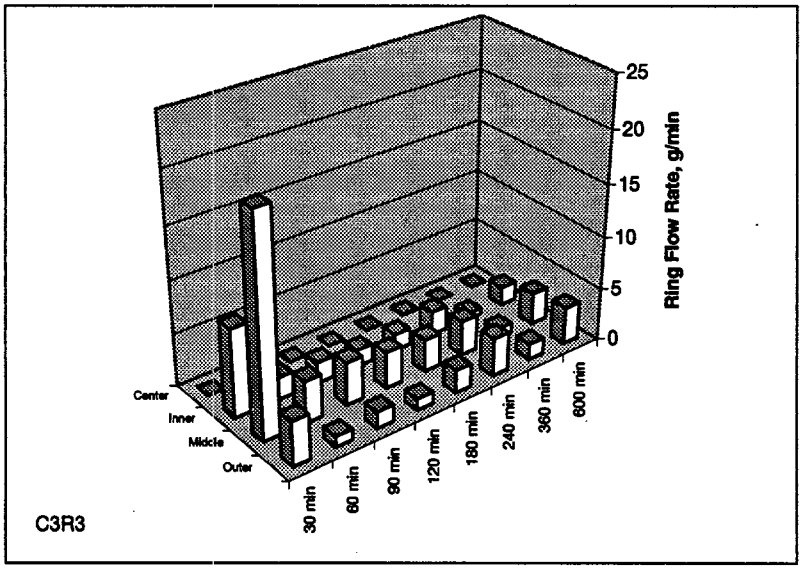
25
20
15
10
5
0
Ring Flow Rate, g/min
Center
Inner
Middle
Outer
30 min
60 min
90 min
120 min
180 min
240 min
360 min
600 min
C3R3

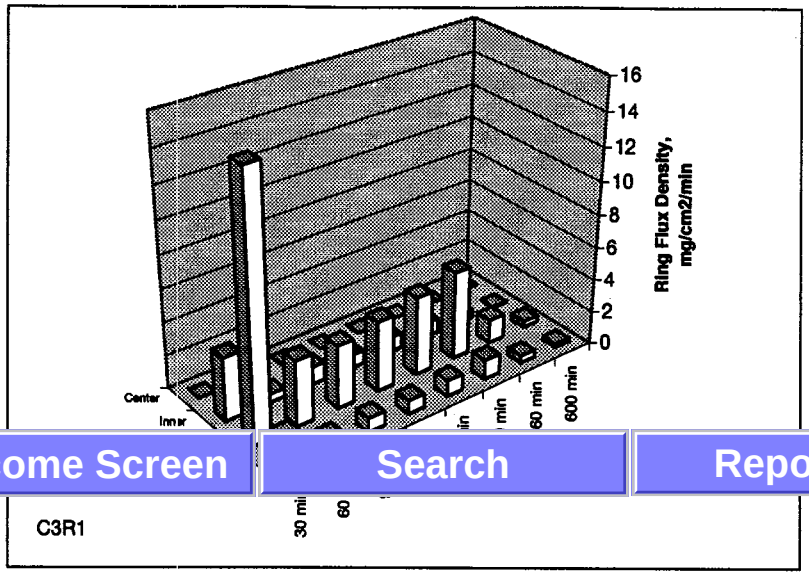

C3R1

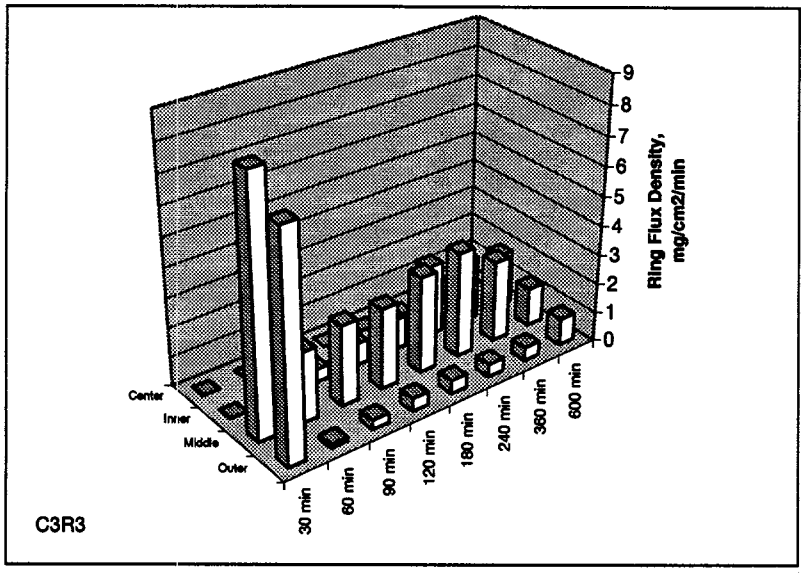

C3R3

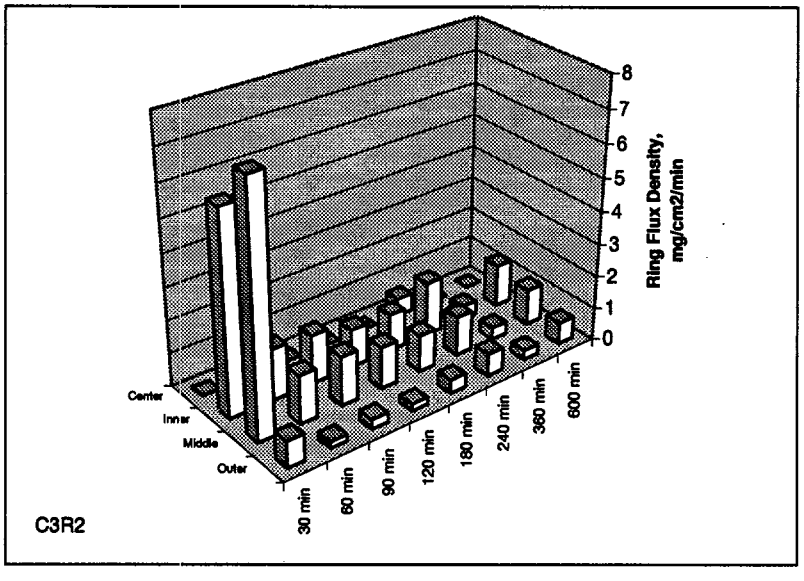

C3R2

APPENDIX VII RULE GOVERNING SOLUBILITY CONTROL IN AQUEOUS SOLUTIONS

The rule governing solubility control of dissolved constituents in an aqueous solution is stated as follows:

> Suppose a solution containing dissolved constituents A and B is in equilibrium with the mineral phase AB. The molar concentrations of A and B are C_A and C_B, respectively. If $C_A >> C_B$ then C_B is controlled by the solubility of AB whereas C_A is not; if $C_A \approx C_B$, then both C_A and C_B are controlled by the solubility of AB; if $C_A << C_B$, then C_A is controlled by the solubility of AB but C_B is not.

To prove this rule, suppose the mineral precipitation reaction, A + B = AB(s), is in equilibrium with molar concentrations of A, B, and AB, designated by CA, C_B, and C_{AB}, respectively. Assuming unity activity coefficients for dissolved constituents A and B, we have

$$C_A \cdot C_B = K_{sp} \qquad \text{Equation 1}$$

where K_{sp} is the thermodynamic solubility product of mineral AB. Now suppose we add AA mol/L of A (but not B) to the solution, AA cc CA. This will overthrow the original equilibrium and a new equilibrium will be reached after some AB is precipitated. The new concentrations of A, B and AB are, respectively, $C_A+\Delta C_A$, $C_B+\Delta C_B$ (note ΔC_B is negative), and $C_{AB}+\Delta C_{AB}$. At this new equilibrium, we again have

$$(C_A+\Delta C_A)(C_B+\Delta C_B)= K_{sp} \qquad \text{Equation 2}$$

In addition, since the amount of A added which is also precipitated is equal to the new phase AB precipitated, we have

$$\Delta A-\Delta C_A=\Delta C_{AB} \qquad \text{Equation 3}$$

Finally, since the amount of B precipitated is equal to the amount of AB created, we have

$$-\Delta C_B =\Delta C_{AB} \qquad \text{Equation 4}$$

Combining and solving Equations 1 to 4, we obtain

$$\frac{\Delta C_A}{AA} = \frac{C_A}{C_A + C_B + \Delta C_B} \qquad \text{Equation 5}$$

If CA >> C_B > $|\Delta C_B|$, then $C_A+C_B+\Delta C_B \approx$ CA, thus $\Delta C_A \approx$ AA. That is, nearly all the A added to the solution stays in solution and the presence of AB is not exerting a control on CA. On the contrary, if ΔC_B c C_A cc C_B, then $C_A+C_B+\Delta C_B \approx C_B$, $\Delta C_A/\Delta A \approx C_A/C_B \rightarrow 0$. That is, virtually all the A added will be precipitated, not allowing C_A to rise and thus exerting a strict control on CA. Finally, if C_A and C_B are comparable in magnitude, e.g., $C_A/C_B \in [0.1, 10]$, then the mineral phase AB exerts some control on both C_A and C_B. For the case $C_A=C_B>>\Delta C_B$, $\Delta C_A/\Delta A \approx 0.5$. That is, about half of the A added to the solution is precipitated and the other half stays in solution.

The above solution can be extended to the case of $aA + bB = A_aB_b(s)$. Applying the Taylor expansion formula on the expression $(C_A+\Delta C_A)^a(C_B+\Delta C_B)^b = K_{sp}$ and ignoring the higher-order terms, for AA cc C_A, we obtain a similar but approximate result: $\Delta C_A/\Delta A = C_A/(C_A+C_B)$. The conclusions are therefore virtually the same as the case of $A + B = AB(s)$.

APPENDIX VIII PROOF OF CONSTANT ZN/S RATIO IN SUCCESSIVE DILUTIONS AND INTER-MIXING

Proof of the fact that successive dilutions of an original solution and mixing of various-stage dilutions maintain a constant Zn/S ratio which is the same as that of the original solution, whereas mixing of two solutions possessing different Zn/S ratios will produce a solution with a Zn/S ratio which is between but unequal to either of the Zn/S ratios of the two original solutions. Solute conservation for Zn and S is assumed.

Let concentrations of Zn and S in the original solution be $C_{Zn,0}$ and $C_{S,0}$ respectively. Thus the Zn/S ratio of the original solution is $R_0 = C_{Zn,0}/C_{S,0}$. Suppose Q_0 litres of this solution is diluted with Q_1 litres of pure water (let us call this dilution a "first-generation dilution"). The dilution factor is $f_1 = Q_0/(Q_0+Q_1)$. After the dilution, the Zn and S concentrations are, respectively, $C_{Zn,1} = f_1 C_{Zn,0}$ and $C_{S,1} = f_1 C_{S,0}$, thus the new Zn/S ratio is $R_1 = C_{Zn,1}/C_{S,1} = (f_1 C_{Zn,0})/(f_1 C_{S,0}) = C_{Zn,0}/C_{S,0} = R_0$. This analysis can be repeated for the second,, third, . . . generations of dilution and we would obtain $R_0 = R_1 = R_2 = \ldots = R_n$.

Now consider the mixing of two first-generation dilutions. Suppose the two solutions mixed have the following characteristics: Q_1, , $C_{S,1}$, R_1 (which is equal to R_0), and Q'_1, $C'_{Zn,1}$, $C'_{S,1}$, R'_1 (which is also equal to R_0). Let mixing factor $f_2 = Q_1/(Q_1 + Q'_1)$. After mixing, the Zn and S solutions are $C_{Zn,2} = f_2 C_{Zn,1} + (1-f_2) C'_{Zn,1} = f_2 f_1 C_{Zn,0} + (1-f_2) f'_1 C_{Zn,0} = C_{Zn,0}[f_2 f_1 + (1-f_2) f'_1]$ and $C_{S,2} = C_{S,0}[f_2 f_1 + (1-f_2) f'_1]$, therefore $R_{2,mix} = C_{Zn,2}/C_{S,2} = C_{Zn,0}/C_{S,0} = R_0$.

By repeating the above analyses it can be shown that any successive dilutions or mixing of any-generation dilutions will maintain the original Zn/S ratio R_0.

Now mixing of two solutions with different Zn/S ratios. Suppose two solutions are mixed: (1) Q_0, $C_{Zn,0}$, $C_{S,0}$, $C_{Zn,0}/C_{S,0} = R_0$ and (2) Q^*_0, $C^*_{Zn,0}$, $C^*_{S,0}$, $C^*_{Zn,0}/C^*_{S,0} = R^*_0$. $f = Q_0/(Q_0+Q^*_0)$. After mixing, the Zn and S concentrations are $C_{Zn,mix} = fC_{Zn,0} + (1-f)C^*_{Zn,0}$ and $C_{S,mix} = fC_{S,0} + (1-f)C^*_{S,0}$, thus $R_{mix} = C_{Zn,mix}/C_{S,mix} = [fC_{Zn,0} + (1-f)C^*_{Zn,0}]/[fC_{S,0} + (1-f)C^*_{S,0}]$. From this expression it can be easily shown that $R_{mix} = R_0$ if and only if $R^*_0 = R_0$. Otherwise, R_{mix} is between R_0 and R^*_0, because R_{mix} is a weighted average of the two.

APPENDIX IX DRAINAGE PORT FLOW RATE HISTOGRAMS FOR Cl AND C2

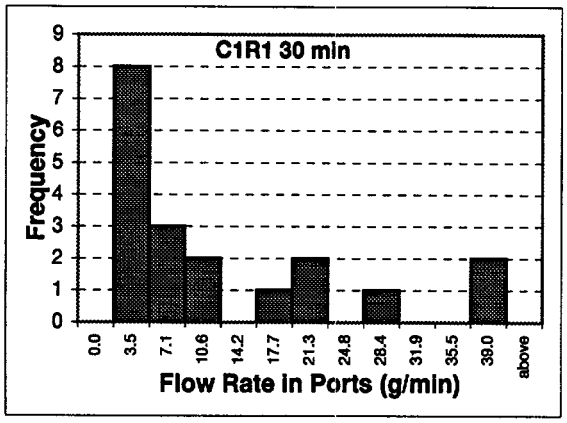
C1R1 30 min
Frequency
0 1 2 3 4 5 6 7 8 9
0.0 3.5 7.1 10.6 14.2 17.7 21.3 24.8 28.4 31.9 35.5 39.0 above
Flow Rate in Ports (g/min)

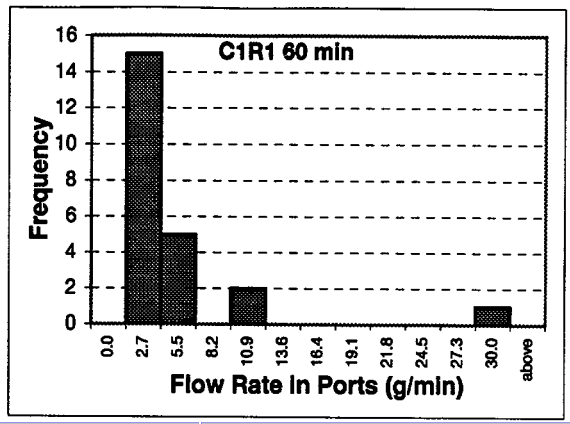
C1R1 60 min
Frequency
0 2 4 6 8 10 12 14 16
0.0 2.7 5.5 8.2 10.9 13.6 16.4 19.1 21.8 24.5 27.3 30.0 above
Flow Rate in Ports (g/min)

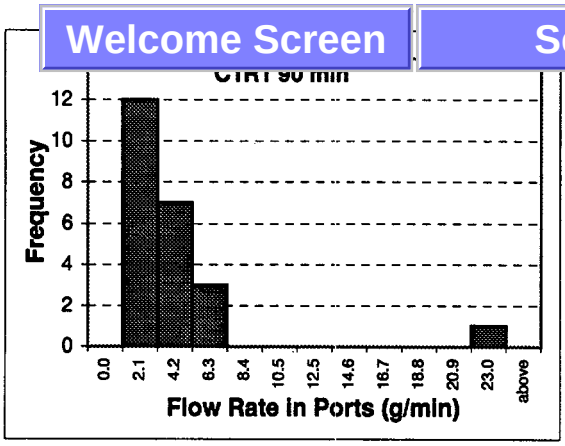
Frequency
0 2 4 6 8 10 12
0.0 2.1 4.2 6.3 8.4 10.5 12.5 14.6 16.7 18.8 20.9 23.0 above
Flow Rate in Ports (g/min)

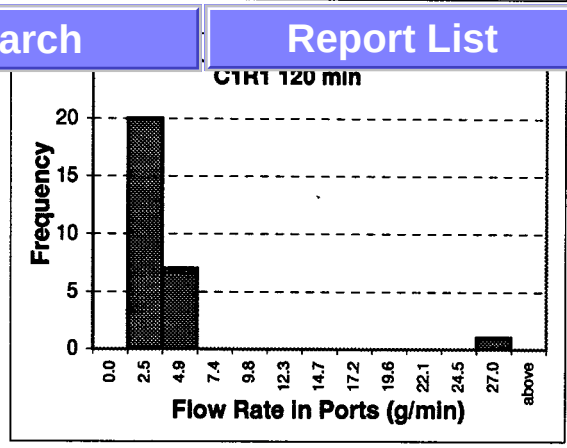
C1R1 120 min
Frequency
0 5 10 15 20
0.0 2.5 4.9 7.4 9.8 12.3 14.7 17.2 19.6 22.1 24.5 27.0 above
Flow Rate in Ports (g/min)

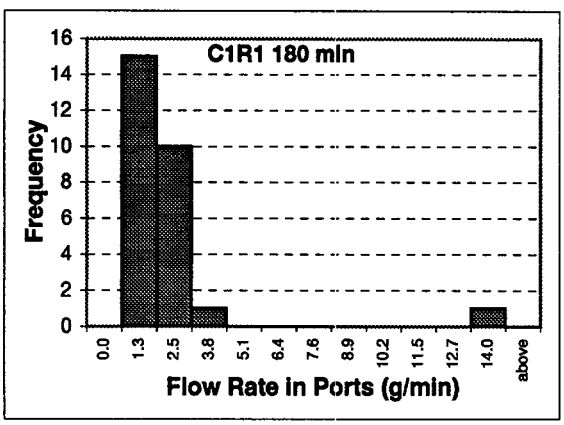
C1R1 180 min
Frequency
0 2 4 6 8 10 12 14 16
0.0 1.3 2.5 3.8 5.1 6.4 7.6 8.9 10.2 11.5 12.7 14.0 above
Flow Rate in Ports (g/min)

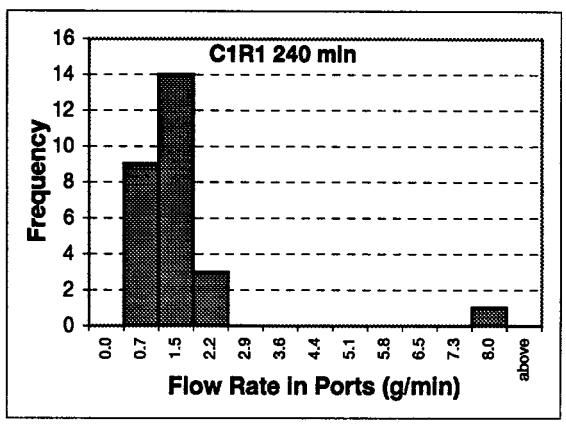
C1R1 240 min
Frequency
0 2 4 6 8 10 12 14 16
0.0 0.7 1.5 2.2 2.9 3.6 4.4 5.1 5.8 6.5 7.3 8.0 above
Flow Rate in Ports (g/min)

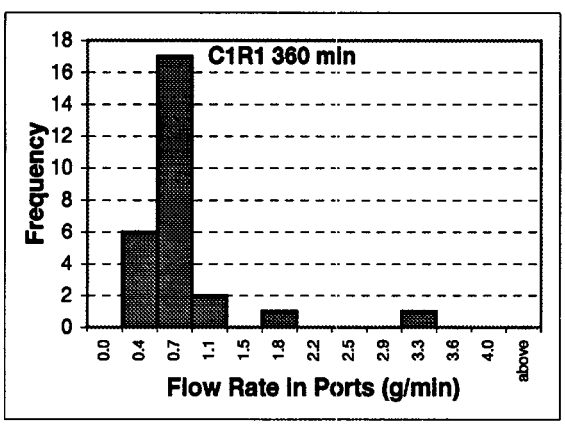
C1R1 360 min
Frequency
0 2 4 6 8 10 12 14 16 18
0.0 0.4 0.7 1.1 1.5 1.8 2.2 2.5 2.9 3.3 3.6 4.0 above
Flow Rate in Ports (g/min)

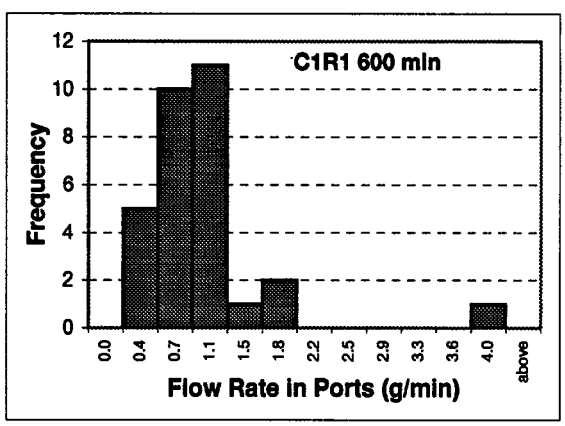
C1R1 600 min
Frequency
0 2 4 6 8 10 12
0.0 0.4 0.7 1.1 1.5 1.8 2.2 2.5 2.9 3.3 3.6 4.0 above
Flow Rate in Ports (g/min)

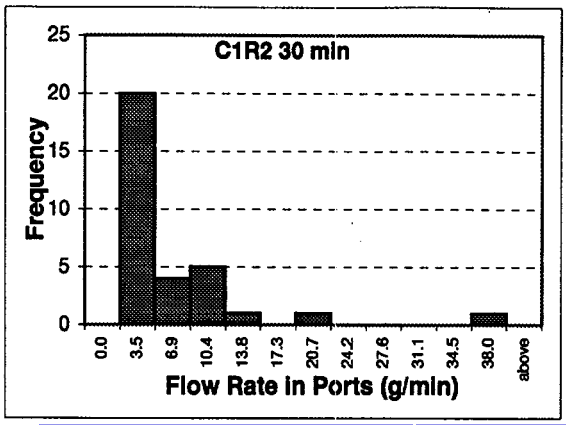
C1R2 30 min
Frequency
Flow Rate in Ports (g/min)
0.0 3.5 6.9 10.4 13.8 17.3 20.7 24.2 27.8 31.1 34.5 38.0 above

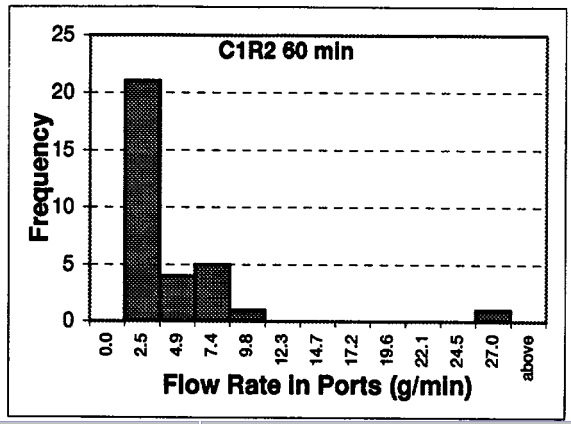
C1R2 60 min
Frequency
Flow Rate in Ports (g/min)
0.0 2.5 4.9 7.4 9.8 12.3 14.7 17.2 19.6 22.1 24.5 27.0 above

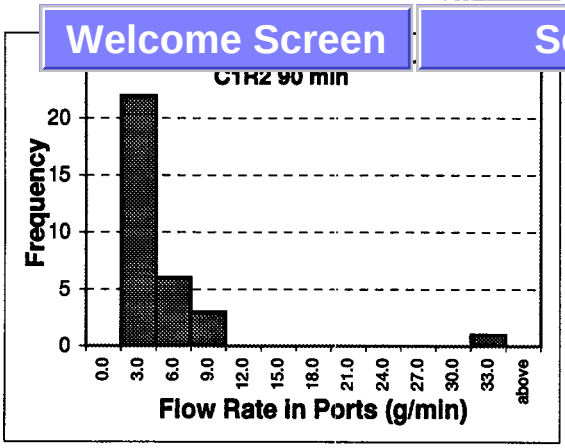
C1R2 90 min
Frequency
Flow Rate in Ports (g/min)
0.0 3.0 6.0 9.0 12.0 15.0 18.0 21.0 24.0 27.0 30.0 33.0 above

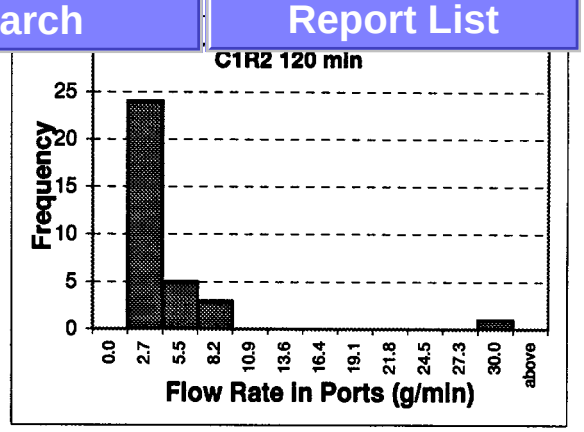
C1R2 120 min
Frequency
Flow Rate in Ports (g/min)
0.0 2.7 5.5 8.2 10.9 13.6 16.4 19.1 21.8 24.5 27.3 30.0 above

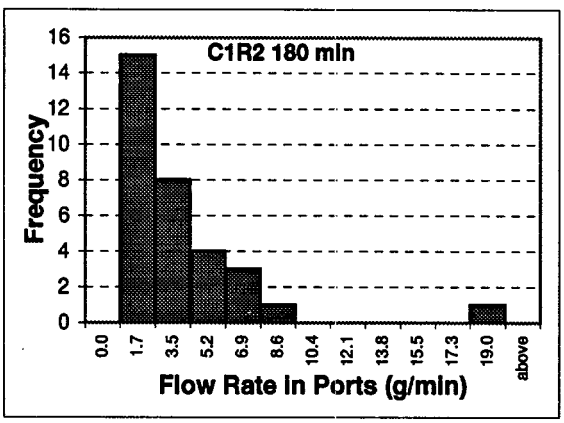
C1R2 180 min
Frequency
Flow Rate in Ports (g/min)
0.0 1.7 3.5 5.2 6.9 8.6 10.4 12.1 13.8 15.5 17.3 19.0 above

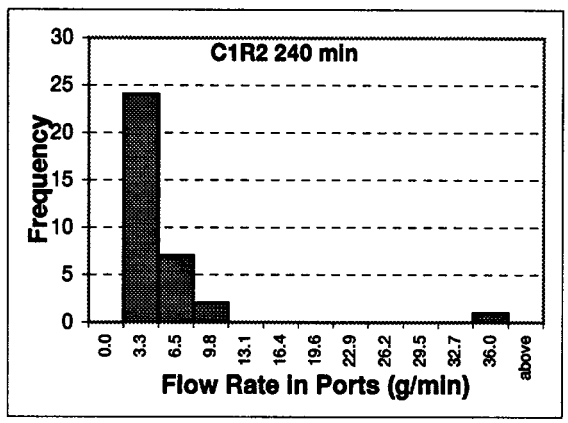
C1R2 240 min
Frequency
Flow Rate in Ports (g/min)
0.0 3.3 6.5 9.8 13.1 16.4 19.6 22.9 26.2 29.5 32.7 36.0 above

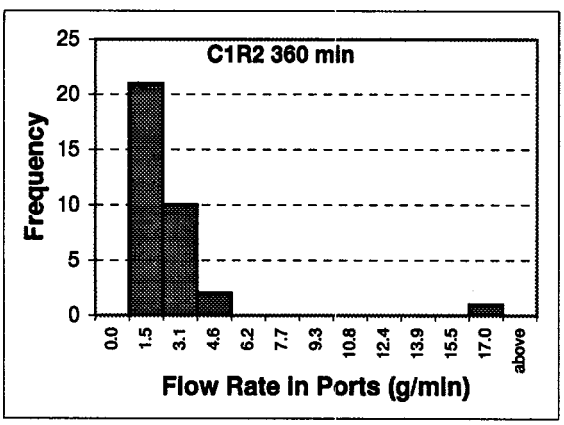
C1R2 360 min
Frequency
Flow Rate in Ports (g/min)
0.0 1.5 3.1 4.6 6.2 7.7 9.3 10.8 12.4 13.9 15.5 17.0 above

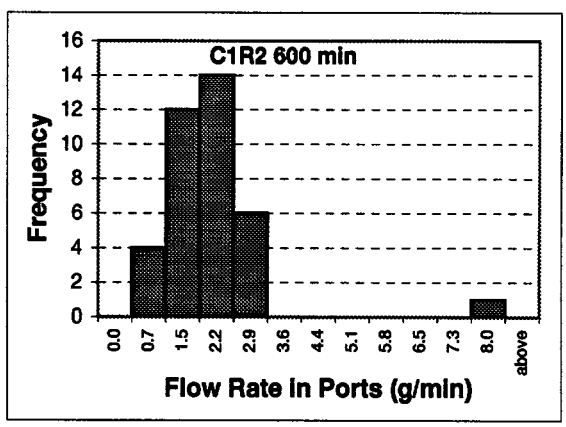
C1R2 600 min
Frequency
Flow Rate in Ports (g/min)
0.0 0.7 1.5 2.2 2.9 3.6 4.4 5.1 5.8 6.5 7.3 8.0 above

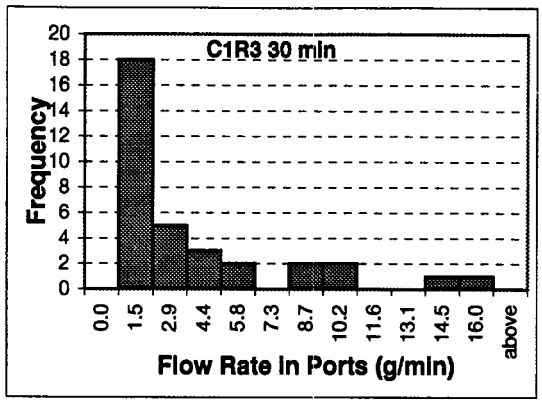

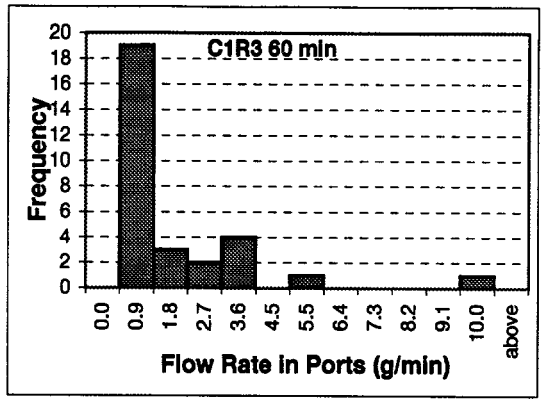

Welcome Screen | Search | Report List

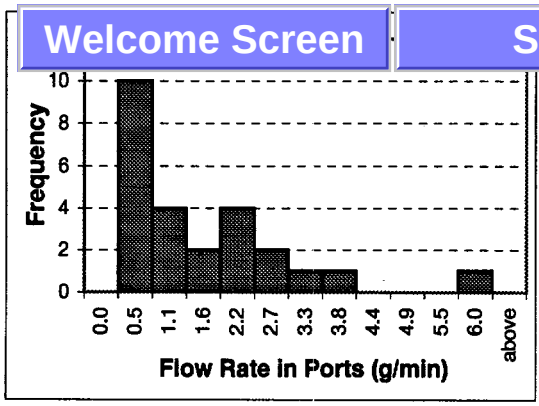

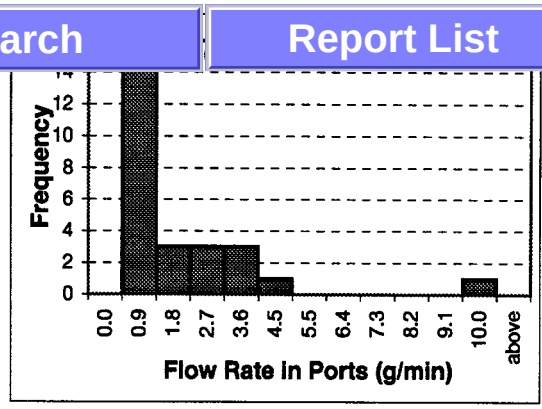

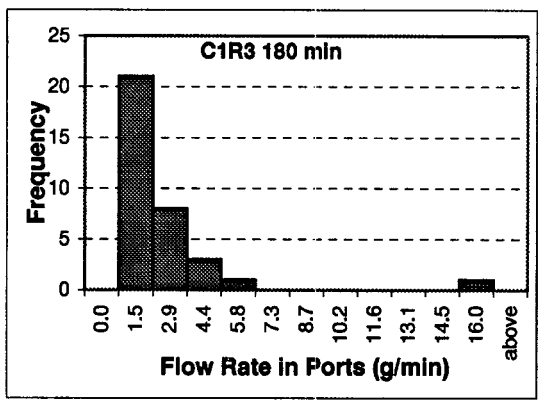

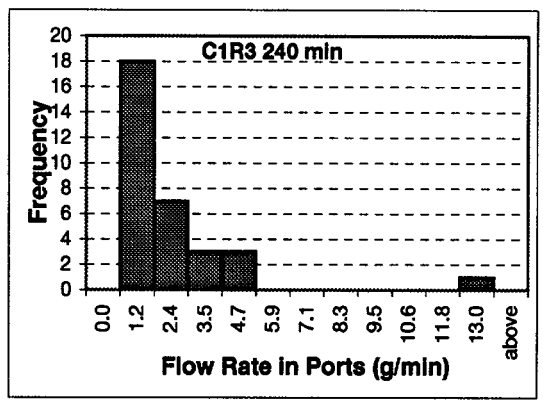

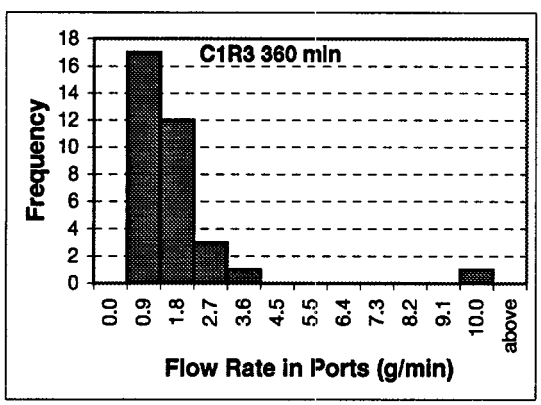

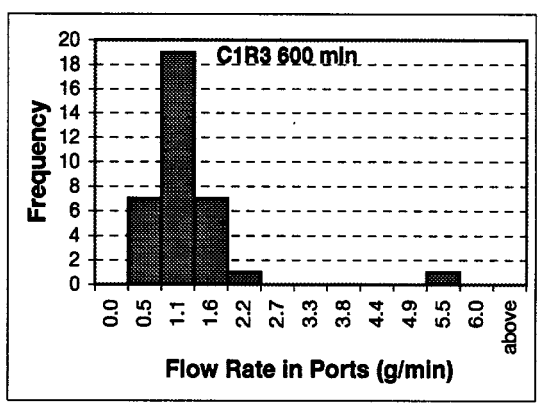

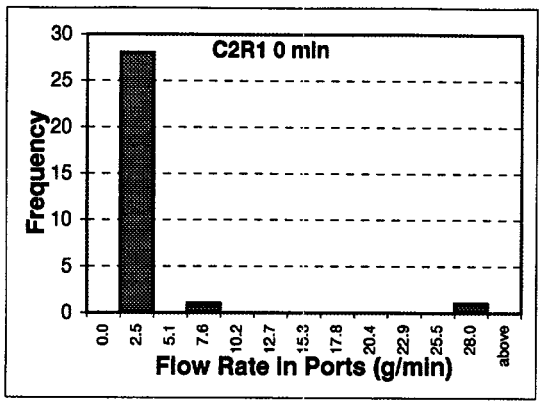

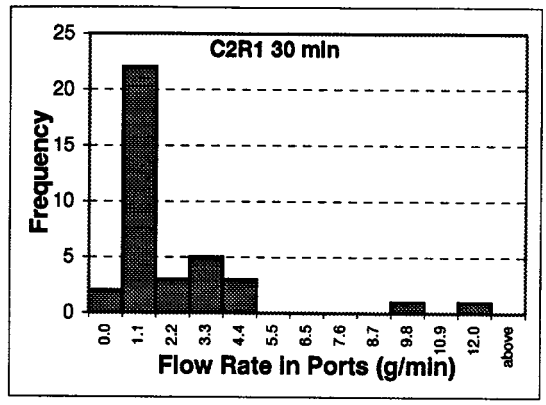

Welcome Screen | Search | Report List

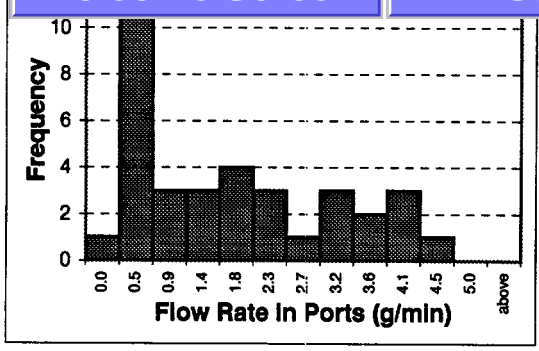

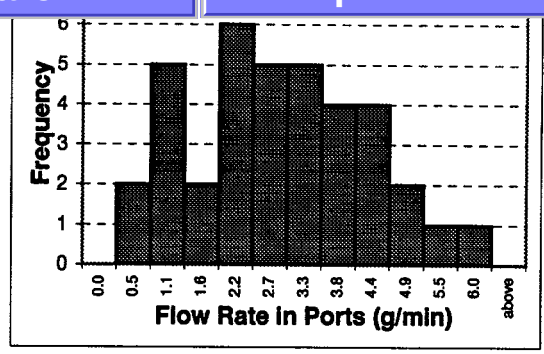

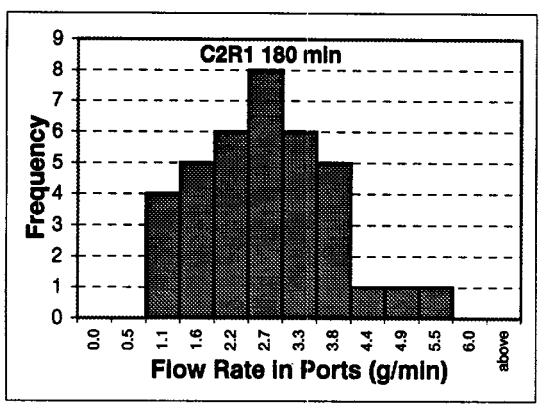

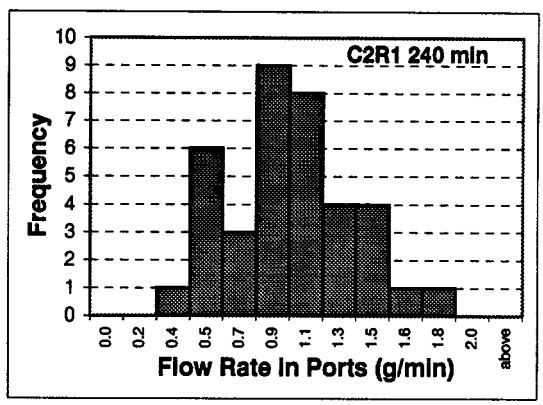

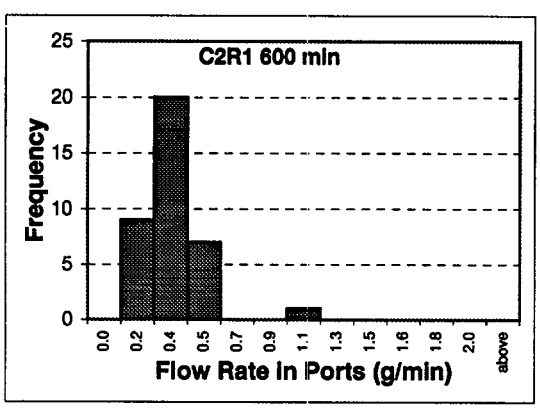

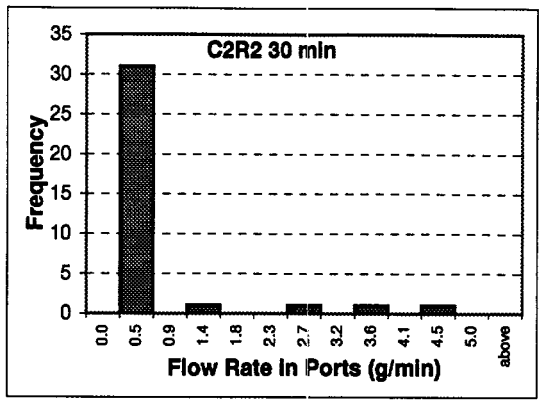

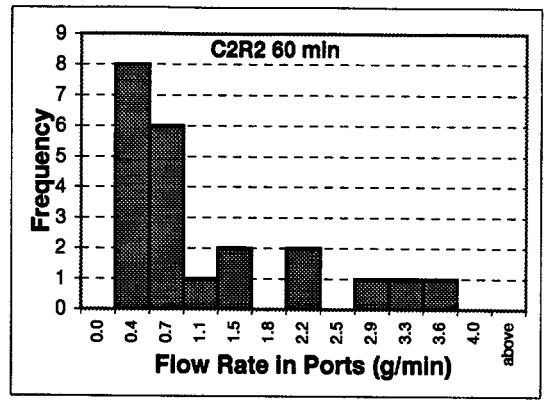

Welcome Screen | Search | Report List

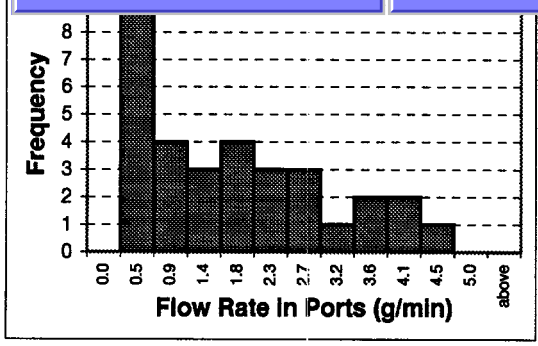

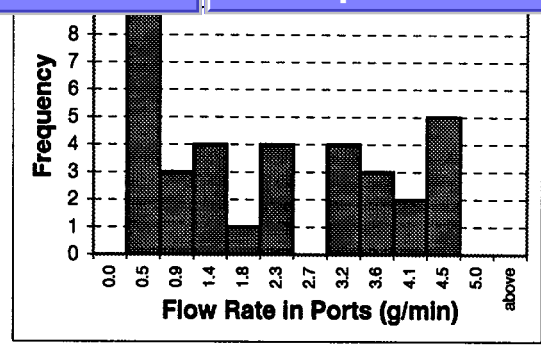

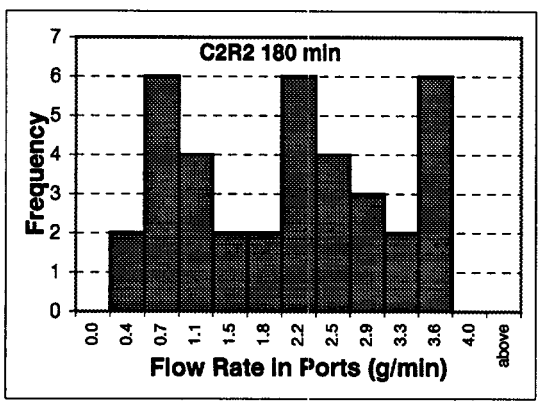

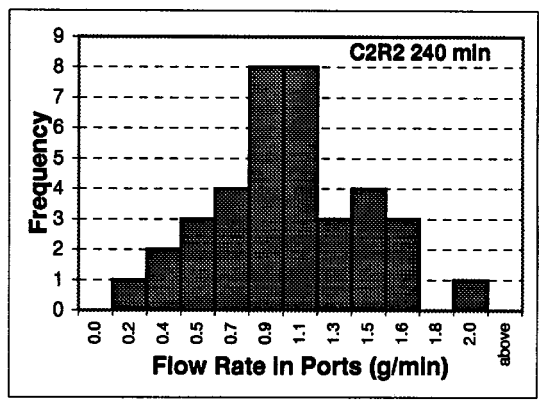

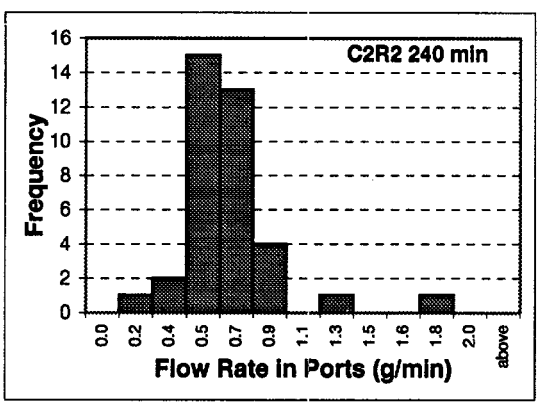

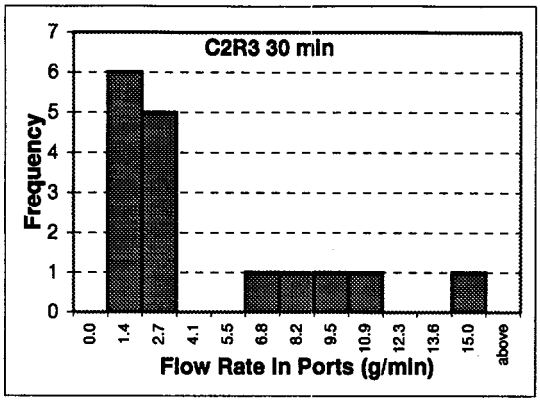
C2R3 30 min
Frequency
Flow Rate in Ports (g/min)
0.0
1.4
2.7
4.1
5.5
6.8
8.2
9.5
10.9
12.3
13.6
15.0
above

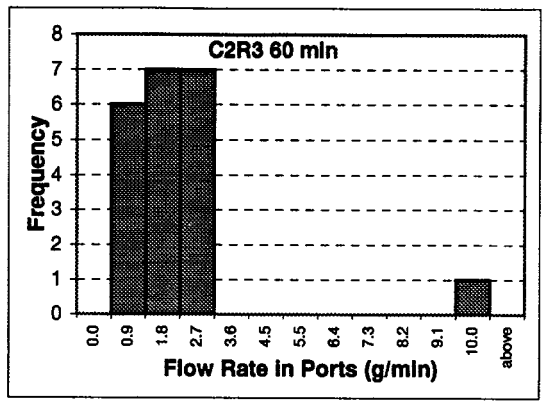
C2R3 60 min
Frequency
Flow Rate in Ports (g/min)
0.0
0.9
1.8
2.7
3.6
4.5
5.5
6.4
7.3
8.2
9.1
10.0
above

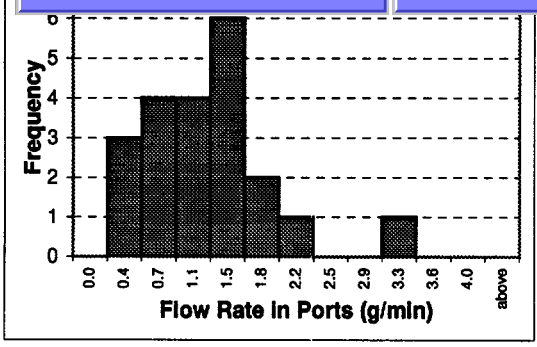
Frequency
Flow Rate in Ports (g/min)
0.0
0.4
0.7
1.1
1.5
1.8
2.2
2.5
2.9
3.3
3.6
4.0
above

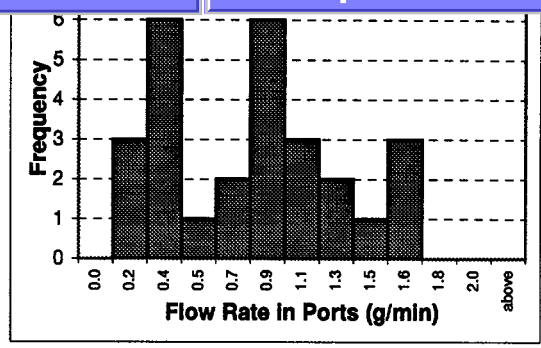
Frequency
Flow Rate in Ports (g/min)
0.0
0.2
0.4
0.5
0.7
0.9
1.1
1.3
1.5
1.6
1.8
2.0
above

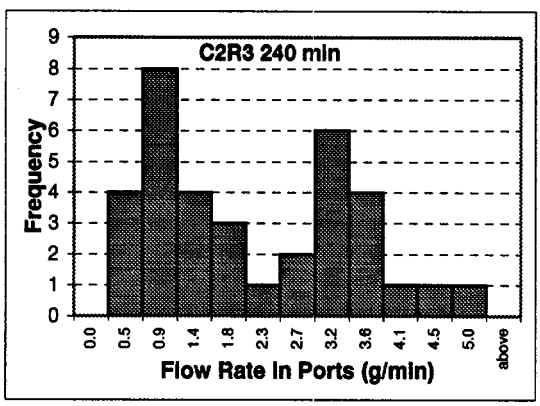
C2R3 240 min
Frequency
Flow Rate in Ports (g/min)
0.0
0.5
0.9
1.4
1.8
2.3
2.7
3.2
3.6
4.1
4.5
5.0
above

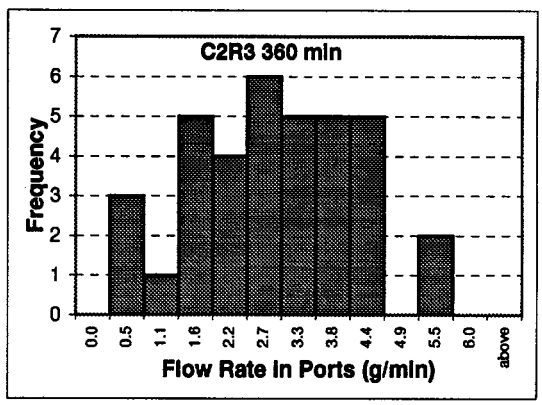
C2R3 360 min
Frequency
Flow Rate in Ports (g/min)
0.0
0.5
1.1
1.6
2.2
2.7
3.3
3.8
4.4
4.9
5.5
6.0
above

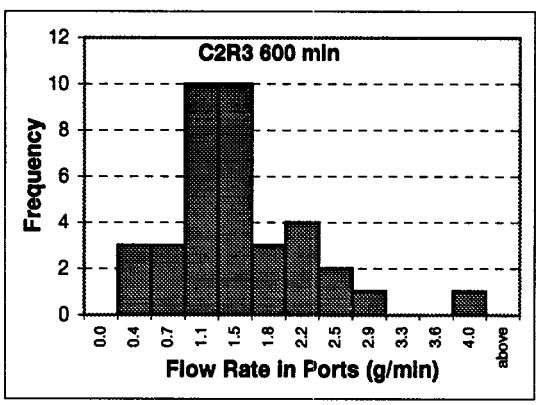
C2R3 600 min
Frequency
Flow Rate in Ports (g/min)
0.0
0.4
0.7
1.1
1.5
1.8
2.2
2.5
2.9
3.3
3.6
4.0
above

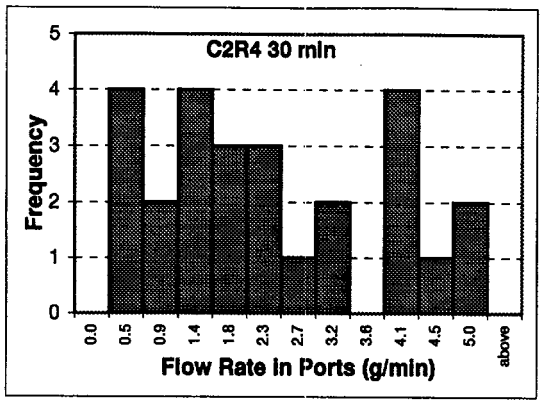
C2R4 30 min
Frequency
0 1 2 3 4 5
0.0 0.5 0.9 1.4 1.8 2.3 2.7 3.2 3.8 4.1 4.5 5.0 above
Flow Rate in Ports (g/min)

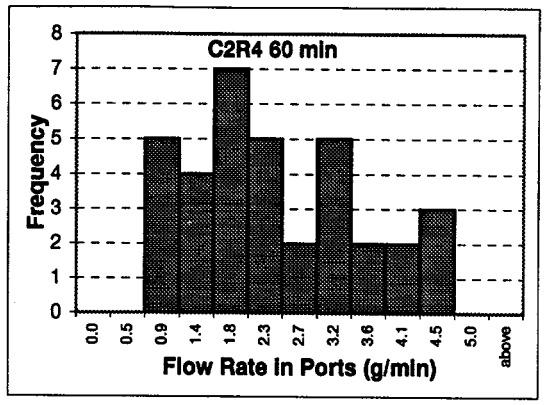
C2R4 60 min
Frequency
0 1 2 3 4 5 6 7 8
0.0 0.5 0.9 1.4 1.8 2.3 2.7 3.2 3.6 4.1 4.5 5.0 above
Flow Rate in Ports (g/min)

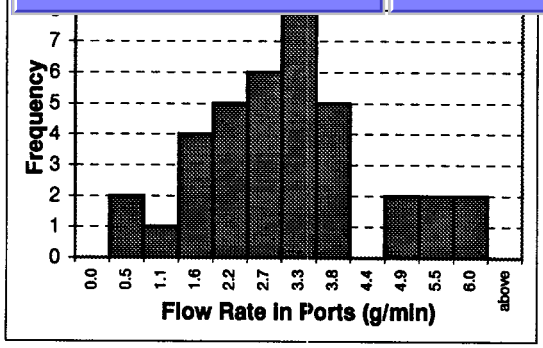
Frequency
0 1 2 3 4 5 6 7
0.0 0.5 1.1 1.6 2.2 2.7 3.3 3.8 4.4 4.9 5.5 6.0 above
Flow Rate in Ports (g/min)

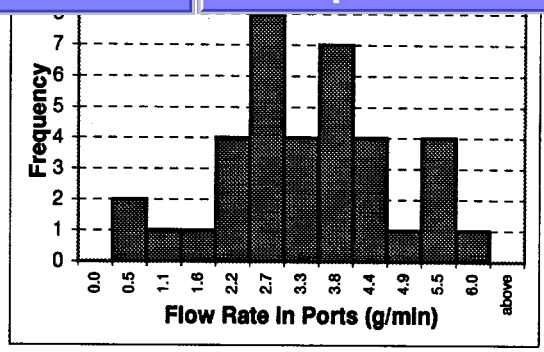
Frequency
0 1 2 3 4 5 6 7
0.0 0.5 1.1 1.6 2.2 2.7 3.3 3.8 4.4 4.9 5.5 6.0 above
Flow Rate in Ports (g/min)

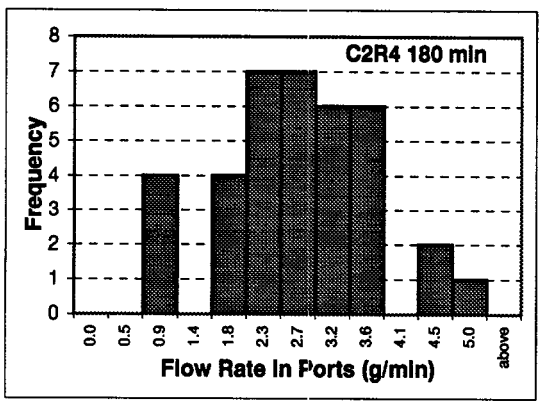
C2R4 180 min
Frequency
0 1 2 3 4 5 6 7 8
0.0 0.5 0.9 1.4 1.8 2.3 2.7 3.2 3.6 4.1 4.5 5.0 above
Flow Rate in Ports (g/min)

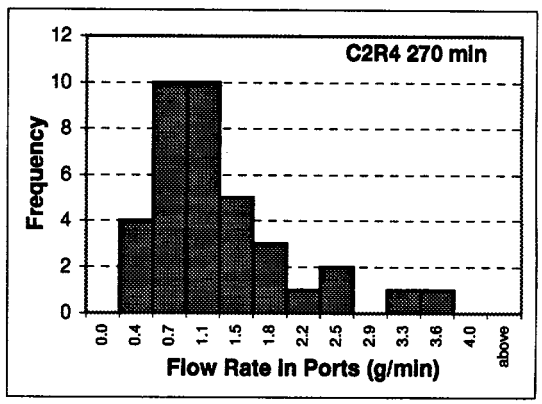
C2R4 270 min
Frequency
0 2 4 6 8 10 12
0.0 0.4 0.7 1.1 1.5 1.8 2.2 2.5 2.9 3.3 3.6 4.0 above
Flow Rate in Ports (g/min)

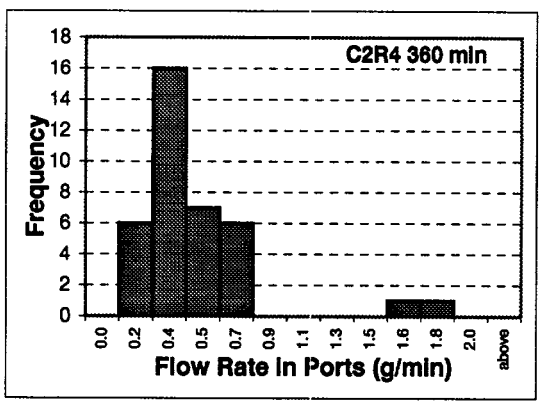
C2R4 360 min
Frequency
0 2 4 6 8 10 12 14 16 18
0.0 0.2 0.4 0.5 0.7 0.9 1.1 1.3 1.5 1.6 1.8 2.0 above
Flow Rate in Ports (g/min)

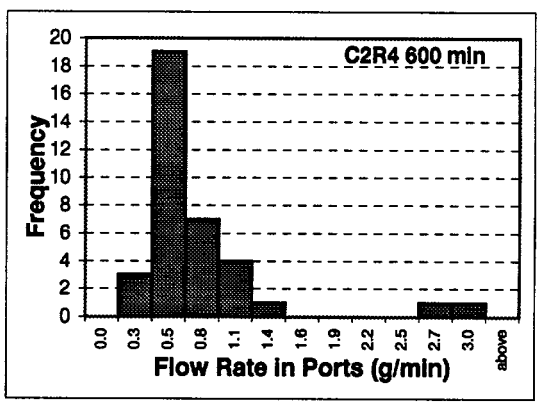
C2R4 600 min
Frequency
0 2 4 6 8 10 12 14 16 18 20
0.0 0.3 0.5 0.8 1.1 1.4 1.6 1.9 2.2 2.5 2.7 3.0 above
Flow Rate in Ports (g/min)

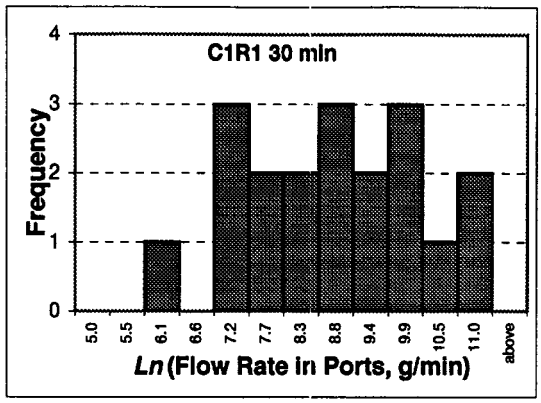
C1R1 30 min
Frequency
Ln (Flow Rate in Ports, g/min)

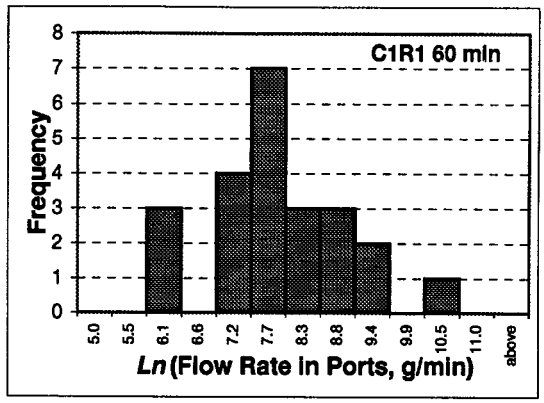
C1R1 60 min
Frequency
Ln (Flow Rate in Ports, g/min)

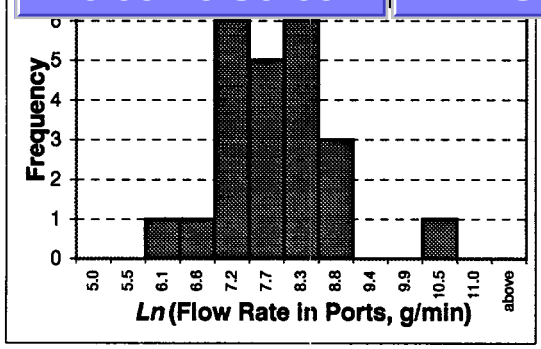
Frequency
Ln (Flow Rate in Ports, g/min)

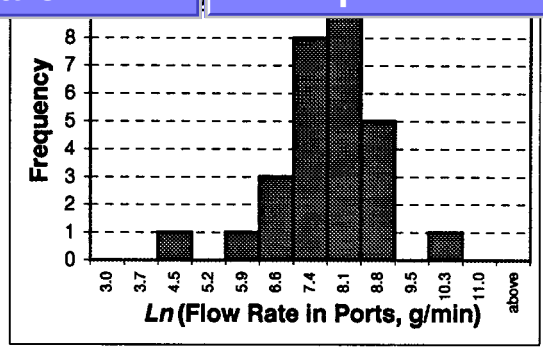
Frequency
Ln (Flow Rate in Ports, g/min)

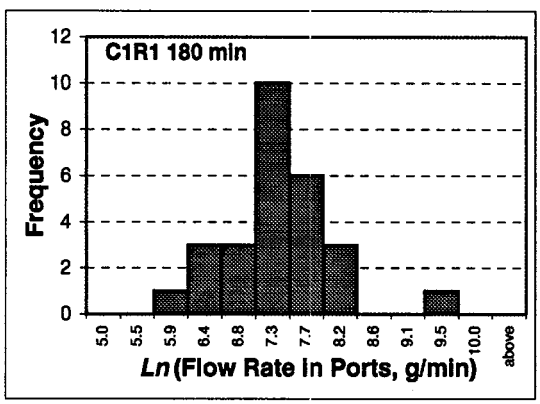
C1R1 180 min
Frequency
Ln (Flow Rate in Ports, g/min)

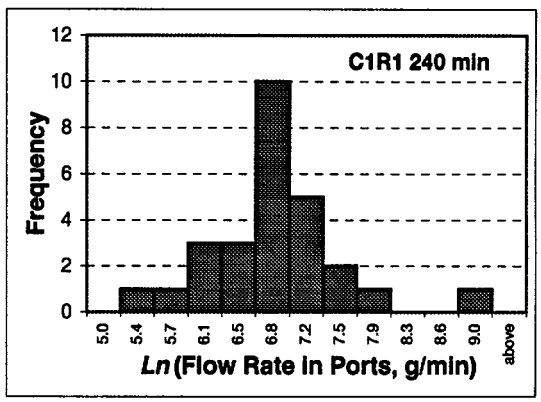
C1R1 240 min
Frequency
Ln (Flow Rate in Ports, g/min)

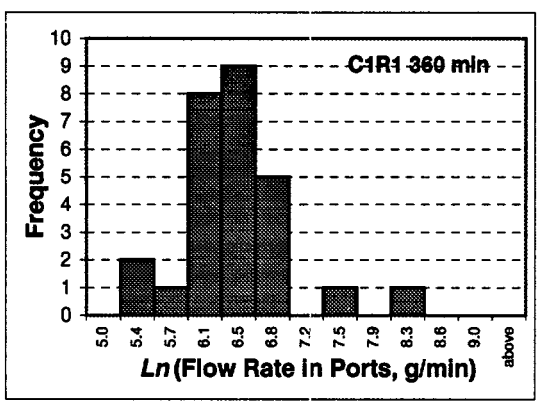
C1R1 360 min
Frequency
Ln (Flow Rate in Ports, g/min)

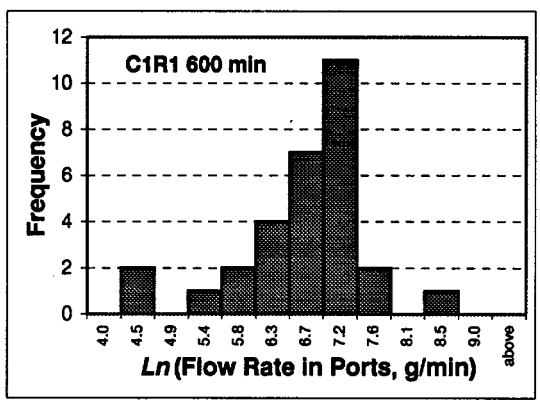
C1R1 600 min
Frequency
Ln (Flow Rate in Ports, g/min)

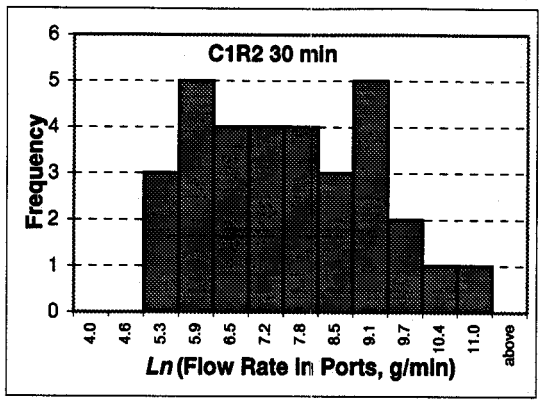

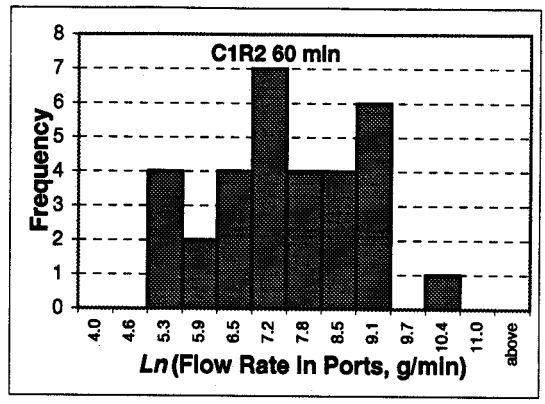

Welcome Screen | Search | Report List

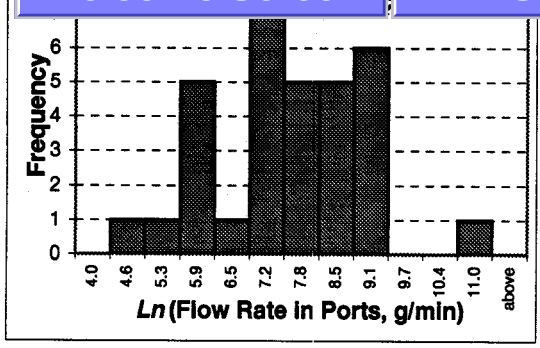

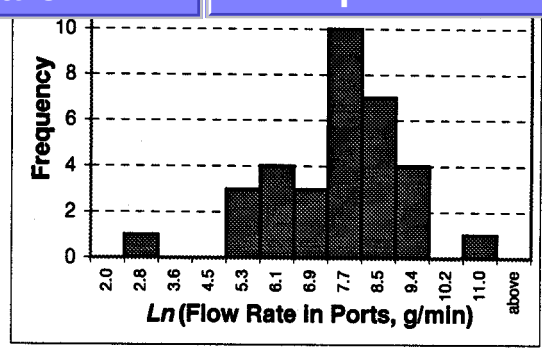

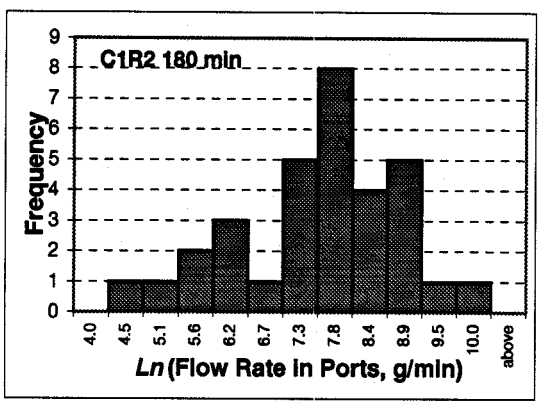

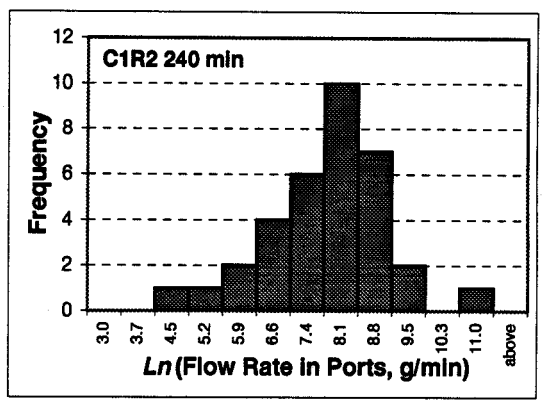

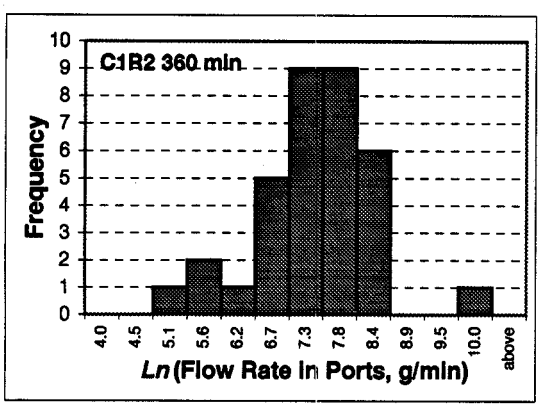

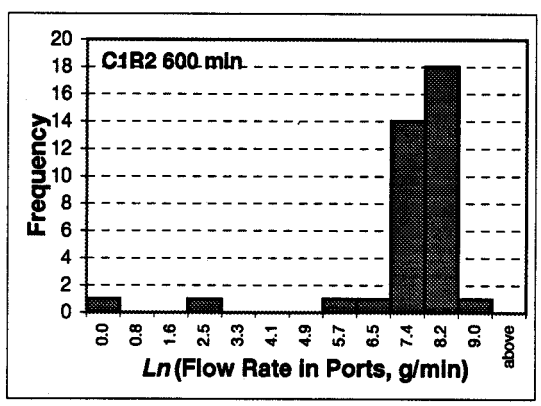

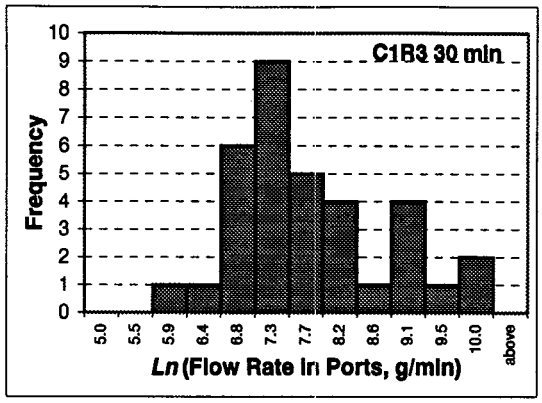
C1B3 30 min
Frequency
Ln (Flow Rate in Ports, g/min)

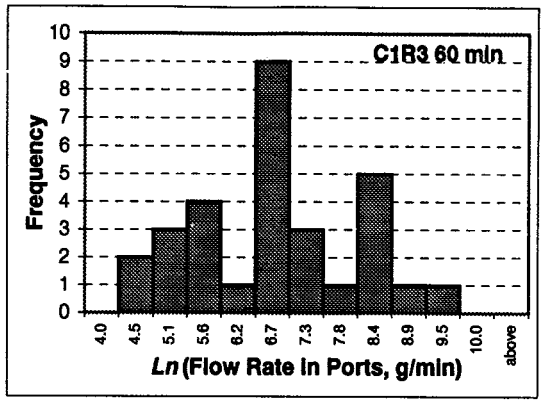
C1B3 60 min
Frequency
Ln (Flow Rate in Ports, g/min)

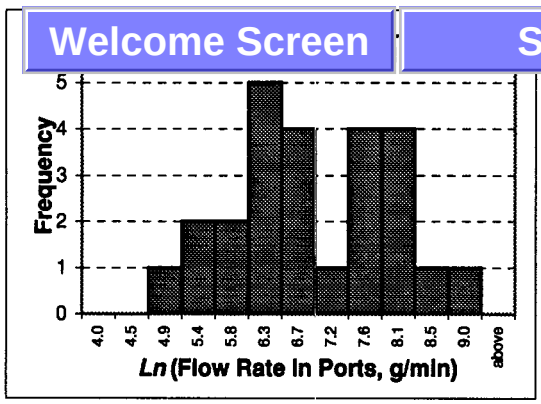
Frequency
Ln (Flow Rate in Ports, g/min)

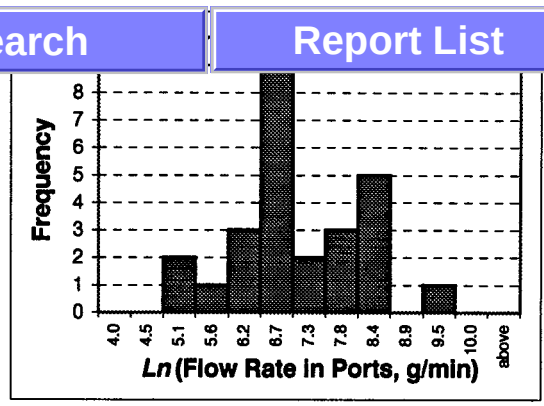
Frequency
Ln (Flow Rate in Ports, g/min)

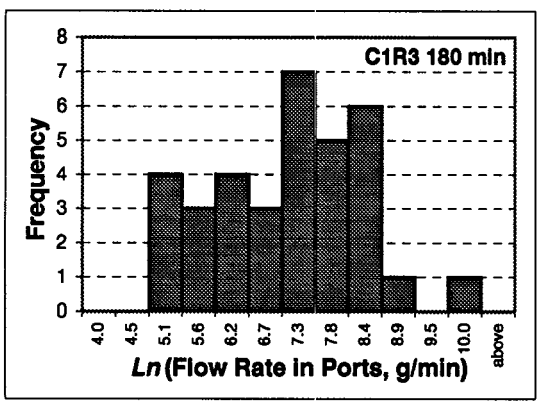
C1R3 180 min
Frequency
Ln (Flow Rate in Ports, g/min)

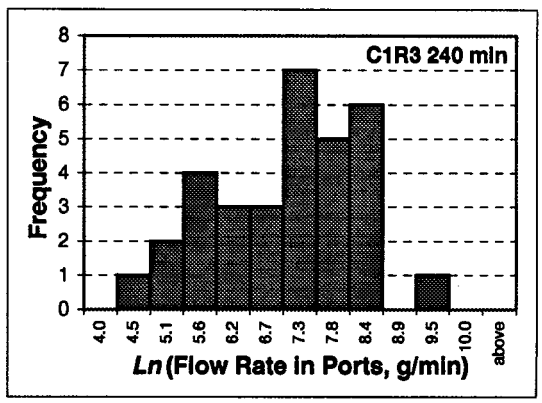
C1R3 240 min
Frequency
Ln (Flow Rate in Ports, g/min)

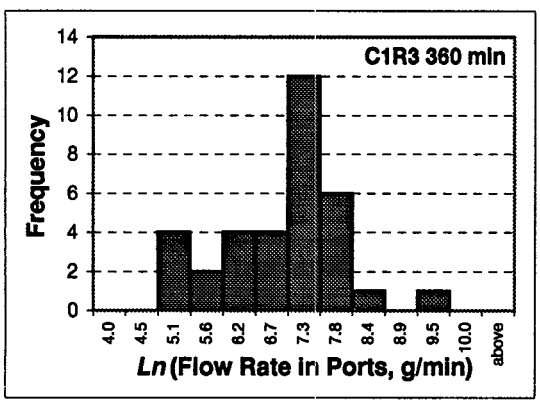
C1R3 360 min
Frequency
Ln (Flow Rate in Ports, g/min)

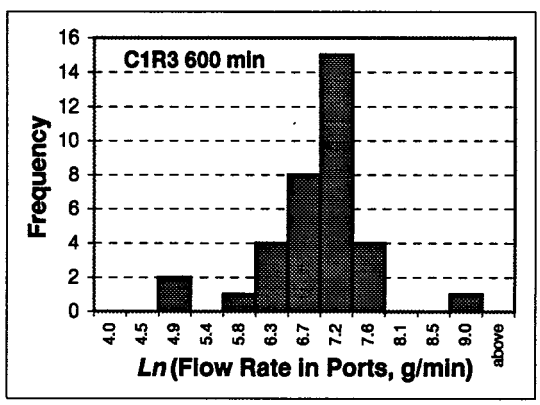
C1R3 600 min
Frequency
Ln (Flow Rate in Ports, g/min)

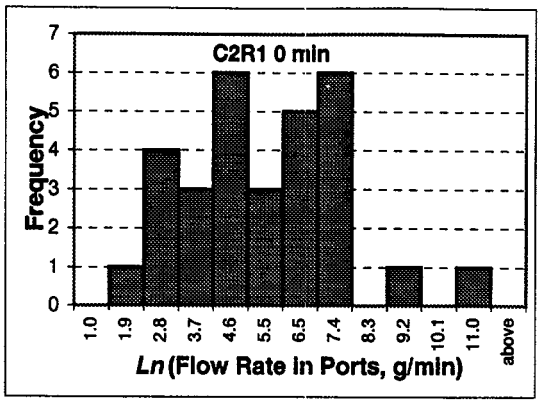
C2R1 0 min
Frequency
0
1
2
3
4
5
6
7
1.0
1.9
2.8
3.7
4.6
5.5
6.5
7.4
8.3
9.2
10.1
11.0
above
Ln (Flow Rate in Ports, g/min)

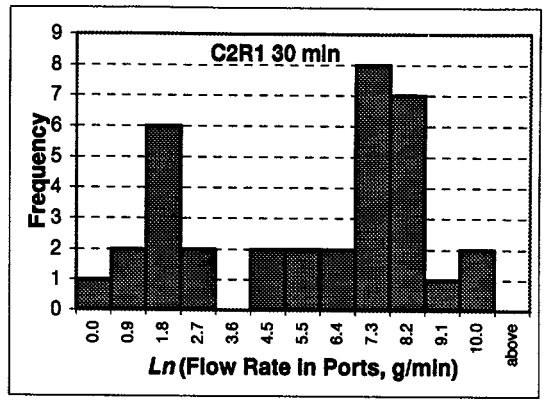
C2R1 30 min
Frequency
0
1
2
3
4
5
6
7
8
9
0.0
0.9
1.8
2.7
3.6
4.5
5.5
6.4
7.3
8.2
9.1
10.0
above
Ln (Flow Rate in Ports, g/min)

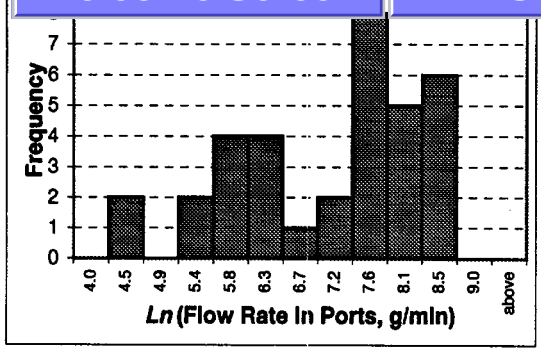
Frequency
0
1
2
3
4
5
6
7
4.0
4.5
4.9
5.4
5.8
6.3
6.7
7.2
7.6
8.1
8.5
9.0
above
Ln (Flow Rate in Ports, g/min)

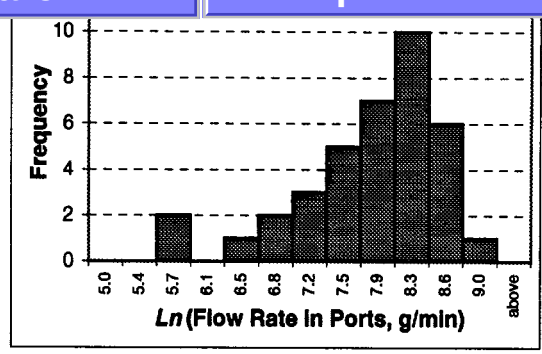
Frequency
0
2
4
6
8
10
5.0
5.4
5.7
6.1
6.5
6.8
7.2
7.5
7.9
8.3
8.6
9.0
above
Ln (Flow Rate in Ports, g/min)

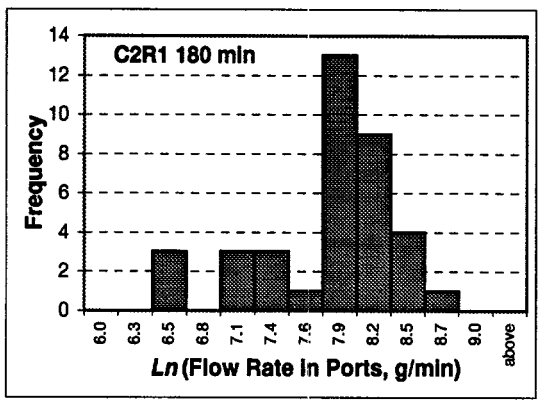
C2R1 180 min
Frequency
0
2
4
6
8
10
12
14
6.0
6.3
6.5
6.8
7.1
7.4
7.6
7.9
8.2
8.5
8.7
9.0
above
Ln (Flow Rate in Ports, g/min)

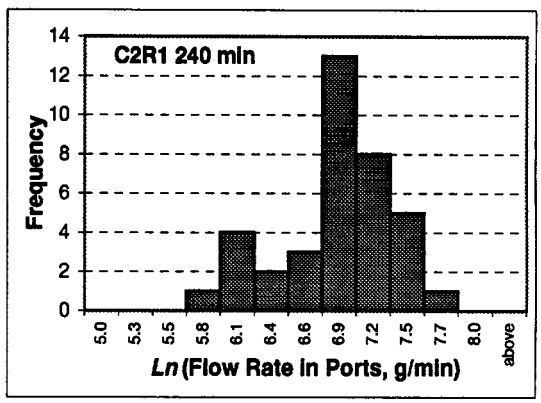
C2R1 240 min
Frequency
0
2
4
6
8
10
12
14
5.0
5.3
5.5
5.8
6.1
6.4
6.6
6.9
7.2
7.5
7.7
8.0
above
Ln (Flow Rate in Ports, g/min)

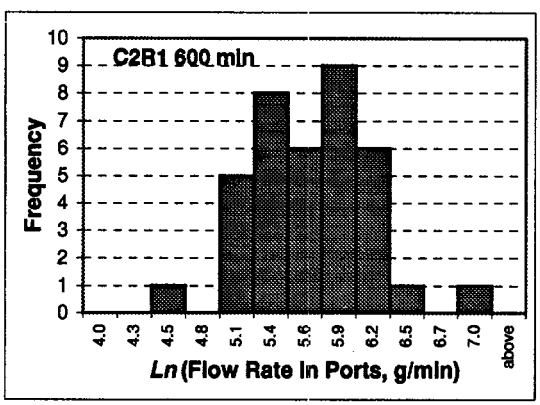
C2R1 600 min
Frequency
0
1
2
3
4
5
6
7
8
9
10
4.0
4.3
4.5
4.8
5.1
5.4
5.6
5.9
6.2
6.5
6.7
7.0
above
Ln (Flow Rate in Ports, g/min)

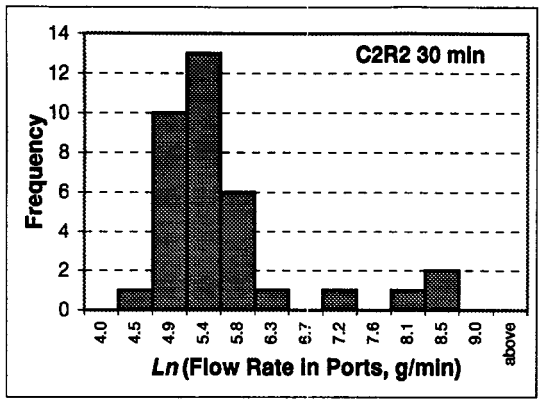

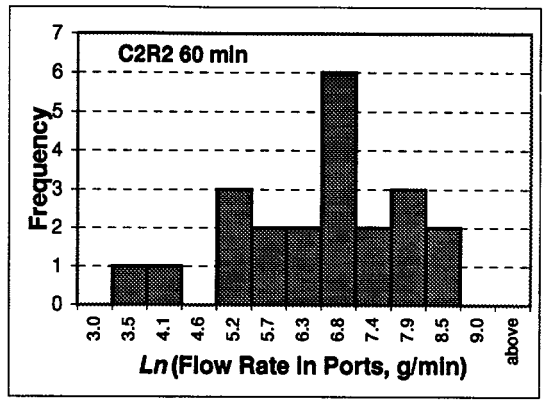

Welcome Screen | Search | Report List

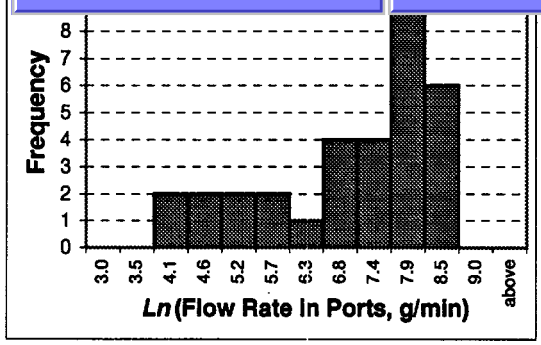

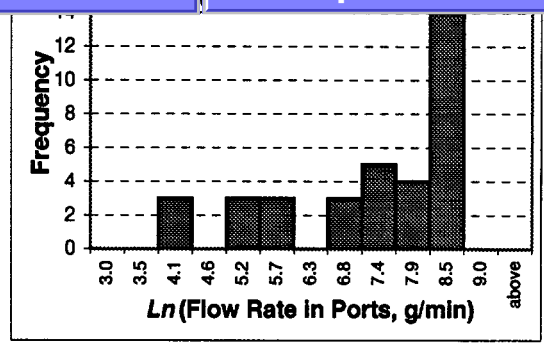

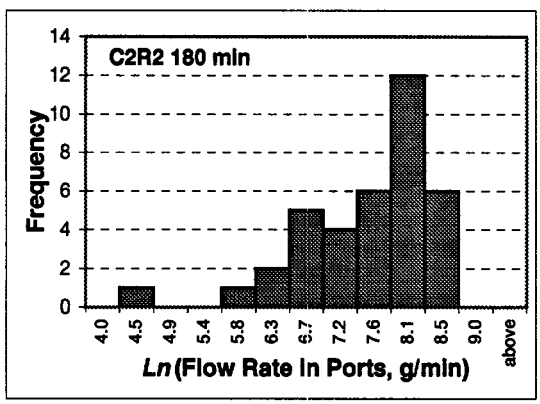

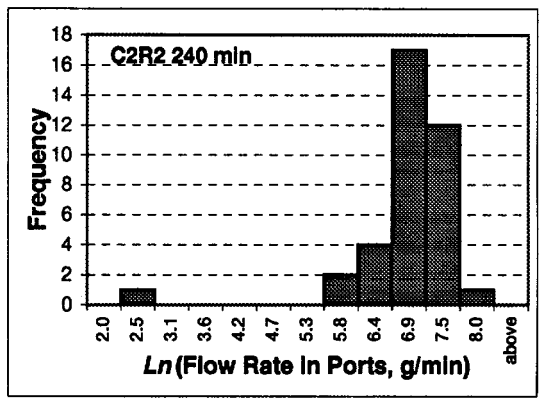

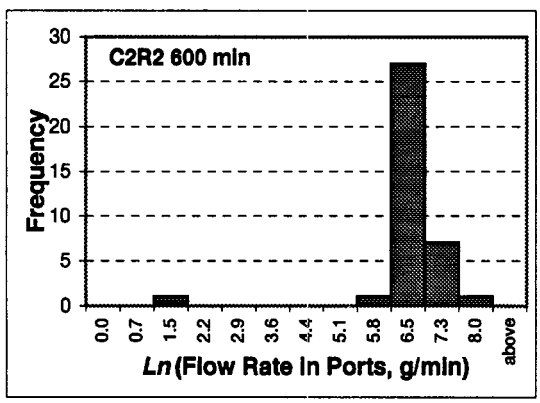

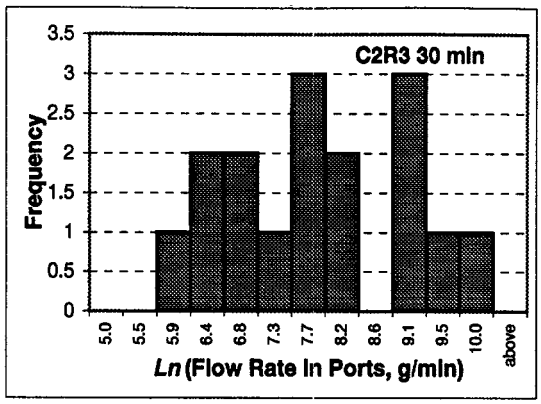
C2R3 30 min
Frequency
0
0.5
1
1.5
2
2.5
3
3.5
5.0
5.5
5.9
6.4
6.8
7.3
7.7
8.2
8.6
9.1
9.5
10.0
above
Ln (Flow Rate in Ports, g/min)

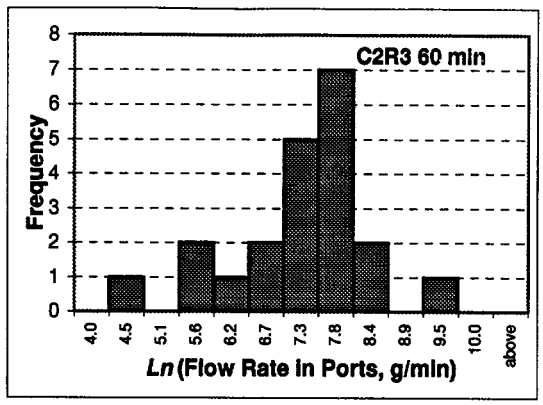
C2R3 60 min
Frequency
0
1
2
3
4
5
6
7
8
4.0
4.5
5.1
5.6
6.2
6.7
7.3
7.8
8.4
8.9
9.5
10.0
above
Ln (Flow Rate in Ports, g/min)

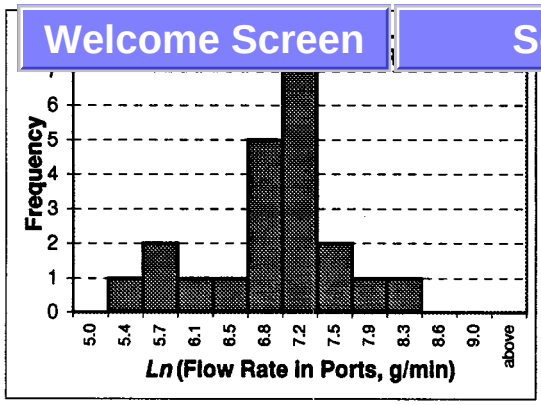
Frequency
0
1
2
3
4
5
6
5.0
5.4
5.7
6.1
6.5
6.8
7.2
7.5
7.9
8.3
8.6
9.0
above
Ln (Flow Rate in Ports, g/min)

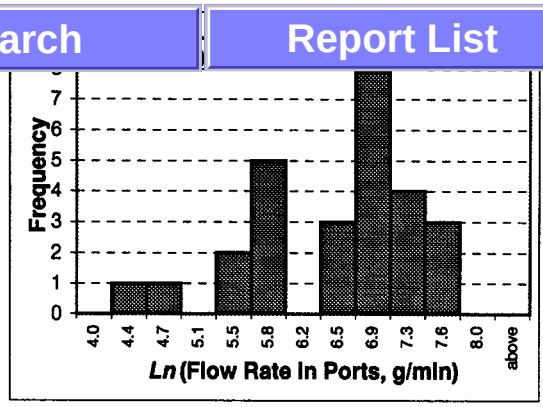
Frequency
0
1
2
3
4
5
6
7
4.0
4.4
4.7
5.1
5.5
5.8
6.2
6.5
6.9
7.3
7.6
8.0
above
Ln (Flow Rate in Ports, g/min)

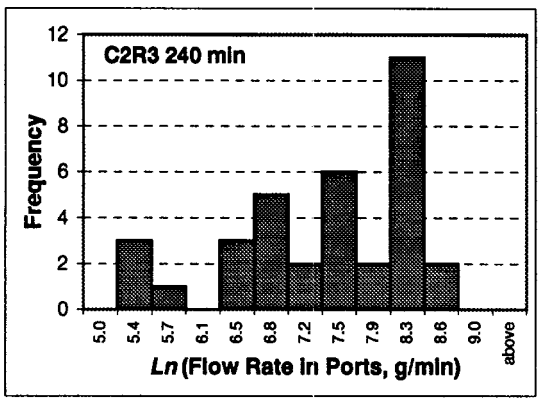
C2R3 240 min
Frequency
0
2
4
6
8
10
12
5.0
5.4
5.7
6.1
6.5
6.8
7.2
7.5
7.9
8.3
8.6
9.0
above
Ln (Flow Rate in Ports, g/min)

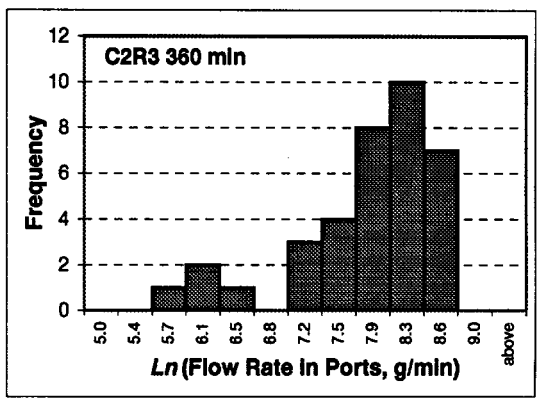
C2R3 360 min
Frequency
0
2
4
6
8
10
12
5.0
5.4
5.7
6.1
6.5
6.8
7.2
7.5
7.9
8.3
8.6
9.0
above
Ln (Flow Rate in Ports, g/min)

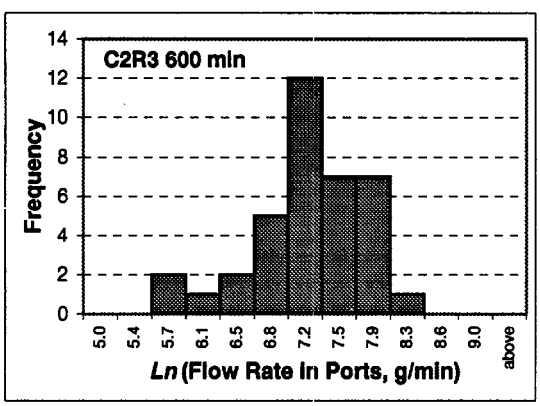
C2R3 600 min
Frequency
0
2
4
6
8
10
12
14
5.0
5.4
5.7
6.1
6.5
6.8
7.2
7.5
7.9
8.3
8.6
9.0
above
Ln (Flow Rate in Ports, g/min)

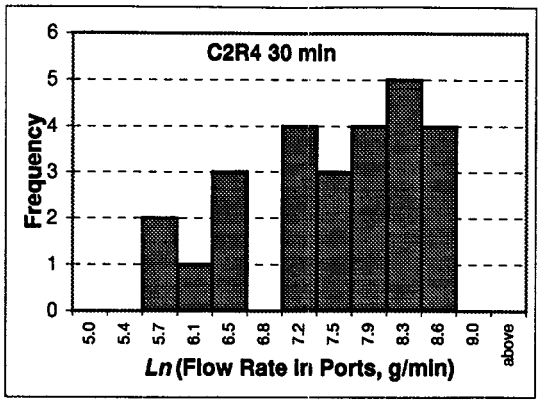

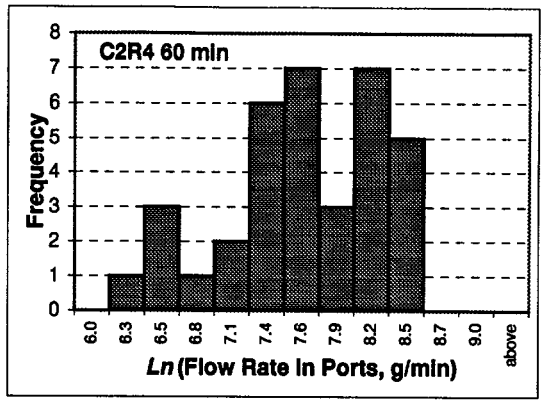

Welcome Screen | Search | Report List

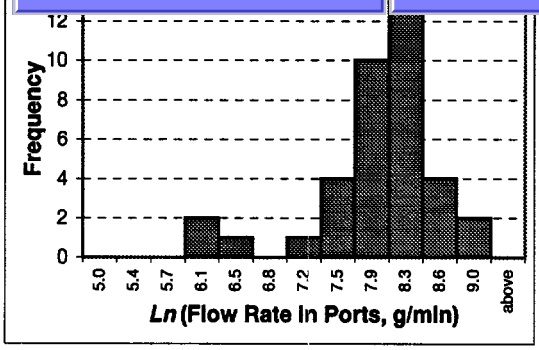

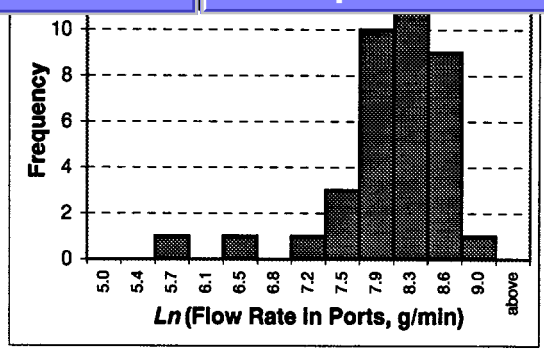

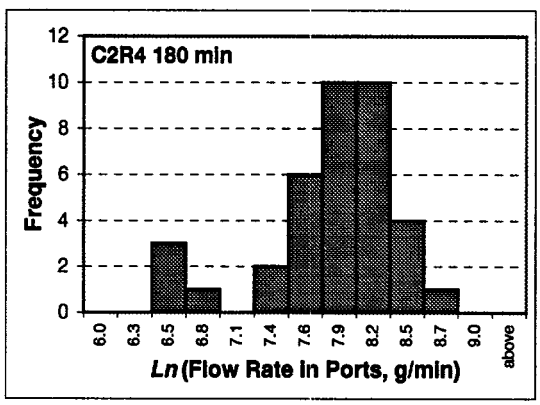

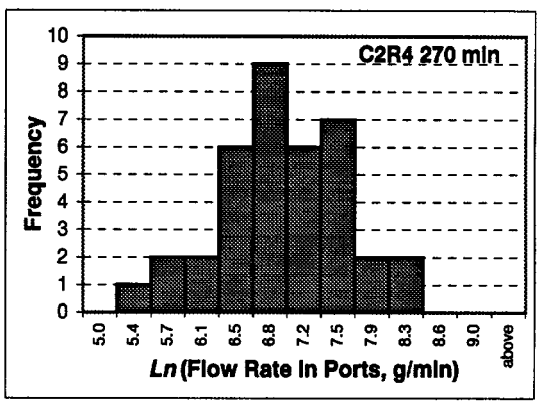

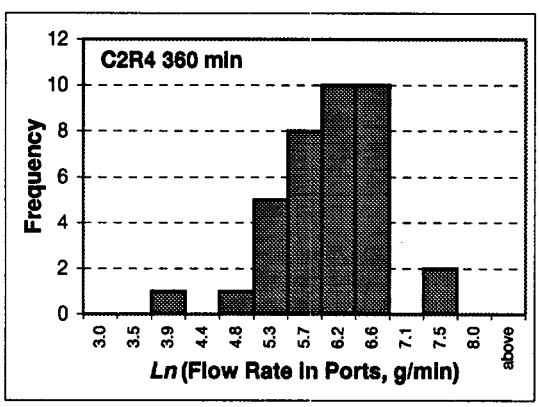

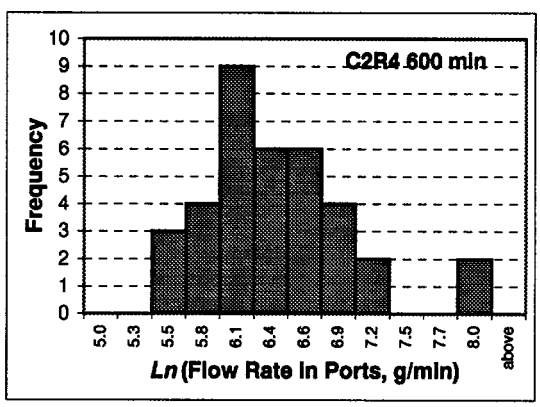

APPENDIX X PHYSICS OF WATER FLOW ON THE SURFACE OF A ROCK PARTICLE

For a unit volume of liquid (water), the gravitational gradient from a point P to another point Q (both on the surface of a rock particle) is

$$\frac{\Delta P}{\Delta s} = \frac{rg(h_Q - h_P)}{\Delta s}$$

where P is the gravitational potential per unit volume of liquid, ρ the density of the liquid, g the constant of gravitational acceleration, h_P and h_Q the elevations of point P and point Q relative to a common datum, Δs the length of a hypothetical route along which the liquid travels from point P to point Q on the surface of the rock particle. Thus the gravitational potential gradient is route-dependent. When point Q → point P, the gravitational potential gradient at point P along the vector Δ**r**, which starts from point P and ends at point Q, is

$$\frac{dP}{d\mathbf{r}} = \lim_{Q \to P} \frac{P_Q - P_P}{\mathbf{r}_Q - \mathbf{r}_P} = rg \lim_{Q \to P} \frac{h_Q - h_P}{\mathbf{r}_Q - \mathbf{r}_P} = rg \frac{dh}{d\mathbf{r}}$$

where $\mathbf{r}_P$ and $\mathbf{r}_Q$ are the two vectors from a common origin to the points P and Q, respectively. A drop of static liquid will tend to flow in the direction of negative greatest gravitational potential gradient, or maximum -dP/d**r**, which is the same as the direction of steepest slope on the particle surface, or maximum -dh/d**r.**

Once the liquid starts to flow and gains inertia, the motion of a fluid element will be governed by Newton's second law,

$$\frac{d^2\mathbf{r}}{dt^2} = \frac{\sum_{all\,i} \mathbf{f}_i}{r\mathrm{V}}$$

where V is the volume of the liquid element, $\mathbf{f}_i$ is the force vector of the ith force, and the summation is over all forces acting on that liquid element. The path of motion of the liquid element is determined by solving the above differential equation with it's initial position and velocity.

The summation of forces includes contributions of the gravitational force, which is a constant force vector acting on the liquid element and always pointing downward with numerical value equal to ρVg, and resistant forces. The resistant forces include friction due to particle surface roughness, surface tension due to factors such as hydrophobicity of the surface, and internal friction due to the viscosity of the liquid. The resistant forces are dependent of many properties of the liquid, the solid, and particle packing, and therefore are impossible to determine in reality. This means that the path of liquid motion cannot be calculated at the level of one particle, let alone the case with an aggregate of many particles. Therefore it is practically impossible to predict flow paths within channelling flow rock from fundamental principles of physics.

APPENDIX XI DEDUCTION OF THE KINEMATIC WAVE MODEL

The kinematic wave theory applied to macropore (channel) flows consists of two equations: one for mass balance and the other for flux relation. The mass balance equation is

$$\frac{\partial q}{\partial t} + \frac{\partial q}{\partial z} = -S \qquad \text{Equation 6-1}$$

where

- q is the volumetric water content, m^3/m^3, in macropores (flow channels) per unit volume of the of the entire soil media,
- q is the volumetric flux, or flow density in the nomenclature of this report, m/s, in the macropores (flow channels) per unit area of the entire soil media,
- S is the water uptake or loss by the soil media from the macropore system,
- z is depth below the soil surface, m
- t is time.

The flow density q is related to the moisture content θ by an empirical, power law,

$$q = bq^{a} \qquad \text{Equation 6-2}$$

where

- b is the macropore conductance, m/s, and
- a is an empirical dimensionless exponent constant, normally having a value in the neighbourhood of 2.5.

The velocity of macropore flow u, m/s, is given by

$$u = \frac{q}{q} = bq^{a-1} \qquad \text{Equation 6-3}$$

The initial and boundary conditions are described by

$$\begin{aligned} q(0,t) &= 0, && t \le 0 \\ q(0,t) &= q_0, && 0 \le t \le T \\ q(0,t) &= 0, && t \ge 0 \\ q(z,0) &= 0, && z \ge 0 \end{aligned} \qquad \text{Equation 6-4}$$

These equations describe a rectangle moisture pulse stating at t = 0 and ending at t = T, such as may be caused by a square pulse steady precipitation of equal duration. Note that θ is the moisture content in macropores, not the soil matrix, hence θ = 0 in the above initial and boundary conditions means there is no water in the macropores; it says nothing about the moisture in the soil matrix.

Equations (25), (26), and (28) can be combined and solved. To solve them, however, we need an expression for S in terms of θ. Now let us consider the case

$$S = rq$$ Equation 6-5

which means that the loss (uptake) term S is proportional to the moisture content in the macropores. R is a constant absorbance, 1/s. Combining (25), (26) and (29) gives

$$\frac{\partial q}{\partial t} + baq^{a-1}\frac{\partial q}{\partial z} = -rq$$ Equation 6-6

This is a first order, linear, nonhomogeneous partial differential equation (PDE) and can be solved using *the method of characteristics*. Farlow (1993) gives a short, but excellent account of this method. Using the method of characteristics, the above PDE can be replaced by a system of two ordinary differential equations (ODE):

$$\frac{dq}{dt} = -rq$$ Equation 6-7

$$\frac{dz}{dt} = abq^{a-1}$$ Equation 6-8

The solution to the above system of equations can be divided into two domains, D_1 ($0 \le t \le T$) and D_2 ($t \ge T$). In D_1, the solution is

$$q(z,t) = q_0\left[1 - \frac{z}{z^*}\right]^{\frac{1}{a-1}}$$ Equation 6-9

where

$$z^* = \frac{abq_0^{a-1}}{(a-1)r}$$ Equation 6-10

is the maximum depth the kinematic water wave can ever reach. The flow density and the flow velocity in D_1 are given by

$$q(z,t) = bq_0^a \left[1 - \frac{z}{z^*}\right]^{\frac{a}{a-1}}$$ Equation 6-11

$$u(z,t) = bq_0^{a-1} \left[1 - \frac{z}{z^*}\right]$$ Equation 6-12

It can be seen that θ, q, u depend only on z (non-uniform), but not on t (steady). The movement of the wetting front of the kinematic wave is given by

$$z_W(t) = z^* \left[1 - \exp\left(-\frac{r(a-1)t}{a}\right)\right]$$ Equation 6-13

and the time history of the wetting front movement is given by

$$t_W(z) = -\frac{a}{(a-1)r} \ln\left[1 - \frac{z}{z^*}\right]$$ Equation 6-14

where t_W denotes the time at which the wetting front position is z.

In domain D_2 ($t \geq T$), the solution of the ODE system is given by

$$q(z,t) = \exp[-r(t-T)] \left(\frac{(a-1)rz}{ab[1-\exp(-r(a-1)(t-T))]}\right)^{\frac{1}{a-1}}$$ Equation 6-15

and the flow density and velocity are

$$q(z,t) = b\exp[-r(t-T)] \left(\frac{(a-1)rz}{ab[1-\exp(-r(a-1)(t-T))]}\right)^{\frac{a}{a-1}}$$ Equation 6-16

$$u(z,t) = \frac{(a-1)rz}{a} \left(\frac{\exp[-r(a-1)(t-T)]}{1-\exp(-r(a-1)(t-T))}\right)$$ Equation 6-17

It can be seen that in D_2 θ, q, u are dependent on both z and t. At t = T, the surface moisture input stops, i.e., θ(0,t) = 0 for $t \geq T$. This causes a downward propagation of a draining front. Since the draining front moves down at a faster speed than the wetting front, eventually, the draining front intercepts the wetting

front at depth z_I and t_I, given by

$$z_I = z^*\left[1 - \exp(-rT)\right] \qquad \text{Equation 6-18}$$

$$t_I = \frac{a}{a-1}T \qquad \text{Equation 6-19}$$

During the time $T \le t \le t_I$, the time history of the draining front is given by $z_D(t)$, the depth of the draining front at time t, and $t_D(z)$, the time at which the draining front is at depth z:

$$z_D(t) = z^* \cdot \left[1 - \exp(-r(a-1)(t-T))\right] \qquad \text{Equation 6-20}$$

$$t_D(z) = T - \frac{1}{r(a-1)\ln(1 - z/z^*)} \qquad \text{Equation 6-21}$$

Now to compute the drainage flow density at a depth $Z \le z_I < z^*$, the following equations are used:

$$0 \le t \le t_W(Z): \quad q(Z,t) = 0$$

$$t_W(Z) \le t \le t_D(Z): \quad q(Z,t) = bq_0^a\left[1 - \frac{Z}{z^*}\right]^{\frac{a}{a-1}} \qquad \text{Equation 6-22}$$

$$t_D(Z) \le t \le t_I \quad q(Z,t) = b\exp\left[-r(t-T)\right]\left(\frac{(a-1)rZ}{ab[1-\exp(-r(a-1)(t-T))]}\right)^{\frac{a}{a-1}}$$

So the flow density q is predictable for t = 0 to $t = t_I$, which according to Equation 43 is equal to $1.67 \cdot T$ for a=2.5. That is to say, the model can be used to predict the flow from the beginning of a precipitation event up to 1.67 times the duration of the precipitation.

This completes the kinematic wave model for description of macropore flows in soils.